UNIVERSITÀ DEGLI STUDI DI TORINO
Dipartimento di Fisica Sperimentale

Intermediate mass di-muons in ultrarelativistic proton-nucleus and nucleus-nucleus collisions at the CERN SPS.

Tesi di Dottorato di Ricerca
di
Cristina Soave

Relatore
Prof.E.Chiavassa

Co-Relatore
Dott.E.Scomparin

Contro-Relatore
Mme.Claudie Gerschel

XI CICLO
Anni Accademici 1995-1998

Coordinatore
Prof.R.Garfagnini

INTRODUCTION

Statistical Quantum Chromodynamics predicts that, in nuclear matter under extreme temperature and/or energy density conditions, a deconfined state of quarks and gluons would be created : the quark gluon plasma (QGP). In ultra-relativistic heavy ion collisions, such extreme nuclear conditions should be reached and the deconfined phase should be characterised by the appearance of theoretically predicted signatures. An exploratory programme was thereafter started at the SPS at CERN, where 200 A GeV/c Oxygen ions were first accelerated in 1986, then followed by 200 A GeV/c Sulphur ions in 1987 and by 158 A GeV/c Pb ions from 1994 up to now. This programme, which main goal is the discovery of the deconfined plasma, also allows for a general study of the properties of hadronic matter as produced in nucleus-nucleus collisions.

The NA50 experiment at the CERN SPS studies the muon pair production in nucleus-nucleus collisions to probe the behaviour of nuclear matter under the aforementioned conditions. Since the dimuons generated in the interaction volume interact weakly with the hot surrounding medium, they can escape undisturbed and carry out informations about the state of the matter where they were generated.

The dimuon mass spectrum can be roughly subdivided in three main regions : the Low Mass Region (LMR) below the ϕ resonance, the Intermediate Mass Region (IMR) between the ϕ and the J/ψ and the High Mass Region (HMR) above the J/ψ. While the HMR is due to the superposition of dimuons from the DY process and from the leptonic decay of the J/ψ and ψ', dimuons in the LMR and IMR originate from different sources (hadron Dalitz decays, charmed meson semi-leptonic decays and DY) with individual shapes and relative contributions not immediately deducible from the data.

The combinatorial background, due to the combination of muons from pion and kaon decays, also gives a very important contribution in the intermediate and low mass regions. In particular, its contribution to the IMR opposite-sign mass spectrum can amount up to 85% in proton-nucleus and central 200 A GeV/c S-U collisions, and up to 95% in central Pb-Pb collisions. Therefore, in order to study the IMR dimuon sources and their behaviour with changing energy and centrality of the collision, the combinatorial background has to be subtracted in such a way that no doubt remains about the nature of the measured signal. The shape of the mass distribution of the opposite-sign combinatorial background is usually extracted from the experimental like-sign background distributions. The normalisation of the background contribution to the opposite-sign dimuon spectrum can also be extracted using the same methods, if we are dealing with interactions where the produced high particle multiplicities simulate the absence of charge correlation effects. When charge correlation effects can not be neglected, they have to be carefully estimated to eventually cor-

rect the background normalisation factor.

Experimental evidences exist that in nucleus-nucleus collisions at SPS energies the dilepton production in the low and intermediate mass regions is enhanced with respect to the expected yields as extrapolated from proton-nucleus results. This motivates the present study, where the IMR for the 450 GeV/c p-A(A=Al,Cu,Ag,W), 200 A GeV/c S-U and 158 A GeV/c Pb-Pb data sets is studied. The intermediate mass region is here assumed to be a superposition of dimuons from DY, charmed hadron decays and combinatorial background. In this thesis, the effect of the residual charge correlation effects on the background normalisation factor is studied with a specifically developed MC chain. Monte-Carlo techniques have been used to generate the DY and open charm mass, transverse momentum, rapidity and angular differential distributions. The Monte-Carlo generated mass distributions have then been used to fit the data in order to determine their relative contributions to the experimental opposite-sign mass spectra. Since the background contribution to the opposite-sign mass spectra is fixed with the calculated normalisation factors and the DY contribution is determined by the high mass region, where only DY muon pairs can be found, our approach corresponds to interpret the dimuon excess in the IMR as due to an enhanced open charm production.

In the first chapter of the present thesis, after a general overview of the physics of heavy ion collisions, the dimuon excess measured in the low and intermediate mass regions by the experiments CERES, HELIOS/3 and NA38/NA50 at SPS is discussed. In the same chapter, the physics of DY pair production and open charm hadro production process is detailed. Chapter 2 describes the NA38/NA50 experimental apparatus, whereas chapter 3 quickly outlines the method used to reduce the experimental data.

Chapter 4 details the Monte-Carlo techniques used to obtain the mass, transverse momentum, rapidity and angular differential distributions for all the processes contributing to the intermediate mass region. In chapter 5 I describe the Monte-Carlo chain specifically developed in order to compute the combinatorial background normalisation factors for each of the considered systems. This approach is new and different from the one adopted by the NA38/NA50 Collaborations in the past.

Chapter 6 details the analysis of the IMR of the 450 GeV/c pA, 200 A GeV/c SU and 158 A GeV/c PbPb systems. The acceptance corrected open charm and DY contributions for each of the studied systems are extracted by means of a fit of the corresponding mass spectra. This study is performed as a function of the centrality of the collision. As a result, the extracted open charm yield in nucleus-nucleus collisions is found to be enhanced with respect to QCD expectations.

In chapter 7 it is shown that the found open charm enhancement quadratically in-

creases with the collision centrality. Since open charm hadro production is a hard process, and is therefore expected to linearly increase with the collision centrality, this result clearly indicates the existence of a new process for open charm production in nucleus-nucleus collisions. The results are then discussed in the light of the existing theoretical models.

INTRODUZIONE

La Cromodinamica Quantistica Statistica predice che, nella materia nucleare ad alte densità di energia e/o temperatura, una transizione di fase da materia adronica confinata a materia di quarks e gluoni deconfinati dovrebbe avere luogo. Nella fase deconfinata la materia consisterebbe dunque di un plasma di quarks e gluoni liberi (QGP). Valori di densità di energia e temperatura sufficienti a provocare suddetta transizione possono essere raggiunti nelle collisioni ultrarelativistiche di ioni pesanti, dove inoltre la formazione del plasma di quarks a gluoni dovrebbe essere segnalata dall'apparire di chiari segnature fisiche. Un programma esplorativo fu dunque inaugurato al Super Proton Syncroton (SPS) al CERN nel lontano 1986, dove ioni ossigeno a 200 GeV/c per nucleone furono inizialmente accelerati, poi seguiti da ioni zolfo a 200 GeV/c per nucleone nel 1987 e finalmente da ioni piombo a 158 GeV/c per nucleone dal 1994 a oggi. Suddetto programma, il cui scopo primo è la scoperta e lo studio del plasma deconfinato, permette inoltre uno studio generale delle proprietà della materia adronica prodotta in collisioni nucleo-nucleo.

L'esperimento NA50 al CERN studia appunto la produzione di coppie di muoni (anche detti di-muoni) in collisioni nucleo-nucleo allo scopo di indagare sul comportamento della materia nucleare quando sottoposta alle summenzionate estreme condizioni. I di-muoni prodotti in una collisione, interagendo solo debolmente con l'ambiente nucleare circostante, possono infatti sfuggire indisturbati dal volume di interazione e portare fino a noi importanti informazioni sullo stato della materia ivi contenuta.

Lo spettro di massa dei di-muoni viene generalmente suddiviso in tre grandi regioni : la regione delle basse masse, delimitata superiormente dal picco della risonanza vettoriale ϕ, la regione delle masse intermedie, compresa tra la ϕ e la J/ψ ($1.3< M <2.5$ GeV/c^2), e la regione delle alte masse, dalla J/ψ in su. La regione delle alte masse è dovuta alla sovrapposizione di di-muoni provenienti dal decadimento delle risonanze vettoriali J/ψ e ψ' e prodotti nel processo di Drell-Yan. Le regioni delle basse masse e delle masse intermedie sono invece di più difficile descrizione, risultando dalla sovrapposizione di distribuzioni di di-muoni prive di struttura risonante, derivanti da sorgenti quali i decadimenti Dalitz degli adroni prodotti nella collisione, i decadimenti semi-leptonici dei mesoni e barioni con charm e il processo di Drell-Yan.

Bisogna inoltre considerare il contributo del fondo combinatoriale generato dalla combinazione dei muoni provenienti dal decadimento dei pioni e kaoni prodotti nella collisione, la cui sottrazione deve avvenire in modo tale da eliminare ogni dubbio sulla natura del segnale analizzato. Il contributo del fondo combinatoriale nella regione delle masse intermedie, dove quest'ultima costituisce l'oggetto dello studio della presente tesi, può ammontare fino all'85% dello spettro di massa in collisioni protone-nucleo ed in collisioni S-U, ed addirittura fino al 95% in collisioni centrali

Pb-Pb. La distribuzione in massa del fondo combinatoriale di di-muoni di segno opposto può essere facilmente dedotta utilizzando le distribuzioni del fondo combinatoriale di di-muoni dello stesso segno, essendo queste ultime costituite da solo fondo combinatoriale. Il contributo assoluto del fondo combinatoriale agli spettri di massa dei di-muoni, può anche essere calcolato a partire dagli spettri di massa di di-muoni dello stesso segno, se la molteplicità dei secondari (pioni e kaoni) prodotti nella collisione è così elevata che ogni correlazione di carica può essere trascurata. In caso contrario, gli effetti della correlazione di carica devono essere accuratamente valutati, e la normalizzazione del fondo combinatoriale corretta di conseguenza.

Sussistono evidenze sperimentali indicanti l'esistenza di un eccesso nella produzione di di-muoni nelle masse basse ed intermedie degli spettri misurati in collisioni nucleo-nucleo alle energie del SPS, se confrontata con estrapolazioni da risultati in protone-nucleo. Appunto l'esistenza di suddetto eccesso motiva lo studio contenuto nella presente tesi, dove la regione delle masse intermedie è studiata su dati ottenuti in collisioni pA (A=Al, Cu, Ag, W) a 450 GeV/c, S-U a 200 GeV/c per nucleone e Pb-Pb a 158 GeV/c per nucleone. In questo studio, la regione delle masse intermedie, dopo un'attenta sottrazione del fondo combinatoriale, viene descritta come una sovrapposizione di di-muoni dal processo duro di DY e dai decadimenti semi-leptonici dei mesoni e barioni charmati, anche generalemente indicati come charm aperto o $D\overline{D}$. L'effetto della residua correlazione di carica sul fattore di normalizzazione del fondo combinatoriale è studiato utilizzando una catena Monte-Carlo specificamente realizzata. Le forme differenziali delle distribuzioni di massa, momento trasverso, rapidità e angolo dei di-muoni da DY e charm aperto sono generate con metodi Monte-Carlo. Lo spettro di massa sperimentale è successivamente interpolato usando le forme in massa così ottenute. La normalizzazione del contributo del processo di DY nello spettro di massa sperimentale è fissata dalla regione delle alte masse, essendo quest'ultima puramente costituita da di-muoni prodotti in suddetto processo. Dato che anche la normalizzazione del fondo combinatoriale è fissata secondo quanto calcolato con la summenzionata catena Monte-Carlo, l'approccio assunto nella presente tesi equivale a interpretare l'eccesso di di-muoni delle masse intermedie come dovuto esclusivamente ad un'aumentata produzione di charm aperto.

Nel primo capitolo, dopo una breve introduzione generale sulla fisica degli ioni pesanti, l'eccesso misurato nelle regioni di massa bassa ed intermedia dagli esperimenti HELIOS/3, CERES e NA38/NA50 al SPS è discusso parallelamente alle esistenti interpretazioni teoriche dello stesso. Nello stesso capitolo è descritta la fisica dei processi duri di Drell-Yan e di produzione adronica di charm aperto. Nel secondo capitolo l'apparato sperimentale di NA38/NA50 è dettagliato, mentre il capitolo terzo spiega brevemente il metodo adottato per processare i dati sperimentali.

Il capitolo quarto contiene una dettagliata descrizione delle tecniche

Monte-Carlo utilizzate onde generare tutte le distribuzioni differenziali dei processi che contribuiscono allo spettro di massa. Il capitolo quinto, che con i capitoli sesto e settimo costituisce il cuore della mia tesi, è completamente dedicato alla descrizione della catena Monte-Carlo specificamente sviluppata per calcolare il fattore di normalizzazione del fondo combinatoriale quando gli effetti di correlazione di carica non possono essere trascurati. Tale approccio è innovativo rispetto a quello fino ad oggi adottato dalla Collaborazione NA38/NA50.

Nel capitolo sesto la regione intermedia degli spettri di massa dei sistemi studiati, 450 GeV/c pA, 200 A GeV/c SU e 158 A GeV/c PbPb, è analizzata. Per ognuno dei detti sistemi, i contributi del DY e del charm aperto sono estratti dallo spettro di massa e sono successivamente corretti per le accettanze. Il contributo del charm aperto dedotto da detto studio, che è stato effettuato in funzione della centralità della collisione, risulta più elevato di quanto atteso nell'ambito della QCD perturbativa.

Nel capitolo settimo, l'eccesso di produzione di charm aperto è mostrato quadraticamente crescere con la centralità della collisione. Dato che la produzione adronica di charm aperto, essendo un processo duro, è supposta crescere linearmente con la centralità della collisione, tale risultato chiaramente indica l'esistenza di anche un altro processo per la produzione di charm aperto in collisioni nucleo-nucleo. La tesi conclude con una discussione sulle teorie esistenti, da cui detto eccesso è interpretato sia nell'ipotesi che si tratti effettivamente di un'aumentata produzione di charm aperto, sia che si tratti di processi di diversa natura contribuenti nello stessa regione di massa.

Contents

List of Tables

Chapter 1

Heavy ion physics

In this chapter a quick overview of the physics of heavy ions is presented. After a general introduction, the study of dimuon production in heavy ion collisions is specifically addressed. The dilepton production from DY, charmed hadron decays, thermal sources, low mass and high mass resonance decays is described. The dimuon excess measured by the CERES, HELIOS/3 and NA38/NA50 experiments in previous analysis of the low and intermediate mass region are discussed and compared with some of the existing theoretical interpretations.

When the structure of the vacuum is violently
disturbed in a high energy nuclear collision
and the soft and colourless hadronic world
suffers the intrusion of the abundantly
produced coloured gluons and quarks..... (D.Kharzeev)

1.1 Introduction

Statistical Quantum Chromodynamics predicts that, in nuclear matter under high temperature and/or energy density conditions, a deconfined state of quark and gluon would be created, the quark gluon plasma (QGP). The temperature reached in the interaction volume of a heavy ion collision at SPS, where $\sqrt{s}$=17.22÷19.37, should be high enough to motivate the search for the predicted phase transition. Important indications on the nature of the mechanisms responsible for the confinement of quarks in hadrons and for the spontaneous chiral symmetry breaking could come from the study of the QGP. Furthermore, cosmological and astrophysical issues such as primordial black hole evaporation, cosmological nucleosynthesis and the search for a dark matter candidate could be better understood. Moreover, the core of neutron stars could consist of a low temperature and high density plasma of quarks and gluons, whose equation of state could be calculated if the equation of state of the high temperature-high density QGP formed in heavy ion collisions was known.

1.2 The phase transition

The strong interaction between partons inside hadrons is characterised by the so called asymptotic freedom at small distances and by a steep grow of the binding force as the distance between the constituents becomes larger, the so called colour confinement. This is due to the typical behaviour of the coupling constant α_s of strong interactions, which increases with growing distance between the constituent quarks. This is the reason why in ordinary nuclear matter quarks are confined inside hadrons.
At sufficiently high temperature and/or density (3 to 5 times higher than the ordinary nuclear matter density) a phenomenon similar to the Debye (charge) screening in a dense medium takes places. In a dense medium, the Coulomb potential between two electric charges, say a proton and a electron, is screened by the presence of a high density of negative charges surrounding the positive one, and it accordingly changes,

$$V(r) = \frac{e}{r} \rightarrow \frac{e}{r} \exp\left(-\frac{r}{r_d}\right) \tag{1.1}$$

where r_d is the Debye radius and $r_d \sim 1/\rho$ if ρ is the matter density. As r_d becomes smaller and smaller, the material undergoes the transition from insulator to (semi)conductor. For the same reason, the colour interquark potential

$$V(r) = \sigma r - \frac{\alpha}{r} \tag{1.2}$$

will experience screening in a medium characterised by a very high density of colour

charges. The effect of the screening can be parametrised as

$$V(r,T) = \left(\frac{\sigma}{\mu(T)}\right)\left\{1 - e^{-\mu(T)r}\right\} - \frac{\alpha}{r}e^{-\mu(T)r} \tag{1.3}$$

were $\mu(T)$=$1/r_c$ is the screening mass and r_c is the colour screening radius : when r_c becomes very small, the potential goes to zero causing the hadrons to dissolve[1]. Quarks confined in a hadron have a non zero mass because of the interaction with the other quarks and gluons. When quarks become free in the deconfined phase, their masses drop to smaller values which ideally tend to zero. The bare or current-quark masses are $m_u \simeq 1.5 \div 5$ MeV, $m_d \simeq 3 \div 9$ MeV and $m_s \simeq 60 \div 170$ MeV[2]. The dropping of the quark masses would cause the so called chiral symmetry restoration of the QCD Lagrangian, where the latter is defined by

$$L_{QCD} = -\frac{1}{4}F^a_{\mu\nu}F^{\mu\nu}_a - \sum_f \overline{\psi}^f_\alpha (i\gamma^\mu \delta_\mu + m_f - g\gamma^\mu A_\mu)^{\alpha\beta}\psi^f_\beta \tag{1.4}$$

The so called chiral operator is the operator γ_5 which causes the chiral rotation of the quarks four-spinor, i.e.,

$$\psi \rightarrow \psi' = e^{(i\alpha\gamma_5)}\psi \tag{1.5}$$

The mass term $\overline{\psi}\psi$ in the QCD Lagrangian is not invariant under such rotation as

$$\overline{\psi'}\psi' = \overline{\psi}e^{(2i\alpha\gamma_5)}\psi \neq \overline{\psi}\psi \tag{1.6}$$

All the other terms in the Lagrangian are invariant under this operation because the matrices γ_μ anti-commute, by definition, with the matrix γ_5. It is quite clear then why a non zero quark mass destroys the chiral symmetry of the Lagrangian, from which the name of chiral symmetry restoration in the case of zero quark masses. In fact, interactions are never really turned off and only a partial chiral symmetry restoration is thus expected. Furthermore, it is still a matter of discussion if the chiral symmetry restoration coincides with the deconfinement or not.
Perturbative QCD can only be applied for small values of the QCD coupling costant. When studying nuclear matter under extreme density and/or temperature conditions, the perturbative approach has to be substituted by models or lattice QCD calculations[3][4]. Lattice QCD calculations predict that the phase transition should take place at the critical energy density ϵ=$2 \div 3$ GeV/fm^3 corresponding to $T_c \simeq$260 MeV for a pure gluon plasma and $T_c \simeq$150 MeV when 2 light quarks are included. It is therefore important to establish if such energy densities are actually released in the interaction volume of a heavy ion collision at SPS energies. This can be done measuring the transverse energy of the collision, defined as

$$E_T = \sum_i E_i \sin\theta_i \tag{1.7}$$

where the sum runs over all the secondary particles (mainly pions) produced in the interaction. In practice, the sum runs over the secondaries which can actually be detected. The transverse energy is usually measured by mean of a hadron calorimeter. In NA38/NA50 practical reasons suggested the use of an electro-magnetic calorimeter or EMCal. The NA50 EMCal measures the energy deposited in the calorimeter by the neutral pions produced in the collision. The relation between energy density and transverse energy is model dependent. Two very different descriptions are given by the fireball model, which calculates the energy density with the assumption of complete stopping in the collision, and the Bjorken model, which assumes a complete transparencies of the two colliding nuclei. The first model can be used when considering low energy heavy ion collisions as, for instance, in the Au-Au collisions at AGS; in this case the stopping power has been measured to be very large, i.e., most of the baryon content of the incoming nuclei can be found in the interaction region. Since in Pb-Pb collisions at the SPS energies only few tenth of nucleons can be found in the interaction volume, the NA38/NA50 Collaboration calculates the energy density from the measured transverse energy on the basis of the Bjorken model, i.e.

$$\epsilon = 3\frac{E_T^0}{\Delta y S_T \tau_0} \tag{1.8}$$

where τ_0 is the so called formation time, i.e. the time needed to pass from the initial hadronic to the partonic degrees of freedom, S_T is the transverse area interested by the collision and Δy is the covered rapidity interval. The factor 3 in eq.1.8 is needed to take into account the transverse energy of the charged secondaries.
The energy density profiles for very central 200 A GeV/c S-U and 158 A GeV/c Pb-Pb collisions are shown in fig.1.1. The average energy density is similar in the two cases, but in Pb-Pb collisions the locally deposited energy density can be 30-40% larger than in S-U collisions. The probability that a quark gluon plasma can be formed is therefore larger in very central Pb-Pb collisions than in very central S-U ones.

1.3 Experimental signals of the phase transition

Many theoretical models predict which kind of new physics would indicate the creation of a deconfined volume of matter in a heavy ion collisions. Strange matter enhancement, thermal dilepton and photon production, J/ψ suppression, charm thermal production are some of the predicted signals. Experimentally, the differential distributions of the dilepton produced in heavy ion collisions can be studied, as later explained. Dileptons can be produced in the semi-leptonic decay of the secondary hadrons in the collision or in the electro-magnetic annihilation of confined or deconfined partons.

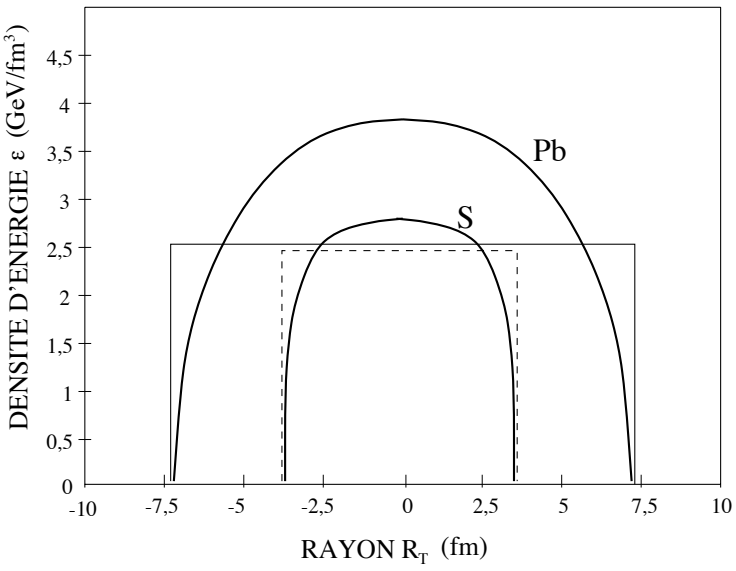

Figure 1.1: *Energy density profile calculated for central 158 A GeV/c Pb-Pb and 200 A GeV/c S-U collisions. The 'Rayon' R_T measures the transverse nuclear size.*

The present section describes important issues as J/ψ suppression, strangeness enhancement, thermal dimuon and charm production and vector meson $in-medium$ modification. In section 1.6 the DY and charm hadro-production processes, whose understanding is essential to the goal of the present thesis, are discussed in some more details. The last section is then dedicated to the discussion of the low and intermediate mass dilepton enhancement measured by NA38/NA50, CERES and HELIOS/3 at the CERN SPS.

1.3.1 Production and suppression of $c\overline{c}$ states

In 1986, Matsui and Satz[5] proposed the J/ψ suppression as an unambiguous signal of the formation of the quark gluon plasma. Since then, many improvements have been done in the understanding of the underlying physics. The 200 GeV/c p-A and 200 A GeV/c S-U NA38 data[6] can be well reproduced by the so called colour octet model. It this model, both the J/ψ and the ψ' are produced as a coloured $(c\overline{c})_8 g$ state. The coloured $(c\overline{c})_8 g$ state propagates in the surrounding medium and can therefore be broken by interactions with gluons which would couple either to the collinear gluon or to the coloured $(c\overline{c})_8$. This would suppress the J/ψ and ψ' production in exactly the same way, resulting in a constant $\psi'/J/\psi$ ratio. If the $(c\overline{c})_8 g$ state survives, the colourless resonance is created with the absorption of the collinear gluon by the $(c\overline{c})_8$ system.

Once the resonance has been formed, it can be suppressed through the exchange of

hard gluons with the co-moving mesons produced in the collision,

$$\psi' + h \longrightarrow D + \overline{D} + X \tag{1.9}$$

Since the ψ' has a much lower binding energy than the J/ψ, 60 MeV and .64 GeV respectively, it can be easily broken in co-movers interactions. This theory well reproduces the $\frac{J/\psi}{DY}$ and $\frac{\psi'}{J/\psi}$ behaviour found in p-A and S-U collisions by the NA38 Collaboration. The measured $\frac{\psi'}{J/\psi}$ is constant for all p-A data but falls down in S-U collisions due to the ψ' suppression by final state interaction with the hadrons produced in the collision. The multiplicity of hadrons in the final state increases with the collision centrality and so does the ψ' suppression.
The NA50 Collaboration has reported a first evidence of strong J/ψ suppression in Pb-Pb collisions at 158 A GeV/c[7]. The observed suppression can not be explained in the frame of the above described theory. Models based on the comover absorption mechanism can not account for both the S-U and Pb-Pb results at the same time[6], whilst a successful reproduction of all data can be obtained in the hypothesis that a deconfined system has been created in central Pb-Pb collisions.

1.3.2 Strangeness enhancement

In 1982 J.Rafelski and B.Muller predicted that strangeness production would be enhanced in a QGP[8]. In a QGP, strange quarks would be abundantly produced in the processes :

$$q\overline{q} \longrightarrow s\overline{s} \tag{1.10}$$

$$gg \longrightarrow s\overline{s} \tag{1.11}$$

(where $q = (u, d)$), because of their dropping mass and because the Fermi levels for the lighter quark species would be quickly filled; the production of s quarks would then be favoured by the Pauli exclusion principle.
Experimentally, an enhancement in strangeness production could be seen as an enhanced strange meson and baryon yield, as ϕ, Λ, $\overline{\Lambda}$, Ω, Ξ, and/or via the appearance of strange matter lumps (the so called 'strangelets'[9]). At the CERN SPS three experiments have been mainly dedicated to this specific signature, WA85, WA94 and WA97[10]. WA85 and WA94 used the 200 A GeV/c S beam, whilst WA97 uses the 158 A GeV/c Pb one. The NA38/NA50 Collaboration has also measured the strangeness enhancement in d-A (A=C,U), 200 A GeV/c S-U and 158 A GeV/c Pb-Pb collisions[11]. Whilst the WA85, WA94 and WA97 experiments measure the production of multistrange hyperons, such as Λ, Ω and Ξ, the NA38/NA50 Collaboration measures the ratio $\phi/(\rho + \omega)$, assuming the ρ and the ω meson to remain unaffected by the hot and dense surrounding medium. The WA97 experiment recently observed a strangeness enhancement, with respect to extrapolation from p-Pb results, which increases with centrality and with the strangeness content of the hyperon[10].

1.3.3 Open-charm thermal production

In 1988-89, Shor[12, 13] studied the possibility of thermal charm production in a quark gluon plasma. His calculations, based on Bjorken hydrodinamical model, showed that the charm thermal contribution could eventually become important for temperature of the plasma above 500 MeV. Even if this was the case, only a slight open-charm enhancement in the dimuon mass spectrum below 1.5-2 GeV/c^2 would be seen.

In a recent publication[14], the charm thermal production in a quark gluon plasma has been studied for the future experiments RHIC and LHC where the energy density should be large enough to enable the QGP creation. The temperature T in the interaction volume is predicted to amount to $\simeq 0.35 \div 0.55$ GeV at RHIC ($\sqrt{s}$=200 A GeV) and to $\simeq 0.7 - 1$ GeV at LHC ($\sqrt{s}$=5.5 A TeV). In the proposed model, partons in a QGP would acquire temperature dependent effective masses favouring the creation of heavy quarks. The final thermal $c\overline{c}$ yield strongly depends on the adopted charm mass. At SPS the temperature in the interaction volume is just above the critical temperature predicted by lattice QCD calculations and the thermal charm production by massive gluons and quarks in a QGP seems highly improbable.

1.3.4 Thermal dileptons

Thermal dileptons can be produced either in a QGP or in a thermalized hadron gas[15, 16, 17]. Thermal dilepton production in a QGP is due to quark and antiquark annihilation in the thermalized medium. This process differs from the DY pair production process, which is due to a single-pair annihilation of hard quarks; thermal dimuons are produced after the quarks from the nucleons have thermalized through the exchange of a number of gluons with the surrounding partons[18]. Thermal dileptons generated in a dense thermalized hadron gas are produced in hadronic secondary collisions such as,

$$\pi\pi \longrightarrow l\overline{l} \tag{1.12}$$

$$\pi\rho \longrightarrow l\overline{l} \tag{1.13}$$

$$\pi a_1 \longrightarrow l\overline{l} \tag{1.14}$$

$$\pi\omega \longrightarrow l\overline{l} \tag{1.15}$$

$$K\overline{K} \longrightarrow l\overline{l} \tag{1.16}$$

$$K\overline{K}^* + c.c. \longrightarrow l\bar{l} \tag{1.17}$$

Both thermal dileptons from a QGP and/or from a dense hadron gas would give precious informations on the temperature of the volume of matter where they were generated.

In ref.[19] the contribution of dimuons generated in a *hadron gas* in the mass range $1< M <2.5\ GeV/c^2$ of the dilepton spectrum is carefully calculated. It is found that the dilepton yield from a hadron gas strongly depends on the temperature and that the most important contribution to the thermal dileptons is due to the $\pi a_1 \longrightarrow l\bar{l}$ annihilation process. This is shown in fig.1.2, where the predicted thermal yield from a hadron gas within the HELIOS/3 experimental acceptance is depicted for central S-W collisions.

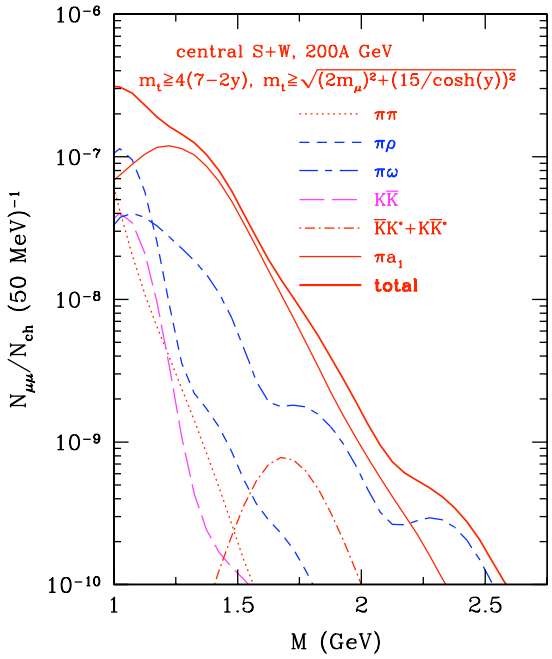

Figure 1.2: *Dimuon spectra in central S-W collisions at 200 A GeV/c from different secondary process as calculated in ref.[19].*

In ref.[20] the expected thermal dimuon contribution from the hot QGP phase and the subsequent HG has been calculated for SPS energies. Different equation of states, corresponding to different values of the critical temperature T_c, have been used. Different initial conditions (IS), corresponding to different initial energy densities and velocity profiles, have also been considered for each equation of state. The theoretically predicted thermal dimuon mass shape depends on the initial conditions for masses $\geq 2\ GeV/c^2$, as shown in fig.1.3. The mass spectrum shape in the IMR

should be therefore used to distinguish between different inital state conditions. Since in the IMR M$\gg T_c$, where $T_c \approx$200 MeV, the main contribution comes from thermal dimuons produced in the hot initial phase.

In ref.[17], the different shapes of the contribution of dileptons from the hadron gas and from the QGP phase to the measurable dilepton mass spectra is depicted for AGS energies. The contribution from the $\pi\pi$ annihilation channel, which dominates from the $2m_\pi$ threshold up to 1 GeV/c^2, is predicted to be suppressed if a QGP is created. This is due to the larger hadronic density in the hadronic scenario, where hadrons are produced in the first stages of the system evolution. For M$>$ 2 GeV/c^2 the contribution of dilepton from the elementary $q\overline{q}$ annihilation in the QGP is predicted to be larger than the contribution from the $\pi\pi$ annihilation channel.

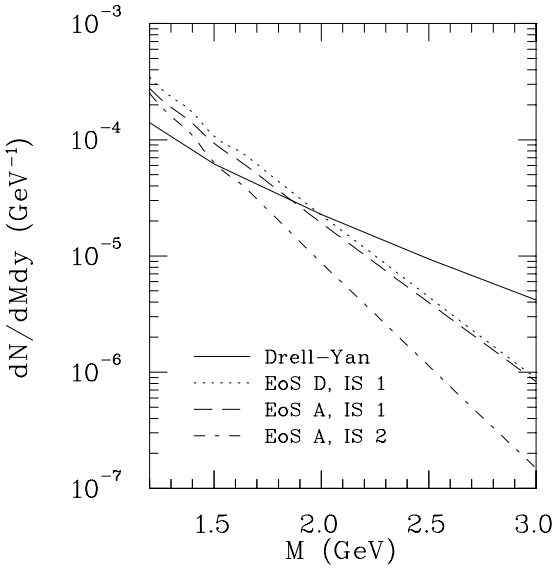

Figure 1.3: *Calculated mass distribution of thermal electron pairs compared to the calculated distribution for DY dileptons at $y_{CM} = 0$. No kinematic cuts have been applied[20].*

The comparison of the above theories with experimental results is later discussed.

1.3.5 Vector meson in-medium characteristics

If chiral symmetry is restored in the hot and dense volume of matter created in heavy ion collisions, the vector meson masses should drop to lower values. Dilepton pairs are generated through vector meson decay

$$V \longrightarrow l^+ l^- \tag{1.18}$$

The study of vector mesons is complicated by the fact that leptons are generated at different times in the interaction volume history. This makes it difficult to deconvolute the signals and separate leptons coming from regions of different temperature and/or baryonic density.

Because of its very small life time, Γ =150.7±1.1 MeV, the ρ meson can decay inside the interaction volume, when its actual mass is still affected by the state of the lump of matter created in the collision. There exist many different models trying to predict the mass and width evolution of vector mesons and of the ρ meson in particular, and not all of them agree in predicting a lowering of its mass with increasing temperature and/or baryonic density[21, 22]. In the following section some of the most successful theoretical predictions and/or descriptions of experimental data are discussed.

1.4 Useful variables

I here give a brief definition of some important variables which will be widely used in the following of the present work.

In the collision of two hadrons, the hadron-hadron center-of-mass energy squared is defined as,

$$s = (p_1 + p_2)^2 \tag{1.19}$$

where p is the hadron four-momentum. In the collision, one parton from one of the two hadrons interacts with a parton from the other hadron. Each of the two interacting partons carries a fraction x of the four-momentum of the hadron it belongs to. For the system of the two colliding partons, the elementary parton-parton center-of-mass energy squared can be defined as

$$\hat{s} = x_1 x_2 s \tag{1.20}$$

where x_i is the *longitudinal momentum fraction* carried by the parton i.

The invariant mass of the elementary reaction is

$$M^2 = (x_1 p_1 + x_2 p_2)^2 \simeq x_1 x_2 s \tag{1.21}$$

A very widely used variable is the *rapidity* y

$$y = \frac{1}{2} ln \frac{(E + p_z)}{(E - p_z)} \tag{1.22}$$

When $p \gg m$ the rapidity y is well approximated by the *pseudo-rapidity* η

$$\eta = -ln(tan(\frac{\theta}{2})) \tag{1.23}$$

where θ is the particle polar angle. An important property of the rapidity y is the invariance of the shape of the rapidity distribution dN/dy with respect to a boost in the z-direction. This means that under a boost in the z-direction with velocity β, $y \rightarrow y + tanh^{-1}\beta$. If p_L^* is the longitudinal momentum and y^* the rapidity in the parton centre of mass frame, the following equation holds,

$$p_L^* = m_T \cdot \sinh y^* \tag{1.24}$$

From the above definitions, the *scaling* variable τ can be defined:

$$\tau \equiv \frac{M^2}{s} = x_1 x_2 \tag{1.25}$$

with which

$$x_1 = \sqrt{\tau} e^{+y^*} \tag{1.26}$$

$$x_2 = \sqrt{\tau} e^{-y^*} \tag{1.27}$$

The *longitudinal momentum fraction of the parton pair*, or Feynman variable x_F, is defined as

$$x_F \equiv \frac{2p_L^*}{\sqrt{s}} = x_1 - x_2 \tag{1.28}$$

1.5 The $Drell - Yan$ process

The Drell-Yan process consists of the electro-magnetic annihilation of a (valence or sea) quark and an antiquark of the same flavour in a hadron-hadron interaction, as shown in fig.1.4. In the annihilation, a lepton pair is created along with some unobserved hadrons.

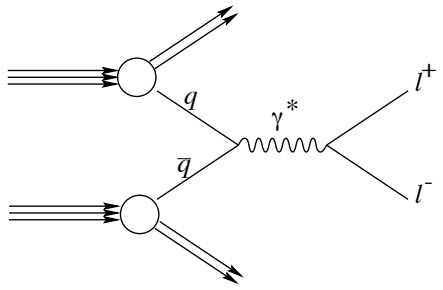

Figure 1.4: *The DY process.*

The cross-section for the elementary process

$$q_i\overline{q_i} \rightarrow \gamma^* \rightarrow l^+l^- \tag{1.29}$$

is

$$\frac{d\sigma}{d\Omega} \mid_{c.m.s.} = \frac{4\alpha^2}{16M^2}e_i^2(1+cos^2\theta) \tag{1.30}$$

which integrated gives

$$\sigma_i(q_i\overline{q_i} \rightarrow \gamma^*) = \frac{4\pi\alpha^2}{3M^2}e_i^2 \tag{1.31}$$

where e_i is the quark electric charge and M is the invariant mass of the produced l^+l^- pair. If we take into account the probability of finding the quark and the antiquark i in the hadrons A and B, we obtain for the DY differential cross section calculated in the frame of the naif parton model :

$$\frac{d^2\sigma}{dx_1dx_2} = \frac{1}{3}\frac{4\pi\alpha^2}{3M^2}\sum_i e_i^2[f_i^A(x_1)\overline{f_i^B}(x_2) + \overline{f_i^A}(x_1)f_i^B(x_2)] \tag{1.32}$$

where the $f_i^H(x_j)$, with H=A, B and $j = 1, 2$, are the so called *parton distribution functions* (PDF's). $f_i^H(x_j)dx$ represents the probability of finding the parton of type i in the hadron H, carrying a longitudinal momentum fraction between x_j and $x_j + dx$ of the total longitudinal hadron momentum. The factor 1/3 ensures that only parton-antiparton annihilation between partons of the same flavour are taken into account. When corrections to the cross-section 1.32 are added in the leading order approximation (LLA), eq.1.32 becomes

$$\frac{d^2\sigma}{dx_1dx_2} = \frac{4\pi\alpha^2}{9M^2}\sum_i e_i^2[f_i^A(x_1,Q^2)\overline{f_i^B}(x_2,Q^2) + \overline{f_i^A}(x_1,Q^2)f_i^B(x_2,Q^2)] \tag{1.33}$$

Q^2 is the so called *scale* where $Q^2 = -q^2$ if q^2 is the transferred four-momentum. The scale dependence in the DY cross section 1.33 is due to the inclusion of the leading corrections to the basic process in the so called leading log or leading order (LO) approximation. These corrections, mainly due to gluons, behave as $log(Q^2)$ and introduce singularities which are then re-absorbed redefining the PDF's. The absorption of the singularities through the redefinition of the PDF's is the *factorisation theorem*. The redefined PDF's depend on the scale Q^2 and their Q^2 evolution can be calculated with the GLAP (Grigov-Lipatov-Altarelli-Parisi) equations.

An important consequence of the *factorisation theorem* is the *universality* of the redefined PDF's. This means that the PDF's are the same for all pQCD processes.

In order to extract information on the PDF's, the cross sections for deep inelastic scattering (DIS) processes can be measured; from the measured cross sections, the nucleon structure functions can be deduced and the PDF's extracted. These PDF's can then be used in the calculation of the cross sections of different pQCD processes.

The LLA theoretical cross section underestimates the experimentally measured values by a factor ≈ 2. The ratio

$$K^{DY} = \frac{\text{experimentally measured cross section}}{\text{Theoretical prediction}} \tag{1.34}$$

measures the discrepancy between the theoretically computed and experimentally measured cross sections. In fig.1.5[7], the K^{DY}_{MRS-A} factor measured by NA38, NA51 and NA50 in p-p, p-d, p-A, S-U and Pb-Pb collisions is shown vs. $A \cdot B$, where A and B are the projectile and target atomic numbers. The measured K_{DY} does not show any energy dependence.

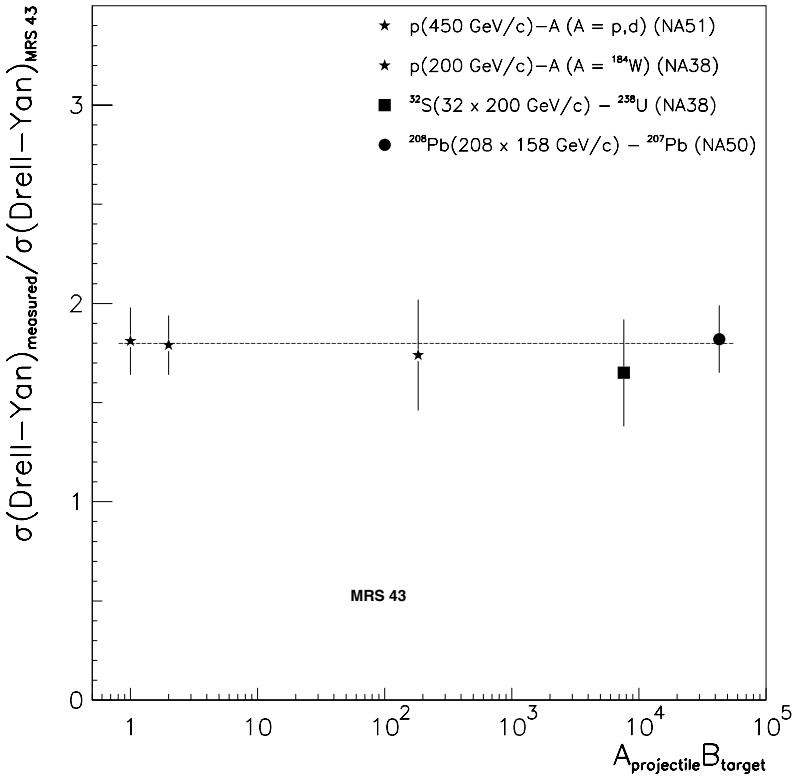

Figure 1.5: *The K^{DY} factor as measured by the NA38/NA51/NA50 experiments. The MRS A (set no.43) PDF's set has been used.*

The DY cross section depends on the valence quark contents of the two colliding hadrons. Therefore, the DY cross section in pp, pn, np, nn collisions is different.

The DY mechanism is a hard process and it is therefore expected to be insensitive to the state of the matter created in the collision. In this hypothesis, the DY nucleus-nucleus cross sections can be obtained as a weighted sum of all the pp, pn, np and nn elementary collisions. For instance, in the collision of two nuclei of atomic number A_1 and A_2, the DY cross section can be written as

$$\sigma_{AB}^{DY} = (Z_1 Z_2)\sigma_{pp} + [Z_1(A_2 - Z_2)]\sigma_{pn} + [Z_2(A_1 - Z_1)]\sigma_{np} + [(A_2 - Z_2)(A_1 - Z_1)]\sigma_{nn} \tag{1.35}$$

If σ_{NN} is the averaged DY cross section in nucleon-nucleon collisions, eq.1.35 can be written as

$$\sigma_{AB}^{DY} = \sigma_{NN}^{DY} A^{\alpha} B^{\alpha} \text{ with } \alpha = 1.0 \tag{1.36}$$

The value of α for the DY process has been experimentally measured in pA and AB collisions and confirms this simple picture. This is shown in fig.1.6 and, indirectly, in fig.1.5, where the measured and calculated DY cross sections are compared. Since the theoretical cross section is computed as from eq.1.35, the constant ratio plotted in fig.1.5 is equivalent to state that

$$K_{DY}\ |_{NN} = \frac{\sigma_{AB}^{DY}\ |_{meas.}}{\sigma_{NN}^{DY}\ |_{th}\ AB} = K_{DY}\ |_{AB} \tag{1.37}$$

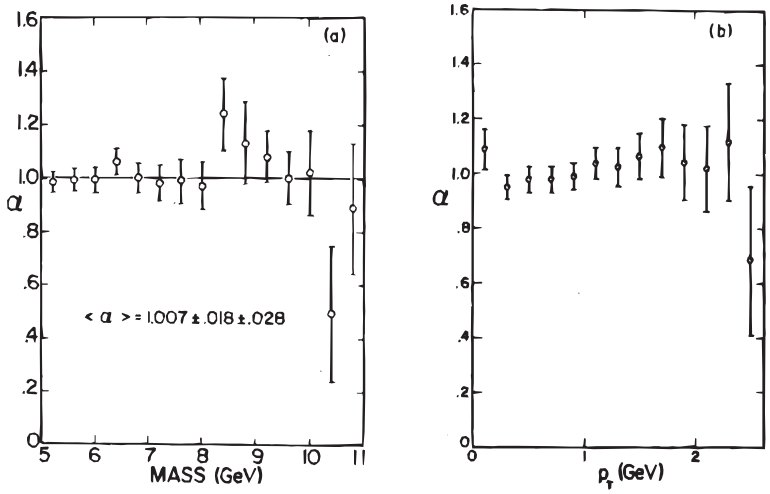

Figure 1.6: *The DY α value as a function of the invariant mass and the transverse momentum p_T as measured by the E288 experiment in 200 GeV/c proton induced collisions[23].*

Whilst the valence quarks in a hadron carry a substantial longitudinal momentum fraction x of the hadron momentum, the sea quark distributions are peaked at low

x values. Therefore, since the DY production in proton-nucleus or nucleus-nucleus collisions relies on the sea contents of the target nucleon, the cross section for DY production is small at large invariant mass M=x_1x_2. Furthermore, since at very low mass DY pairs are mainly produced in sea-sea quark interactions, the isospin dependence of the DY cross section should decrease with the invariant mass of the produced lepton pair.
Many different sets of theoretical parton distribution functions exist as deduced from muon or neutrino deep inelastic scattering or related hard scattering data for different values of the transferred momentum Q^2. Modern parametrisations include the new results on the sea quark asymmetry, as measured by NA51[24]. In the frame of the naif parton model, the parton distribution functions of the light sea quarks $\overline{u}$ and $\overline{d}$ are supposed to be identical, i.e., the light quark sea is supposed to be symmetric, with $\overline{u}/\overline{d}$=1. In this hypothesis, the DY asymmetry, defined by

$$A_{DY} = \frac{\sigma_{pp} - \sigma_{pn}}{\sigma_{pp} + \sigma_{pn}} \tag{1.38}$$

is expected to be equal to 0.09 when the ratio $\lambda_V = u_V/d_V$ (V=valence) in a proton is equal to 2[24]. The DY asymmetry measured by NA51 clearly indicates that the symmetry of the light quark sea is broken. The measured value, A_{DY}=-0.09$\pm$0.02$\pm$0.025, corresponds to a sea quark ratio $\overline{u}/\overline{d}\simeq$0.51 for $\sqrt{\tau} = M/\sqrt{s} = 0.18$.

Up until when the new MRS A set[25, 26] including the light sea quark asymmetry as measured by NA51 was proposed[24], the NA38/NA50 Collaboration always adopted the GRV LO (1992)[27] set of nucleon structure functions [28]. In fig.1.7 the Drell-Yan asymmetry measured by NA51 and predicted by the old MRS H and CTEQ2M parametrizations and by the new MRS A is shown as a function of $\sqrt{\tau} = M/\sqrt{s}$. The MRS A PDF's are calculated at the next-to-leading order (NLO), which amounts to the inclusion of $O(\alpha_s)$ higher order corrections. Since at low Q^2 the perturbative approach ceases to be valid, the PDF's can be evolved down to $Q^2 \approx 4GeV^2$. For lower Q^2, the PDF evolution can be computed with ad-hoc effective parametrizations tuned to give a good reproduction of the experimental data, as in ref.[26]. The minimum allowed Q^2 in the MRS A (1995) set is $Q^2_{min,MRSA}$=0.625 GeV^2. The GRV LO (1992) set of functions also allows for very low Q^2, $Q^2_{min,GRVLO}$=0.250 GeV^2, but a different technique is used to deduce the low Q^2 behaviour of the PDF's[26].

PDF's in a nucleus and in a free nucleon

In fig.1.8[29], the ratio of the PDF's for gluons and for valence and sea quarks in a lead nucleus and in a free proton is plotted as a function of the longitudinal momentum fraction x carried by the partons. The shown curves, corresponding to two different values of the Q^2 scale, clearly indicate that the PDF's in a nucleus and

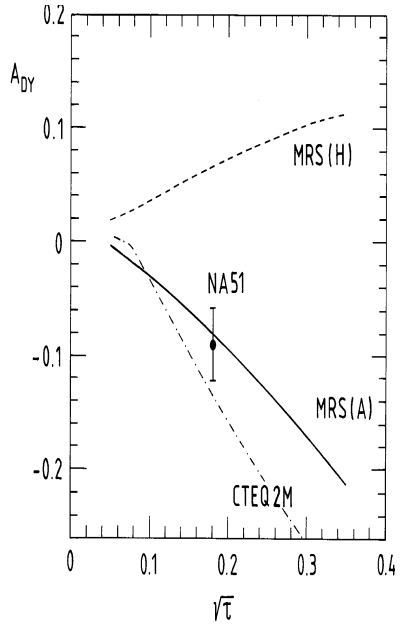

Figure 1.7: *The DY asymmetry in pp and pn collisions as a function of* $\sqrt{\tau} = M/\sqrt{s}$. *The MRS A set includes the results from the NA51 asymmetry measurement, whilst the MRS H and CTEQ2M are previous to it[25].*

in a free nucleon can strongly differ. The behaviour of R for gluon and quark with the Bjorken x can be subdivided in the following four different regions :

- The behaviour of R in the region below the value of x for which R=1, is denominated as shadowing; the gluon or quark component seen in a nucleus at small x is smaller than the one seen in a free nucleon. This effect is negligible in the NA38/NA50 acceptance window, where $x \geq 0.1$.

- When (and if) R becomes larger than 1, the corresponding effect is called anti-shadowing. In this case, the gluon or quark component seen in a nucleus at the corresponding x is larger than the one seen in a free nucleon. This effect is not negligible in the NA38/NA50 acceptance window as far as the gluon and valence quark component are concerned; since the DY process in nucleon-nucleon collisions mostly involves sea quarks, for which the effect is negligible, the anti-shadowing effect on the DY can be neglected.

- Then R starts decreasing again and reaches a minimum; the corresponding effect is named after the collaboration where it was originally measured (EMC)[30].

- The last rise of the ratio R is associated with the Fermi motion of nucleons within the nucleus; only when very large x ($x > 0.5$) are investigated, the effect of Fermi motion has to be taken into account[31]. In the NA38/NA50 acceptance window this effect has been estimated to be negligible[32].

Eq.1.35 amounts to state that the modification of the PDF's in a nucleus with respect to the PDF's in a free nucleon do not play a substantial role as far as the DY cross section is concerned. On the other hand, in ref.[33] the DY α value is predicted to change as a consequence of the above modifications. In fig.1.9 the α dependence on the lepton pair invariant mass and collision energy is shown as calculated in ref.[33] in proton-gold collisions for $\sqrt{s} \geq 39$ GeV and for different PDF's. Even if the calculation has not been performed for 158 A GeV/c Pb-Pb collisions, from an extrapolation of the shown curves down to SPS energies we can argue that $\alpha \approx 1.0$, in agreement with experimental results.

The isospin correction

Since the DY cross section in proton-proton and proton-neutron collisions is not the same, a correction is needed when comparing the DY cross sections measured on systems characterised by a different protons to neutrons ratio. The so called isospin correction has to be applied on the measured cross sections, and amounts to calculate the DY cross section which would have been measured if the projectile and target nucleus were made by protons only.

For instance, if the DY cross section has been measured in A-B collisions, with A$\geq$1 and B>1, the isospin correction can be calculated as

$$I_{DY} = \frac{\sigma_{pp}^{DY}\ |_{th.} \cdot A \times B}{\sigma_{AB}^{DY}\ |_{th.}} \tag{1.39}$$

where the two cross sections in eq.1.39 have to be derived using the same set of parton distribution functions. The isospin correction is then applied on the experimentally measured cross section, i.e.

$$\sigma_{AB}^{DY}\ |_{meas.}^{cor.} = \sigma_{AB}^{DY}\ |_{meas.} \cdot I_{DY} \tag{1.40}$$

which gives

$$\sigma_{AB}^{DY}\ |_{meas.}^{cor.} = K_{DY}\ |_{meas.} \cdot \sigma_{pp}^{DY}\ |_{th.} \cdot A \times B \tag{1.41}$$

The isospin correction has to be applied every time a comparison is drawn between DY cross sections or between ratios of cross sections where the DY is used as a reference.

1.6 Open-charm hadro-production

Hadrons consisting of charmed *and* non-charmed valence quarks are generically indicated as *open-charm*,

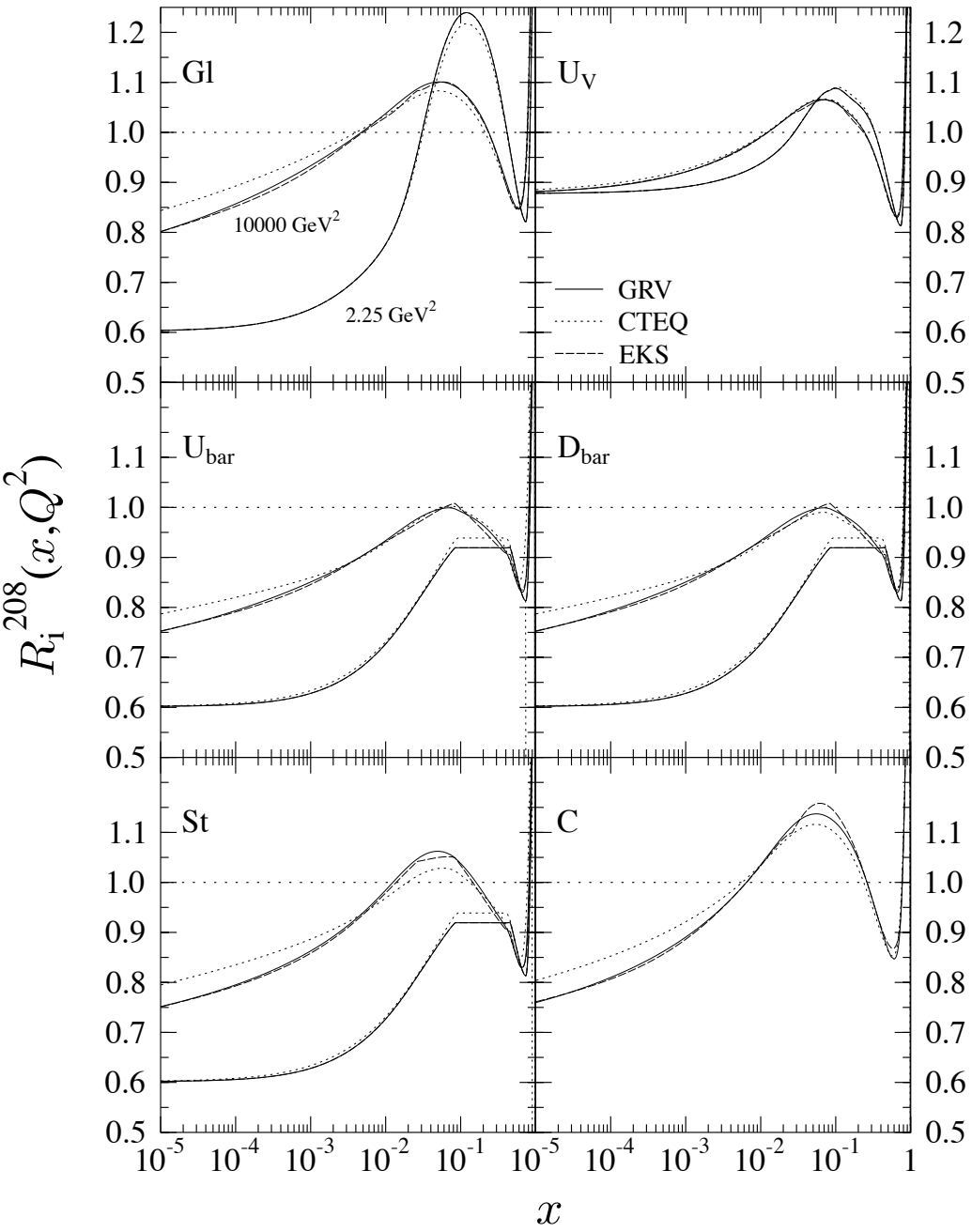

Figure 1.8: *The nuclear ratio $R^{A=208}$, defined as the ratio of the parton PDF in a lead nucleus and in a free proton, is plotted for the parton flavours i=g,u_V,$\overline{u}$,$\overline{d}$, s,c as a function of x and for two fixed values of Q^2=2.25 GeV^2 and Q^2=10000 GeV^2[29]. The two PDF's set GRV LO (solid lines) and CTEQ (dotted lines) have been used in the calculation of the free proton PDF's. The parametrization of the nuclear effect obtained with the GRV LO PDF's is also shown (ESK) as proposed by the authors in the same ref.[29].*

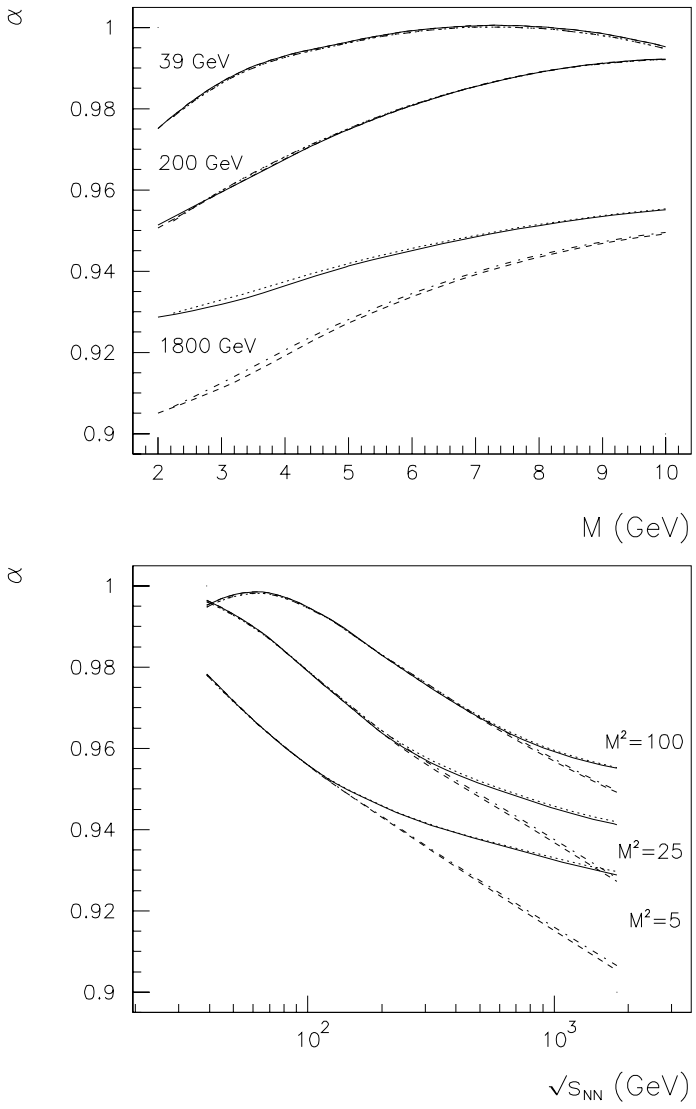

Figure 1.9: *Mass (top) and energy (bottom) dependence of* α *for DY pair production in proton-gold collisions for GRV HO (solid and dashed curves) and MRS-A (dotted and dashed-dotted curves)[33].*

- Charmed mesons (C= ± 1) :

$$D^+ \equiv (c\overline{d}) \text{ [M=1869.3±0.5 MeV]} \tag{1.42}$$

$$D^- \equiv (d\overline{c}) \text{ [M=1869.3±0.5 MeV]} \tag{1.43}$$

$$D^0 \equiv (c\overline{u}) \text{ [M=1864.6±0.5 MeV]} \tag{1.44}$$

$$\overline{D^0} \equiv (u\overline{c}) \text{ [M=1864.6±0.5 MeV]} \tag{1.45}$$

- Charmed-strange mesons (C = S = ± 1) :

$$D_s^+ \equiv (c\overline{s}) \text{ [M=1968.5±0.6 MeV]} \tag{1.46}$$

$$D_s^- \equiv (s\overline{c}) \text{ [M=1968.5±0.6 MeV]} \tag{1.47}$$

- Charmed baryons (C = +1) :

$$\Lambda_c^+ \equiv (udc) \text{ [M=2284.9±0.6 MeV]} \tag{1.48}$$

$$\Xi_c^+,\ \Xi_c^0 \equiv (qsc) \text{ [M=2465.6±1.4, 2470.3±1.8 MeV]} \tag{1.49}$$

$$\Sigma_c^+,\ \Sigma_c^0,\ \Sigma_c^{++} \equiv (q_1q_2c) \text{ [M=2453.6±0.9, 2452.2±0.6, 2452.8±0.6 MeV]} \tag{1.50}$$

$$\Omega_c^0 \equiv (ssc) \text{ [M=2704±4 MeV]} \tag{1.51}$$

Of all the semi-leptonic and hadronic decay modes, only the ones having one μ in the final state, e.g.

$$D \longrightarrow \mu\nu_\mu X \tag{1.52}$$

can contribute to the dimuon mass spectrum.

Open-charm hadro-production is described by leading order perturbative QCD as being mainly due to the process of 'fusion' of two partons,

$$gg \longrightarrow c\overline{c} \tag{1.53}$$

$$q\overline{q} \longrightarrow c\overline{c} \tag{1.54}$$

Since in the parton fusion model 80% of the produced open-charm originates from gluon fusion, no isospin correction is needed when comparing open-charm cross sections measured for different colliding systems.

The parton fusion model describes the open-charm hadro-production process as a superposition of elementary processes at the partonic level. In general, the cross section for the inclusive process $hh \rightarrow HX$, where h,H and X are hadrons, can be written as

$$d\sigma^{h_1 h_2 \rightarrow HX} = \sum_{a,b,c,d} \int dx_a dx_b dz \cdot f_1(x_a, Q^2) f_2(x_b, Q^2) \cdot d\sigma^{ab \rightarrow cd} D_H^d(z, Q^2) \tag{1.55}$$

where $d\sigma^{ab \rightarrow cd}$ is the cross section for the elementary process (a, b, c, d are generic partons) and $z = P_H/p_d$ is the fraction of the momentum of the hadronizing parton carried away by the hadron H. $D_H^d(z, Q^2)$ is the so called *fragmentation function* describing the fragmentation (hadronization) of the parton d in the hadron H. The Q^2 dependence of the fragmentation function originates from the factorisation theorem (see previous section) and fragmentation functions are considered to be *universal*. Fragmentation functions are calculated in the frame of phenomenologic models and then compared with the experimental cross section for the process $e^+e^- \rightarrow HX$, because the cross section for this process can be simply written as

$$d\sigma^{e^+e^- \rightarrow HX} = \sum_d d\sigma^{e^+e^- \rightarrow d\overline{d}} \cdot D_H^d(z, Q^2) \tag{1.56}$$

The *universality* of the fragmentation functions implies that the fragmentation process of the parton d in the hadron H is supposed to be completely independent from the projectile flavour composition.

The above described parton fusion model gives satisfactory results for x_F<0.5. The absolute value of the open-charm cross section has to be multiplied by a K factor, as for the DY process, to reproduce the measured cross section. The measured $K_{open-charm}$ is a function of the charm mass value used in the theoretical calculations and can also depend on the adopted PDF set. In this same model, the nuclear dependence of the open-charm hadro-production cross section can be simply parametrized as

$$\sigma_{pA}^{D\overline{D}} = \sigma_{pp}^{D\overline{D}} A^{\alpha} \tag{1.57}$$

with $\alpha = 1$. On the other hand, in ref.[33] α is predicted to depend both on the collision energy and on x_F. Fig.1.10 shows the calculated energy dependence for proton-gold interactions.

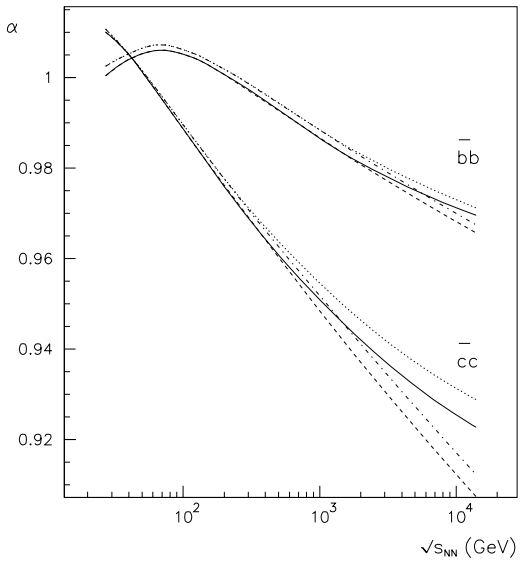

Figure 1.10: *Energy dependence of α for charm and beauty production in proton-gold collisions for GRV HO (solid and dashed lines) and MRS-A (dotted and dashed-dotted lines) PDF's[33].*

Furthermore, the parton fusion model alone does not fully reproduce the differential open-charm hadro-production cross sections $d^2\sigma/dx_F dp_T^2$ for x_F >0.5. Moreover, there is experimental evidence of an existing asymmetry in the cross section of leading and non-leading D meson production

$$A(x_F) = \frac{\sigma_{leading} - \sigma_{non-leading}}{\sigma_{leading} + \sigma_{non-leading}} \tag{1.58}$$

A charmed meson is said to be *leading* if it contains projectile valence quarks and *non-leading* if it does not; as an example, in $\pi^- \equiv (d\overline{u})$ induced reactions the D^0 and D^- are leading, whilst the $\overline{D^0}$ and the D^+ are not. The measured asymmetry implies that the fragmentation process depends on the quark content of the projectile.

Different models have been developed to explain the above mentioned non perturbative aspects of heavy quark hadro-production; in the following some of them are briefly described and their prediction compared with experimental results.

In the intrinsic-k_T model[34], intrinsic transverse momenta k_T are assigned to the incoming partons and then added to the total transverse momentum of the created heavy quark pair. If the fragmentation process is taken into account, for $\langle k_T^2 \rangle$=1.00 GeV^2/c^2 and m_c=1.5 GeV/c^2, a fair reproduction of experimental data can be obtained, as shown in fig.1.11. A better agreement can be achieved when the (too high)

value $\langle k_T^2 \rangle$=2.00 GeV^2/c^2 is used for the same charm mass value or when $\langle k_T^2 \rangle$=1.00 GeV^2/c^2 but m_c=1.8 GeV/c^2. On the other hand this latter value for the charm mass is excluded when comparing pQCD NLO theoretical predictions with the $c\overline{c}$ total cross section measurement[34], as shown in fig.1.15 and later explained.

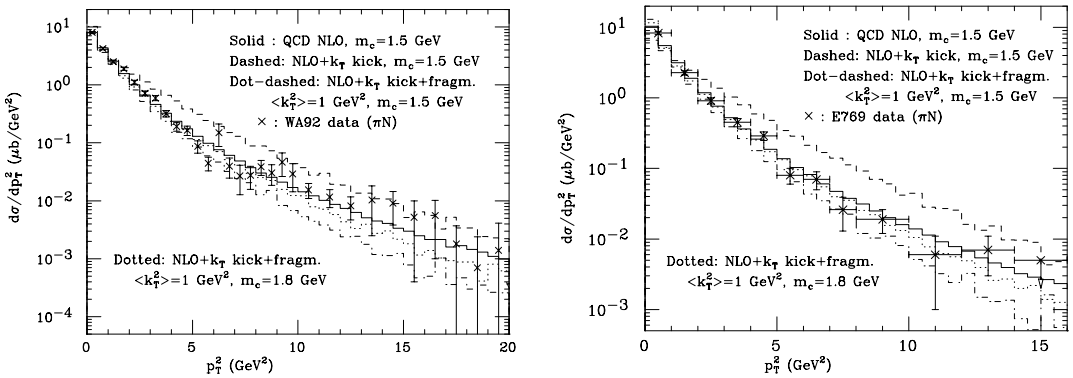

Figure 1.11: *Comparison between the single inclusive p_T^2 distributions measured in 350 GeV/c π^--N collisions by WA92 (left) and 250 GeV/c π^--N collisions by E769 (right) and the Next to Leading Order QCD predictions, with and without the inclusion of non-perturbative effects.*

The Intrinsic Charm Coalescence model[35, 36, 37] predicts the existence of the leading/non-leading asymmetry and tries to reproduce the differential cross section for open-charm production for x_F >0.5. It is based on the pQCD prediction that, at a certain order of the perturbative calculation, fluctuations of the projectile wave function could appear which would create virtual $q\overline{q}$ states within the projectile wave function itself. In proton induced reactions, where the parton composition of the projectile is (uud), the proton wave function at a certain time t could be thus described by ($uudc\overline{c}$). Soft interactions of the light valence quarks with the target can put the virtual $c\overline{c}$ on its mass-shell. Both charmed quarks can then either hadronize or independently coalesce with the co-moving valence quarks in the proton. When the c quarks hadronize, non-leading charmed hadrons are created, whilst leading charmed hadrons are generated through the coalescence mechanism. The intrinsically created charmed quarks co-move with the projectile valence quarks and therefore have large longitudinal momentum fraction x and a small p_T. Therefore, the effect of intrinsic coalescence could be seen at large longitudinal momentum x_F >0.5 and low p_T. The coalescence of the c quarks created via the intrinsic charm production process is an *initial* state process. Furthermore, the c quarks generated in the parton fusion process can also coalesce with collinear valence quarks. This *final* state coalescence can take place only when the $c\overline{c}$ pair has been created a very low p_T, where collinear quarks can be found. It is therefore expected to dominate when the created c quark and the valence quarks have the same velocity, at very

large x_F.
In the frame of the IC model, the cross section for open-charm production in pA collisions can be written as

$$\sigma^{pA} = \sigma_{pf}^{pp} A^{\alpha} + \sigma_{ic}^{pp} A^{\beta} \tag{1.59}$$

where $\alpha \simeq 1$ and $\beta \simeq 2/3$ because the intrinsic process is a surface effect. If the predictions of the IC model were correct, the measured α should show a clear dependence on x_F. The α values measured in beam dump experiments[38], where the charmed hadrons were detected through the produced leptons (neutrino, muon) and no determination of the decay vertex was feasible, give an average value of $\langle\alpha\rangle$=0.79±0.03. The latter is larger than the predicted 2/3 when the above surface correction is taken into account, and lower than 1.0. In ref.[38] this, and the measured α dependence on x_F and the found leading meson asymmetry, are motivated by the existence of more than one production mechanism at the quark level, as predicted by the IC model. However, modern direct measurements of heavy quark production, with experimental apparatus allowing for a precise determination of the decay vertex, indicate that α is compatible with 1 and does not depend on x_F or p_T, as briefly summerized in the following.

In ref.[39] the nuclear dependence of charm hadro production has been measured with a 800 GeV/c proton beam on beryllium and gold targets, giving α=1.02±0.03±0.02. There is no evidence for any α dependence on either x_F or p_T, but this could be due to the limited range in x_F and p_T covered by the experiment, 0.0< x_F <0.08 and 0.0< p_T < 1.1 GeV/c.
The E769 experiment[40] has measured α=1.00±0.05±0.02 in 250 GeV/c π induced reactions on Be, Al, Cu and W targets. The E769 experiment covers the range $0 < p_T < 4$ GeV/c and $0 < x_F < 0.5$. They do not find any dependence of the measured α on the beam polarity (π^+ or π^-), transverse p_T or longitudinal x_F momentum of the detected D mesons or the type (neutral or charged) of D meson.
The WA92 experiment[41] has measured the charmed meson production in 350 GeV/c π^- induced reactions on Cu and W targets and in a wide x_F and p_T range : 0.0< x_F <0.8 and 0.0< p_T <7 GeV/c. They have also measured the leading meson asymmetry, finding an evident evolution of the asymmetry with x_F. No x_F or p_T dependence of α has been measured, as shown in fig.1.12. The found α=0.95±0.06±0.03 is in agreement with the parton fusion model predictions.

In order to check if the available data on open-charm hadro-production can be reasonably well described by leading order QCD calculations, in ref.[42] the prediction of the well known PYTHIA event generator have been compared with recent experimental measurement of differential and absolute open-charm cross sections. In fig.1.13 the $D\overline{D}$ x_F, p_T^2, mass and rapidity difference distributions from π-Cu collisions at $\sqrt{s}$=26 GeV/c[42] are also compared with the scaled PYTHIA predictions. Fig.1.14[42] shows the x_F and p_T distributions for D mesons produced in pp

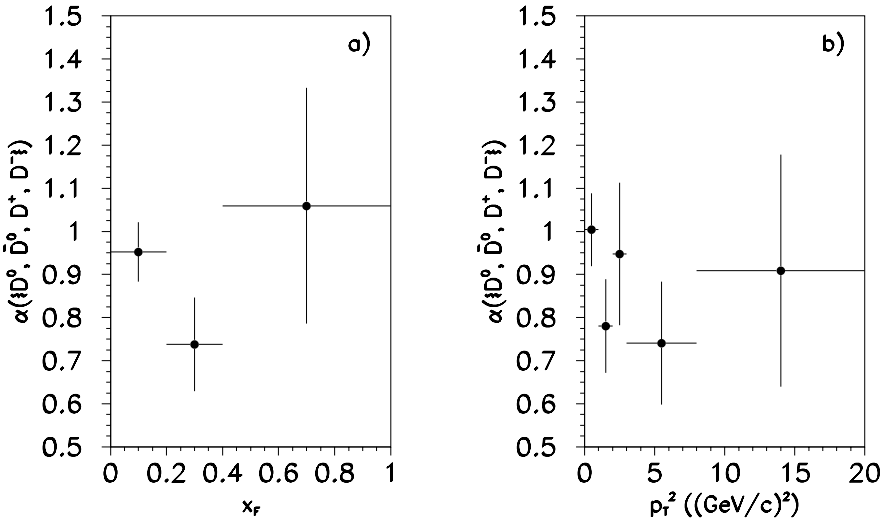

Figure 1.12: *Dependence of* $\alpha(\{D^0, \overline{D^0}, D^+, D^-\})$ *on* x_F *(left) and* p_T^2 *(right) as measured by the WA92 experiment[41].*

collisions at 250 GeV/c, compared with the leading order pQCD predictions of the PYTHIA event generator. In PYTHIA the dimuon transverse momentum originates from the intrinsic transverse momentum k_T assigned to the partons inside the colliding hadrons. PYTHIA reproduces reasonably well the experimental distributions if scaled up by an ad-hoc K-factor, leaving the shape of the PYTHIA distributions unchanged.

This is the reason why, as explained in chapter 4 and chapter 7 of the present thesis, the PYTHIA event generator has been used in the present work to generate the open-charm differential and absolute cross sections. Besides, in the NA38/NA50 acceptance window, x_F is never larger than ≈ 0.4, and dimuon from open charm are detected for $x_F \approx 0.2$; therefore, the above detailed higher twist effects can be comfortably neglected. On the other hand, when studying the open charm production in nucleus-nucleus collisions at SPS energies, since $x_1 \approx 0.2$ where the gluon antishadowing effect is large (see fig.1.8), the latter can increase the open charm dimuon produced in the NA38/NA50 acceptance window. This effect has been estimated to account for no more than 20% of the dimuon excess measured in nucleus-nucleus collisions at SPS (see chapter 7 and references therein).

The charm mass

The exact value of the charm mass is not precisely known. In fig.1.15, the cross-sections for charm (top part) and bottom (bottom part) pair production measured by FNAL and CERN experiments are shown[34]. The experimental points are compared with theoretical predictions based on QCD NLO calculations, using the MRS

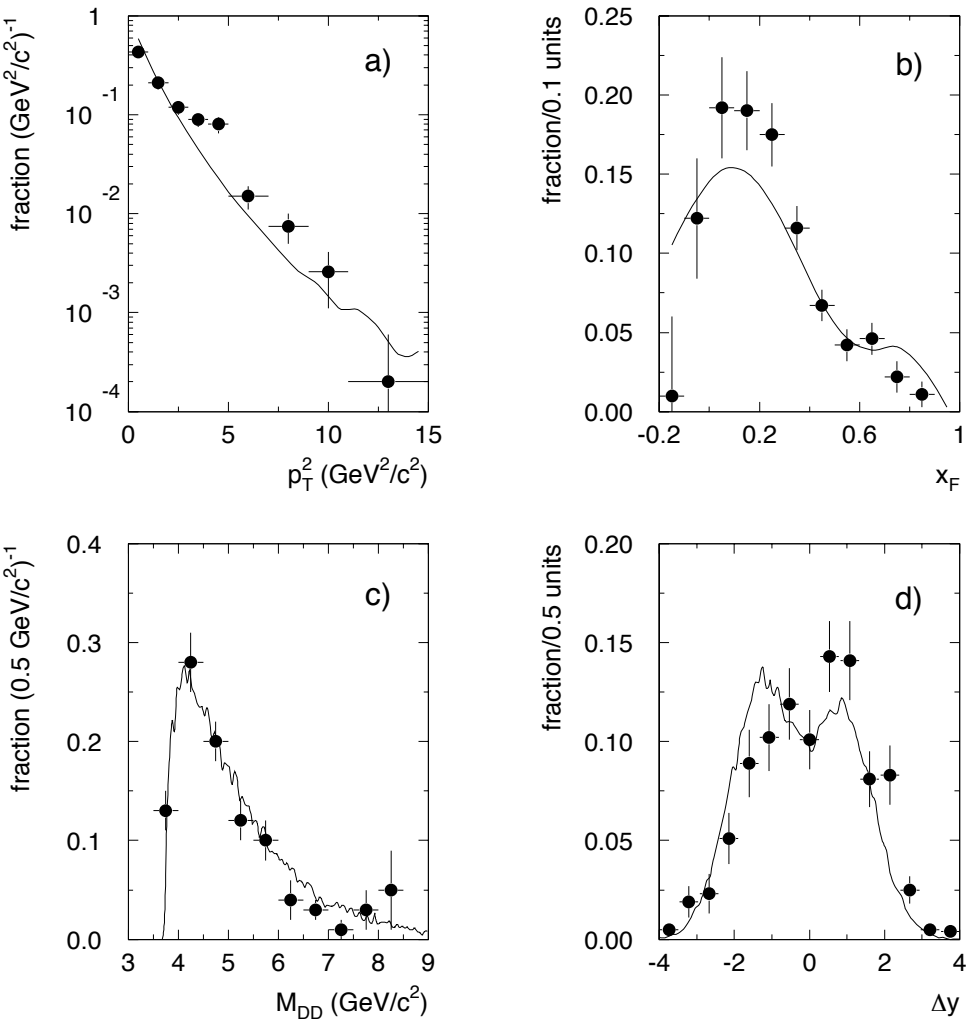

Figure 1.13: *$D\overline{D}$ x_F, p_T^2, mass and rapidity difference distributions from π-Cu collisions at $\sqrt{s}$=26 GeV/c compared with PYTHIA predictions[42].*

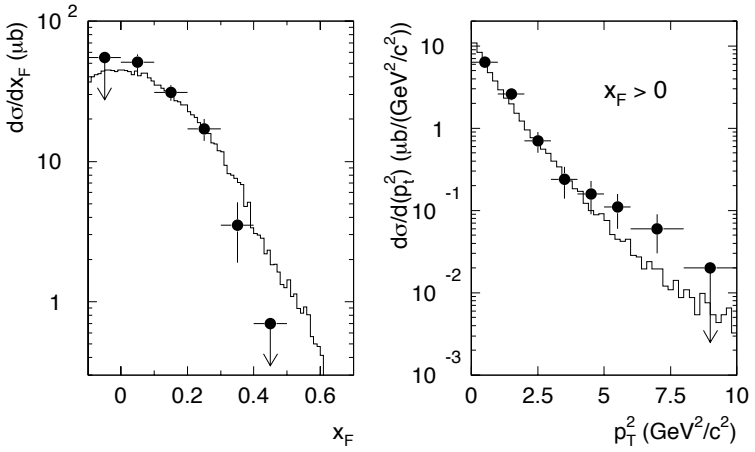

Figure 1.14: *x_F and p_T distributions for D mesons produced in p-p collisions at 250 GeV/c, compared with the scaled PYTHIA predictions[42]. See text for details.*

45 nucleon structure function set[28]. The solid line corresponds to the standard charm mass value $m_c = 1.5\ GeV/c^2$; the theoretical predictions for $m_c = 1.2\ GeV/c^2$ and $m_c = 1.8\ GeV/c^2$ are also shown. When theoretical uncertainties are taken into account, the hadro-production data are compatible with the value m_c=1.5 GeV/c^2.

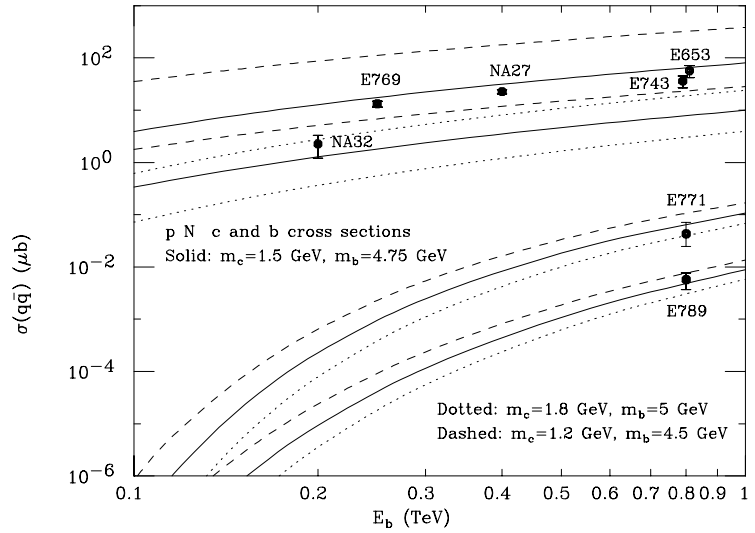

Figure 1.15: *Pair cross sections for c (and b) production in p-N collisions versus experimental results. The effect of changing the charm mass value is shown (top bands)[34]. See text for details.*

1.7 The dilepton mass spectrum

In Fig.1.16, where the 450 GeV/c pAg dimuon mass spectra measured by the NA50 experiment at CERN is shown, the different known contributing processes are indicated. In fig.1.17 the dielecron mass spectra measured by CERES in 450 GeV/c pBe and pAu collisions is also shown.

The dilepton differential mass spectrum can be subdivided in three different regions :

- The low mass region (LMR) for $M < 1.5\ GeV/c^2$.

  The low mass region can be still subdivided in two main regions : the low mass resonance region and the region below the ρ peak (M≤750 MeV). The dilepton production in the region above the ρ peak is dominated by the leptonic decay of the ρ, ω ,ϕ vector mesons. Below the ρ peak dileptons are mainly produced in the Dalitz decay of hadrons, i.e.

$$\eta \longrightarrow l\bar{l}\gamma \tag{1.60}$$

$$\eta' \longrightarrow l\bar{l}\gamma \tag{1.61}$$

$$\omega \longrightarrow l\bar{l}\pi^0 \tag{1.62}$$

$$\pi^0 \longrightarrow l\bar{l}\gamma \tag{1.63}$$

- The intermediate mass region (IMR) for $1.5 < M < 2.5\ GeV/c^2$.

  In the IMR the following processes are known to contribute :

  - Dileptons from the DY process.
  - Dileptons from the semi-leptonic decay of charmed mesons and baryons.

- The high mass region (HMR) for $M > 2.5\ GeV/c^2$.

  The high mass region below the Υ consists of DY dileptons and dileptons produced in the decays of open-charm, J/ψ and ψ'; in particular, the region $4.5 < M < 8.0\ GeV/c^2$ consists of high mass DY dileptons only.

Another important contribution to the opposite-sign mass spectrum, both in the low and in the intermediate mass region, is the combinatorial background. The combinatorial background originates from the combination of leptons generated in the decays of K's and π's. Since the combinatorial background heavily contributes to the IMR spectra, its subtraction is one of the most important issues in the IMR data analysis. For instance, the background contribution in the IMR amounts to 85% in 450 GeV/c p-A and 200 A GeV/c S-U collisions and to 95% in 158 A GeV/c Pb-Pb central ones. A detailed description of the techniques used to compute the combinatorial background contribution to the opposite-sign mass spectrum can be found in chapter 5.

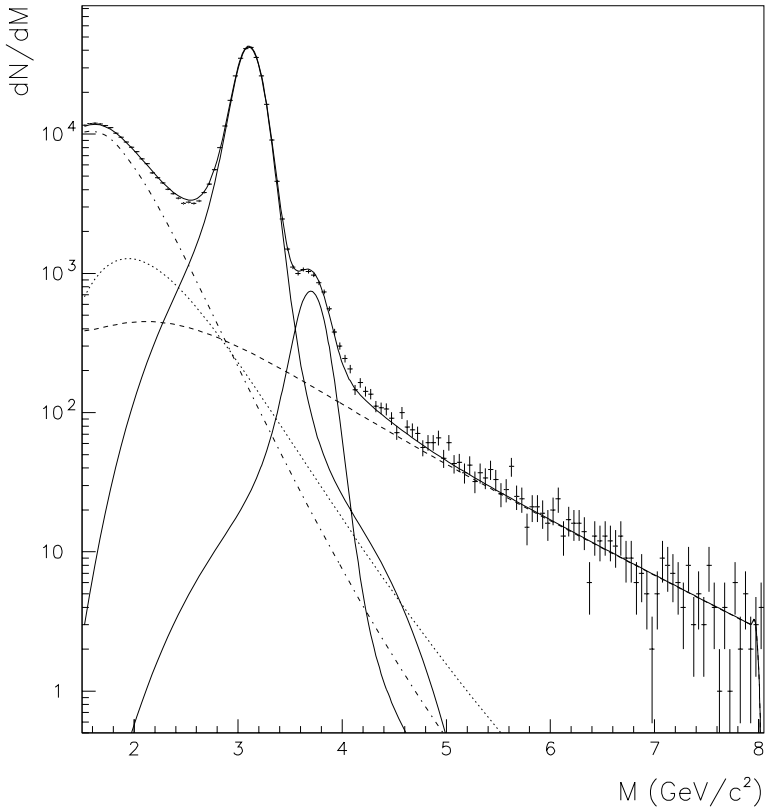

Figure 1.16: *Dimuon invariant mass spectrum of opposite-sign dimuons for the NA50 450 GeV/c pAg system. The processes contributing to the high and intermediate mass region are shown : the high mass J/ψ and ψ' resonances (full line), the DY muon pair (dashed line), the contribution from the semi-leptonic decay of charmed hadron pairs (dotted line) and the combinatorial background from the leptonic decay of kaons and pions (dash-dotted line).*

1.8 The dilepton production enhancement

The dilepton mass spectra, measured in proton induced collisions on nuclear targets, can be well described by a superposition of the known contributions listed in the previous section, as clearly shown in fig.1.17. On the other hand, an excess has been measured in the low and intermediate mass regions of the dilepton spectrum produced in nucleus-nuclues collisions at SPS energies. The measured dilepton yield exceeds the expected dilepton production as extrapolated from p-A interactions. Furthermore, the excess measured by CERES in the low mass region, suggests a stronger than linear dependence of the enhanced dilepton source on the collision centrality. Hard processes, like *DY* pair production and open charm hadro-production, are expected to linearly depend on the number of effective nucleon-nucleon collisions and the latter is predicted to linearly depend on the measured transverse energy

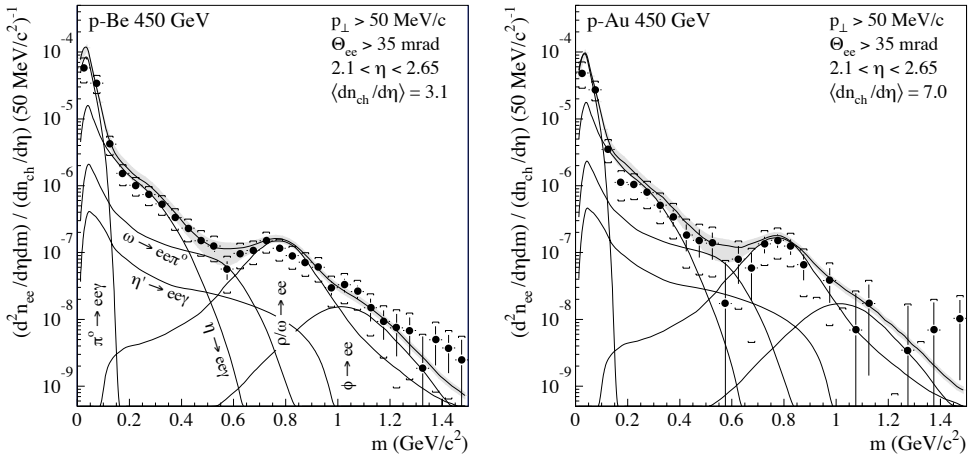

Figure 1.17: *Inclusive e^+e^- mass spectrum measured by CERES in 450 GeV/c p-Be and p-Au collisions in the low mass region. The thick line represents the summed yield of all the shown sources (dash-dotted lines).*

E_T[43]. The multiplicity of secondaries produced in a nucleus-nucleus collision is also proportional to E_T. On the other hand, the production of thermal dileptons from a thermalized QGP is expected to increase quadratically with the collision centrality[18]. In fact, when the production from the mixed quark-hadron phase is taken into account, an even more complicated dependence on the hadron multiplicity is predicted[44, 45]. Other processes could be responsible for an enhanced open charm production, as explained in chapter 7 (and references therein). A larger than linear dependence on the final hadron multiplicity and/or transverse energy E_T therefore clearly indicates the on-set of an alternative mechanism for lepton pair production.

In the following the results of the CERES, HELIOS/3 and NA38/NA50 experiments in the low and intermediate mass regions are discussed, along with the most promising theoretical interpretations of the found excess.

1.8.1 Experimental results

Evidence of an enhanced dilepton production in the LM and IM regions with respect to extrapolations from pA results, has been first observed in S induced collisions at 200 A GeV/c by the NA38 (S-U)[46, 47], CERES (S-Au)[48] and HELIOS/3 (S-W)[49] at the CERN SPS.

Preliminary results on Pb induced collisions were presented at the QM96 conference by NA50[50]; the measured $Data/(Expected - Sources)$ (or D/S) in the intermediate mass range for the (1992) 200 A GeV/c S-U and (1995) 158 A GeV/c Pb-Pb

amounted to $D/S_{S-U,200AGEV/c}$=1.26$\pm$0.10 and $D/S_{Pb-Pb,158AGEV/c}$=2.03$\pm$0.09. In fig.1.18[50], the expected dimuon yield in 158 A GeV/c Pb-Pb collisions is compared with the measured dimuon mass spectrum. The two solid lines correspond to the expected charm production $\pm 1\sigma$. In fig.1.19[50] the excess measured by NA38/NA50 for the 200 A GeV/c S-U 1992 and 158 A GeV/c Pb-Pb 1995 data sets is plotted against the collision centrality. From the data presented at QM'96 it is difficult to conclude on the actual centrality dependence of the excess.

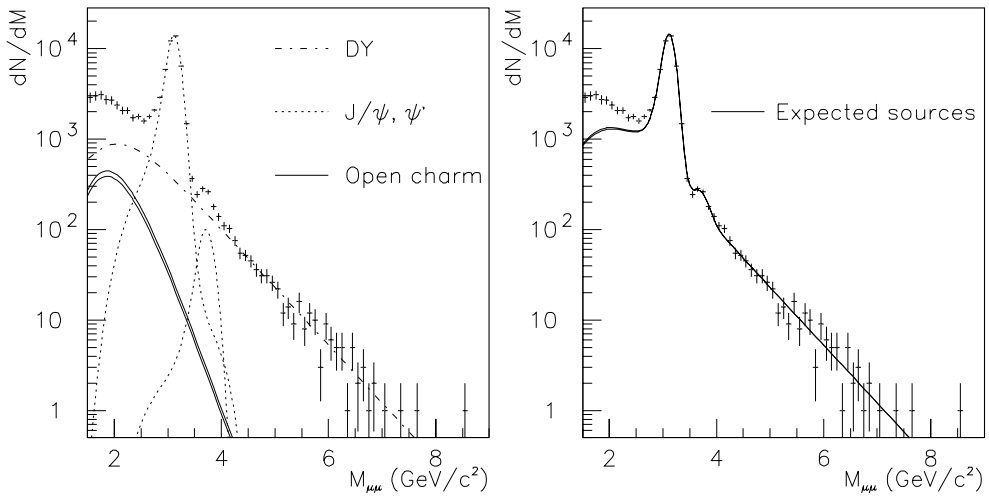

Figure 1.18: *Comparison of measured dimuon yield with expected sources in Pb-Pb collisions at 158 A GeV/c for the 1995 NA50 data set[50].*

CERES[51] at the same conference presented the results of the analysis of the 200 GeV/c S-Au low mass spectrum, where an excess is found for $M \geq 2m_\pi$. This threshold suggests that the observed excess could be due to the production of thermal dileptons in $\pi\pi$ (and $\pi\rho$) annihilations. The measured D/S ratio is $5.0\pm0.8(sta)\pm2(sys)$ for $0.2< M <1.5\ GeV/c^2$. CERES recently measured the excess in Pb-Au collisions at 158 A GeV/c, finding D/S=$3.4 \pm 0.4 \pm 0.9$ for $0.2< M <2.0\ GeV/c^2$. In fig.1.20 the CERES mass spectra for 158 A GeV/c Pb-Au is shown. The summed and individual contributions from hadronic decays is also shown and it clearly indicates that conventional sources alone can not reproduce the low mass spectra. In fig.1.21 the excess measured by CERES in 158 A GeV/c Pb-Au collisions is plotted as a function of the charged multiplicity[52]. Here again it is difficult to conclude about the actual centrality dependence of the excess, even if a quadratical dependence can not be excluded.

HELIOS/3 in its recent analysis of the 200 A GeV/c S-W data[53], finds an excess expanding from the low to the intermediate mass region, up to the J/ψ threshold.

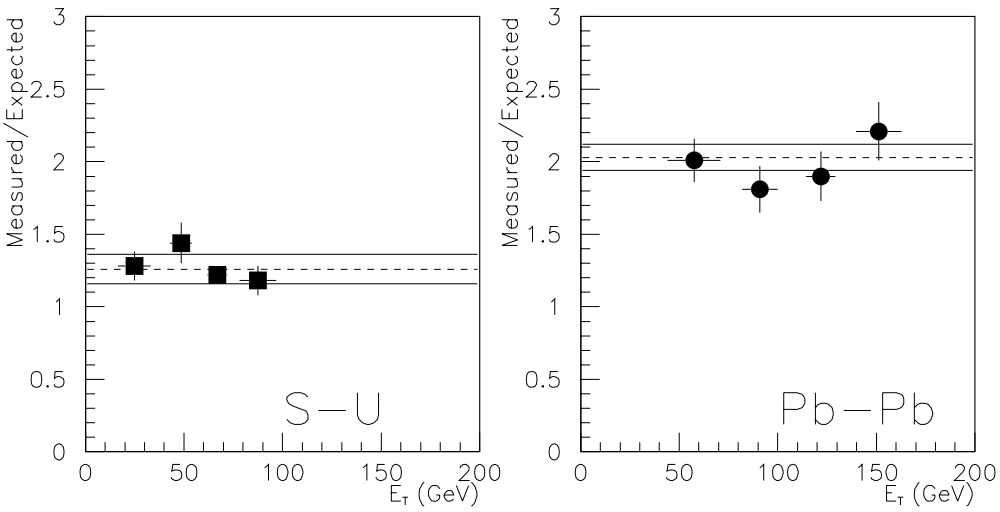

Figure 1.19: *Centrality dependence of the excess in the 1992 NA38 200 A GeV/c S-U and in the 1995 NA50 158 A GeV/c Pb-Pb data sets[50].*

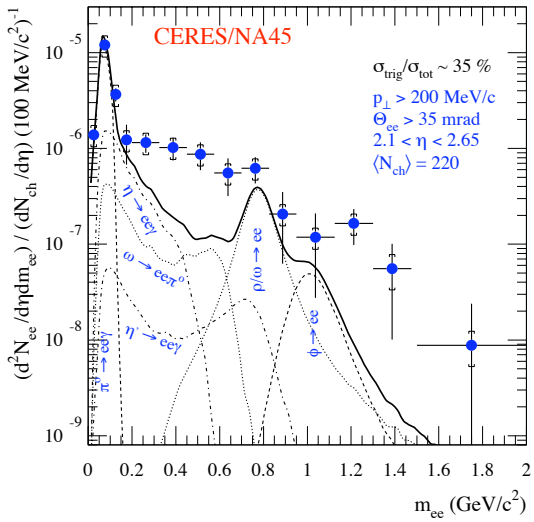

Figure 1.20: *Inclusive e^+e^- mass spectrum measured by CERES in 160 A GeV/c Pb-Au collisions normalised to the observed charged particle density. The individual and summed contributions from hadronic sources are also shown[52].*

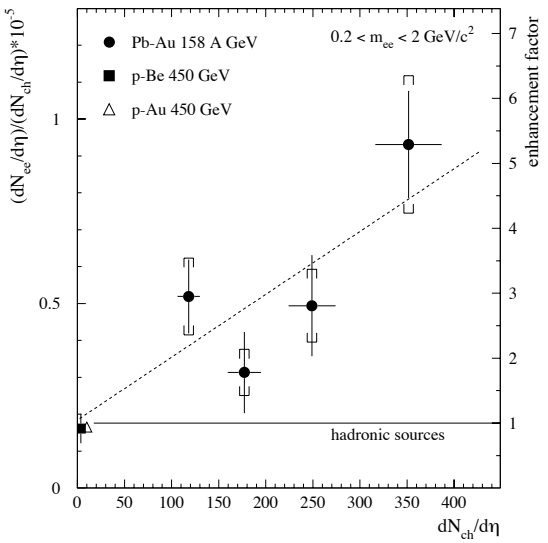

Figure 1.21: *Multiplicity dependence of the normalised pair yield for Pb-Au collisions as measured by the CERES Collaboration. Systematic and statistical uncertainties are shown separately. The dashed line represents a fit to the Pb-Au data assuming quadratical multiplicity dependence. The solid line represents the expectation from known hadronic sources. The normalised yield measured in proton-nucleus collisions is also shown[52].*

In the IMR, the measured D/S ratio is 5.91 ± 1.11 for 1.35< M <2.5 GeV/c^2 and 4.13 ± 1.24 for 1.6< M <2.5 GeV/c^2. In fig.1.22 the ratio D/S measured by HELIOS/3 in the IMR is plotted against the charged particle multiplicity[53]. Since the more peripheral bins are affected by a too little statistics, only the four charged multiplicity classes corresponding to the most central events have been analysed and are shown. It is therefore difficult to draw any definitive conclusion on the centrality dependence of the measured excess. In chapter 7 the results of the HELIOS/3 Collaboration will be discussed in some more detail in the attempt of drawing a comparison between their results and the results of the present work.

1.8.2 Comparison with theoretical models

When compared with the CERES experimental results, as shown in fig.1.23, the thermal dilepton contribution predicted in ref.[20] (see sec.1.5.4 of the present chapter) does not correctly reproduce the data for M≈500 MeV/c^2. A factor 10 enhancement in the total (QGP+HG) thermal dimuon yield is needed in order to describe the data. In fact, there is a general consensus in concluding that the additional production of thermal dimuons from a hadron gas alone can not account for the observed excess[16].

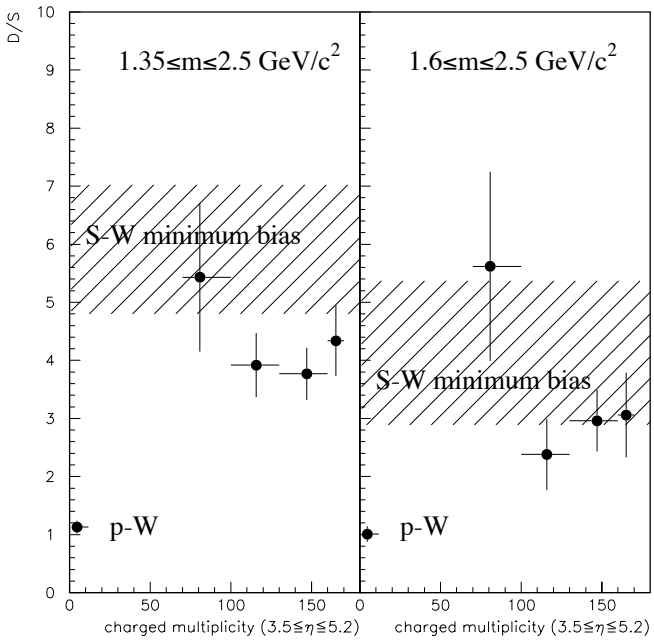

Figure 1.22: *Charged multiplicity dependence of the IMR dimuon excess as measured by the HELIOS/3 Collaboration[53]. The shaded areas correspond to* $Data/Sources = 5.91 \pm 1.11$ *(left) and* $Data/Sources = 4.13 \pm 1.24$ *(right).*

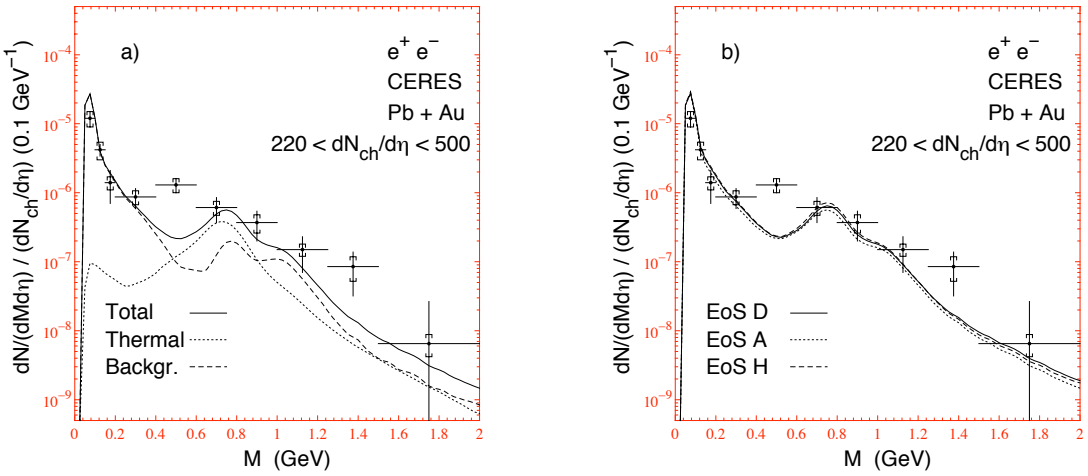

Figure 1.23: *Calculated electron pair spectrum compared to CERES data. (a) The emission from the fireball, background and the total spectra.(b) The total spectrum obtained using three different EoSs but always the same initial conditions. CERES kinematic cuts and experimental resolution have been taken into account[20].*

In fig.1.24 the low mass region data from CERES are compared to the prediction of the model described in ref.[54], where the thermal yield from a hadron gas is calculated including the ρ width broadening in the hot and dense medium with in-medium modifications of the ρ spectral function. In fig.1.25 the same model is compared to the low mass data of HELIOS/3.

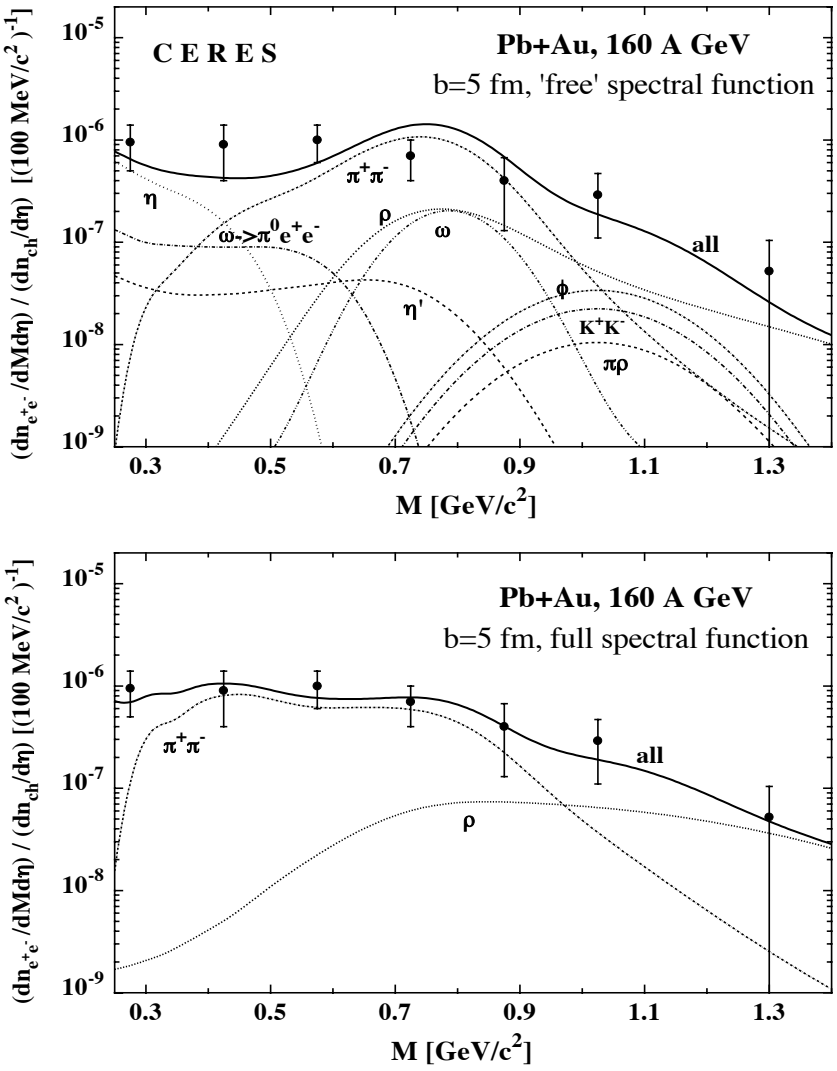

Figure 1.24: *Calculated dielectron invariant mass spectra for central 158 A GeV/c Pb-Au collisions compared to the CERES data[54], with (full) and without (free) in-medium modification of the ρ spectral function.*

In fig.1.26 the CERES and HELIOS/3 data are compared in the low mass region with the theoretical curves obtained in ref.[55] when the vector meson in-medium

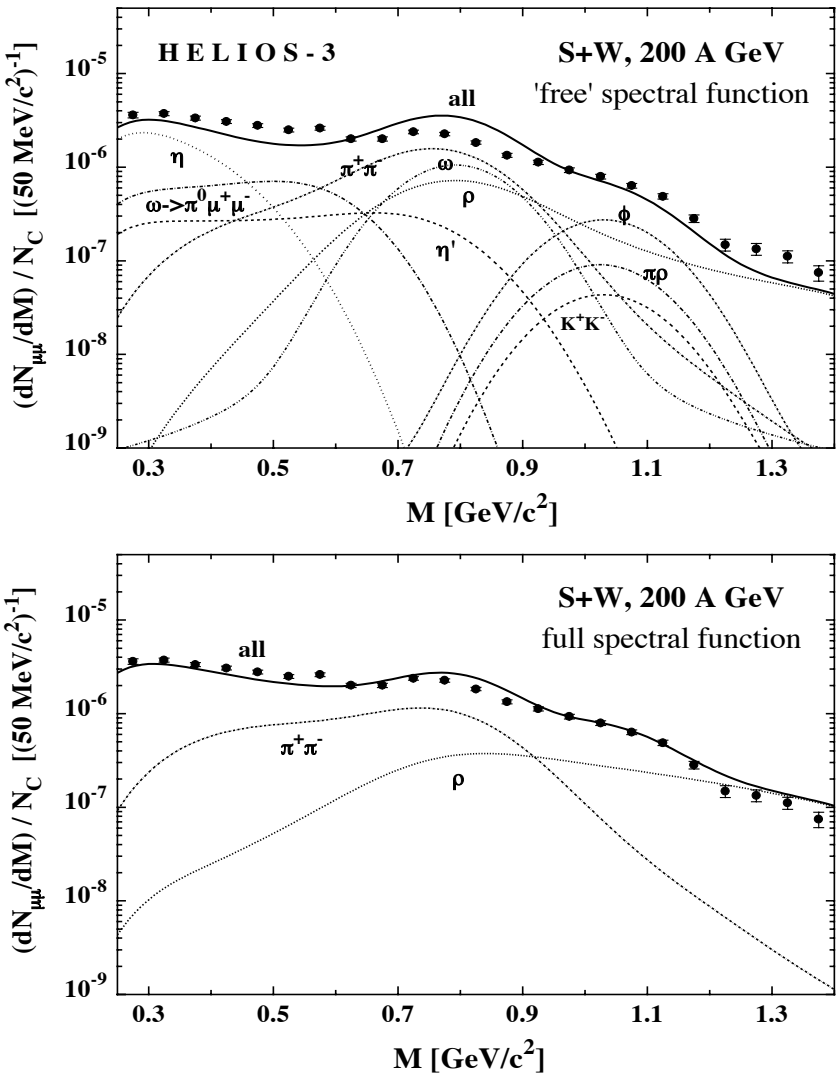

Figure 1.25: *Calculated dimuon invariant mass spectra for central 200 A GeV/c S-W collisions compared to the HELIOS/3 sets of data[54], with (full) and without (free) in-medium modification of the ρ spectral function.*

mass shift is taken into account.

In fig.1.27 the HELIOS/3 IMR data are compared with the model of ref.[19] (see sec.1.5.4 of the present chapter); the background contribution consists of dimuons from open-charm, DY and primary vector mesons, which is then added to the secondary contribution from thermal dimuons produced in a HG to give the final curve. The shape of the theoretical curve does not well reproduce the experimental mass spectrum in the range $1.5 < M < 2.5\ GeV/c^2$. The possible contributions from an enhanced charm production and/or secondary Drell-Yan pairs (see chapter 7) have not been included in the model. The inclusion of these mechanisms could perhaps lead to a better agreement between theoretical predictions and experimental data in the IMR for M$> 1.5\ GeV/c^2$.

1.8.3 Previous knowledge and things to come

We have seen that for the low mass region some successful theories can well reproduce the observed excess in the dilepton spectrum. On the other hand, the excess measured in the intermediate mass region can originate from different sources (enhanced open charm production, secondary DY, thermal dileptons from a HG or QGP...), which actual role in the dimuon enhanced production is not yet clear. It is therefore necessary to assume $a-priori$ how to interpret the dilepton excess in the IMR and subsequently verify if a good description of all experimental data can be achieved within the chosen assumption.

In the present work the NA38/NA50 IMR excess is described as a simple superposition of dimuons from open-charm and DY, after combinatorial background subtraction. The 450 GeV/c p-A (NA50), 200 A GeV/c S-U (NA38) and 158 A GeV/c Pb-Pb (NA50, high statistics) sets of data are studied. The thermal dimuon contribution is not taken into account, because the theoretical description of such dimuon source is still affected by incertitudes.

It has been shown [42] that in order to describe the low mass region excess measured by CERES in S-Au collisions as originating from an enhanced open-charm production, the expected open-charm yield should be enhanced by a factor 150. Fig.1.28 from ref.[42] has been obtained in this hypothesis. Such a large enhancement factor is excluded by the results presented by the NA38/NA50 Collaboration at QM96 (see fig.1.18). Therefore, if the IMR excess originates from an enhanced open-charm production, this would clearly distinguish between the low and intermediate mass region excess.

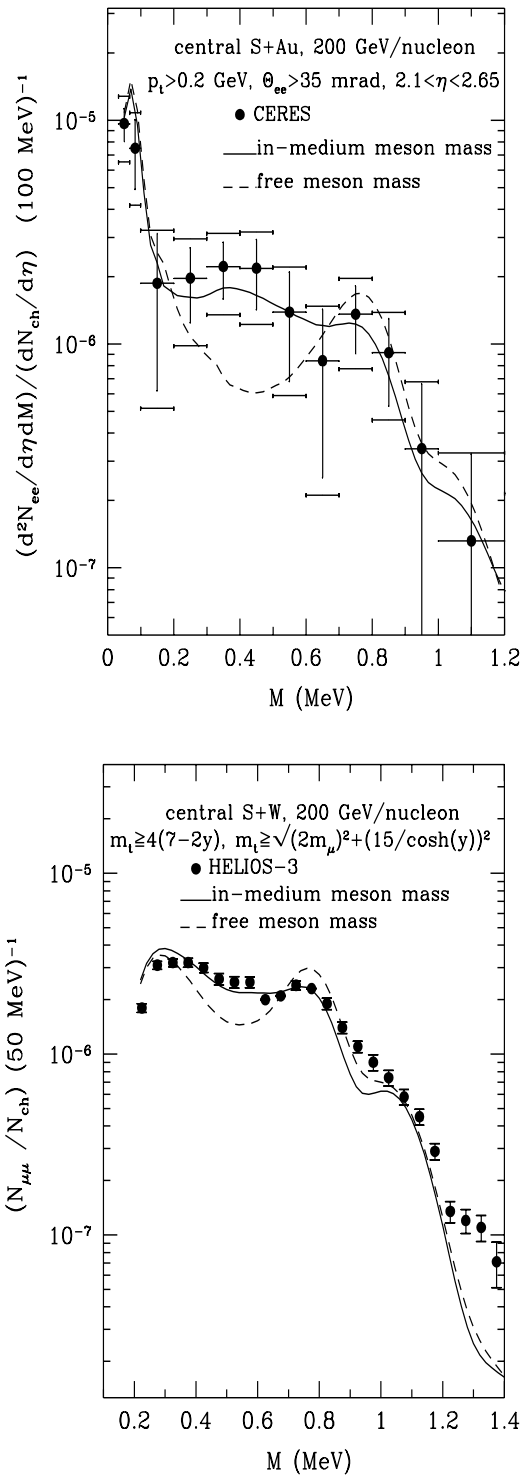

Figure 1.26: *CERES invariant mass spectra of dilepton from central 200 A GeV/c S-Au and HELIOS/3 invariant mass spectra of dilepton from central 200 A GeV/c S-W collisions compared with the theoretical curves obtained with (in-medium) and without (free) in-medium modification of the ρ mass shift[55].*

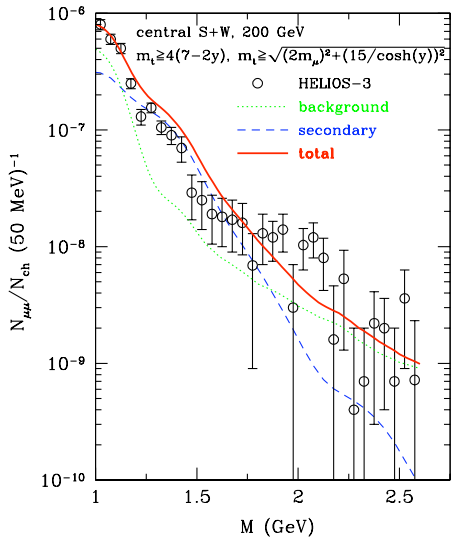

Figure 1.27: *Dimuon spectrum in central S-W collisions at 200 A GeV/c compared with calculations taking into account thermal dimuons from a hadron gas (indicated as secondary in the figure). The background contribution from open-charm, DY and primary vector mesons is added to the secondary contribution to give the total predicted yield.*

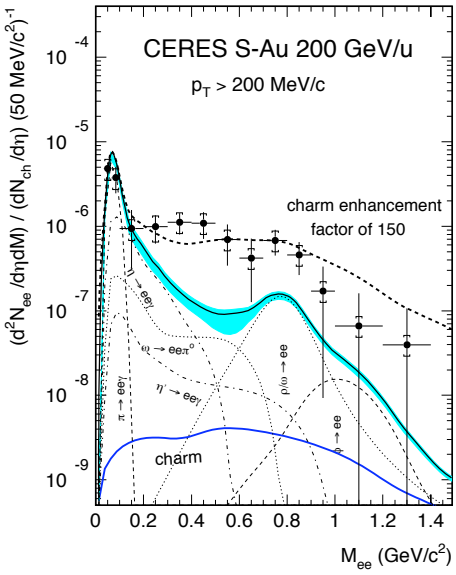

Figure 1.28: *Invariant mass spectrum of e^+e^- pairs measured by CERES in 200 A GeV/c collisions. The solid line gives the contribution expected from charm production in the standard scenario. The dashed line results from adding to the hadron decay background a charm contribution enhanced by a factor 150[42].*

Bibliography

[1] F.Karsh et al., Z.Phys.C-Particles and Fields 37 (1988)617

[2] Review of particle physics, The Eur.Phys.Journal, 1998.

[3] H.Satz, CERN-TH.7410/94

[4] E.Laermann, Nucl.Phys. A610 (1996) 1c-12c

[5] T.Matsui *et al.*, Phys. Lett. B 178 (1986) 416

[6] D.Kharzeev *et al.*, Z. Phys. C 74 (1997) 307-318

[7] Abreu M.C. *et al.* (NA50 collaboration), Phys.Lett. B410(1997)337

[8] J.Rafelski *et al.*, Phys. Rev. Lett. 48 (1982) 1066-1069

[9] J.Schaffner-Bielich, nucl-th/9711044 21 Nov 1997

[10] E.Anders et al., WA97 Collaboration, CERN-EP/98-64, 22 April 1998

[11] D.Jouan, for the NA38 Collaboration, at the Quark Matter '97 Conference, Japan (1997).

[12] A.Shor, Phys.Lett. B215 (1988)375.

[13] A.Shor, Phys.Lett. B233 (1989)231.

[14] P.Levai et al., Phys.Rev. C 56-5(1997)2707-2717

[15] P.V.Ruuskanen, Nuclear Physics A525 (1991) 255c-268c.

[16] R.Baier *et al.*, Invited talk at the 28th International Conference in High Energy Physics, Warszawa (1996).

[17] L.H.Xia et al., Phys.Rev. C 41, no.2 (1990) 572

[18] R.C.Hwa et al.,Phys.Rev D 32,no.5 (1985) 1109

[19] G.Q.Li et al., Preprint nucl-th/9807005 (1998)

[20] P.Huovinen *et al.*, Preprint nucl-th/980707

[21] B.Friman, Nucl. Phys. A610 (1996) 358c-372c

[22] T.Hatsuda *et al.*, Nucl. Phys. A590 (1995) 545c-548c

[23] Ito et al. E288 Collaboration, Phys.Rev. D23 (1991) 604

[24] A.Baldit et al., Phys.Lett., B332 (1994)244-250

[25] A.D.Martin et al., hep-ph/9409257

[26] A.D.Martin et al., Phys.Rev. D 51(1995)4856

[27] M.Gluck et al., Z.Phys. C53 (1992) 127

[28] PDFLIB 7.09, Users's Manual, CERN/PPE (1997)

[29] K.J.Eskola, Preprint hep-ph/9807297, 1998

[30] J.J.Aubert et al., the EMC Collaboration, Phys.Lett. 123B, no.3,4 (1983) 275

[31] A.Bodek et al., Phys.Rev.D 23,no.5 (1981) 1070

[32] C.Lourenço, Ph.D. thesis, Universidade tecnica de Lisboa, 1995

[33] N.Armesto, Preprint hep-ph/9609296, 1996

[34] S.Frixione et al., CERN-TH/97-16, hep-ph/9702287

[35] S.J. Brodsky et al., Nucl.Phys. B360 (1991)67-96

[36] S.J. Brodsky et al., Nucl.Phys. B383 (1992)643-684

[37] S.J. Brodsky et al., Nucl.Phys. B 438 (1995)261-277

[38] H.Nowak, Fortschritte der Physik, 39, no.5,6 (1991) 347

[39] M.J.Leitch et al. (E789 Collaboration), Phys.Rev.D51(1995)4756

[40] G.A. Alves et al. (E769 Collaboration), Phys.Rev.Lett.70 (1993)722.

[41] M.Adamovich et al., Nucl.Phys. B 495 (1997)3-34

[42] P.Braun-Munzinger *et al.*, subm. Z.Phys. C (1997)

[43] J.Ftacnik et al.,Phys. Lett. B196, no.3, 1987

[44] M.I.Gorentstein et al., Z.Phys.C-Particles and Fields 37 (1988)611; M.I.Gorentstein et al., Phys.Lett. 192,np1,2 (1987)198

[45] B.Kampfer et al., Z.Phys.C-Particles and Fields 45 (1990) 491

[46] C.Lourenco, for the NA38 Collaboration at the Quark Matter '93 Conference, Borlange, Sweden (1993).

[47] C.Lourenco, for the NA38 Collaboration, Proc.of the 5th Conference on Intersections between Particle and Nuclear Physics, St.Petersburg, FL(1994)

[48] P.Wurm, for the NA45/CERES Collaboration at the Quark Matter '95 Conference, Monterey, California, USA (1995)

[49] M.Masera, for the HELIOS/3 Collaboration at the Quark Matter '95 Conference, Monterey, California, USA (1995)

[50] E.Scomparin, for the NA50 Collaboration, at the Quark Matter '96 Conference, Heidelberg, Germany (1996),Nucl. Phys., A : 610(1996) (331c-341c).

[51] Th.Ullrich, for the NA45/CERES Collaboration, at the Quark Matter '96 Conference, Heidelberg, Germany (1996).

[52] G.Agakichiev *et al.*, nucl-ex/9712008 (1997), sub. Phys. Lett. B, 422(1998)405 1/4

[53] A.L.S.Angelis *et al.*, the HELIOS/3 Collaboration, CERN-EP/98-82 and to be submitted to Zeit.fur.Physik.

[54] W.Cassing *et al.*, Preprint nucl-th/9708020, Subm. to Phys. Rev., C. (13 p) (1997)

[55] G.Q.Li *et al.*, Nucl.Phys. A611, 539 (1996)

Chapter 2

The experimental apparatus

In this chapter the NA38/NA50 experimental apparatus is described. The differences existing between the set-ups used to collect the pA, SU and PbPb data analysed in the present work are also pointed out.

2.1 Introduction

The NA50 experiment is located at CERN (European Laboratory for Particle Physics) and uses the SPS (Super Proton Synchroton) proton and lead beams. The aim of the experiment is the study of the dimuon production in ultra-relativistic Pb-Pb and proton-nucleus interactions.
The NA38/NA50 experimental apparatus is based on the upgraded NA10 spectrometer[1]. The NA50 apparatus has also been improved with respect to NA38 : two new detectors for the measurement of the centrality of the interaction (the multiplicity detector and the zero degree calorimeter) have been added, the Beam Hodoscope and the target detector have been rebuilt in quartz to be radiation resistant and the pseudo-rapidity coverage of the electro-magnetic calorimeter (EMCal) has been shifted to larger angles.
Since NA50 uses both the proton and the lead ion beam from the SPS, the target system can be correspondingly changed. When the experiment is running with a proton beam, the target is single and thick and no interaction vertex recognition is possible. On the other hand, the target used when running with lead ions, consists of a number of lead sub-targets with corresponding interaction vertex recognition system. During the NA38 S-U data taking period the target was also segmented. In the last section of the present chapter, the characteristics of the targets used during the NA50 1996-97 450 GeV/c p-A and 1996 158 A GeV/c Pb-Pb and the NA38 1992 200 A GeV/c S-U data taking periods are described.
In the following a detailed description of the NA38/NA50 spectrometers is given and the most important differences between the two apparata are pointed out.

2.2 The muon spectrometer

The NA38/NA50 muon spectrometer is used to reconstruct the dimuon events and the associated kinematic variables. It consists of a hadron absorber, a toroidal field magnet and of a system of MWPC's and scintillator hodoscopes placed both before and after the magnet as shown in fig.2.1
In NA38 muon pairs were detected in the pseudo-rapidity interval $2.8< \eta <4.1$ whilst in NA50 muon pairs are detected in the pseudorapidity interval $2.8< \eta <4.0$.

2.2.1 The hadron absorber

The hadron absorber, see fig.2.2, is composed by different layers of materials. In Tab.2.1 the characteristics of all the absorber materials are listed. In NA38 the very central part, the so called plug, was a cone of W-U which absorbed the beam which did not interact in the target. In NA50 the first 80 cm of W in the plug have been replaced by 65 cm of Ta corresponding to the zero degree calorimeter (see section 2.3.3.) followed by 15 cm of air. The plug is surrounded by carbon cylinders, for a total length of 4 m followed by 80 cm of iron at the very back of the absorber. Iron

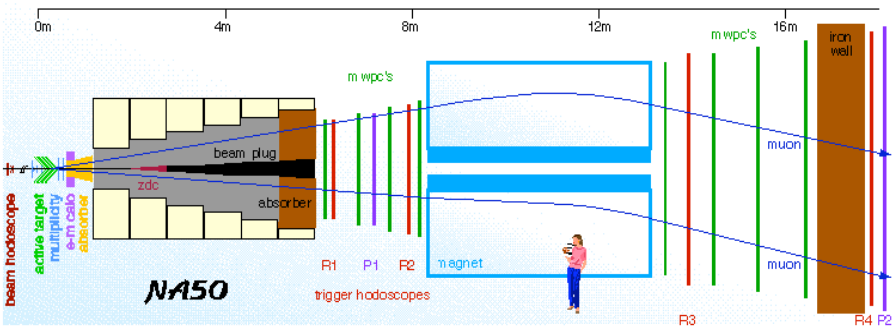

Figure 2.1: *The NA50 muon spectrometer.*

and concrete blocks are finally placed all around the carbon cylinders. The carbon cylinders and the last 80 cm of iron absorb hadrons coming from the interaction region but introduce small angular deflections on the muon track because of the multiple scattering effect : $\Delta\theta_\mu$ (C) $= \simeq 64$ mrad/p(GeV) and $\Delta\theta_\mu$ (Fe) $= \simeq 101$ mrad/p(GeV) if the Gaussian angular distribution is used[7]; the muon angle θ_μ is defined as

$$\theta_\mu = tan^{-1}(\frac{p_T}{p_l}) \tag{2.1}$$

where p_T and p_l are the transverse and longitudinal muon momenta in the laboratory frame.
Before the main absorber a preabsorber is placed to diminish the hadron (kaon and pion) disintegration : 59.1 cm BeO (p-W and Pb-Pb 96) or 60.8 cm Al_2O_3 (p-A 1997 with A=Al, Cu, Ag). The BeO preabsorber is placed in the innest EMCal part, and it is therefore used together with the EMCal. During the p-W 96 data taking period the BeO has also been used because the Al_2O_3 preabsorber was not yet available. During the following p-A NA50 data taking periods, the EMCal has been moved out of the spectrometer and the Al_2O_3 adopted. The BeO preabsorber covers the pseudo-rapidity range $2.42 < \eta < 4.43$, whilst the Al_2O_3 one covers the range $2.17 < \eta < 4.93$. A central hole along the beam axis allows the passage of the ions which did not interact in the target.
At the very end of the whole spectrometer, just before the last trigger hodoscope, a 1.2 m thick iron wall stops the surviving mesons to avoid the counting of fake triggers.

2.2.2 The toroidal field magnet

The hexagonally shaped magnet is 4.8 m long with an internal radius of 29.5 cm and an external one of 1.54 m, as shown in fig.2.3. It is placed at 1046.45 cm from the target centre, and covers the pseudo-rapidity interval $2.6 < \eta < 4.26$.

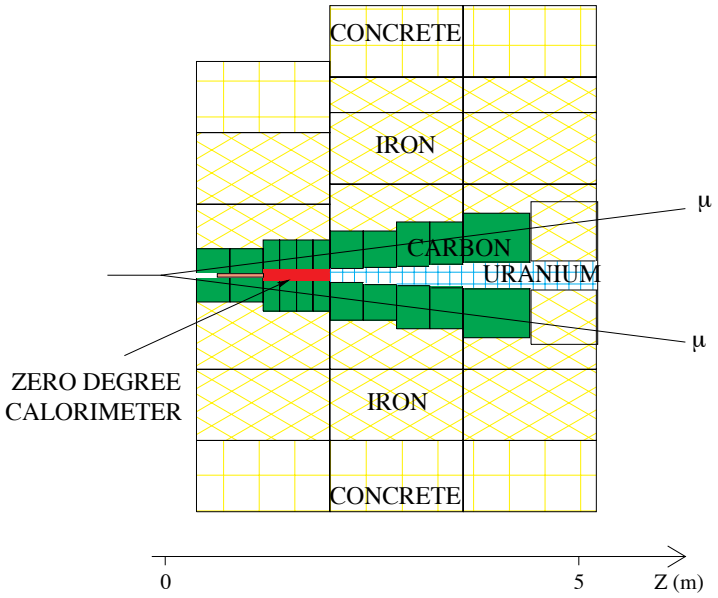

Figure 2.2: *The hadron absorber*

Material	Aim	Length (cm)	λ_i (g/cm^2)	ρ (g/cm^3)	X_0 (g/cm^2)
Al_2O_3	Pre-abs.	60.8	98.70	3.82	27.90
BeO	Pre-abs.	59.1	84.90	2.81	41.30
C	Main-abs.	400.0	86.30	1.93	42.70
Fe	Main-abs.	80.0	131.90	7.20	13.84
Air	Plug	80.0	84.40	38.30	36.66
Ta	ZDC(plug)	65.0	197.95	16.6	6.83
W	Plug	80.0	185.00	17.80	6.76
U	Plug	320.0	199.00	18.95	6.00

Table 2.1: *Characteristics of the absorber and pre-absorber materials.*

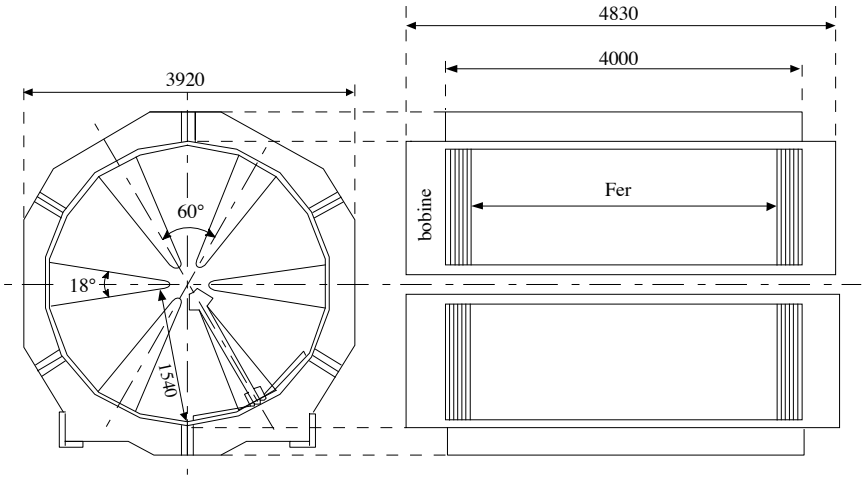

Figure 2.3: *The NA50 magnet*

The magnetic field is generated by a pulsed current circulating in 6 coils mounted on 6 iron supports occupying an azimuthal angle of 18^0. The generated azimuthal field, shown in fig.2.4, is characterised by a radial intensity, i.e.

$$\vec{B} = \frac{B_0}{r}\vec{e_\phi}$$

where B_0 depends on the current intensity, i.e., $B_0 = 0.383$ T m for 7000 A (NA50) and $B_0 = 0.550$ T m for the 10000 A current used in the NA38 p-A data taking. In NA38, for the S-U data taking period a 4000 A current was used corresponding to $B_0 = 0.219$ T m. In NA50 the current value has been raised to 7000 A in order to eliminate the soft muon background and have a good J/ψ mass resolution ($\simeq 3\%$ in NA50 and $\simeq 5\%$ in NA38).
Particles are deflected in the same azimuthal plane they belonged to when entering the magnetic field and the deflection can be calculated as[4]

$$\Delta\theta \simeq \frac{qB_0}{p_T} ln(\frac{z_2}{z_1}) = \frac{b}{p_T} \tag{2.2}$$

where z_1-z_2 is the magnet length, the z_i being computed from the target, and b = 0.023 rad GeV in NA38 for a 4000 A current and b = 0.0402 rad GeV in NA50.

2.2.3 The trigger hodoscopes

The 4 hodoscopes in the muon spectrometer provide the signal for the dimuon trigger and allow a first determination of the dimuon trajectory. They have the same hexagonal shape than the magnet and they consist of 6 azimuthal units of scintillator blades. They are organized in two sets, one placed between the main

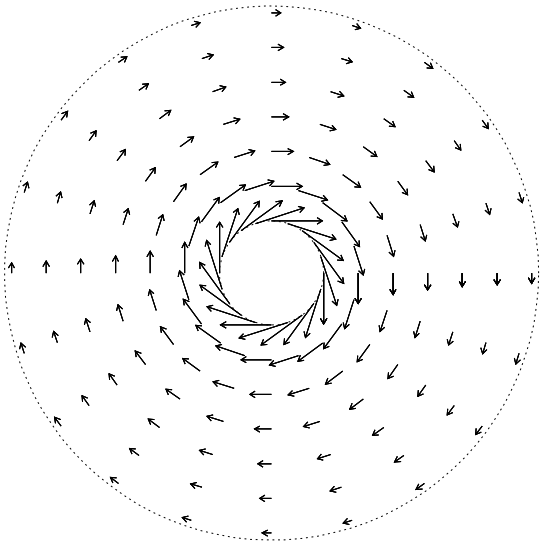

Figure 2.4: *The azimuthal magnetic field*

absorber and the magnet (R_1 and R_2) and one after the magnet, R_3 and R_4, as visible in fig.2.1.
R_1 and R_2 are homothetic copies of each other with respect to the central sub-target position. They consist of 30 blades for each sextant. Since the dimension of the blades grows with the radial distance from the beam axis, a particle coming from the interaction vertex will cross the blades R_{1i} and R_{2i} (or $R_{2(i+1)}$).
R_3 and R_4 have blades of identical dimension (23 blades for R_3 and 32 for R_4). R_3 is placed after the magnet and before the ending iron wall whilst R_4 comes just after it.

2.2.4 The proportional wire chambers

The two sets of 4 MWPC's, see fig.2.5, are used to precisely (some tenth of a mrad) reconstruct the muon tracks before and after the deflecting magnet. The first set of four chambers is placed just after the main absorber and reconstructs the part of the track which is pointing at the interaction vertex. The second set is placed after the magnet and reconstructs the track after it has been bent in the magnet. Each chamber is hexagonally shaped and consists of three independent planes rotated of 0^0, 60^0, 120^0 with respect to the vertical axis. The three planes are placed 2.2 cm from each other, the distance between the wires is 3 mm for all chambers and each wire has a diameter of 20 μm. The radius of the chambers in the first set is 1.3 m and each chamber consists of 749 wires, whereas the radius of the chambers in the second set is 3 m and each chamber consists of 1229 wires. The MWPC's are filled

with a mixture of Argon (80%), ISO-butane (19.8%) and Freon (0.2%).

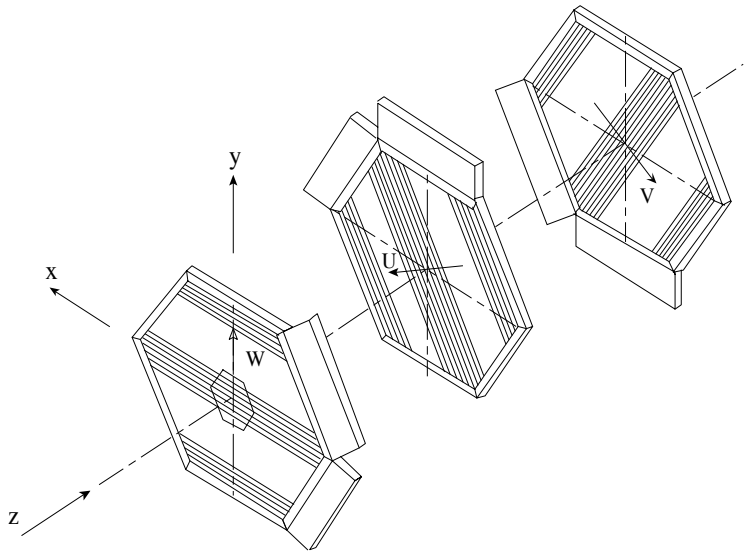

Figure 2.5: *The multi-wire proportional chambers.*

2.3 The centrality detectors

In order to search for threshold effects taking place when a certain temperature and/or energy density is created in the interaction volume, it is important to be able to select different ranges of centrality in the ion-ion collisions. In NA50, the centrality measurement is performed by three independent detectors in the experimental apparatus : the multiplicity detector (MD), the electro-magnetic calorimeter (EMC) and the zero degree calorimeter (ZDC). The MD measurement is strongly correlated with the EMC one and both are anti-correlated with the ZDC. In the NA38 S-U 1992 data taking period, the collision centrality was uniquely measured with the EMC[6].

2.3.1 The multiplicity detector

The MD measures the multiplicity of particles produced in a Pb-Pb collision. It consists of two silicon strip detectors organised in 2 discs each. Each detector consists of $\approx$ 7000 silicon micro-strips. In fig.2.6 one of the detector is shown.

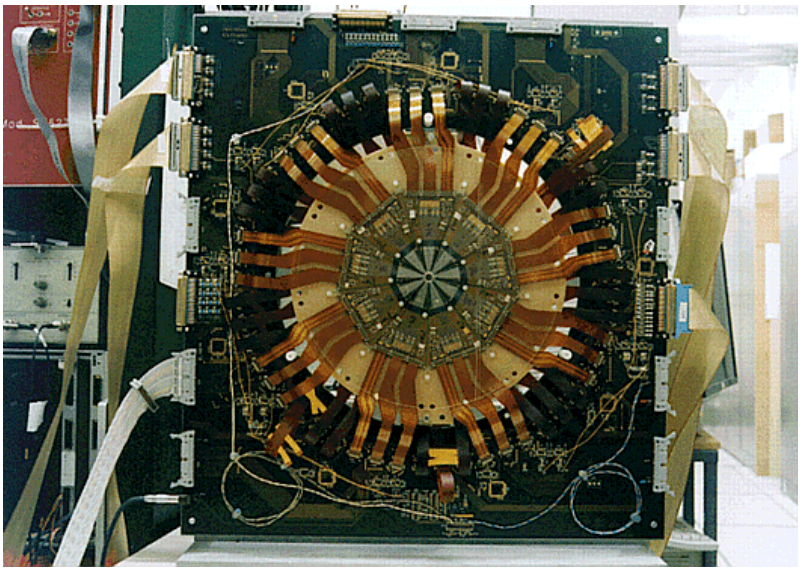

Figure 2.6: *One of the two Multiplicity Detector planes.*

The MD detector is placed after the target system and before the preabsorber, as shown in fig.2.7 and covers the pseudo-rapidity interval $1.5 < \eta < 3.9$. A very detailed description of the MD can be found in[2].

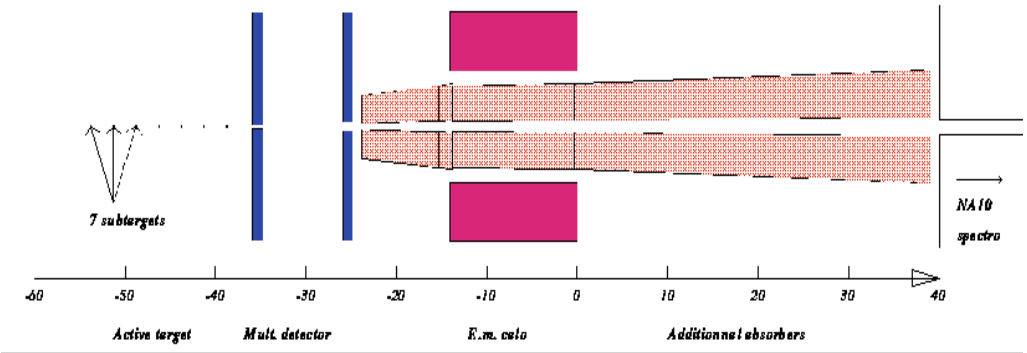

Figure 2.7: *View of the target region. The Multiplicity Detector and the Electromagnetic Calorimeter are shown.*

2.3.2 The electro-magnetic calorimeter

The electro-magnetic calorimeter (EMCal) is 14 cm long, with an internal radius of 8.2 cm and an external one of 24.2 cm. It consists of polystyrene scintillating fibres ($\oslash = 2mm$) which are placed parallel to the beam axis and embedded in an alloy of lead and bismuth, for a fibres to alloy ratio of 1/2. The EMCal has the

same hexagonal shape of all the detectors placed in the muon spectrometer and it is subdivided in four crowns, each of them covering a pseudo-rapidity interval $\Delta\eta = 0.34$. The calorimeter, positioned 32 cm downstream from the central sub-target as shown in fig.2.7, measures the neutral transverse energy produced in every nucleus-nucleus collision. The EMCal, which in NA38 covered the pseudo-rapidity interval $1.7 < \eta < 4.1$, in NA50 has been shifted to $1.1 < \eta < 2.3$ in order to reduce the amount of heavy material crossed by the muons and therefore improve the J/ψ and ψ' mass resolution.

2.3.3 The zero degree calorimeter

The zero degree calorimeter (ZDC), sketched in fig.2.8, measures the energy of the projectile nucleons which did not interact in the target, i.e., the projectile spectators. By subtraction the energy deposited in the collision can be obtained

$$E_{dep} = E_{beam} - E_{ZDC}$$

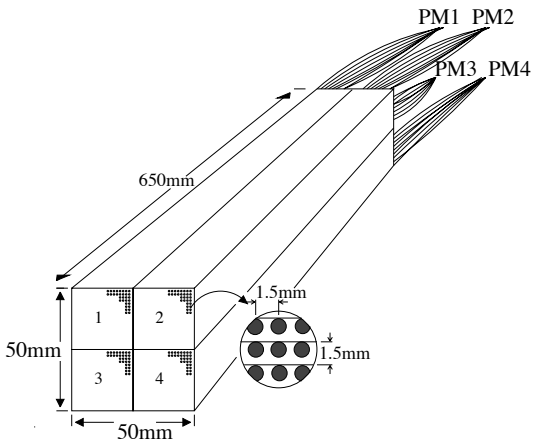

Figure 2.8: *The Zero Degree Calorimeter*

The ZDC is placed inside the main absorber, in the W-U internal cone of which it replaces the innest part, 165 cm downstream from the target. It has a cross section of 5X5 cm^2 for 65 cm of length. It consists of 900 quartz fibres ($\oslash = 365\mu$m for a length of 1.8 m) embedded in 30 tantalum blades (1.56 mm thick) for a Si/Ta ratio of 1/17. Since the ZDC has to stand extremely high radiation level, $\simeq 70$ MRaD on average during the 1996 158 A GeV/c Pb-Pb data taking period (corresponding to 4 GRaD in the ZDC central region), quartz fibres are used instead of the commonly adopted scintillating ones. The calorimeter reveals particles via the Cerenkov effect. The fibres are parallel to the beam axis for the first 65 cm, the active part, then they bend and guide the light to four photo-multipliers. To obtain a beam position sensitive device, the fibres are organised in four groups, each read by one of the four

PM's. The ZDC acceptance is delimited by a copper collimator 60 cm long and with a conical aperture of 3.5 mrad ($\eta \geq 6.3$).
The energy resolution of the ZDC has been measured with proton, deuteron, alpha and lead beams[3]. The ZDC energy resolution for a 158 A GeV/c Pb beam is 5% before and 7% after $\approx$ 40 days of data taking.

2.4 The beam

The NA50 experiment is located in the ECN3 hall where a high intensity beam is extracted. In fig.2.9 the beam line is shown[5].

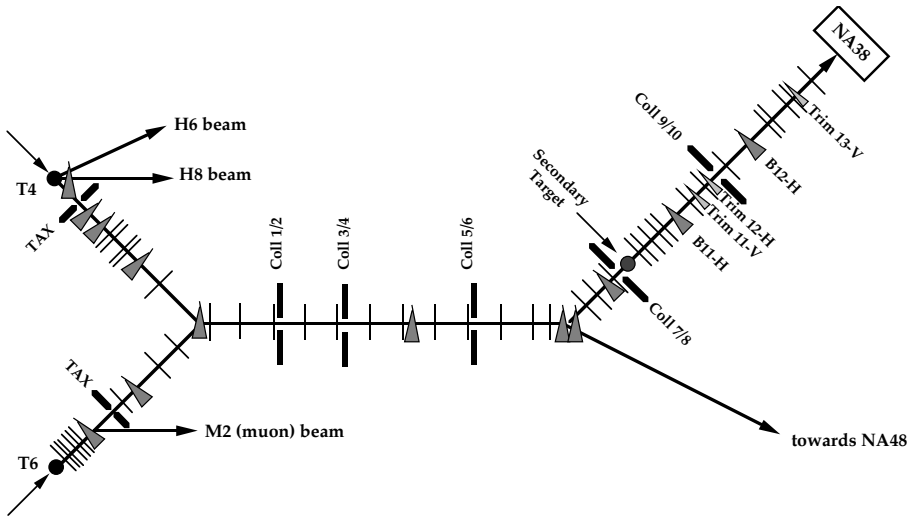

Figure 2.9: *Schematic view of NA38/NA50 beam line*

The primary beam, coming from the SPS, is either a proton or an ion beam. Protons are delivered with an energy of 450 GeV/c per charged particle whilst ions have 400 GeV/c per charged particle (158 GeV per nucleon for a Pb ion beam). The beam intensity is different in the case of proton and ion beam : the maximum number of particles (ions) per burst is 10^{11} for the former and around $5 \cdot 10^7$ for the latter. In NA38, during S-U data taking, the beam intensity was 10^8 S ions/burst. The beam intensity during ion-ion data taking periods has been chosen as a compromise between the safety and efficiency of the detectors which are directly placed on the beam line and the small J/ψ cross section in the $\mu\mu$ decay channel, $B_{\mu\mu}\sigma_{J/psi} = 2.10 \pm 0.15$ nb/nucleon in pp collisions at 200 GeV/c with

$$B_{\mu\mu}\sigma^{AB}_{J/psi} = B_{\mu\mu}\sigma^{pp}_{J/psi} \cdot (AB)^{\alpha} \tag{2.3}$$

where $\alpha = 0.920 \pm 0.015$[8]. As for the p-A data taking period, the maximum intensity is imposed by the chamber efficiency which is affected by a too high chamber

occupation level : in 450 GeV/c p-A the chamber reconstruction efficiency is 100% at low (10^8 protons/burst) intensity and falls down to 90-95% when higher ($\simeq$ 2.5 10^9 protons/burst) intensities are used.
The beam cycle is 20 s, for a 5 s effective spill.
A beam hodoscope (BH) placed 22 m upstream from the target counts the incoming ions and measures the luminosity during ion-ion data taking periods. The crossing ions produce Cerenkov light in the BH quartz blades. This same hodoscope is used to reject events where more than one ion have crossed the detector blades in the same trigger time window of 20 ns, as explained in the next chapter.
When running with the proton beam, the beam hodoscope can not be used because of the too high number of impinging projectiles and the too little produced Cerenkov light. Three independent Argon counters are therefore used to measure the luminosity and no pile-up rejection is possible.

2.4.1 The Beam Hodoscope

Placed 22 m upstream the target, the NA50 Beam Hodoscope (BH) consists of one plane of 16 quartz blades, detecting the incoming ions by Cerenkov effect. Each blade is associated with a photo-multiplier and the blade transverse size is adjusted so that each blade receives the same fraction of the total incoming number of ions. This is also possible because of the large cross section the beam has when crossing the BH, σ_x=0.8 mm and σ_y = 6 mm. The overall efficiency has been found to be better than 99% but the maximum intensity the BH can stand is 10^8 particles/burst. If more than one ion cross the BH in the same 20 ns trigger gate, the corresponding dimuon event is eventually rejected during off-line data analysis. This is the so called beam pile-up rejection. In fact during ion-ion data taking periods piling-up ions can lead to a wrong centrality measurement if more than one of the piling-up ions also interact in the target.
In NA38, where the radiation level was much lower, the BH was entirely built with plastic scintillator.

2.4.2 The BHI and BHIN

The BHI and BHIN are placed just after the BH in order to detect any interaction having taken place in the BH itself. The BHI consists of two scintillator blades of 1X3X8 cm^3 in z, x and y respectively, and is placed 17 cm from the BH, covering the pseudo-rapidity interval $2< \eta <3.1$.

The BHIN (or BHI new) is placed after the BHI. It consists of four scintillator blades organised around a central hole. The central hole is as wide as the BH in order to avoid the interaction of the incoming ions in the BHIN blades. The BHIN covers the pseudo-rapidity interval $3.3< \eta <5.1$, therefore complementing the BHI.

2.4.3 The Argon counters

Three ionisation chambers, filled with Argon, measure the proton beam intensity integrating over the current produced by ionisation in the gas. Once known the calibration constant, C_{argo}, which translates the number of argonium counts in number of incident protons, the luminosity measurement is straightforward. The Argon counters can properly work over a wide intensity range (10^6 to 10^{11} protons per second).

2.5 Trigger selection and data acquisition

The so called dimuon trigger selects events on the basis of the information given by the four R_i hodoscopes. If the two hodoscopes R_1 and R_2 have been hit in coincidence, i.e, on blades R_{1n} and R_{2n} (or $R_{2(n+1)}$), this makes a first positive selection of the muons which track points at the target region: this is called the V coincidence and defines the first half of the dimuon tracks. The dimuon is considered good if the hodoscopes R_3 and R_4, defining the last half of the dimuon tracks, are also in spatial and temporal coincidence with the first ones. This global hodoscopes coincidence is called VXR_3XR_4. This type of trigger allows a measurement of the bending of the muon tracks in the magnet, obtained extrapolating both half of the muon track up to the magnet middle plane. A good trigger is found when the extrapolated half of the track spatially coincide.
During Pb data taking periods, a maximum of 5000 events per burst can be recorded on tape (16Mbytes) within the 15 s inter-burst time. The data transfer takes place every burst; during the burst the data are kept in a temporary memory location. The maximum amount of events stored on a single tape defines the number of events per 'run'.

2.6 The target system

The NA38/NA50 target system used during heavy ion data taking periods has been designed in order to allow an easy determination of the interaction vertex. Therefore, the target is segmented and each sub-target is followed by two radiation resistant quartz blades whose signal identify the sub-target where the interaction took place. During p-A data taking periods the segmented target is replaced by a single thick one of the desired material.

In the present work, the 1996-1997 450 GeV/c p-A(A=Al, Cu, Ag, W), the 1996 158 A GeV/c Pb-Pb and the 1992 200 A GeV/c S-U sets of data are analysed. From now on those sets will be simply indicated as pA, PbPb and SU, otherwise specified when necessary.

2.6.1 PbPb 1996

During the 1996 PbPb data taking period, the target system consisted of 7 sub-targets each followed by two quartz blades, as shown in fig.2.10. This system allowed for the identification of the sub-target where the interaction took place and the one where eventually a projectile fragment had re-interacted. The radiation resistant quartz blades were placed on both sides of each sub-target and detected the Cerenkov light produced by the high energy secondary particles generated in the collision. The first and last sub-targets were 1 mm thick while the 5 middle ones had a thickness of 2 mm. This system corresponded to a total of 30% λ_i, where $\lambda_i(Pb)$= 194 $gr\ cm^{-2}$.
Just before the first sub-target, two quartz blades recognised when the interactions took place in the air before the target system. Since, at the target level, the cross section of the Pb beam is $\sigma_x \approx \sigma_y \approx 0.4$ mm, a couple of anti-halo detectors counted the number of ions arriving at the target out of a 3 mm diameter.

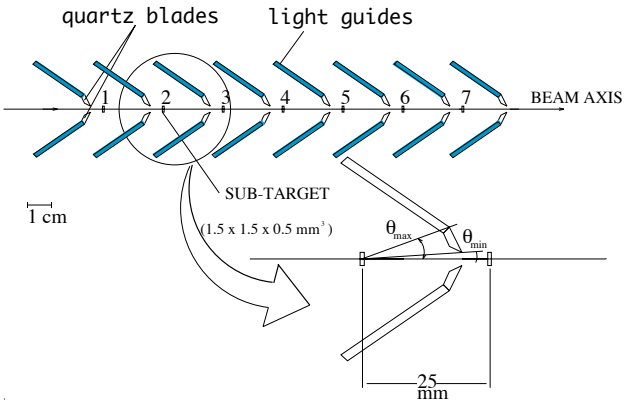

Figure 2.10: *The active target*

2.6.2 SU 1992

During the 1992 SU data taking period, the active target consisted of 12 sub-targets and 32 scintillating rings. The first sub-target had a x and y half-size of 5 mm and a thickness of 1 mm, whereas the following sub-targets were 0.5 mm in x and 1 mm in y for a thickness of 1 mm. The total interaction length was 20% $\lambda_i(U)$, where $\lambda_i(U) = 199\ g\ cm^{-}2$[6].

2.6.3 pA 1996-1997

During the 1996-1997 pA data taking periods the target was single and thick, not allowing for vertex recognition or re-interaction rejection. The characteristics of the 4 targets used between 1996 and 1997 are listed in tab.2.2.

Target	A (g)	L (cm)	λ_i ($\frac{gr}{cm^2}$)	ρ ($\frac{gr}{cm^3}$)	χ_0 (cm)
Al	26.98	12	106.4	2.70	8.9
Cu	63.54	7.5	134.9	8.960	12.86
Ag	107.87	7,5	156	10.5	6.37
W	183.85	4.5	185.0	17.80	0.35

Table 2.2: *Targets characteristics for the data taking periods p-A 1996-1997.*

Bibliography

[1] L.Anderson et al., Nucl.Inst.Meth. 223(1984)26

[2] Stefania Beolè, PhD Thesis , February 1998, Torino.

[3] R.Arnaldi et al., Nuclear Instruments and Methods in Physics Research A411(1998)1

[4] Frederic Fleuret, PhD thesis, April 1997, E.P.,Paris.

[5] Carlos Lorenço, PhD thesis, January 1995, Lisboa.

[6] Amir Bohrani, PhD thesis, April 1996, Uni. Paris 6.

[7] C.Caso et al., Review of Particle Physics, The European Physics Journal C3 (1998) 1

[8] M.C.Abreu et al., Physics Letters B410(1997)337

Chapter 3

Data reduction

In this chapter I briefly describe the method used to process the data in order to reconstruct the dimuon events and compute the related physical quantities. The 1992 S-U and 1996 Pb-Pb data have been organised in subsamples corresponding to different bins of transverse energy E_T, which are also listed at the end of the chapter.

3.1 Run selection

Raw Data Tapes are first analysed with a dedicated program[1] which reconstructs the dimuon tracks and gives all useful informations on the related kinematic quantities. When important intensity oscillations or hard-ware problems or related anomalies have been detected, the corresponding runs, defined as a single slot of raw data, are rejected. For instance, during pA data taking periods the ratio of the number of collected J/ψ over the number of incident particles is constantly checked in every run. This ratio is strictly related to the J/ψ production cross-section and gives an immediate picture of its evolution during data taking periods. In fig.3.1 the J/ψ over argonium ratio is shown for the pAl data taking period. Argonium detectors are only used during proton-nucleus data taking in order to measure the beam intensity. The number of argonium counts is directly related to the number of incident particles via a known calibration constant ($C_{argo} = 6750$). At low intensity ($\approx 2{\cdot}10^8$ proton/burst) the measured J/ψ over argonium ratio is larger because the MWPC track reconstruction efficiency is 100%, whilst at higher intensity the MWPC reconstruction efficiency is reduced by the large number of tracks which have to be processed in order to reconstruct a single dimuon event. This systematic effect can be corrected off-line, using the low intensity runs as a normalisation in the calculation of the absolute cross-sections.

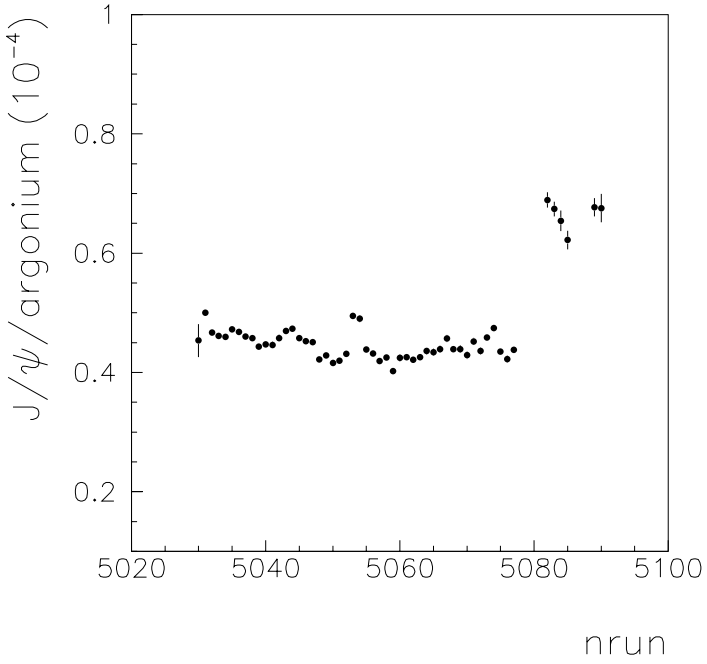

Figure 3.1: *Ratio $\frac{J/\psi}{argonium}$ vs. the run number for the pAl data taking period. The MWPC reconstruction efficiency was 100% during the low intensity beams, where a larger $\frac{J/\psi}{argonium}$ has been measured.*

3.2 Dimuon track reconstruction

A dimuon event is found when at least two tracks have been reconstructed from the hits in the MWPC's. The dimuon event is accepted if it has been signalled by the trigger hodoscopes and if the reconstructed tracks do not cross the magnet iron support.
During nucleus-nucleus data taking periods, the target detector system ensures a very precise vertex determination. On the other hand, during proton-nucleus data taking periods the single thick target does not allow for vertex recognition; thus, the vertex is always assigned at the centre of the target itself. This does not affect the quality of the invariant mass computation since the length of the targets used in p-A periods never exceeds some centimetres.
An additional cut is then applied on the final set of events in order to ensure that the acceptance of the spectrometer is independent of the electric charge of the detected muons. This additional selection is obtained cutting all events where one of the muon would have been rejected if it had the opposite charge when entering the magnet. For the same reason the magnetic field sign is regularly changed during data taking periods. Another selection can also be applied at the vertex level. The distance DTARG between the vertex, which coordinates are (x,y,z)$\equiv$(0,0,z_V) and the muon track at (x_T,y_T,$z_T = z_V$) is computed; x_T and y_T are the generic x and y coordinates of the track starting point. Since multiple scattering depends on the particle momentum, a direct cut on DTARG would differently affect tracks with different momenta. Therefore, the variable PxDTARG is obtained multiplying the muon track DTARG by the corresponding muon momentum P, and the χ^2 distribution of the PxDTARG variable is constructed for each considered set of events. The cut is then applied on the χ^2 distribution obtained for the specific set of events. When a x% cut on PxDTARG is applied, events with a χ^2 probability ¿x% are accepted. The PxDTARG selection ensures the elimination of dimuons generated outside the target region which would be reconstructed at a much higher or lower mass than their actual one. For the same reason it also ensures a partial cleaning of the background from pion and kaon decays. The effect of a 1% PxDTARG cut on the pAl set of data is shown in fig.3.2.

3.3 Event selection

An additional selection is applied on nucleus-nucleus events in order to ensure a good evaluation of the centrality of the events. The centrality selection uses the information given by the centrality detectors, the target vertex recognition system and the Beam Hodoscope, as briefly explained hereafter. One and only one interaction in one of the 7 sub-targets must have been signalled by the vertex recognition system, otherwise the event is eliminated because corresponding to the interaction of more than one ion or to the re-interaction of a projectile fragment. A stricter selection can be applied requesting that one and only one incoming Pb ion has been

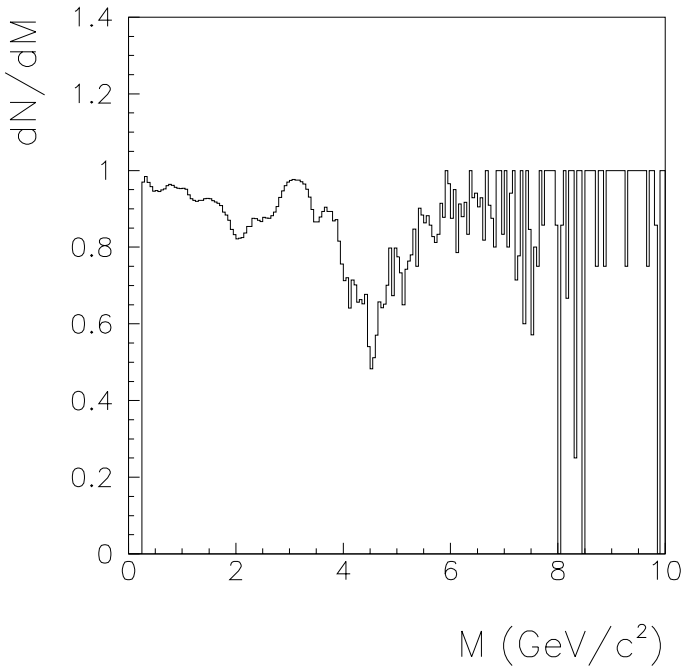

Figure 3.2: *Ratio of dimuon mass spectra with and without 1% PXDTARG cut for the pAl data set.*

detected by the BH and by the ZDC within the 20 ns trigger gate. Although the beam cut based on the BH ensures the selection of pile-up free events, it also induces the loss of a large fraction of events ($\approx 28\%$ of the total number of events in the 1996 PbPb data taking period). Notice that, when inefficiency are neglected, the selections based on the ZDC and on the BH are by definition redundant. All events presenting interaction in the BH, in the BHI or in the anti-halo counters are also eliminated.

3.4 Kinematic cuts

In order to compute the dimuon kinematic variables, the two muon tracks are assigned to the centre of the identified sub-target. The invariant mass M, the rapidity y, the transverse momentum p_T and the polar and azimuthal angles θ_{CS} and ϕ_{CS} in the Collin-Soper reference frame are then calculated. The Collin-Soper reference frame is defined in the following way : if $\vec{P_1}$ and $\vec{P_2}$ are the projectile and target momenta in the dimuon centre of mass, the CS $\hat{z}$ axis is defined as the bisector of $\vec{P_1}$ and -$\vec{P_2}$ and the CS $\hat{y}$ axis is parallel to $\vec{P_1} \times \vec{P_2}$.
In order to eliminate dimuons coming from kinematic regions where the acceptance of the apparatus is very low, kinematic cuts are applied on the dimuon rapidity y and $cos\theta_{CS}$. Tab.3.1 lists the kinematic domain D within which events are accepted

System	$P_{projectile}$ $(AGeV/c)$	$\sqrt{s}$ (GeV)	y_{cms}	y^* $[min:max]$	$cos\theta_{CS}$ $[min:max]$
pA	450	29.05	3.43	[-0.52:0.48]	[-0.5:0.5]
PbPb	158	17.22	2.91	[0.:1.]	[-0.5:0.5]
SU	200	19.37	3.03	[0.:1.]	[-0.5:0.5]

Table 3.1: *Kinematic cuts imposed on the dimuon kinematic variables.*

for all the studied systems. The rapidity in the centre of mass reference frame can be obtained from the rapidity in the laboratory system, and vice-versa, with the following equation,

$$y_{lab} = y^* + y_{cms} \tag{3.1}$$

where y^* is the rapidity in the centre of mass reference system and y_{cms} is the rapidity of the centre of mass system in the laboratory frame.
Fig.3.3 and 3.4shows the mass, rapidity, p_T and $cos\theta_{CS}$ differential distributions of the accepted events for the pAl and PbPb systems. For the SU system see[2].

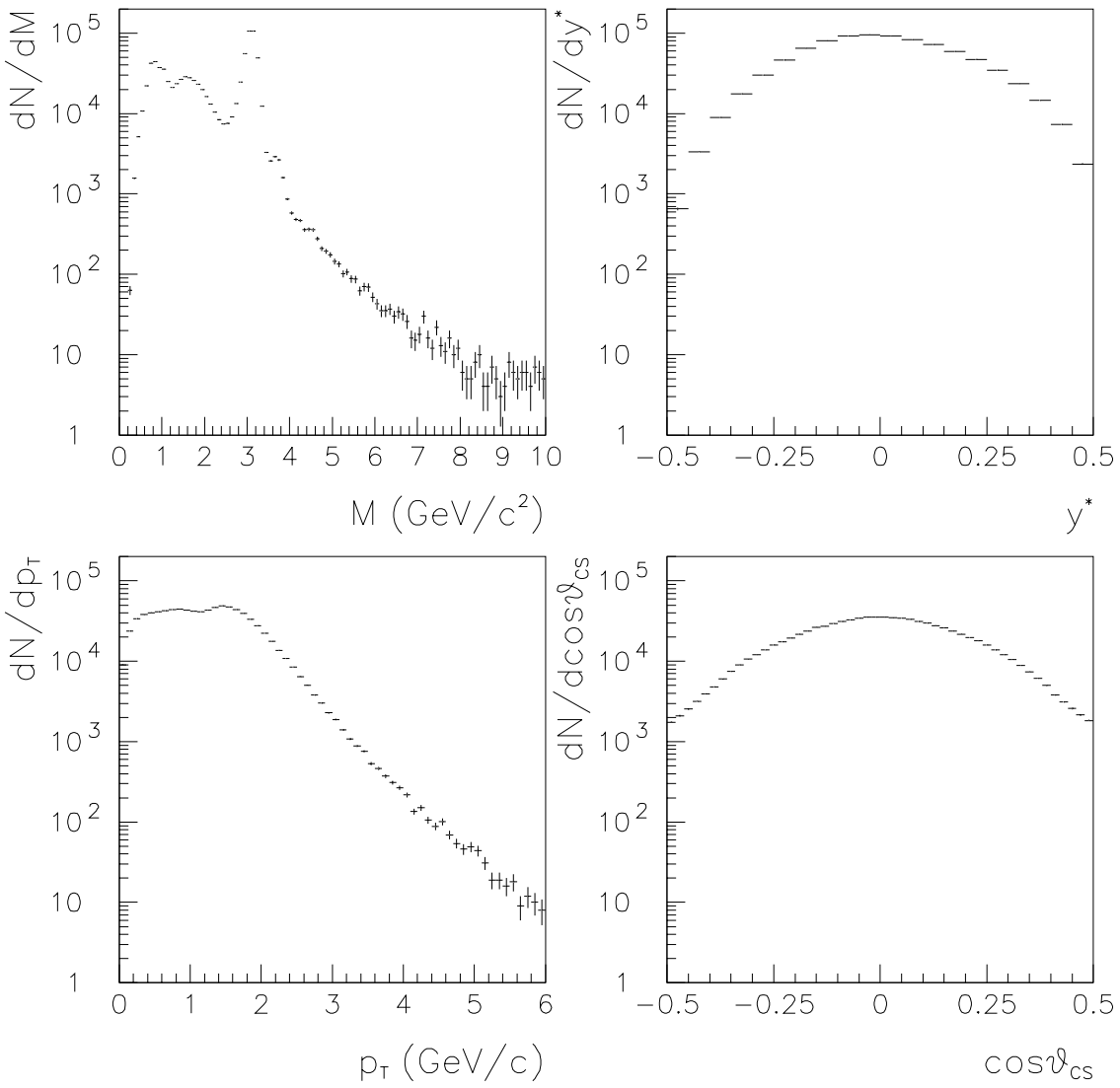

Figure 3.3: *Mass, rapidity, p_T and cosθ_{CS} distributions of accepted events for pAl.*

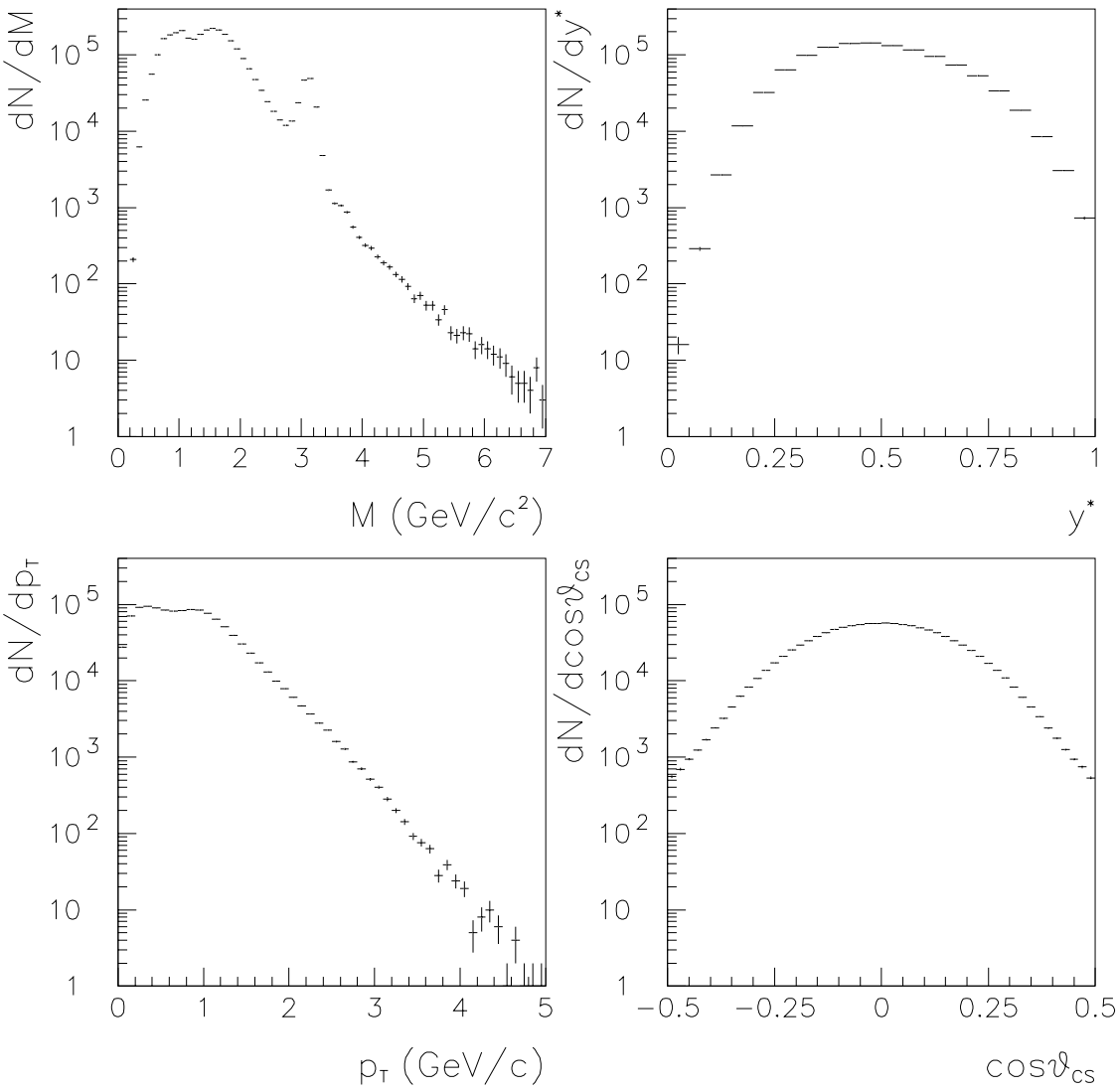

Figure 3.4: *Mass, rapidity, p_T and cosθ_{CS} distributions of accepted events for PbPb.*

3.5 Pb-Pb and S-U final selection

3.5.1 The PbPb sub-target identification cut

The PbPb sub-target identification system consists of two independent quartz blades placed after each of the 7 sub-targets; the two quartz blades gives two independent signals. When the interaction vertex has not been identified the corresponding event is rejected. The very weak signal associated with peripheral events can often be detected by only one of the two sub-targets. In this case, the independent behaviour of the two blades can be used to relax the cut at the vertex recognition level. Fig.3.5 shows the different effect of the single blade and the two blades cuts on the PbPb E_T distribution. In very peripheral events ($E_T < 25$ GeV) the two blades cut induces a loss of $\simeq 30\%$ with respect to the single blade one.

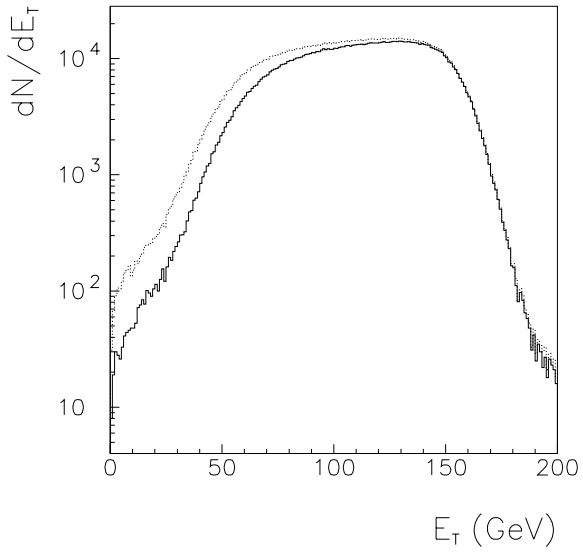

Figure 3.5: *Differential E_T distribution for OS dimuons with target selection : 2 blades recognised (full line) and 1 blade only (dashed line). Kinematic cuts have been applied.*

The top left part of fig.3.6 shows the E_T.vs.E_{ZDC} correlation when the cut at the vertex recognition level has not been applied. Since peripheral and central events follow the same E_T vs. E_{ZDC} correlation, the cut at the target level can be replaced with a simple geometrical cut excluding events with $E_T < 5GeV$ and outside of the main E_T.vs.E_{ZDC} correlation area, as shown in the bottom right part of fig.3.6. This geometrical cut, called the "banana" cut, has been applied on the PbPb data. In fig.3.6 the E_T versus E_{ZDC} energy correlation is also shown after the 1 blade (top right) and 2 blades (bottom left) cut at the vertex recognition level.

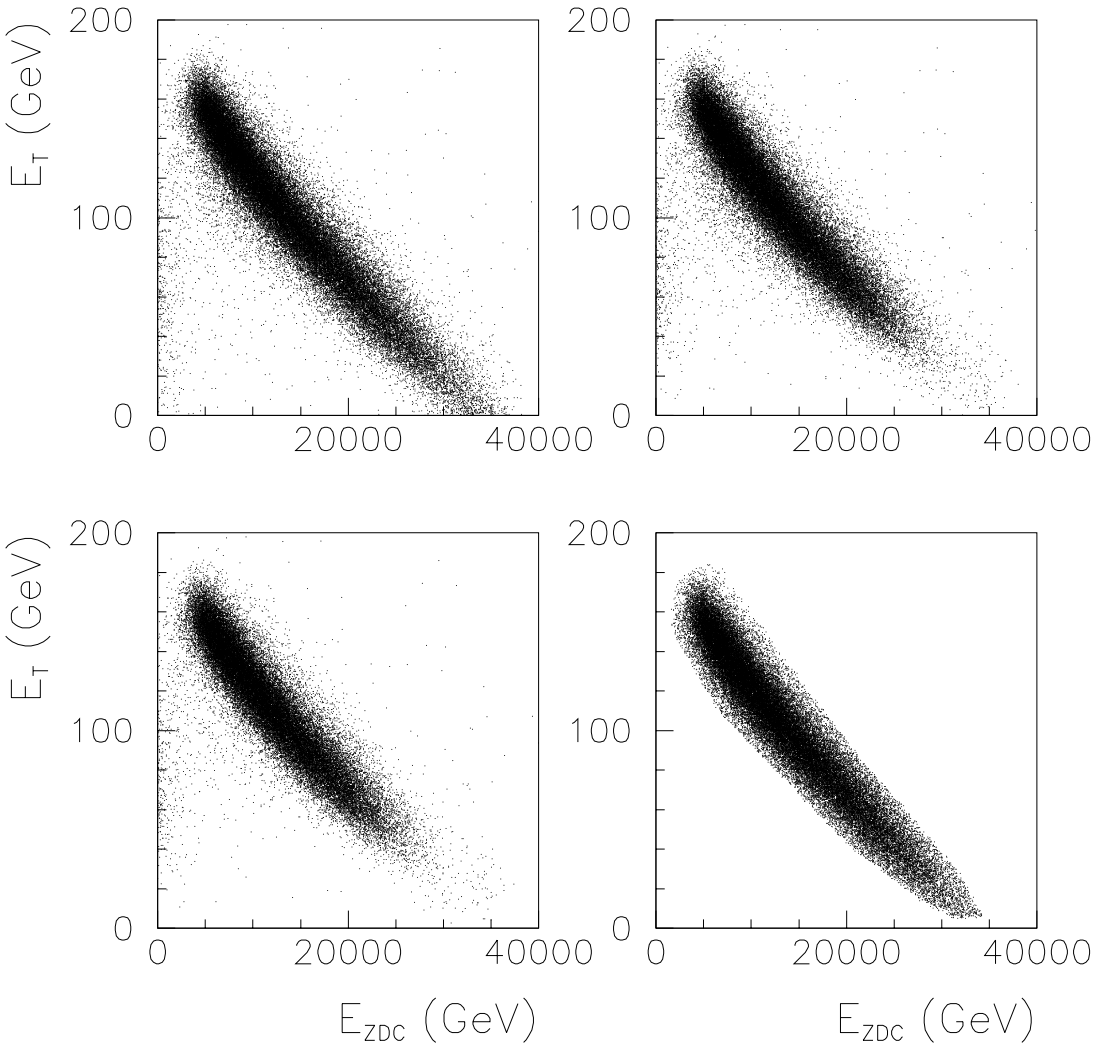

Figure 3.6: *Correlation E_T vs. E_{ZDC} for opposite-sign dimuons without any target cut (top left), with 1 blade cut (top right), with 2 blades cut (bottom left) and with the banana cut (bottom right). The shown correlations refer to the PbPb data. Kinematic cuts have been applied.*

System	energy ($AGeV/c$)	E_T bin	E_T $[min:max]$
SU	200	1	13 : 34
SU	200	2	34 : 50
SU	200	3	50 : 64
SU	200	4	64 : 77
SU	200	5	77 : 88
PbPb	158	1	< 25
PbPb	158	2	25 : 40
PbPb	158	3	40 : 55
PbPb	158	4	55 : 70
PbPb	158	5	70 : 85
PbPb	158	6	85 : 100
PbPb	158	7	100 : 115
PbPb	158	8	115 : 130
PbPb	158	9	> 130

Table 3.2: *E_T binning used in the analysis of the PbPb and SU sets of data.*

3.5.2 PbPb and SU centrality bins

Both the PbPb and SU sets of data have been analysed as a function of centrality. Central collisions are characterised by large E_T and low E_{ZDC} values, and vice-versa for peripheral ones. The all E_T data can be organised in smaller samples corresponding to different E_T bins. These smaller samples of data can be then separately analyzed in order to study the evolution of the measured physical processes with the collision centrality. In table 3.2 the E_T bins corresponding to the subsamples of events used in the analysis of the PbPb and SU data are listed.

Bibliography

[1] DIMUREC USER GUIDE 2.00/02 (1997)

[2] Amir Borhani, PhD Thesis, April 1996, Paris

[3] Frederic Fleuret, PhD Thesis, April 1997, Paris

Chapter 4

Monte-Carlo simulation of physical sources

In this chapter I describe the Monte-Carlo simulation used to generate the processes which are known to contribute to the intermediate mass region of the dimuon mass spectrum. These are the DY process and the semi-leptonic decays of charmed hadron pairs. The high mass resonance simulation is also described since both the J/ψ and the ψ' are needed in the following analysis (see chapter 6) and since the reconstructed J/ψ partially contributes to the IMR dimuon yield. The generated processes are reconstructed using the same dedicated program which has been used to reconstruct the data. The Monte-Carlo mass differential distributions are fitted with ad-hoc functions. The same functions will be used in chapter 6 in the fit of the experimental mass spectrum. The latter is in fact a superposition of the above listed different processes, the relative contribution of which can be only determined by mean of a fit of the experimental mass spectrum itself. The contribution of the combinatorial background from pion and kaon decays, which is one of the most important source of (fake) dimuons in the IMR, will be separately discussed in chapter 5.

4.1 Introduction

The dimuon invariant mass spectrum is a convolution of contributions from different physical sources. The differential distributions of the contributing processes are obtained with the use of Monte-Carlo simulations which take into account the theoretical knowledge about the processes them-self plus the deforming action of the experimental apparatus on the shapes of the generated differential distributions. This is accomplished generating the theoretical shapes with a dedicated program[1], whilst for the reconstruction the same program used to reconstruct experimental data is used[2]. Kinematic cuts, which were already discussed in chapter 3, are also applied on the reconstructed spectra, that is

$$0 < y^* < 1 \tag{4.1}$$

$$-0.5 < cos\theta_{CS} < 0.5 \tag{4.2}$$

for the PbPb and SU set-ups and

$$-0.52 < y^* < 0.48 \tag{4.3}$$

$$-0.5 < cos\theta_{CS} < 0.5 \tag{4.4}$$

for the 4 pA ones. A respective 1% and 18% PXDTARG selection (see chapter 3) has also been applied on the pA and PbPb data.

Once the reconstructed differential distributions have been obtained, they are fitted with ad-hoc functions. The same functions are then used in the fit of the experimental mass spectrum. When fitting the experimental mass spectrum, the normalisation factors are left as free parameters. If needed, some other parameters can be also left free, as explained in the chapter 6.

4.2 The Monte-Carlo DY generation

The DY differential distributions have been generated with the following parametrisations :

- *Mass and rapidity differential distribution*

  The leading order pQCD DY cross section has been used (see chapter 1), i.e.

$$M^3 \frac{d^2\sigma}{dMdy^*} = \frac{8\pi\alpha^2}{9}\tau \sum_i e_i^2 [f_1^i(\sqrt{\tau}e^{y^*})\overline{f}_2^i(\sqrt{\tau}e^{-y^*}) + \overline{f}_1^i(\sqrt{\tau}e^{y^*})f_2^i(\sqrt{\tau}e^{-y^*})] \tag{4.5}$$

and the MRS A set (no.43, 1995) of parton distribution functions[3] has been used for the PbPb and the 4 pA systems. The Monte-Carlo distributions for the SU system have been generated before the MRS A set of parton distribution functions, including the sea quark asymmetry, was available. The GRV LO set (no.4, 1992) of parton distribution functions had therefore been adopted for the SU system in ref.[4], whose results we here directly use. The adoption of two different PDF's sets in the present analysis does not influence the final results since the shapes of the generated distributions do not substantially differ and since only ratios of DY cross sections are anyway involved in the final calculations.

- *p_T differential distribution*

  The p_T differential distribution has been generated as a Bessel function of the transverse mass m_T, i.e.

$$\frac{d\sigma}{dp_T} \propto p_T m_T K_1(\frac{m_T}{T}) \tag{4.6}$$

  K_1 is the first order modified Bessel function, i.e

$$K_1(\frac{m_T}{T}) = \frac{e^{-(m_T/T)}}{\sqrt{(m_T/T)}} \cdot P_6(T/m_T) \tag{4.7}$$

  where P_6 is a polynomial of order 6 and T=0.236 GeV/c^2

- *$cos\theta_{CS}$ differential distribution*

  The experimental angular distribution has been used, i.e,

$$\frac{d\sigma}{dcos\theta_{CS}} \propto 1 + \lambda cos\theta^2_{CS} \tag{4.8}$$

  with λ=1.

In fig.4.1 the DY generated and reconstructed mass, rapidity, cosθ_{CS} and p_T distributions are shown for the PbPb and pAl set-ups.

4.2.1 Fit of the Monte-Carlo Drell-Yan mass distribution.

The DY Monte-Carlo mass distribution has been fitted with the following functions :

- **pA**

$$\frac{dN}{dM} = par1 \cdot [e^{-a_1} + par5 \cdot e^{-a_2} + par6 \cdot e^{-a_3}] \tag{4.9}$$

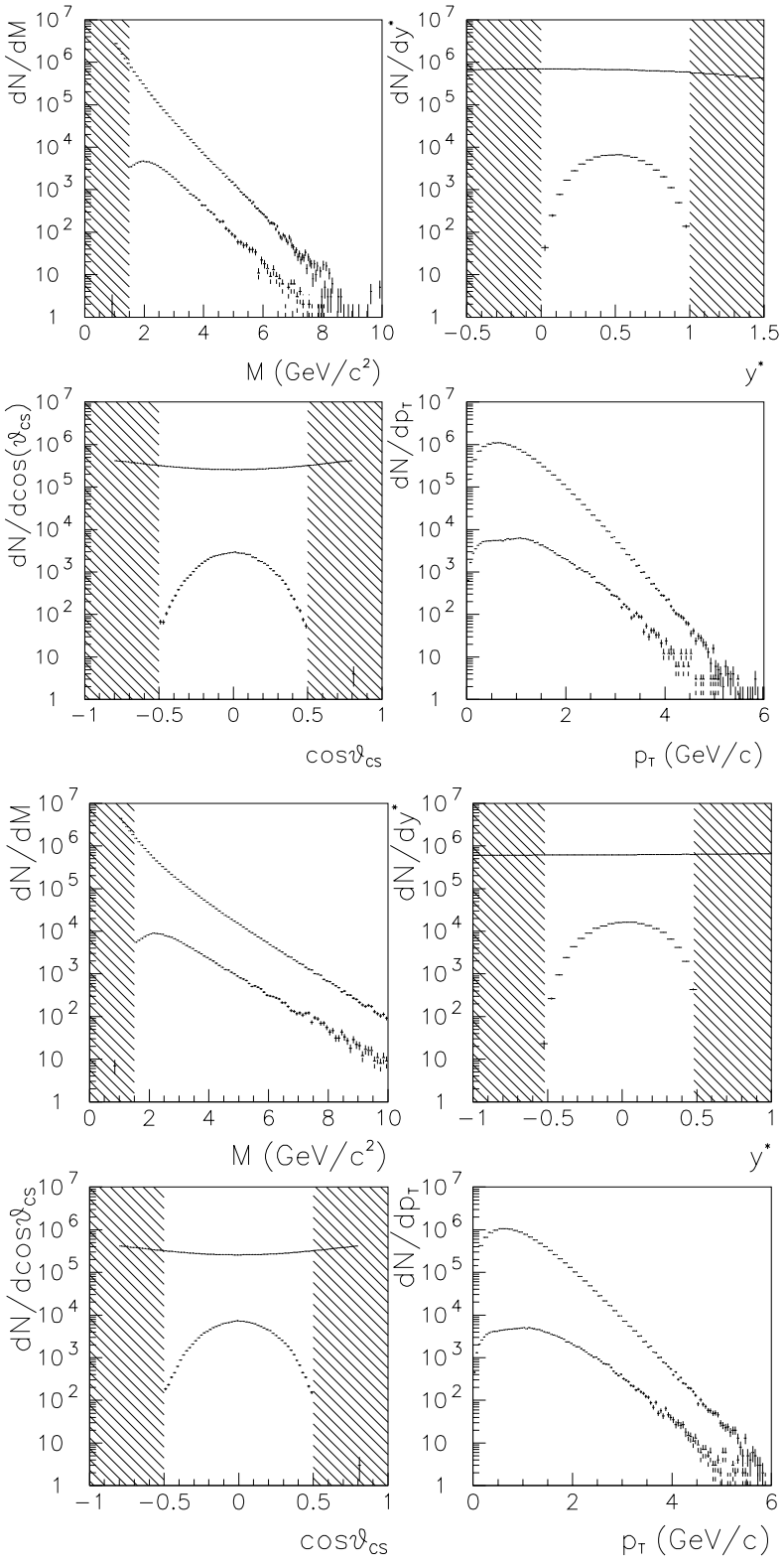

Figure 4.1: *DY generated and reconstructed mass, rapidity, cosθ_{CS} and p_T distributions for the PbPb (top) and for the pAl (bottom) set-ups. The applied kinematic cuts are represented by the shaded areas.*

system	par2 (GeV/c^2)	par3 (GeV/c^2)	par4 (GeV/c^2)	par5 $(GeV/c^2)^{-1}$	par6 $(GeV/c^2)^{-1}$
pAl	1.097±0.004	0.545±0.002	-1.299±0.002	5.15±0.08	-1.96±0.01
pCu	1.107±0.003	0.5547±0.002	-1.311±0.001	5.06±0.06	-1.97±0.01
pAg	1.116±0.003	0.5694±0.002	-1.323±0.003	5.18±0.06	-2.04±0.01
pW	1.187±0.003	0.606±0.001	-1.325±0.003	8.66±0.03	-3.26±0.01

Table 4.1: *Values of the parameters of the Monte-Carlo DY fitting function.*

System	par2 $(GeV/c^2)^{-1}$	par3 $(GeV/c^2)^{-1}$	par4 (GeV/c^2)
PbPb	1.543±0.005	0.2445±0.007	0.46±0.01

Table 4.2: *Values of the parameters of the Monte-Carlo DY fitting function.*

where

$$a_1 = M/par2 \tag{4.10}$$

$$a_2 = M/par3 \tag{4.11}$$

$$a_3 = M^2/par4^2 \tag{4.12}$$

- **AB**

$$\frac{dN}{dM} = par1 \cdot \{e^{(-par2 \cdot M)} - par3 \cdot e^{[-(M-par4)^2]}\} \tag{4.13}$$

The values of the parameters of the Monte-Carlo DY fitting functions are listed in tab.4.1 and 4.2. Since the first normalisation parameter is always left as a free parameter in the fit of the experimental mass spectrum, its value has not been listed. Fig.4.2 shows the fits of the DY mass spectrum for the pA and PbPb systems. For the SU system the results of a previous analysis[4] have been used.

4.3 The Monte-Carlo open charm generation

Since it has been verified that the PYTHIA event generator[5] well reproduces the differential distributions of D mesons produced in proton and pion induced interactions[7] (see chapter 1), the charmed meson and baryon contribution has been generated using PYTHIA 5.7. The shape of the differential charm distribution depends on the used charm mass value, on the intrinsic transverse momentum k_T

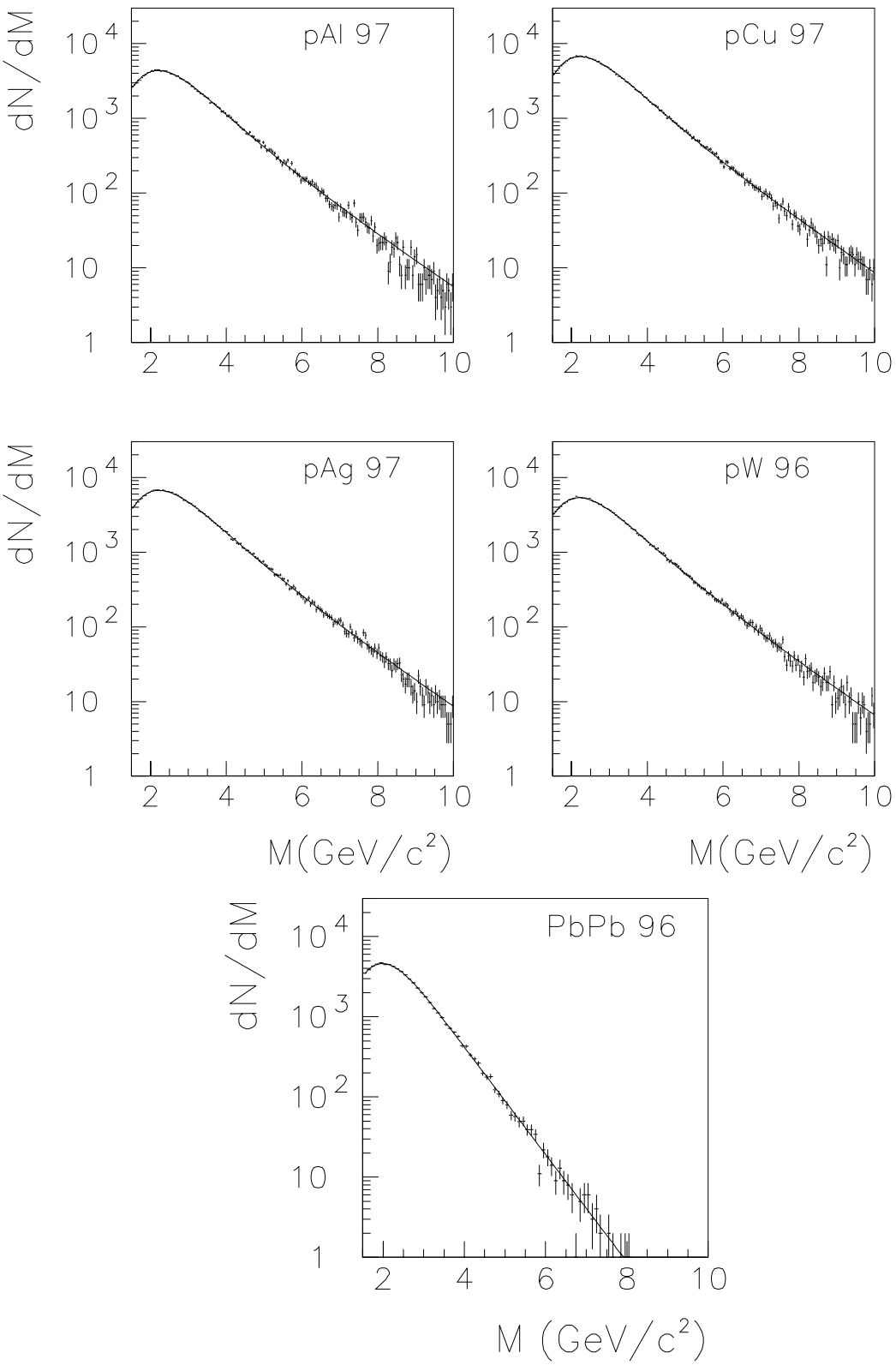

Figure 4.2: *Reconstructed and then fitted DY Monte-Carlo mass distributions for the PbPb (bottom) and the four pA set-ups (top).*

given to the incoming partons and on the chosen set of PDF's.

The commonly accepted values for the charm mass range between 1.2 up to 1.8 GeV/c^2 but the standard value m_c=1.5 GeV/c^2 seems to be favoured by experimental measurement of the $c\overline{c}$ cross section (see chapter 1). The value m_c=1.5 GeV/c^2 has been therefore used in the present work. In fig.4.3 the ratio of the Monte-Carlo mass distributions generated with $m_c = 1.2$ GeV/c^2 and $m_c = 1.5$ GeV/c^2 is shown (left) and the corresponding fitting functions are shown superimposed in the IMR region (right).

In PYTHIA, the transverse momentum of the generated charm pair originates from the intrinsic (or primordial) transverse momentum given to the colliding partons. The intrinsic transverse momentum distribution has been simulated in PYTHIA with a Gaussian k_T distribution of width σ_{k_T}, with $\langle k_T^2 \rangle = \sigma_{k_T}^2$. We have used σ_{k_T}=0.8 GeV/c, which had been previously tuned on the experimental p_T distributions by the NA38/NA50 Collaboration and was already used in order to generate the open charm component for the SU system in the analysis of ref.[4].

As far as the PDF are concerned, the same set used for the DY has been adopted.

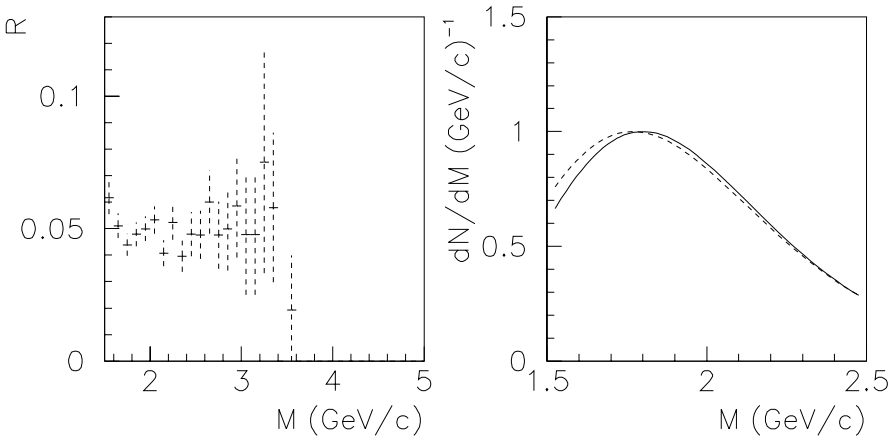

Figure 4.3: *Right : comparison of the reconstructed Monte-Carlo open charm mass spectra for Pb-Pb 158AGeV, after kinematic cuts, for* $m_c = 1.2$ GeV/c^2 *(dashed line) and* $m_c = 1.5$ GeV/c^2 *(full line). Left : ratio of the two fitting functions.*

With PYTHIA a large statistics of D^+,D^0,D_s^+ mesons and Λ_c^+, Ξ_c^0, Ξ_c^+, Ω_c^0 baryons have been generated. A 100% branching ratio has been assigned to the semi-leptonic decay channel $\longrightarrow \mu\nu_\mu X$, and 0% to all the remaining ones. The Monte-Carlo distributions of open charm dimuons are then weighted with the real branching ratios listed in tab.4.3. This procedure avoids the use of enormous CPU time, since we impose that all the generated mesons and baryons effectively decay into a muon.

open charm state	$B.R.(H_{(c)} \rightarrow \mu\overline{\nu}_{mu}X)$
$D^{\pm}$	0.172 ± 0.019
D^0	0.066 ± 0.008
D^s	$0.08 + 0.06 - 0.05$
Baryons	0.045 ± 0.017

Table 4.3: *Total B.R. of charmed hadrons H_c in the semi-leptonic decay channel ($\rightarrow \mu\overline{\nu}_{mu}X$)[6].*

In fig.4.4 the reconstructed differential mass distribution of open charm dimuons for the PbPb system is shown with and without branching ratio weighting.

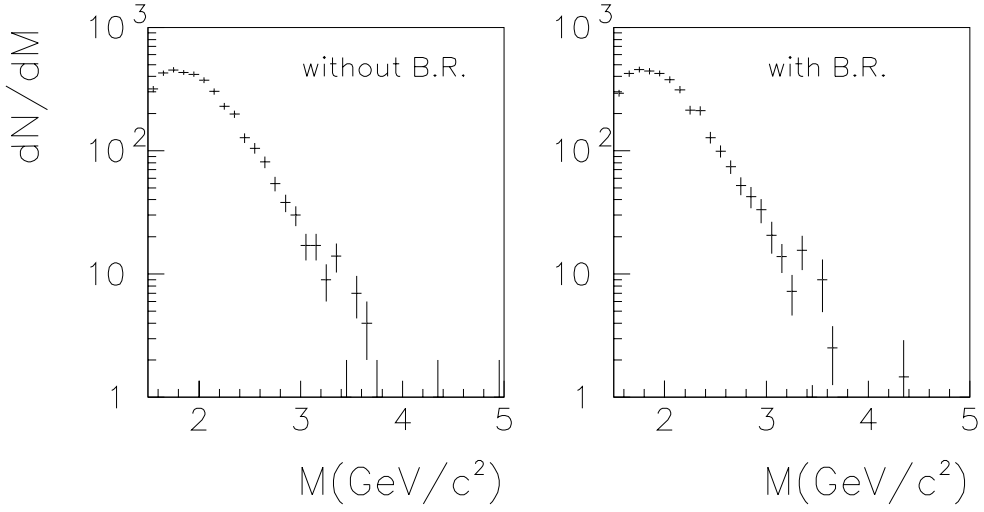

Figure 4.4: *Reconstructed mass distributions of open charm dimuons for the PbPb system before (left) and after (right) branching ratio weighting. The area of the weighted distribution has been renormalised to the unweighted one.*

In fig.4.5 the generated and reconstructed mass, rapidity, p_T and $\cos\theta_{CS}$ differential distributions of open charm dimuons are shown for the pA and PbPb set-ups. Branching ratio weighting has been applied and kinematic cuts imposed on the reconstructed distributions.

4.3.1 Fit to the Monte-Carlo open charm mass distribution

The Monte-Carlo mass differential distribution of open charm dimuons has been fitted with the following function :

$$\frac{dN}{dM} = par1 \cdot e^{\{-0.5\cdot[(M-par2)/\sigma]^2\}} \tag{4.14}$$

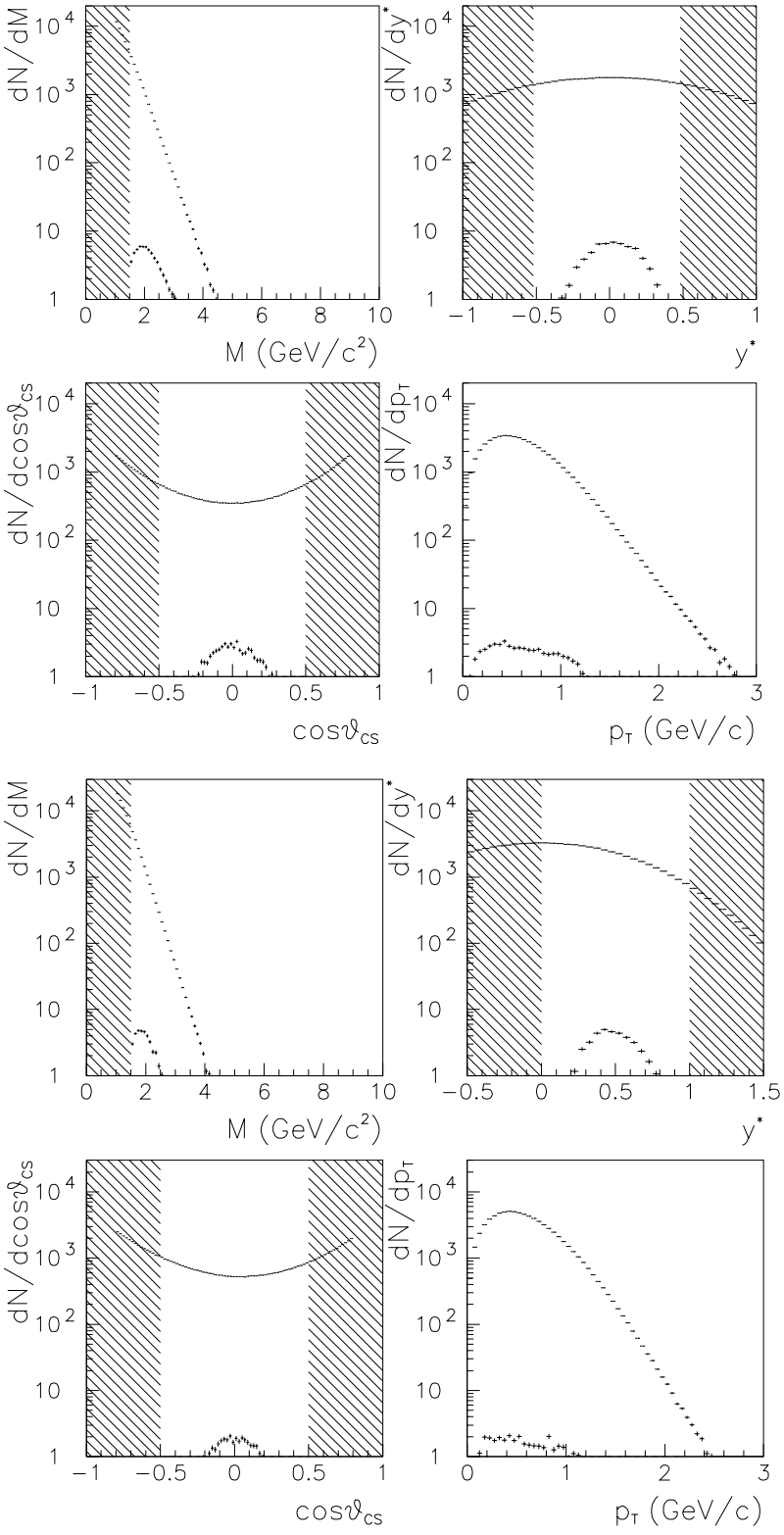

Figure 4.5: *Generated ($m_c = 1.5\ GeV/c^2$) and reconstructed mass, rapidity, $cos\theta_{CS}$ and p_T distributions of open charm dimuons for the pAl (top) and PbPb (bottom) set-ups. B.R. weighting has been applied. The applied kinematic cuts are represented by the shaded areas.*

System	par2 (GeV/c^2)	par3 (GeV/c^2)	par4 $(GeV/c^2)^{-1}$	par5 (GeV/c^2)
pAl	1.931±0.009	0.37±0.02	0.35±0.04	1.5±0.1
pCu	1.975±0.007	0.35±0.03	0.34±0.03	1.3±0.2
pAg	1.997±0.008	0.37±0.03	0.38±0.03	1.8±0.2
pW	1.933±0.008	0.37±0.032	0.35±0.03	1.5±0.3
PbPb	1.800±0.01	0.30±0.04	0.42±0.06	1.5±0.3

Table 4.4: *Values of the parameters of the Monte-Carlo open charm fitting function.*

where

$$\sigma = \begin{cases} par3 & \text{for } M < par5 \\ par3[1 + par4(M - par5)] & \text{for } M > par5 \end{cases} \tag{4.15}$$

Fig.4.6 shows the fit of the pA and PbPb reconstructed open charm mass distributions. Branching ratio weighting has been applied and the shown distributions have been renormalised to the unweighted ones.
Table 4.4 lists the values of the parameters of the Monte-Carlo open charm fitting functions. The values of the SU parameters have been taken from reference[4].

4.4 The Monte-Carlo J/ψ and ψ' simulation

The J/ψ and ψ' Monte-Carlo mass distributions have been obtained using the following parametrisations :

- *Mass differential distribution*

$$M_{J/\psi} = 3.097\ GeV/c^2 \tag{4.16}$$

$$M_{\psi'} = 3.686\ GeV/c^2 \tag{4.17}$$

- *Rapidity differential distribution*

  Gaussian with

$$\mu_{y^*} = 0 \tag{4.18}$$

  and

$$\sigma_{y^*} = 0.6 \tag{4.19}$$

- *Transverse momentum distribution*

  The same p_T distribution used for the DY.

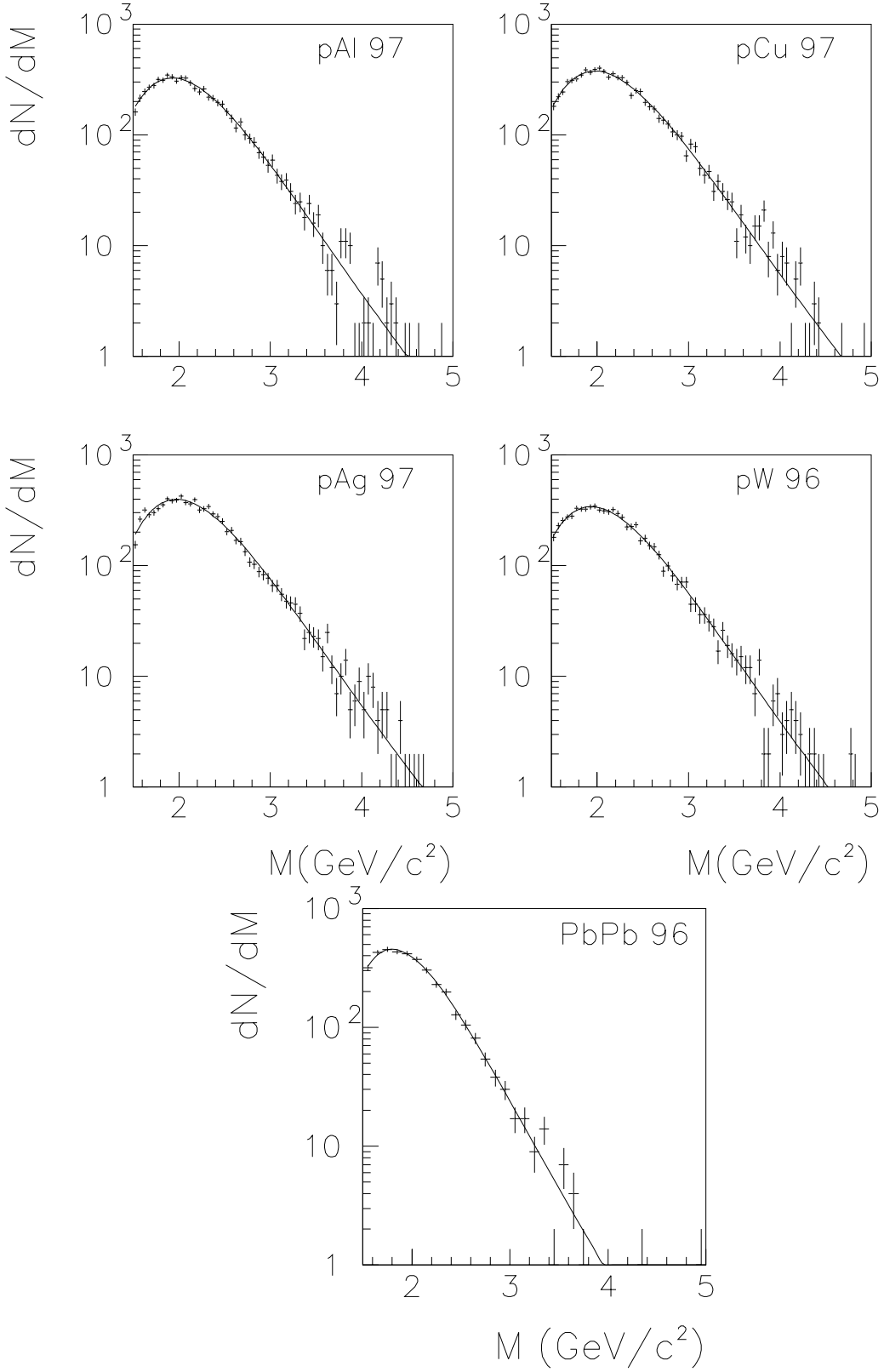

Figure 4.6: *Fit of the Monte-Carlo generated and then reconstructed pA (top) and PbPb (bottom) mass distributions of dimuons from open charm decays.*

- $\cos\theta_{CS}$ *distribution*

  Uniform distribution in $\cos\theta_{CS}$

In 4.7 the J/ψ generated and reconstructed mass, rapidity, p_T and cosθ_{CS} distributions are shown for the pAl and PbPb set-ups. The same is shown in fig.4.8 for the ψ'.

4.4.1 Fit of the Monte-Carlo J/ψ and ψ' mass distributions

The reconstructed mass differential distributions have been fitted with the following functions :

$$\frac{dN}{dM} = par1 \cdot e^{\{-0.5\cdot[((M-par2)/\sigma)^2]\}} \tag{4.20}$$

where

$$\sigma = \begin{cases} par3 & \text{for M}\geq M_1 \text{ and M}\leq M_2 \\ par3\{1+[par4(M_1-M)]\}^{[par5-par6(M_1-M)^{\alpha}]} & \text{for M}\leq M_1 \\ par3\{1+[par7(M-M_2)]\}^{[par8-par9(M-M_2)^{\beta}]} & \text{for M}\geq M_2. \end{cases} \tag{4.21}$$

and

$$M_1 = par10 \cdot par2 \tag{4.22}$$

$$M_2 = par11 \cdot par2 \tag{4.23}$$

The same functions have been used for the J/ψ and the ψ'. The α and β coefficients listed in tab.4.8 have been determined case by case in order to obtain the best possible fit. Table 4.5, 4.6 and 4.7 list the values of the parameters of the Monte-Carlo J/ψ and ψ' fitting functions.
In fig.4.9 and 4.10 the recontructed and then fitted J/ψ and ψ' mass differential distributions are shown for the pA and PbPb set-ups.

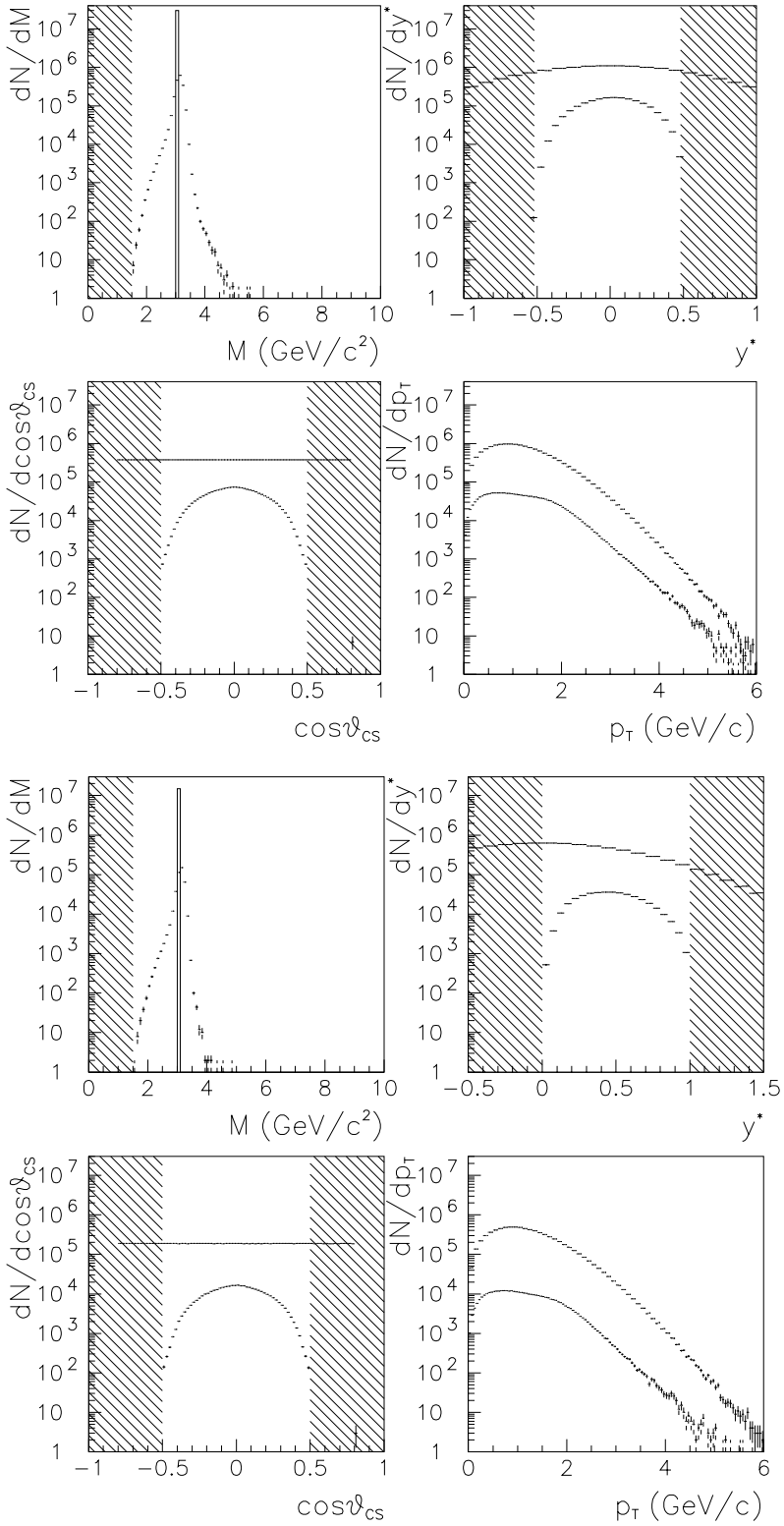

Figure 4.7: *Generated and reconstructed J/ψ mass, rapidity, $cos\theta_{CS}$ and p_T distributions for the pAl (top) and PbPb (bottom) set-ups. The applied kinematic cuts are represented by the shaded areas.*

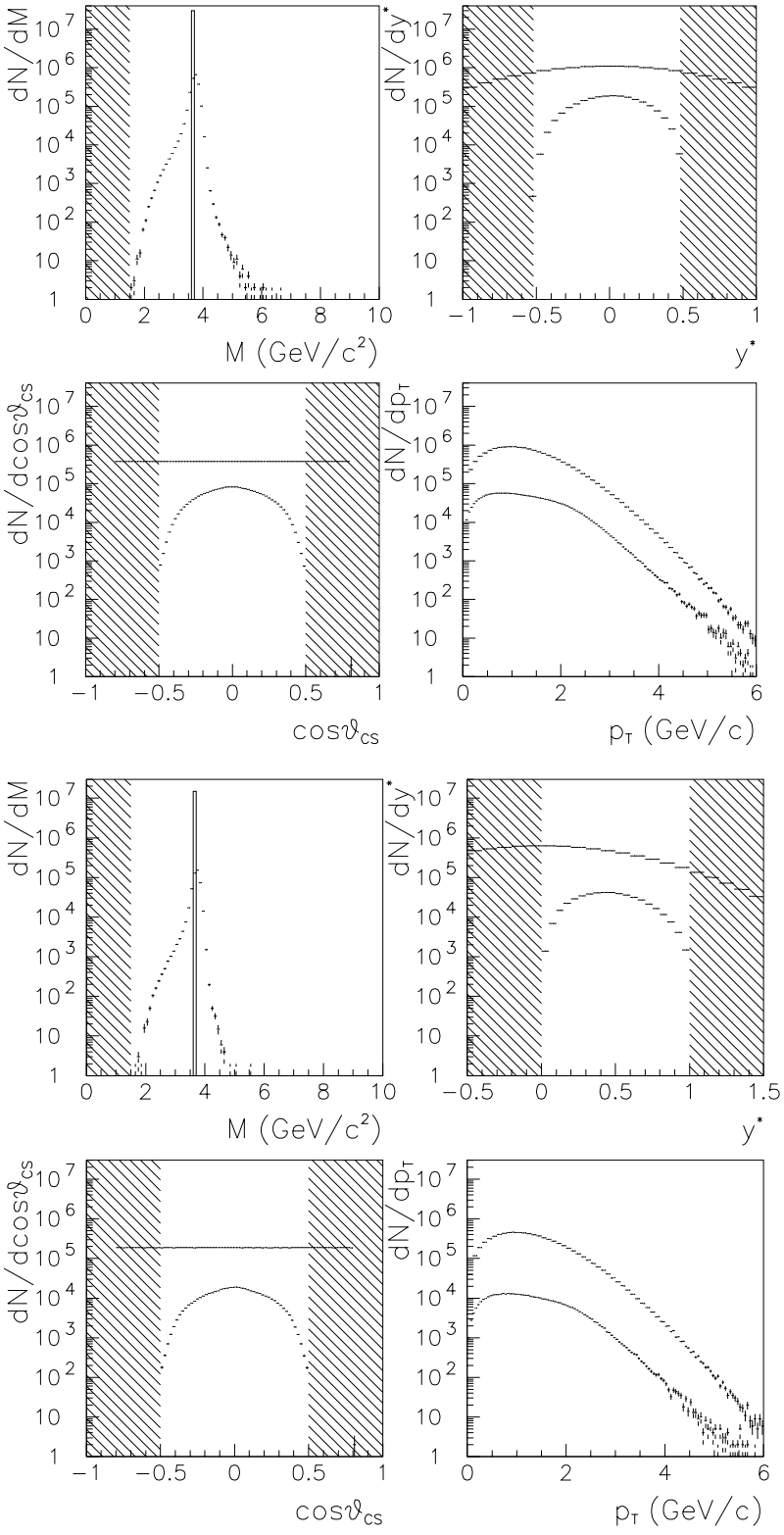

Figure 4.8: *Generated and reconstructed ψ' mass, rapidity, $cos\theta_{CS}$ and p_T distributions for the pAl (top) and PbPb (bottom) set-up. The applied kinematic cuts are represented by the shaded areas.*

	pAl	pCu	pAg	pW
par2(GeV/c^2)	3.133±0.1E-3	3.139±0.3E-3	3.142±0.3E-3	3.146±0.3E-3
par3(GeV/c^2)	0.1027±0.1E-3	0.1070±0.3E-3	0.112±0.3E-3	0.107±0.2E-3
par4$(GeV/c^2)^{-1}$	1.934±0.004	0.273±0.006	0.273±0.004	1.829±0.009
par5	1.404±0.005	1.322±0.002	1.355±0.002	1.39±0.02
par6$(GeV/c^2)^{-\alpha}$	0.455±0.007	1.741±0.004	1.724±0.003	0.43±0.01
par7$(GeV/c^2)^{-1}$	1.479±0.009	1.31±0.01	1.24±0.03	1.383±0.004
par8	1.50±0.02	2.07±0.06	2.1±0.1	1.50±0.02
par9$(GeV/c^2)^{-\beta}$	0.30±0.02	0.77±0.08	0.8±0.1	0.21±0.02
par10	0.9659±0.1E-3	0.976±0.001	0.976±0.001	0.965±0.001
par11	1.070±0.001	1.049±0.001	1.046±0.006	1.059±0.001

Table 4.5: *Values of the parameters of the Monte-Carlo J/ψ fitting functions for the pA set-ups.*

	pAl	pCu	pAg	pW
par2(GeV/c^2)	3.727±0.1E-3	3.730±0.3E-3	3.735±0.3E-3	3.740±0.1E-3
par3(GeV/c^2)	0.1119±0.1E-3	0.1158±0.3E-3	0.1216±0.4E-3	0.1158±0.1E03
par4$(GeV/c^2)^{-1}$	0.1689±0.9E-3	0.160±0.002	0.162±0.002	0.170±0.001
par5	1.0370±0.5E-3	0.996±0.003	1.009±0.004	1.049±0.6E-3
par6$(GeV/c^2)^{-\alpha}$	1.402±0.001	1.328±0.004	1.316±0.006	1.391±0.001
par7$(GeV/c^2)^{-1}$	1.305±0.008	1.16±0.01	1.07±0.01	1.248±0.006
par8	1.57±0.03	2.78±0.09	2.79±0.07	1.51±0.02
par9$(GeV/c^2)^{-\beta}$	0.27±0.02	1.5±0.1	1.5±0.2	0.173±0.009
par10	0.9699±0.4E-3	0.9667±0.8E-3	0.963±0.001	0.968±0.4E03
par11	1.060±0.002	1.034±0.002	1.028±0.002	1.054±0.001

Table 4.6: *Values of the parameters of the Monte-Carlo ψ' fitting functions for the pA set-ups.*

	PbPb	PbPb
	J/ψ	ψ'
par2(GeV/c^2)	3.126±0.2E-3	3.718±0.2E-3
par3(GeV/c^2)	0.090±0.1E-3	0.102±0.2E-3
par4$(GeV/c^2)^{-1}$	0.227±0.001	0.168±0.1E-2
par5	1.131±0.001	1.006±0.9E-3
par6$(GeV/c^2)^{-\alpha}$	1.655±0.002	1.436±0.002
par7$(GeV/c^2)^{-1}$	0.18±0.01	0.21±0.01
par8	1.041±0.005	1.256±0.006
par9$(GeV/c^2)^{-\beta}$	1.35±0.01	1.51±0.01
par10	0.9817±0.2E-3	0.9729±0.6E-3
par11	1.073±0.001	1.066±0.002

Table 4.7: *Values of the parameters of the Monte-Carlo J/ψ and ψ' fitting functions for the PbPb set-up.*

System	$\alpha_{J/\psi}$	$\beta_{J/\psi}$	$\alpha_{\psi'}$	$\beta_{\psi'}$
pAl	1.0	1.0	0.5	1.0
pCu	0.5	0.5	0.5	0.5
pAg	0.5	0.5	0.5	0.5
pW	1.0	1.0	0.5	1.0
PbPb	0.5	0.5	0.5	0.5

Table 4.8: *Values of the coefficients α and β of the Monte-Carlo J/ψ and ψ' fitting functions.*

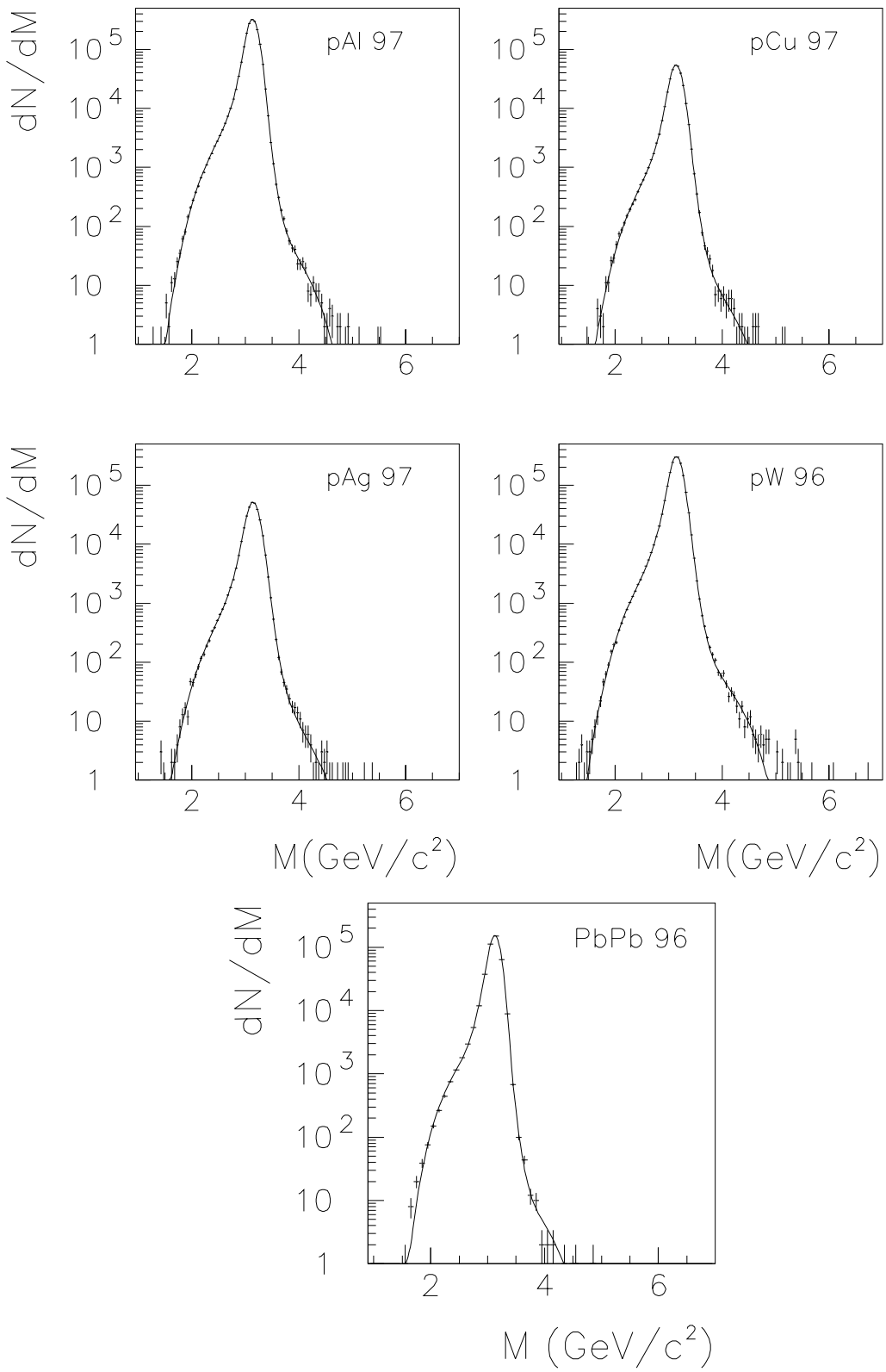

Figure 4.9: *Fit of the reconstructed J/ψ Monte-Carlo mass distributions for the 4 pA (top) and the PbPb (bottom) set-ups.*

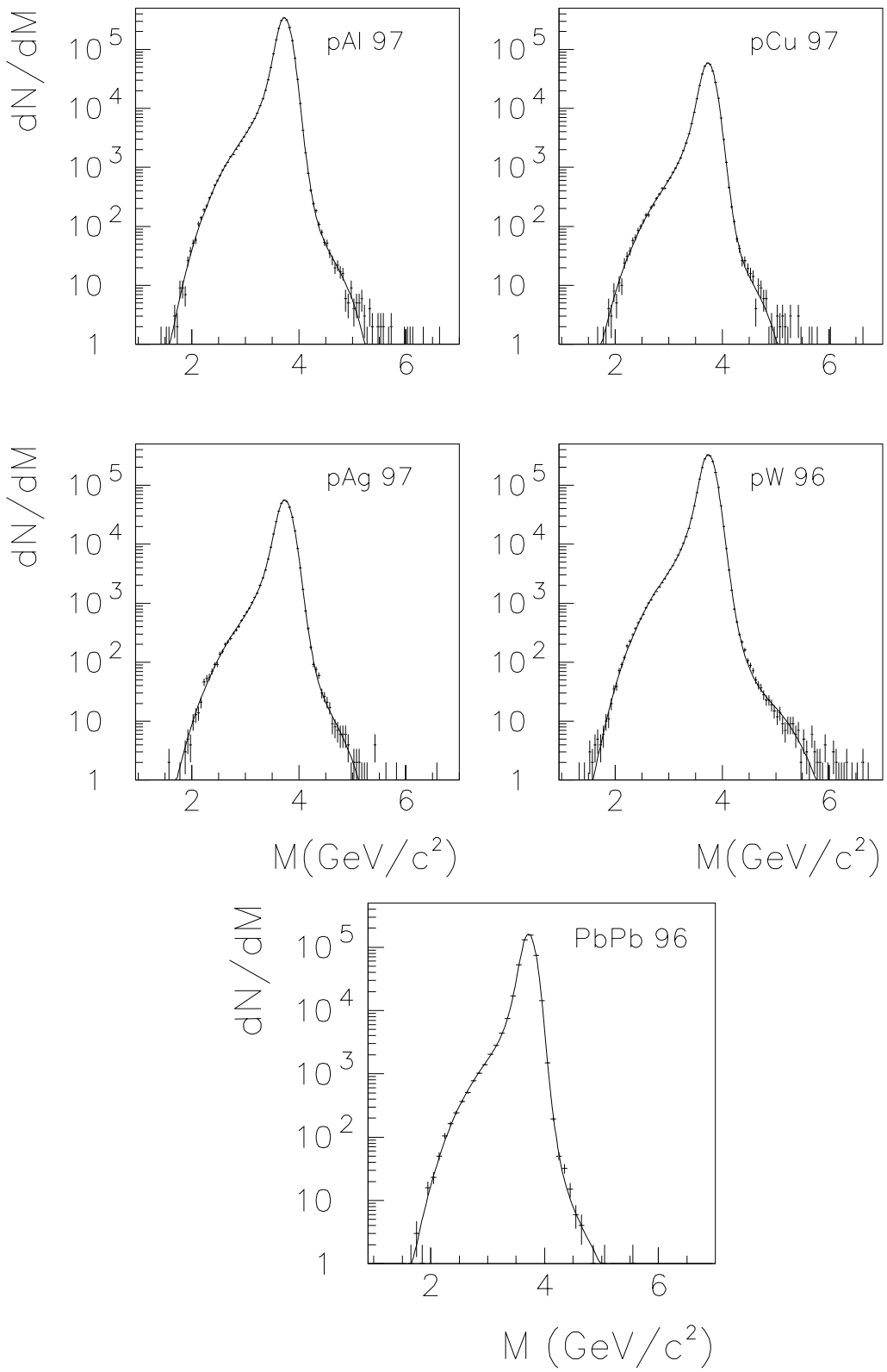

Figure 4.10: *Fit of the reconstructed ψ' mass distributions for the 4 pA (top) and the PbPb (bottom) set-ups.*

System	A_{DY} %	$A_{D\overline{D}}$ %	$A_{J/\psi}$ %	$A_{\psi'}$ %
	$M > 1.5\ GeV/c^2$	$M > 1.5\ GeV/c^2$		
pAl	6.08±0.01	2.04±0.02	14.50±0.01	16.96±0.01
pCu	6.56±0.01	1.84±0.02	14.99±0.03	17.55±0.03
pAg	6.42±0.01	1.92±0.02	14.94±0.03	17.49±0.03
pW	6.19±0.01	2.14±0.02	14.44±0.01	16.80±0.01
PbPb	2.81±0.01	1.08±0.02	7.44±0.01	8.69±0.01

Table 4.9: *Calculated acceptances (in %) for the indicated physical process.*

4.5 Acceptances

The acceptance of the apparatus for a given physical process is defined as the ratio of the numbers of Monte-Carlo reconstructed and generated events,e.g. :

$$A = \frac{\int_{M_1}^{M_2} \frac{dN^{rec}}{dM}\, dM}{\int_{M_1}^{M_2} \frac{dN^{gen}}{dM}\, dM} \tag{4.24}$$

when the rapidity and $\cos\theta_{CS}$ kinematic cuts have been applied on both distributions. For DY and open charm M_1=1.5 GeV/c^2 and M_2 is the upper value of the mass range covered by the considered process, whereas the whole mass distributions of the J/ψ and ψ' have been integrated. Tab.4.9 lists the acceptances for the physical processes discussed in the present chapter.

Bibliography

[1] DIMUJET USER GUIDE 2.00/02 (1997)

[2] DIMUREC USER GUIDE 2.00/02 (1997)

[3] PDFLIB 7.09, Users's Manual, CERN/PPE (1997)

[4] A.Borhani, Ph.D. Thesis, Uni. Paris 6 (1996)

[5] T.Sjostrand, Pythia 5.7 and Jetset 7.4 (1993)

[6] C.Caso et al., Review of Particle Physics, The European Physical Journal C3 (1998)1.

[7] P.Braun-Munzinger et al., CERN-PPE/97-65 (1997) subm. Z.Phys.C

Chapter 5

The combinatorial background

One of the most important contributions to the intermediate mass region (IMR) opposite-sign dimuon spectra is the background from pion and kaon decays. Its contribution to the IMR mass spectrum amounts up to 85% in p-A collisions at 450 GeV/c and S-U collisions at 200 A GeV/c and to 95% in the most central Pb-Pb collisions at 158 A GeV/c. To study the IMR dimuon sources and their behaviour with changing energy and centrality of the collision, the combinatorial background has to be subtracted in such a way that no doubts remain about the nature of the measured signal. There exist widely used methods to evaluate the combinatorial background shape basically starting from the experimental like-sign background distributions. The normalisation of the background contribution to the opposite-sign dimuon spectrum can also be extracted using the same methods, if we are dealing with interactions where the produced high particle multiplicities simulate the absence of charge correlation effects. When charge correlation effects can not be neglected, they have to be carefully estimated to eventually correct the background normalisation factor.

The first part of this chapter describes the commonly used methods for the determination of the opposite-sign combinatorial background mass differential distribution and normalisation, when charge correlation effects can be neglected. The second part presents the detailed description of the Monte-Carlo simulation used in this work to estimate the charge correlation effects on the background normalisation factor.

5.1 The background shape and normalisation

The background contribution to the opposite-sign dimuon mass spectrum is usually evaluated using the like-sign dimuon mass distributions. This is due to the fact that the π and K meson decays,

$$\pi^+(orK^+) \longrightarrow \mu^+\nu \tag{5.1}$$

and

$$\pi^-(orK^-) \longrightarrow \mu^-\overline{\nu} \tag{5.2}$$

contribute both to the opposite and to the like-sign spectra. While the opposite-sign distribution is the superposition of many different sources, the like-sign distributions are purely due to combinatorial background.
The background computation is based on the following reasoning[1] : consider a set of N_0 dimuon events. If each primary interaction produces N^+ positive mesons and N^- negative ones, with the associated $P(N^+)$ and $P(N^-)$ muon decay probabilities, the number of produced like-sign dimuons is

$$N^{++} = N_0 \int A^{++} \frac{dP(N^+)}{dN^+} \frac{N^+(N^+-1)}{2} dN^+ = \frac{N_0}{2}(< N^{+^2} > - < N^+ >) A^{++} \tag{5.3}$$

where A^{++} is the acceptance for positive like-sign dimuons. The same holds for negative like-sign dimuons. If the numbers N^+ and N^- of produced positive and negative mesons are uncorrelated, the number of opposite-sign dimuons resulting from the combination of their decay products can be written as

$$N^{+-} = N_0 \int A^{+-} \frac{dP(N^+)}{dN^+} \frac{dP(N^-)}{dN^-} N^+ N^- dN^+ dN^- = N^0 < N^+ >< N^- > A^{+-} \tag{5.4}$$

where A^{+-} is the acceptance for opposite-sign dimuons.
Since the meson multiplicity follows the Poisson law, which implies

$$< N >=< N^2 > - < N >^2 \tag{5.5}$$

we can easily obtain

$$N^{+-} = 2\sqrt{N^{++}N^{--}} \cdot \frac{A^{+-}}{\sqrt{A^{++}A^{--}}} \tag{5.6}$$

If the acceptance is the same for positive and negative muons, condition which is fulfilled in NA38/NA50 because of the image cut imposed on the data at processing time (see chapter 3), we can write

$$N^{+-} = 2\sqrt{N^{++}N^{--}} \tag{5.7}$$

In NA50, to correct for a possible image cut inefficiency, the sign of the magnetic field is regularly changed in order to have a set of data of equal statistics for both magnetic field sign. This means that eq.5.7 has to be modified in

$$N^{+-} = 2\left\{\sqrt{(N^{++}N^{--})_{(+)}} + \sqrt{(N^{++}N^{--})_{(-)}}\right\} \tag{5.8}$$

Eq.5.8 is strictly valid only for events where the meson production is completely charge uncorrelated. This is of course not the case in the real physical situation, where positively and negatively charged mesons are linked by the total charge conservation law. On the other hand, when the multiplicity of charged particles generated in the interaction is so large that the existing physical charge correlation is smeared out, eq.5.8 is still valid. This is the case for very central Pb-Pb collisions, whilst charge correlation effects are still expected in the peripheral ones. When it perfectly holds, eq.5.8 defines the shape and normalisation of the background contribution. Otherwise, if it is necessary to correct for charge correlation effects, eq.5.8 has to be multiplied by an R factor which is expected to be equal to 1 in very central A-B collisions and larger than 1 in p-A or peripheral A-B collisions,

$$N^{+-} = 2R_{bck}\left\{\sqrt{(N^{++}N^{--})_{(+)}} + \sqrt{(N^{++}N^{--})_{(-)}}\right\} \tag{5.9}$$

In fig.5.1 the like-sign dimuon distributions and in fig.5.2 the resulting opposite-sign distribution are shown for the pAl set of data for R_{BCK}=1.
The above described technique for the determination of the combinatorial background differential distribution and normalisation, is from now on referred to as the 2sqrt method.

5.1.1 The FOS method

The FOS (Fake Opposite Sign)[2] method is used to compute the shape of the combinatorial background contribution when a better degree of accuracy is needed. Therefore, it has been used in the analysis of the PbPb set of data which is characterized by a very large background contribution to the IMR.
The PbPb set of data has been subdivided in subsamples corresponding to the 9 E_T bins used in the analysis (see chapter 3). Within each of this subsamples, or class of events, the positive and negative single muon distributions are extracted from the

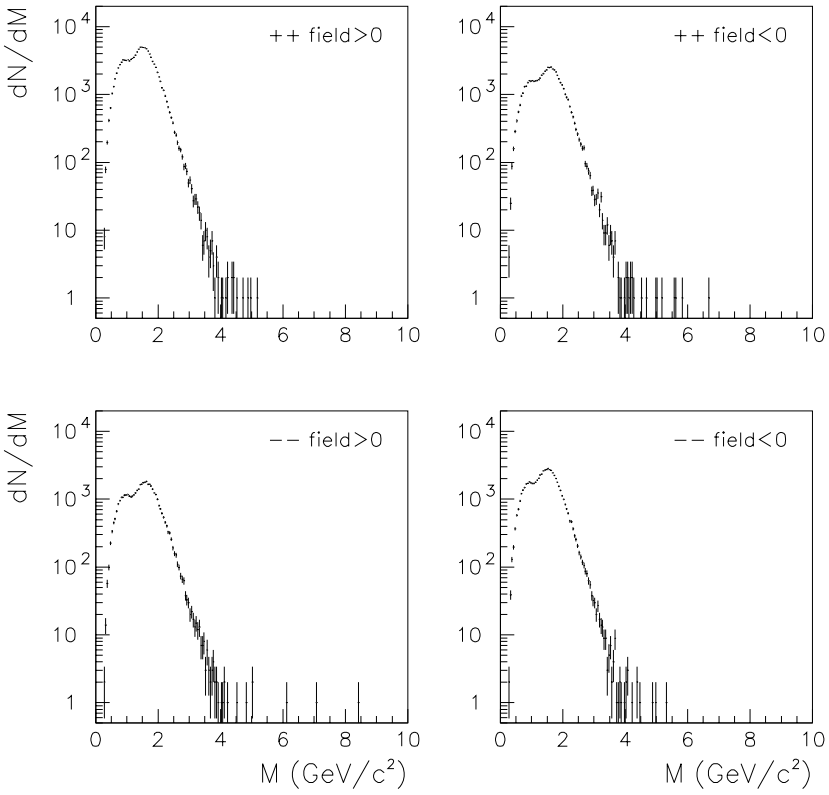

Figure 5.1: *Like sign dimuon distributions for the pAl set of data.*

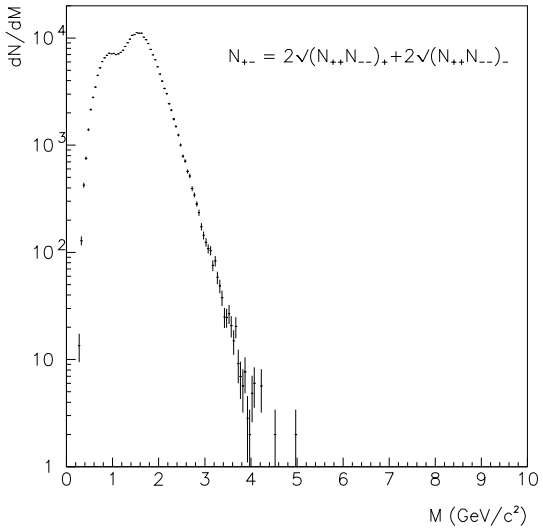

Figure 5.2: *OS Background calculated with the 2sqrt method (R_{bck}=1) for the pAl set of data.*

like-sign ones. The single muon momenta are stored for each class of events. Within each class of events, all the single muon combinations allowed by the trigger are made. The resulting spectra can then be normalised using eq.5.9, where the total quantities N^{++} and N^{--} are known.
The validity of this method has been checked by the authors. In ref.[2], where a detailed description of the method can be found, the like-sign dimuon distributions have been reconstructed from the single muon ones; they have then been compared with the experimental like-sign mass distributions and a satisfactory agreement has been found.
In fig.5.3 the difference in the background shape determination as obtained with the FOS and 2sqrt methods is shown for the second, very peripheral, PbPb E_T bin. Eq.5.9, with R_{BCK}=1, has been used to normalise. The difference is well evident when subtracting the background contribution from the total opposite-sign mass spectrum, obtaining the so called signal mass distribution. In fig.5.4 the same is shown for the PbPb most central E_T bin. When the FOS method is used, the signal distribution is smoother than when using the usual 2sqrt method; this is the reason why the former has been adopted for the PbPb system.

5.2 The R_{BCK} factor

Up to now, within the NA38/NA50 Collaboration, the R_{BCK} factor was either obtained from the fit of the mass spectrum, where it was left as a free parameter, or it was imposed equal to 1 in all the nucleus-nucleus interactions. This last approximation turns out to be applicable if the region of mass $M > 2.8\ GeV/c^2$ is under study, since the background contribution in the high mass region is very small.
On the other hand, in the IMR the combinatorial background appears to be the most important contribution as shown in fig.5.5 for the PbPb, SU and pW systems. A precise calculation of the R_{BCK} factor is therefore needed.
In the following I give a detailed description of the Monte-Carlo simulation used to compute the R_{BCK} factors for all the analysed systems.

5.2.1 Pion and kaon distributions from VENUS

Using the VENUS 4.02[4] event generator, a large number ($\simeq 4 \cdot 10^5$)of p-A, S-U and Pb-Pb events, at the relevant energies, have been generated. For each system, the produced pions and kaons, and the related kinematic variable values, have been stored. As an example, fig.5.6 shows the π and K energy distributions versus the pseudo-rapidity η as obtained from VENUS in p-W events at 450 GeV/c. The shaded areas correspond to the region outside the apparatus angular acceptance.
Once the pions and kaons produced by VENUS have been stored, they are tracked through the NA50 hadron absorber and there forced to decay. A decay probability is associated to each of them with the following reasoning :

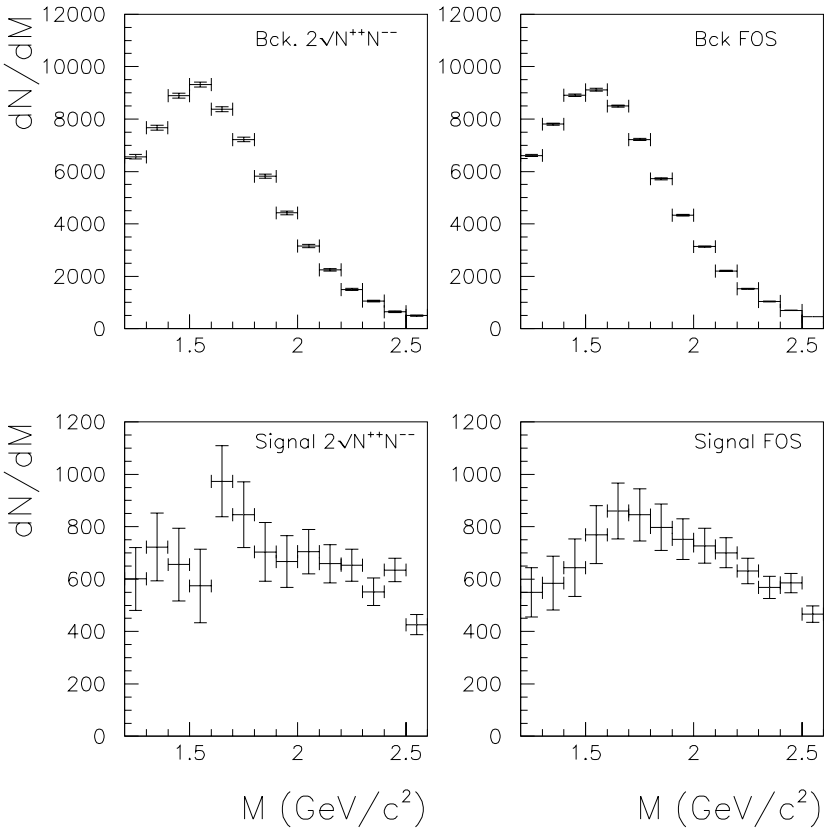

Figure 5.3: *Comparison between the 2sqrt (R_{bck}=1) and FOS background computation on the 2^{nd} PbPb E_T bin and the resulting signals, defined as the total opposite-sign dimuon mass distribution subtracted for the combinatorial background.*

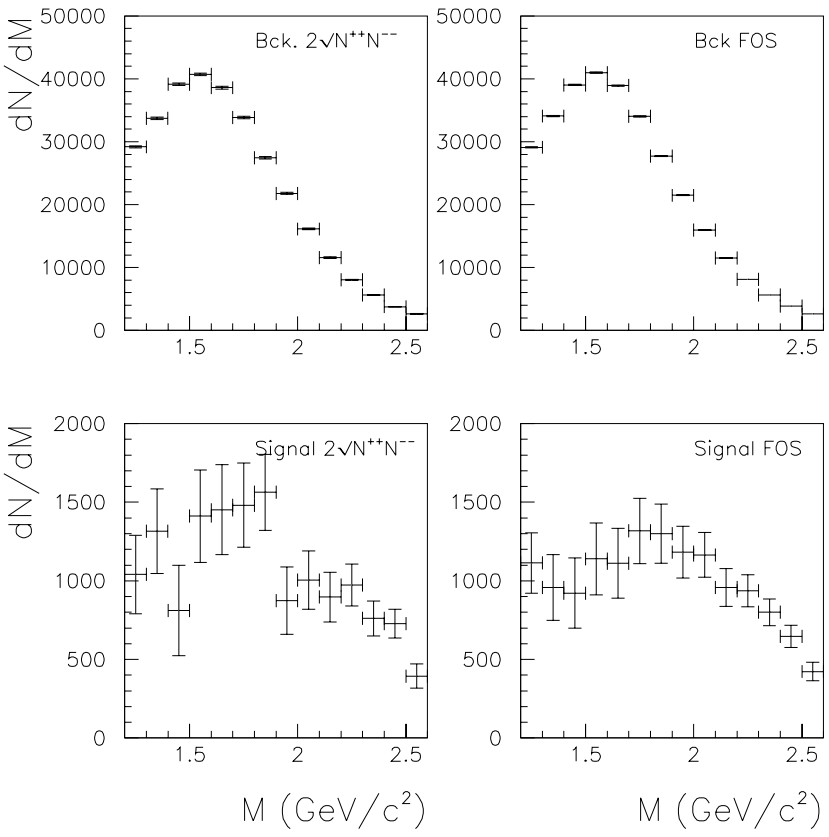

Figure 5.4: *Same as fig.5.3 but for the most central PbPb E_T bin (R_{bck}=1).*

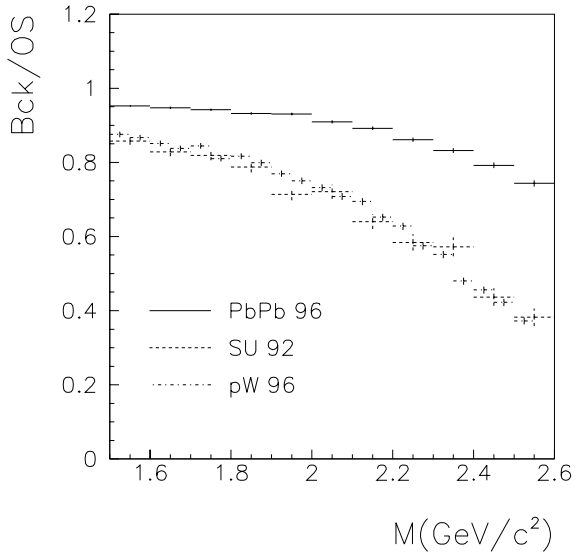

Figure 5.5: *Ratio of combinatorial background and total opposite-sign dimuon mass distribution in the IMR and for the three shown systems, when R_{bck}=1.*

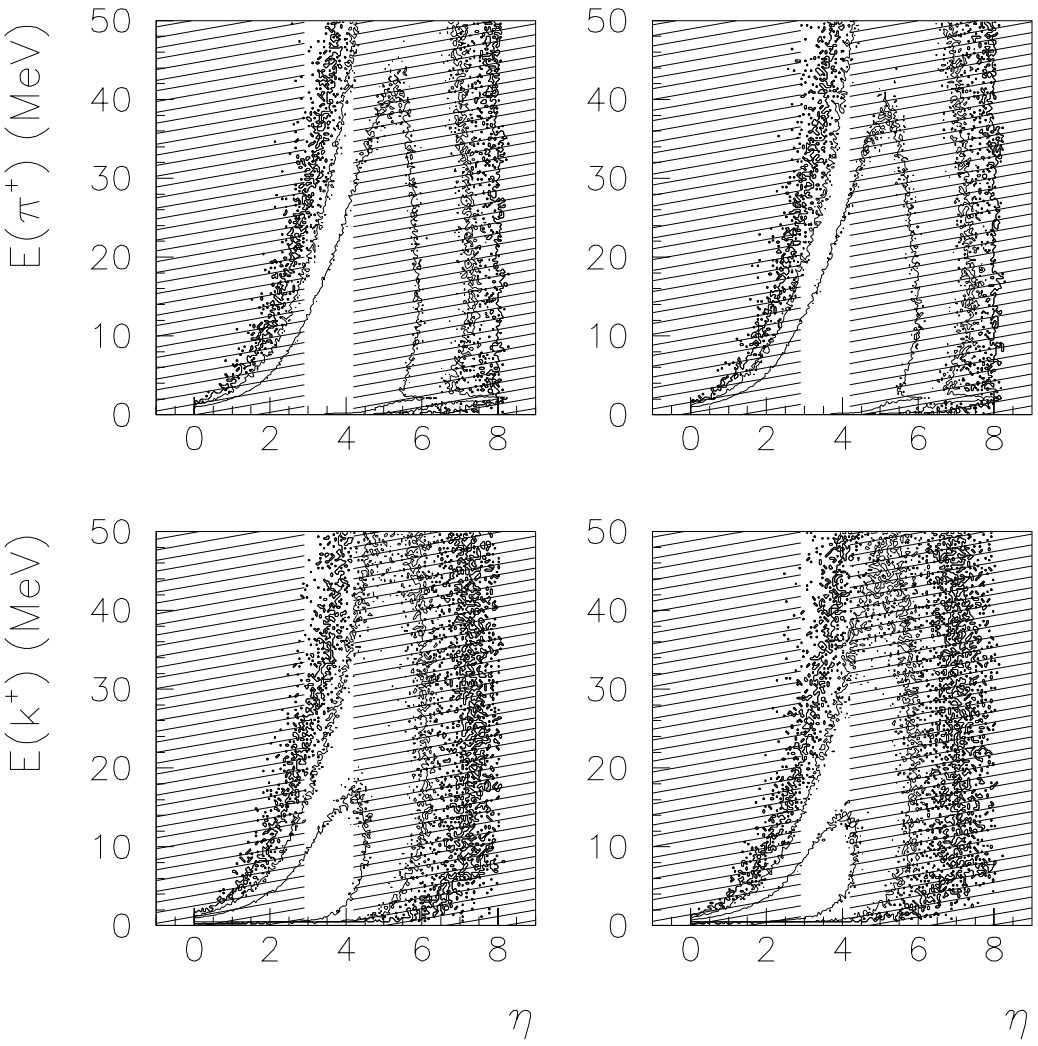

Figure 5.6: *Pion and kaon energy distribution vs. η as produced by VENUS in p-W events at 450 GeV/c. The shaded areas correspond to the region outside the apparatus angular acceptance.*

- Suppose a meson has been generated at $x = 0$; its probability of having survived up until the point x_0 without undergoing an hadronic interaction is

$$P^h(x_0) = e^{(-x_0/\lambda_i)} \tag{5.10}$$

where λ_i is the hadronic interaction length in cm if x is measured in cm.

- If the meson has survived up until the point x_0, the differential probability that it decays between x_0 and $x_0 + dx$ is

$$\frac{dP^d(x)}{dx} \mid_{x_0} = \frac{Mc}{p(x_0) \cdot X_L} \cdot e^{\frac{(-Mcx_0)}{(p(x_0)X_L)}} \ (cm^{-1}) \tag{5.11}$$

where M (GeV/c^2) is the meson mass, c is the velocity of light, X_L=τc (cm) where τ (s) is the meson mean life time and $p(x_0)$ (GeV/c) is the meson momentum at the point x_0,

$$p(x_0) = \sqrt{E^2(x_0) - M^2} \ (GeV/c) \tag{5.12}$$

with

$$E(x_0) = E(0) - \Delta E \ (GeV) \tag{5.13}$$

where $E(0)$ is the energy the meson had at production and $\Delta E(x)$ is the energy lost by the meson between x=0 and x_0,

$$\Delta E = \int_0^{x_0} \frac{dE}{dx} dx \ (GeV) \tag{5.14}$$

where dE/dx is the energy loss in GeV/cm.

- The differential probability for a meson produced at $x = 0$ to decay at x_0 is given by the combined probability

$$\frac{dP^{hd}(x)}{dx} \mid_{x_0} = P^h(x_0) \cdot \frac{dP^d(x)}{dx} \mid_{x_0} \ (cm^{-1}) \tag{5.15}$$

Material	Length (cm)	λ_i (g/cm^2)	ρ (g/cm^3)
Air	25.4	84.40	1.2
Al_2O_3	51.6	98.70	3.82
BeO	59.0	84.90	2.81
C	400.	86.30	1.93

Table 5.1: *Characteristics of the materials crossed by pions and kaons when going through the hadron absorber.*

- The decay probability $P^{hd}(x_i)$ is computed at each discrete point x_i along the meson path. The decay probability at the point x_i is strictly connected with the material where the point x_i is and with the previously crossed materials. Globally, each meson has to cross 25.4 cm of air followed by 51.6 cm of Al_2O_3 (or 59 cm of BeO in PbPb and pW) and then 400 cm of C. The decay probability $P^{hd}(x_i)$ is computed in steps of 1 cm. Table.5.1 lists the length, interaction length and density of the hadron absorber materials. All mesons which did not decay within the above listed materials, are considered to be stopped in the last 80 cm of Fe.

  The total decay probability for a single meson j is then given by

$$P_j^{tot} = \int_0^{L_{abs}} \frac{dP_j^{hd}(x)}{dx} dx \tag{5.16}$$

where L_{abs} is the total absorber plus pre-absorber length.
The calculated decay probabilities are then used as relative weights in the π and K distributions.

5.2.2 Monte-Carlo dimuon distributions

The next step consists in the combination of the generated mesons, which are then forced to decay. Within each VENUS event, every single pion and kaon is combined with all the other produced mesons in the same event. This means that the same meson is used $N_e - 1$ times for combination if N_e is the total number of stored mesons in a single VENUS event. Next, the mesons are forced to decay into a muon; this is accomplished using the two body decay process with isotropic angular distribution in the centre of mass frame[5]. The kinematic variables (rapidity y, polar

and azimuthal angle in the Collin-Soper frame, transverse momentum p_T, invariant mass) of the resulting dimuons are then computed. Each dimuon is weighted by the product of the decay probabilities of its two parents,

$$P_{jk}^{ab} = P_j^a P_k^b \tag{5.17}$$

with ab = $(--)$ or $(++)$ or $(+-)$ and j,k=1....N_e
In fig.5.7 the weight distribution obtained for π's and K's pairs in semi-peripheral (b=10 fm) Pb-Pb interactions at 158 A GeV/c is shown.

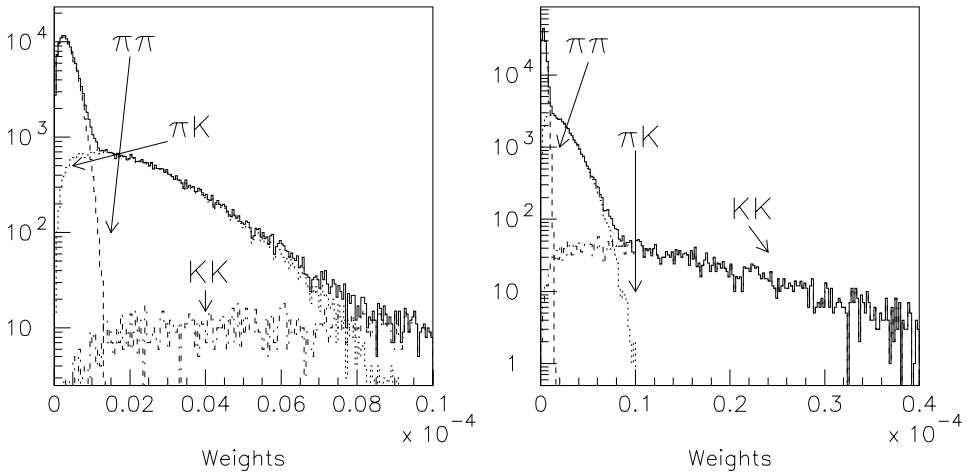

Figure 5.7: *Weights associated to pion and kaon pairs resulting from the combination of π's and K's produced by VENUS in Pb-Pb collisions at 158 GeV/c per nucleon. The small probabilities region is better shown in the left panel.*

Of all the created dimuons, only the ones falling in the apparatus acceptance are kept. We thus apply on the dimuon distributions the following cuts :

1. At the dimuon level

   The usual rapidity and $cos\theta_{CS}$ cuts,

   $$3 < y_{lab} < 4 \tag{5.18}$$

   $$-0.5 < cos\theta_{CS} < 0.5 \tag{5.19}$$

2. On single muons

   A cut which approximates the single muon angular and energy acceptance of the muon spectrometer can be obtained from experimental data. In fig.5.8 the

muon energy versus the muon angle θ_μ is shown as deduced from the NA38 and NA50 experimental data. The muon angle θ_μ is defined as

$$\theta_\mu = tan^{-1}(\frac{p_T}{p_l}) \tag{5.20}$$

where p_T and p_l are the transverse and longitudinal momenta of the muon at the point where its parent decay takes place. In fig.5.8 the region in the E_μ-θ_μ plane corresponding to accepted muons can be individuated; the shown regions can be delimited with the following cuts,

- NA50
  $E_\mu > 8.$ GeV for $0.065 \leq \theta_\mu \leq 0.090$
  $E_\mu > 16000\ (\theta_\mu - 0.065)^2 + 8.$ GeV for $0.037 \leq \theta_\mu < 0.065$
  $E_\mu > 13000\ (\theta_\mu - 0.090)^2 + 8.$ GeV for $0.090 < \theta_\mu \leq 0.108$
- NA38
  $E_\mu > 2.5$ GeV for $0.070 \leq \theta_\mu \leq 0.080$
  $E_\mu > 13000\ (\theta_\mu - 0.070)^2 + 2.5$ GeV for $0.032 \leq \theta_\mu < 0.070$
  $E_\mu > 13000\ (\theta_\mu - 0.080)^2 + 2.5$ GeV for $0.080 < \theta_\mu \leq 0.102$

The defined acceptance cut is then applied on the Monte-Carlo generated muons. This last cut is only imposed to muons belonging to dimuons which survived the y and $cos\theta_{CS}$ cut previously applied.

In fig.5.9 the resulting dimuon mass, rapidity, p_T and $cos\theta_{CS}$ distributions are shown for peripheral (b=10 fm) Pb-Pb events at 158 GeV/c per nucleon, before kinematic cuts. In fig.5.10 the same is shown after kinematic cuts have been applied. The difference in the binning of the two plots is due to the reduced statistics after kinematic cuts.

5.2.3 R_{BCK} factor from dimuon Monte-Carlo distributions

From the histograms for the dimuon mass, p_T, rapidity and $cos\theta_{CS}$ distributions, the R_{BCK} factor can be extracted as a function of the dimuon kinematic variables. For each value x in the distribution of the kinematic variable X (X=p_T, y, M, $cos\theta_{CS}$), we can write

$$R_{Monte-Carlo}(x) = \frac{\sum_{n=1}^{N_V} \sum_{i,j} P^{+-}(x)_{i,j}}{2\sqrt{(\sum_{n=1}^{N_V} \sum_{i,j} P^{++}(x)_{i,j})(\sum_{n=1}^{N_V} \sum_{i,j} P^{--}(x)_{i,j})}} \tag{5.21}$$

where N_V is the total number of produced VENUS events and $i, j = 1....N_e$ if N_e is the number of produced mesons in the VENUS event e.

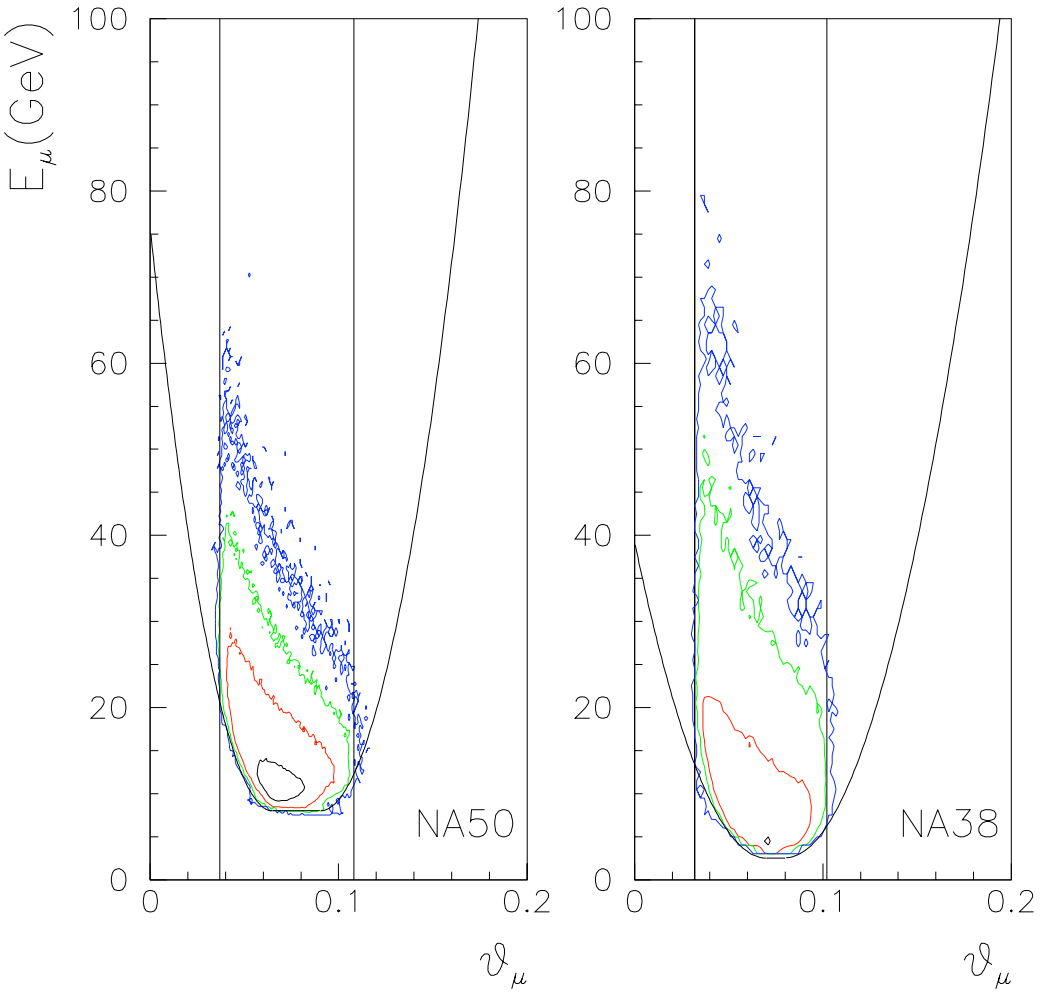

Figure 5.8: *Muon energy vs. muon polar angle as deduced from NA50 and NA38 data. The delimited areas correspond to the acceptance cut imposed to the Monte-Carlo single muon distributions to simulate the tracking of the muons through the whole muon spectrometer.*

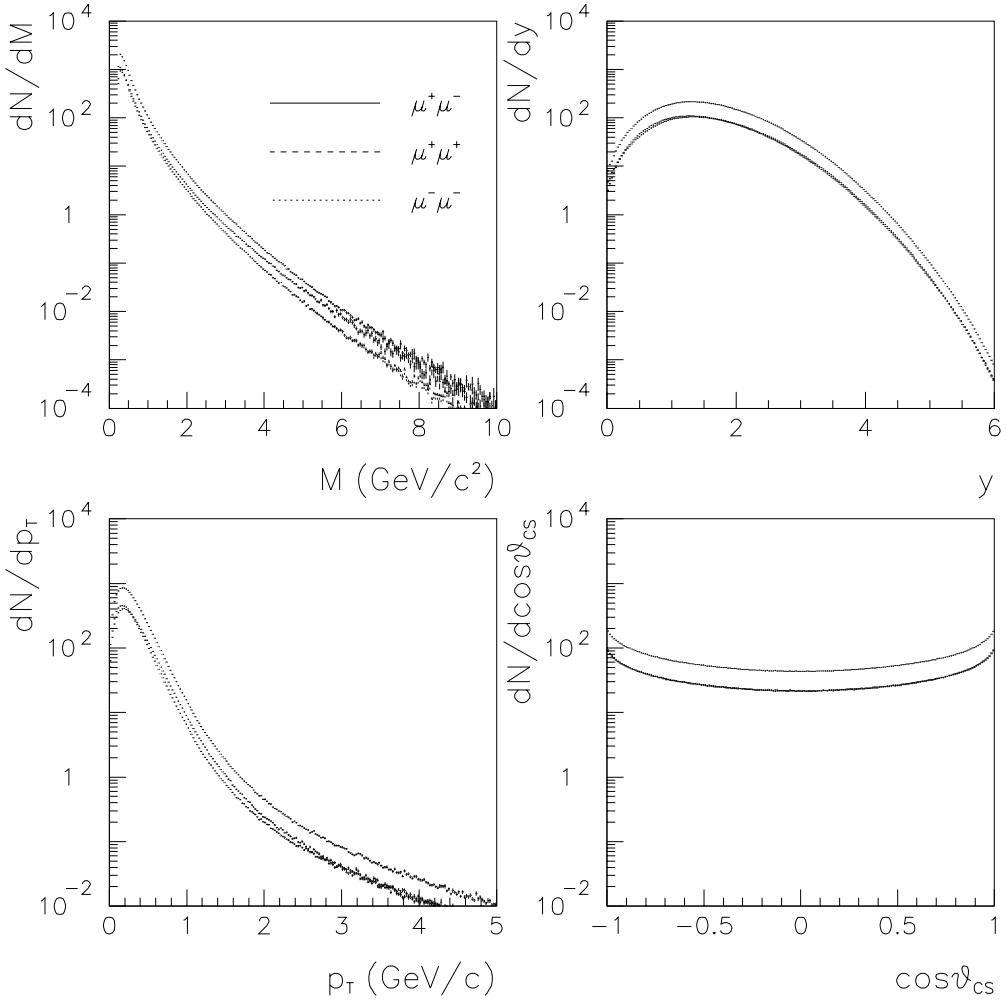

Figure 5.9: *Differential distributions of Monte-Carlo generated dimuon kinematic variables* before *kinematic cuts for peripheral (b=10 fm) Pb-Pb events at 158 A GeV/c.*

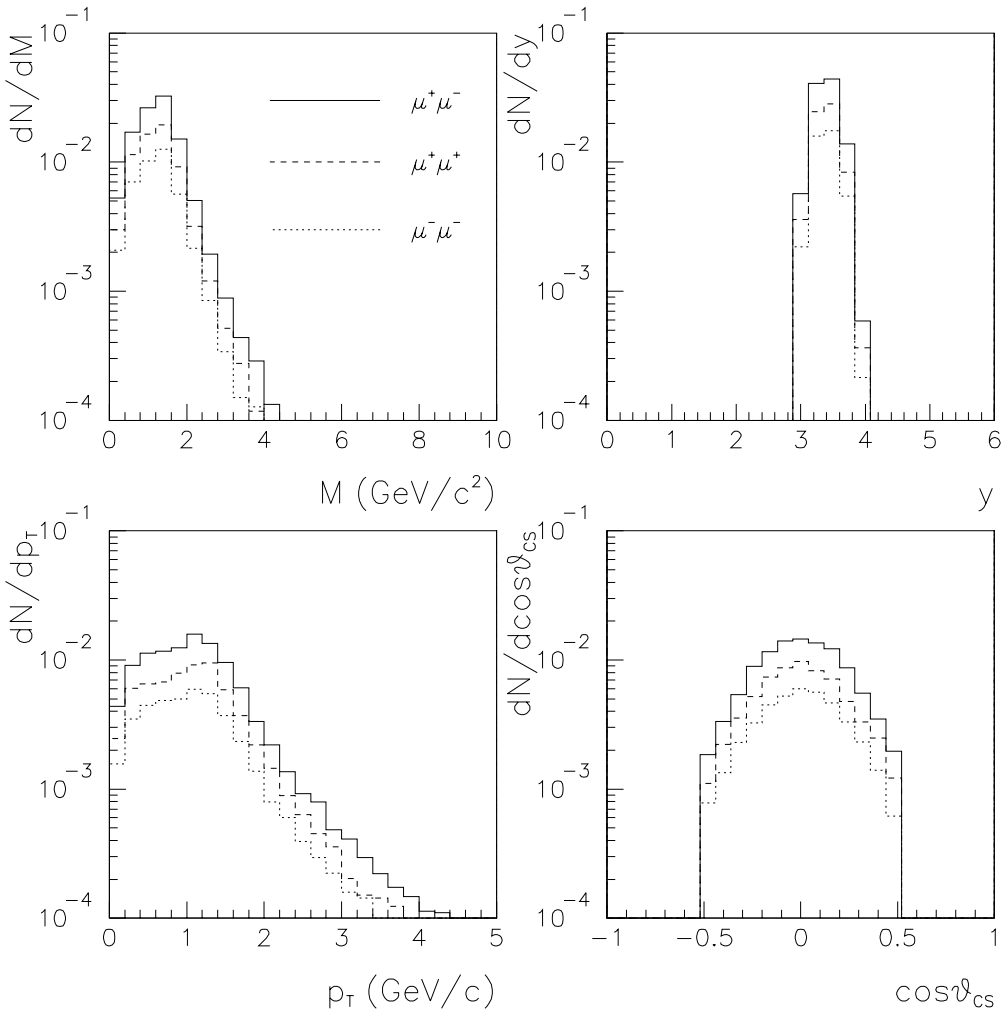

Figure 5.10: *Differential distributions of Monte-Carlo generated dimuon kinematic variables* after *kinematic cuts for peripheral (b=10 fm) Pb-Pb events at 158 A GeV/c.*

In other words, the ratio $N_{+-}^{Monte-Carlo}/2\sqrt{N_{++}^{Monte-Carlo}N_{--}^{Monte-Carlo}}$ is calculated bin per bin for each of the dimuon variables. In fig.5.11 the R_{BCK} factor distribution as a function of the dimuon mass, rapidity, p_T and $cos\theta_{CS}$ is shown for peripheral (b=10 fm) Pb-Pb 158 A GeV/c events. Kinematic cuts have not been applied. In fig.5.12, where kinematic cuts have been applied, the R_{BCK} factor does not show any strong dependence on the dimuon kinematic variables.

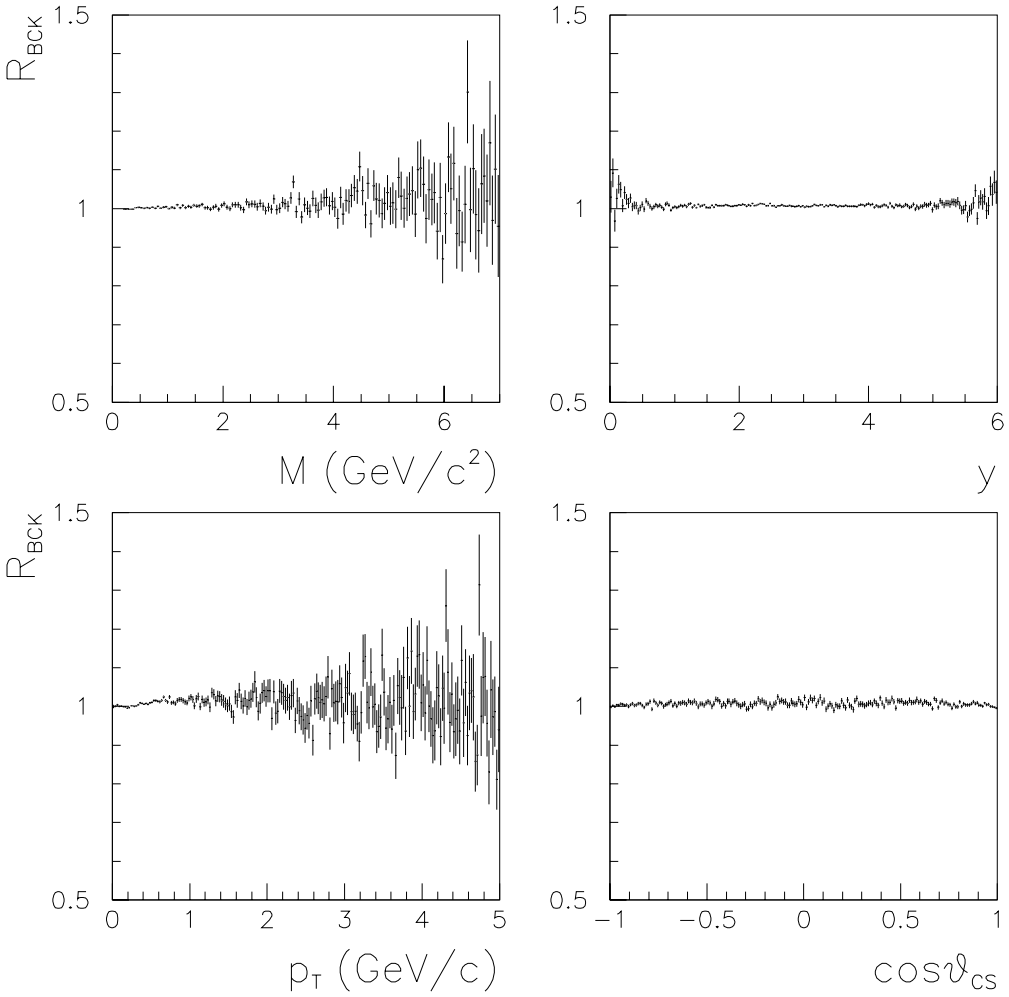

Figure 5.11: *Monte-Carlo R_{BCK} factor vs. dimuon mass, y, p_T and $cos\theta_{CS}$ before kinematic cuts for peripheral (b=10 fm) Pb-Pb 158 A GeV/c events.*

To compute the average R_{BCK} value we then integrate over the dimuon kinematic variable distributions

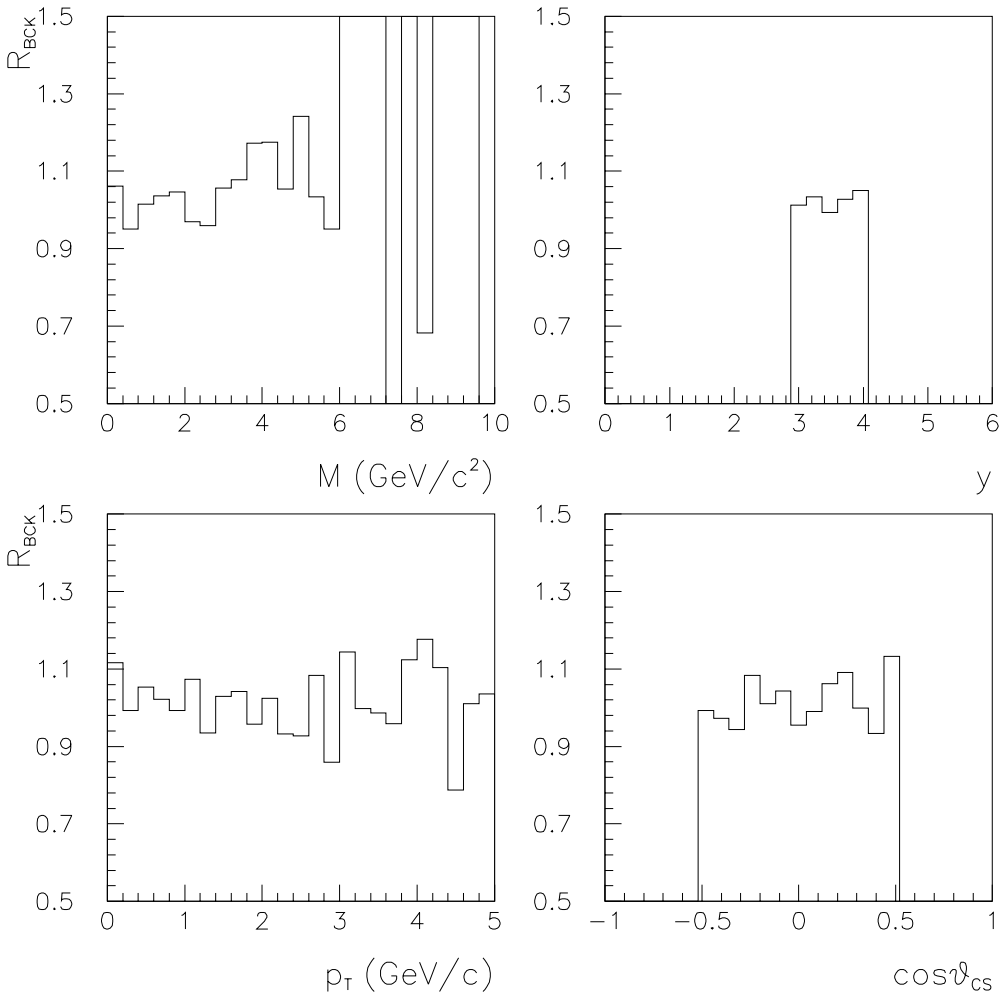

Figure 5.12: *Monte-Carlo R_{BCK} factor vs. dimuon mass, y, p_T and $cos\theta_{CS}$* after *kinematic cuts for peripheral (b=10 fm) Pb-Pb 158 A GeV/c events.*

System	b (fm)	$R \pm \sigma_R$
PbPb 158 A GeV/c	4	1.002 ± 0.005
PbPb 158 A GeV/c	7	1.004 ± 0.007
PbPb 158 A GeV/c	10	1.028 ± 0.013
PbPb 158 A GeV/c	13	1.073 ± 0.019
SU 200 A GeV/c	1	1.006 ± 0.003
SU 200 A GeV/c	4	1.007 ± 0.003
SU 200 A GeV/c	7	1.019 ± 0.003
SU 200 A GeV/c	10	1.069 ± 0.007

Table 5.2: *Monte-Carlo R_{BCK} factor obtained for the 4 impact parameter b values chosen for the PbPb and SU systems.*

$$\langle R_{Monte-Carlo} \rangle = \frac{\int dx \ \{\sum_{n=1}^{N_V} \sum_{i,j} P^{+-}(x)_{i,j}\}}{\int dx \ \{2\sqrt{(\sum_{n=1}^{N_V} \sum_{i,j} P^{++}(x)_{i,j})(\sum_{n=1}^{N_V} \sum_{i,j} P^{--}(x)_{i,j})}\}} \quad (5.22)$$

where $x = M, p_T, y, cos\theta_{CS}$. This average value is then used to correctly normalise the background contribution to the opposite-sign mass spectrum.

5.2.4 R_{BCK} centrality dependence

For the SU and PbPb systems the R_{BCK} factor has been computed for 4 different values of the impact parameter b, to investigate the R_{BCK} centrality dependence. In tab.5.2 the obtained R_{BCK} values are listed. As expected, R_{BCK} shows a marked dependence on centrality.
In fig.5.13 the points correspond to the 4 R_{BCK} values obtained in the Monte-Carlo simulation while the connecting curve is a fit to the Monte-Carlo points. For the PbPb system the value R_{BCK}=1.000 when $b = 0\ fm$ has been imposed in order to avoid the use of too long CPU times.
We thus have a parametrisation of the R_{BCK} factor as a function of the impact parameter b for the two systems :

- PbPb 158 A GeV/c

$$R_{BCK} = 1.000 + 0.073 \cdot (b/13)^{4.04} \quad (5.23)$$

- SU 200 A GeV/c

$$R_{BCK} = 1.006 + 0.063 \cdot (b/10.)^{4.43} \quad (5.24)$$

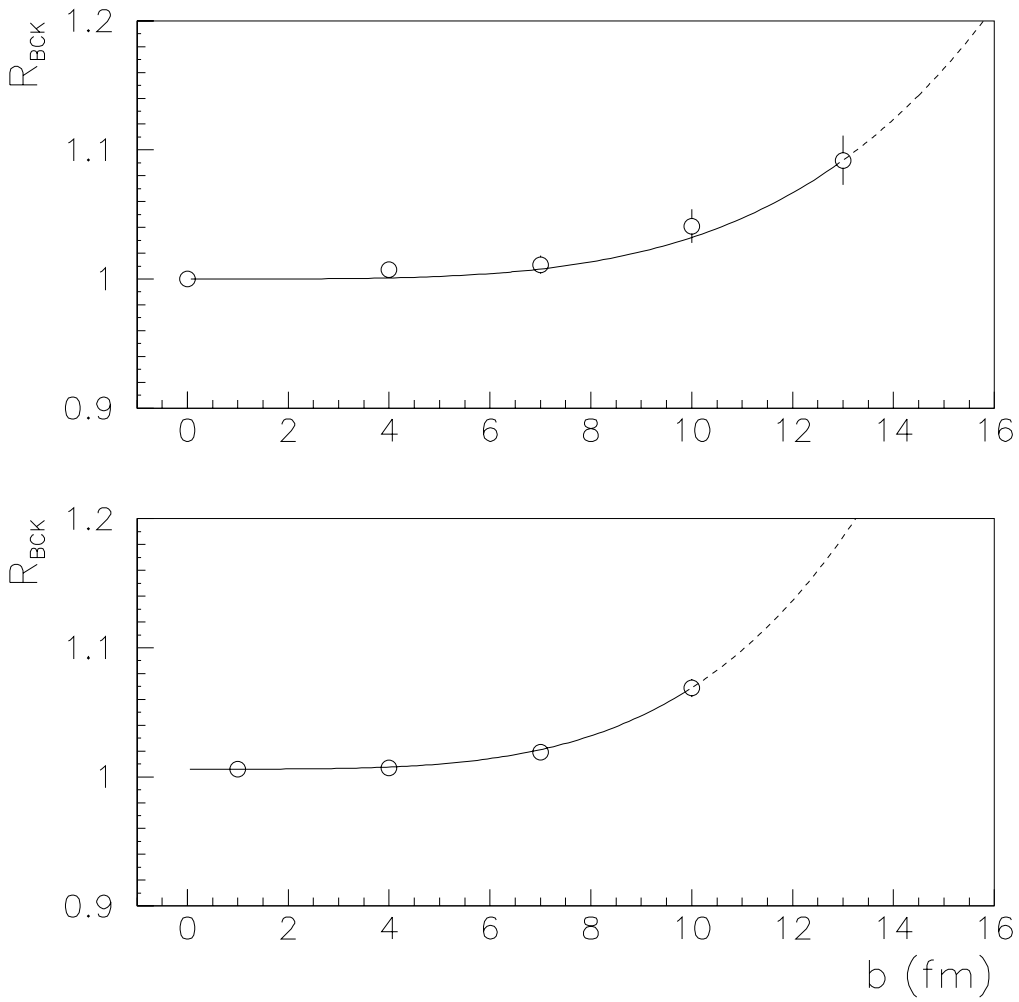

Figure 5.13: *Calculated R_{BCK} factor vs. impact parameter b for Pb-Pb collisions at 158 GeV per nucleon (top) and for S-U at 200 GeV per nucleon (bottom). The curves are fits to the Monte-Carlo points (plus an added point at b=0 fm for the PbPb system to which has been imposed a corresponding R_{BCK} value of* 1.000 ± 0.000*).*

In fig.5.14 the correlations between the impact parameter b and the transverse energy E_T are shown as obtained from the model described in[1], taking into account realistic nuclear densities.

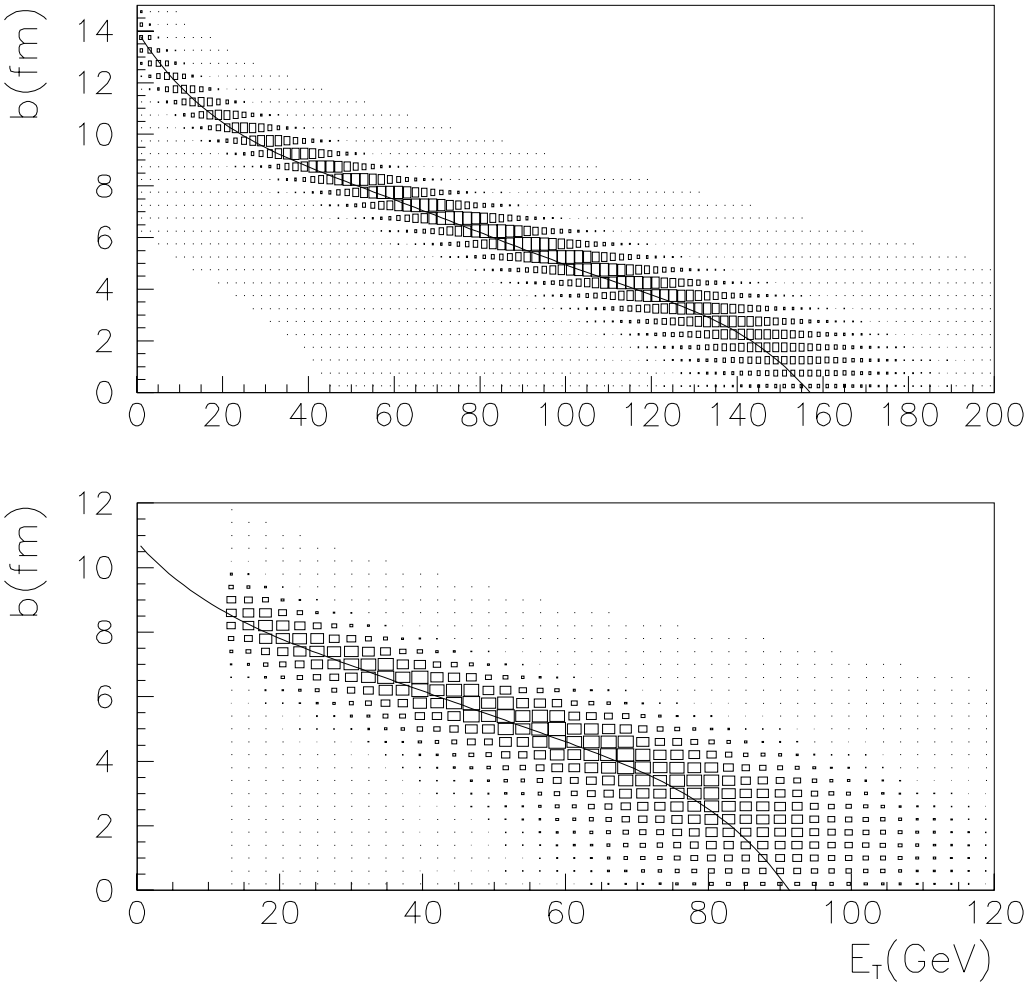

Figure 5.14: *Correlation between impact parameter b and transverse energy E_T for the PbPb 158 A GeV/c (top) and SU 200 A GeV/c (bottom) systems as obtained from[1].*

Each b vs. E_T correlation can be parametrised with a 5^{th} degree polynomial. The coefficients for the two polynomials corresponding to the PbPb and SU systems are listed in tab.5.3.
From the R vs. b and b vs. E_T correlations, the R vs. E_T one can be deduced, as it is shown in fig.5.15 where the centrality bins used in the PbPb and SU analysis are also indicated. To obtain the average $\langle R_{BCK} \rangle$ factor corresponding to a particular E_T bin, a weighted average over the events in that centrality bin is then performed, i.e., the distribution dN/dE_T vs. E_T is extracted from the data for each of the PbPb

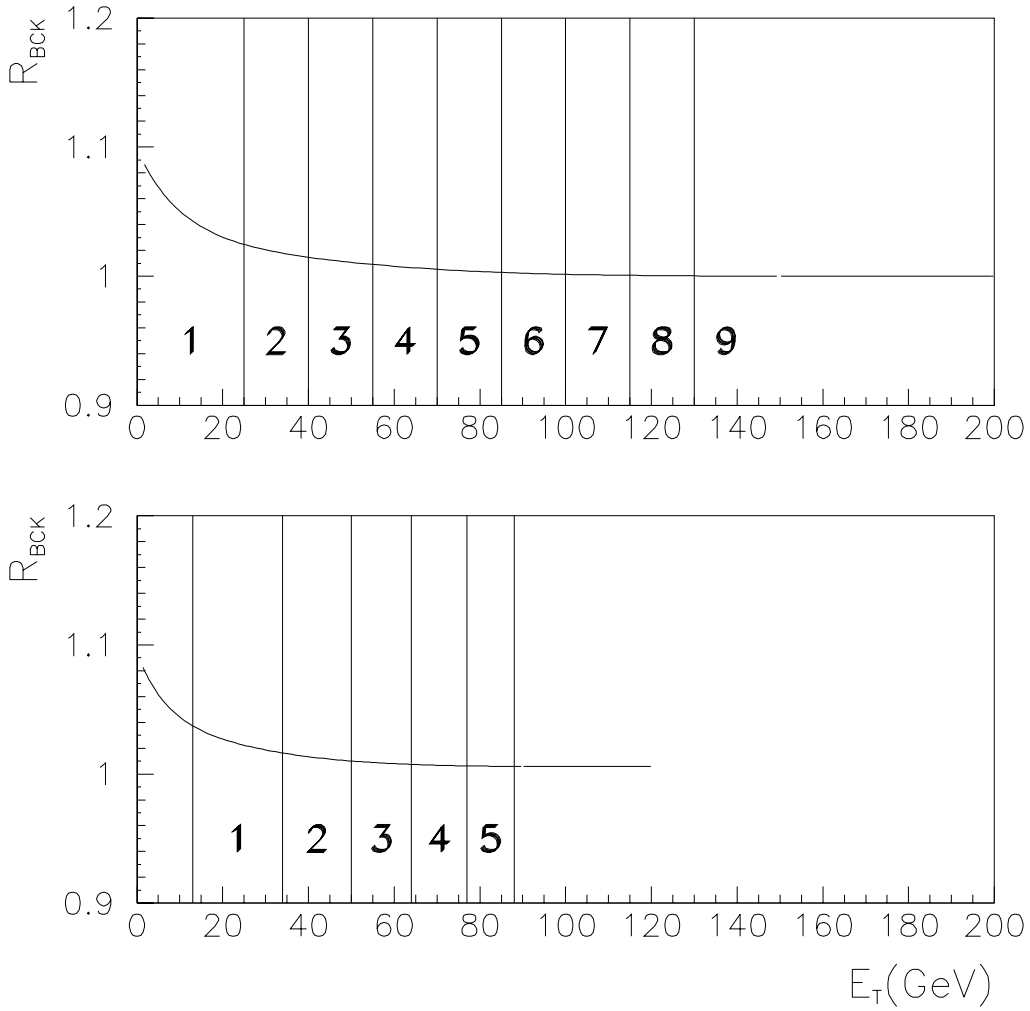

Figure 5.15: *Calculated R_{BCK} factor vs. transverse energy E_T for the PbPb 158 A GeV/c (top) and SU 200 A GeV/c (bottom) systems. See text for more details.*

		PbPb	SU
a_0 (10^0)	(fm)	$13.990 \pm 0.2\ 10^{-4}$	$10.800 \pm 0.1\ 10^{-4}$
a_1 (10^0)	(fm/GeV)	$-0.260 \pm 0.1\ 10^{-6}$	$-0.251 \pm 0.7\ 10^{-6}$
a_2 (10^{-2})	(fm/GeV^2)	$0.547 \pm 0.7\ 10^{-7}$	$0.798 \pm 0.4\ 10^{-5}$
a_3 (10^{-4})	(fm/GeV^3)	$-0.731 \pm 0.5\ 10^{-7}$	$-1.842 \pm 0.2\ 10^{-4}$
a_4 (10^{-6})	(fm/GeV^4)	$0.469 \pm 0.3\ 10^{-7}$	$2.113 \pm 0.8\ 10^{-4}$
a_5 (10^{-8})	(fm/GeV^5)	$-0.115 \pm 0.2\ 10^{-7}$	$-0.963 \pm 0.9\ 10^{-4}$

Table 5.3: *Coefficients of the 5^{th} degree polynomials parametrising the b vs. E_T correlations for the PbPb and SU systems.*

and SU E_T bins and the corresponding R_{BCK} value is computed for each of the E_T values in the bin; the R_{BCK} values are then weighted using the dN/dE_T distribution to obtain the final dN/dR_{BCK} one, where

$$\frac{dN}{dR_{BCK}^{Monte-Carlo}} dR_{BCK}^{Monte-Carlo} = \frac{dN}{dE_T} dE_T \tag{5.25}$$

If ΔR_{BCK} is the bin in the R_{BCK} variable corresponding to a particular E_T bin, the average value of R_{BCK} in that bin is

$$\langle R_{BCK}^{Monte-Carlo} \rangle = \frac{\int_{\Delta R_{BCK}} \{ R_{BCK}^{Monte-Carlo} \frac{dN}{dR_{BCK}} dR_{BCK} \}}{\int_{\Delta R_{BCK}} \{ \frac{dN}{dR_{BCK}} dR_{BCK} \}} \tag{5.26}$$

5.2.5 Pile-up effects

Combinatorial background dimuons are usually thought as being the combination of muons from $\pi's$ and $K's$ produced in a single interaction. This is correct only in the case where no pile-up effects exist. The pile-up of projectiles interacting in the same trigger time window leads to an overlapping of consecutive events. As a result, the detected dimuons can be combinations of muons generated in different events. During the SU and PbPb data taking periods, the Beam Hodoscope detected the incoming ions and signalled if more than one ion fell in the 20 ns trigger time window. Because of this $a-priori$ beam pile-up rejection, the pile-up effects can be thus neglected. It is instead mandatory to calculate their impact on the final R_{BCK} factor values in the case of the NA50 high intensity pA data taking periods, where no pile-up rejection was applied. To take the pile-up effect into account the following reasoning can be used [6] :

every time a good trigger is detected by the NA50 Hodoscopes, a 20 ns gate is opened. If we assume that the incoming projectile distribution follows the Poisson law, the probability of not having beam pile-up in the time window Δt is

$$P(0) = e^{-\overline{n}} \tag{5.27}$$

where $\overline{n}$ is the mean number of ions in the time interval Δt,

$$\overline{n} = \Delta t \cdot \frac{I}{B} \tag{5.28}$$

where I is the beam intensity (number of incident projectiles per burst) and B is the burst time length (effective-spill).
To compute the pile-up effects in the frame of our simulation, we proceed as follows : every-time an event is processed we randomly extract from the Poisson distribution

the number of projectiles which could pile-up. Taking into account the target thickness, the number N_{pu} of piling-up projectiles which actually interact in the target is computed.
Kaons and pions from the N_{pu} piling-up consecutive events are then combined. Again, every single kaon/pion is combined in all possible ways with all the kaons and pions in the sample of mesons from all the piling-up events. The previous procedure is then applied as in the case of no pile-up.

5.2.6 Results

In table 5.6, 5.4, 5.5 the R_{BCK} factors are shown for all the studied systems. In table 5.4 the pA low intensity R values are compared with the ones obtained taking into account the pile-up effects existing at the used experimental high intensity of $\simeq 2.5$ 10^9 p/burst. At higher intensities the R_{BCK} factor value becomes smaller because charge correlation effects are smeared out by the piling-up of different events.
The pW 200 GeV/c NA38 system has also been studied in the aim of cross checking with the R factor already obtained for that system in a previous analysis[3] developed within the NA38 Collaboration. The R_{BCK} factor value for the pW 200 GeV/c system had been measured on two sets of data collected with two slightly different hadron absorber set-ups.[3]. The signal distributions for the two pW set-ups had to be the same, whilst the measured background distributions were expected to reflect the difference between the used hadron absorber. A simultaneous fit of the two mass spectra was therefore performed, leaving the common R_{BCK} factor as a free parameter in the fit. The R_{BCK} factor obtained in that previous analysis is,

$$R_{BCK} \mid_{pW200} = 1.19 \pm 0.04 \tag{5.29}$$

to be compared with the one obtained in the present one,

$$\langle R \rangle \mid_{pW200} = 1.21 \pm 0.02 \tag{5.30}$$

The results obtained with the two different methods appear to be consistent; this gives as confidence in the reliability of our Monte-Carlo simulation.

In the following chapter, the pA, SU and PbPb sets of data are analysed and it is shown that when letting the R_{BCK}'s as free parameters in the fit or when imposing R_{BCK}=1 for all nucleus-nucleus systems, the risk of an unpredictable under or overestimation of the background exists. Therefore, the R_{BCK} factors listed in tab. 5.6, 5.4, 5.5 have been used to fix the background normalisation.

System	Energy (GeV/c)	$R \pm \sigma_R$ (low intensity)	$R \pm \sigma_R$ (I=2.5·10^{9}p/burst)	$R \pm \sigma_R$ (measured)
pW	200	1.21±0.02		1.19±0.04
pAl	450	1.19±0.05	1.06±0.02	
pCu	450	1.26±0.04	1.06±0.02	
pAg	450	1.21±0.04	1.06±0.01	
pW	450	1.21±0.03	1.05±0.01	

Table 5.4: *R factor for the pA systems. The high-intensity R_{BCK} values have been computed including the pile-up effect as explained in the previous paragraph. The pW 200GeV/c has been included to compare with the R_{BCK} factor obtained in the analysis of the two NA38 pW systems[3].*

System	Energy ($A\ GeV/c$)	E_T bin	E_T interval (GeV)	$R \pm \sigma_R$
PbPb	158	1	$E_T < 25$	1.035 ± 0.011
PbPb	158	2	$25 < E_T < 40$	1.017 ± 0.003
PbPb	158	3	$40 < E_T < 55$	1.010±0.002
PbPb	158	4	$55 < E_T < 70$	1.006±0.001
PbPb	158	5	$70 < E_T < 85$	1.003±0.0006
PbPb	158	6	$85 < E_T < 100$	1.001±0.0003
PbPb	158	7	$100 < E_T < 115$	1.001±0.0002
PbPb	158	8	$115 < E_T < 130$	1.000±0.0001
PbPb	158	9	$E_T > 130$	1.000±0.000

Table 5.5: *R_{BCK} factor for the 9 E_T bins of the PbPb 158 A GeV/c system. The error on R_{BCK} comes from the fit to the 4 (+1 imposed for b=0 fm) R_{BCK} Monte-Carlo values vs. b.*

System	Energy ($A\ GeV/c$)	E_T bin	E_T interval (GeV)	$R \pm \sigma_R$
SU	200	1	$13 < E_T < 34$	1.023 ± 0.005
SU	200	2	$34 < E_T < 50$	1.013 ± 0.002
SU	200	3	$50 < E_T < 64$	1.009 ± 0.0007
SU	200	4	$64 < E_T < 77$	1.007 ± 0.0004
SU	200	5	$77 < E_T < 88$	1.006 ± 0.0001

Table 5.6: *R factor for the 5 E_T bins of the SU 200 A GeV/c system. The error on R_{BCK} comes from the fit to the 4 R_{BCK} Monte-Carlo values vs. b.*

Bibliography

[1] Frederic Fleuret, PhD thesis, April 1997, Paris

[2] "Study of the estimation of the combinatorial muon pair background"- S. Constantinescu, S. Dita and D. Jouan, NA50 Collab.

[3] Carlos Lourenço, PhD thesis, January 1995, Lisbon

[4] K.Werner, Phys.Rep. 232(1993)87.

[5] GEANT-Detector Description and Simulation Tool-CERN Geneva(CH).

[6] "The correct way to calculate pileup"-C.Gerschel-NA50 Collab.

Chapter 6

Intermediate mass region analysis

In this chapter, after a detailed introduction, the pA, SU and PbPb dimuon mass spectra are analysed. The intermediate mass spectrum is described as a superposition of DY and open charm (also indicated as $D\overline{D}$), after combinatorial background subtraction. The DY and $D\overline{D}$ contributions are extracted from the fit of the mass spectra. Since the DY contribution in the IMR is determined by the high mass region above the ψ', and since the background normalisation is fixed $a - priori$ using the R_{BCK} calculated in chapter 5, it is the $D\overline{D}$ contribution which will change accordingly with the experimental dimuon yield in the IMR.

For each system the $D\overline{D}/DY$ ratios are then derived. Since both the DY process and the $D\overline{D}$ hadro-production are hard processes and are therefore expected to scale with the number of effective nucleon-nucleon collisions in a nucleus-nucleus interaction (see chapter 1), any anomalous behaviour of the $D\overline{D}$ contribution will clearly show in the $D\overline{D}/DY$ ratio.

The pA systems, where no excess has been measured, are also analysed. The extracted $D\overline{D}/DY$ can then be used as a reference when calculating the absolute value of the excess for the SU and PbPb systems.

To support the results obtained with the analysis of the mass distributions, the dimuon p_T, y and $cos\theta$ distributions are also studied.

6.1 Introduction

In the present chapter, which with chapter 5 and 7 constitutes the core of my work, the analysis of the mass, p_T, rapidity and cosθ spectra of the SU, PbPb and pA systems is described. The different aspects of the analysis are dealt with in the following order :

- In sec.6.2, the general method used to fit the mass spectra is discussed. The aim of the fit of the mass spectra is the extraction of the $D\overline{D}$ contribution to the IMR region. The contribution to the IMR of all the other components are therefore established in some independent way. For instance, the DY contribution in the IMR is determined by the high mass region for M>4.5 GeV/c^2, where only DY events can be found. Moreover, the background contribution in the IMR mass spectra is fixed with the R_{BCK} factors calculated in chapter 5.

  It is perhaps important to stress that, since the combinatorial background contribution in the IMR amounts up to 85% in central S-U and in p-A collisions and up to 95% in central Pb-Pb collisions, the determination of the combinatorial background contribution to the IMR is one of the most important issues of the present analysis. In chapter 5, which has been completely devoted to the discussion of the combinatorial background, the so called R_{BCK} factor has been introduced. The R_{BCK} factor corrects the normalisation of the opposite-sign background when the multiplicity of secondaries produced in the collision (pions and kaons) is not large enough to motivate the assumption of a complete charge UN-correlation between the same produced secondaries. The R_{BCK} factor is expected to be larger than 1 in peripheral nucleus-nucleus collisions and in proton-nucleus ones, whereas it should be compatible with 1.0 in central nucleus-nucleus collisions. Chapter 5 gives a detailed description of the Monte-Carlo chain used to determine the R_{BCK} values for all the considered systems and for all the used E_T bins within the same system.

- Once the fit has been performed, the $D\overline{D}$ can be extracted and normalised to the corresponding DY contribution. In sec.6.3, the method used to obtain the ratio $D\overline{D}/DY$ is outlined.

  The DY contribution is used as a reference because it has been experimentally proved that the DY does behave as hard processes are expected to, i.e., the cross section for DY pair production in proton-nucleus and nucleus-nucleus interactions scales with the total number of effective nucleon-nucleon collisions (see chapter 1). The open charm hadro production is also a hard process and is therefore expected to behave as the DY does. This has been proved in proton-nucleus collisions, but up until now no direct measurement of open charm production in nucleus-nucleus collision has been performed. In

nucleus-nucleus collisions charm production could also proceed through some alternative processes (see chapter 7 and references therein). Thereafter, if the $D\overline{D}/DY$ presents any anomalous behaviour, this can be associated with the intervention of a new contribution to the open charm component.

- Section 6.4 and 6.5 present the results of the analysis of the PbPb and SU mass differential distributions, which are then gathered and discussed in sec.6.6.

- In section 6.7, the p_T, y and cosθ differential distributions are studied.

  When in sec. 6.4, 6.5 and 6.6 the mass differential distributions of the SU and PbPb systems are studied, the extracted $D\overline{D}/DY$ is found to increase with the size of the system and with the collision centrality. In order to support the hypothesis that the found excess in the IMR can be interpreted as an enhanced open charm production, the p_T, y and cosθ differential distributions can be studied. The p_T, y and cosθ Monte-Carlo differential distributions are normalised from the results of the fit of the mass spectra. The normalised Monte-Carlo distributions are then superimposed on the experimental ones. No additional hypothesis are introduced. In the p_T spectra the shapes of the DY and open charm contributions can be well distinguished, whereas in the y and cosθ ones the different contributions are all similar in shape. Thereafter, the p_T spectra are studied in detail.

- In sec.6.8, the pA systems are analysed in two slightly different ways and the pA reference value is given as a weighted average of the two extracted $D\overline{D}/DY$ values. In the same section, the pA p_T, y and $cos\theta$ differential distributions are also studied.

- In the last section, the results obtained in the present analysis are compared with the results which would have been obtained if the R_{BCK} values would have been set to 1.0 for all the E_T bins of the two considered nucleus-nucleus systems. This approach has been widely used in the past by the NA38/NA50 Collaboration and it is therefore important to be aware of the approximations induced by such an assumption.

  Next, the effect of leaving the R_{BCK} factor as a free parameter in the fit is studied. This approach being generally wrong, it is still interesting to see if and when the shape of the experimental mass distribution alone is able to give a satisfactory estimation of the combinatorial background contribution.

  The systematic error associated with the method used for the combinatorial background subtraction is also estimated.

6.2 Fit of the mass spectra : general method.

The fit of the opposite-sign experimental mass spectrum is performed using the Monte-Carlo fitting functions for all the participating processes. The following function is therefore constructed,

$$\frac{dN^{+-}}{dM} = R_{BCK}\frac{dN^{bck}}{dM} + n_{D\overline{D}}\frac{dN^{D\overline{D}}}{dM} + n_{DY}\frac{dN^{DY}}{dM} + n_{J/\psi}\frac{dN^{J/\psi}}{dM} + n_{\psi'}\frac{dN^{\psi'}}{dM}$$

where $n_{D\overline{D}}$, n_{DY}, $n_{J/\psi}$ and $n_{\psi'}$ are the normalisation factors whose value is determined in the fit and $dN^{D\overline{D}}/dM$, dN^{DY}/dM, $dN^{J/\psi}/dM$, $dN^{\psi'}/dM$ are the Monte-Carlo fitting functions obtained as outlined in chapter 4. dN^{bck}/dM is the function resulting from the fit of the combinatorial background mass distribution and R_{BCK} is the background normalisation factor calculated as detailed in chapter 5. Finally, dN^{+-}/dM is the experimental opposite-sign mass distribution which has to be fitted.

In chapter 4 the Monte-Carlo mass distributions have been fitted with ad-hoc functions whose parameter values are typical of the system and set-up for which the Monte-Carlo distributions have been generated. For each of the Monte-Carlo functionals, only the normalisation factor has been left unspecified, since it is then left as a free parameter in the fit of the experimental mass spectrum. In order to improve the quality of the fit, some other Monte-Carlo parameters can be freed in the fit of the experimental mass spectrum. In the present analysis, the following parameters are left *free*

- J/ψ, ψ', DY and $D\overline{D}$ normalisation factors.
- J/ψ mass and width, because the Monte-Carlo generated shape does not exactly reproduce the mass and width of the measured J/ψ.

and the following are *fixed*

- The ψ' mass and width, using the Monte-Carlo results for the J/ψ and ψ' mass difference and width ratio, i.e.,

  $$M^{data}_{\psi'} = M^{data}_{J/\psi} + M^{MC}_{\psi'} - M^{MC}_{J/\psi} \tag{6.1}$$

  and

  $$\sigma^{data}_{\psi'} = \sigma^{data}_{J/\psi}\frac{\sigma^{MC}_{\psi'}}{\sigma^{MC}_{J/\psi}} \tag{6.2}$$

- The R_{BCK} values calculated in chapter 5.

The signal mass distribution can be obtained subtracting the background contribution from the opposite-sign mass spectrum,

$$\frac{dN^{+-}_{signal}}{dM} = \frac{dN^{+-}}{dM} - R_{BCK}\frac{dN^{bck}}{dM} \tag{6.3}$$

The signal mass spectrum is then compared with the background subtracted opposite-sign fitting function, i.e.

$$\frac{dN^{+-}_{signal}}{dM} = n_{D\overline{D}}\frac{dN^{D\overline{D}}}{dM} + n_{DY}\frac{dN^{DY}}{dM} + n_{J/\psi}\frac{dN^{J/\psi}}{dM} + n_{\psi'}\frac{dN^{\psi'}}{dM} \tag{6.4}$$

6.3 $D\overline{D}/DY$ ratios from the fit of the mass spectra

The DY and $D\overline{D}$ normalisation factors found in the fit of the opposite-sign mass spectrum can be used to normalise the Monte-Carlo DY and $D\overline{D}$ functions in order to derive the ratio $D\overline{D}/DY$. Since the acceptance of the apparatus for DY pairs and for dimuons from the semi-leptonic decays of charmed pairs are different, the $D\overline{D}/DY$ ratio has to be acceptance corrected, i.e.

$$\frac{D\overline{D}}{DY} = \frac{\left\{\frac{n_{D\overline{D}}\int_{M_0}^{M_1}\frac{dN^{D\overline{D}}}{dM}dM}{A_{D\overline{D}}}\right\}}{\left\{\frac{n_{DY}\int_{M_0}^{M_1}\frac{dN^{DY}}{dM}dM}{A_{DY}}\right\}} \tag{6.5}$$

where $M_1 \leq 8\ GeV/c^2$ and M_0=1.5 GeV/c^2 or M_0=1.3 GeV/c^2. Even if starting the fit at M_0=1.5 GeV/c^2 excludes all possible contamination from the low mass resonances, when the lower starting point is used only a $\leq 2\%$ discrepancy is found on the $D\overline{D}/DY$ ratio. The values of the acceptances $A_{D\overline{D}}$ and A_{DY} have been listed in the last section of chapter 4. The Monte-Carlo $D\overline{D}$ fitting functions generated with m_c=1.5 GeV/c^2 are always used, unless differently specified.

Since the aim of the present work is the comparison of the $D\overline{D}/DY$ ratios obtained from the fit of the mass spectra with the expected $D\overline{D}/DY$, and since in the present chapter we only compare $D\overline{D}/DY$ ratios within the same nuclear system, the isospin correction (see chapter 1) can be neglected when dealing with the SU and PbPb systems. The energy and rapidity corrections, which are also needed when comparing cross sections measured for system covering a different rapidity region and for different energies, can also be neglected because of the above reason. On the other hand, when analysing the pA systems the isospin correction has to be taken into account because a common $D\overline{D}/DY$ is imposed in the fit, as explained in sec.6.8.

6.4 Fit of the PbPb mass spectra.

In fig.6.1 the fit of the 9 PbPb opposite-sign mass spectra, in the mass region 1.5 $< M <$ 7.0 GeV/c^2, is shown. In fig.6.2 the fitting curves are superimposed on the signal mass spectra, after background subtraction. In fig.6.3 the same curves are superimposed on the IMR signal mass spectra. The extracted $D\overline{D}/DY$ ratios are listed in tab.6.1 together with the corresponding χ^2 of the fit; the associated $\simeq 10\%$ error is purely statistical.

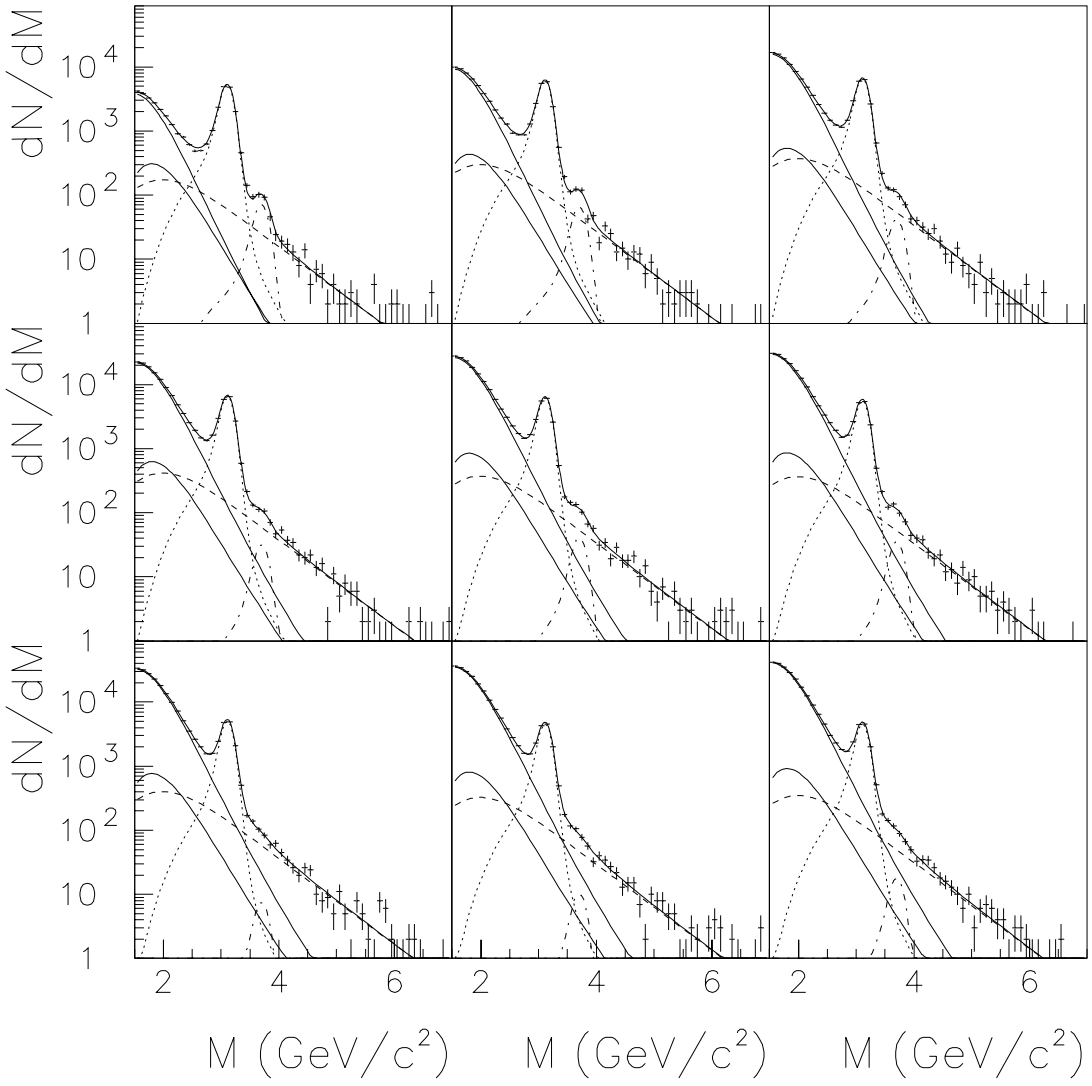

Figure 6.1: *Fit of the 9 PbPb opposite-sign mass distributions in the mass range 1.5< M <7.0 GeV/c^2.*

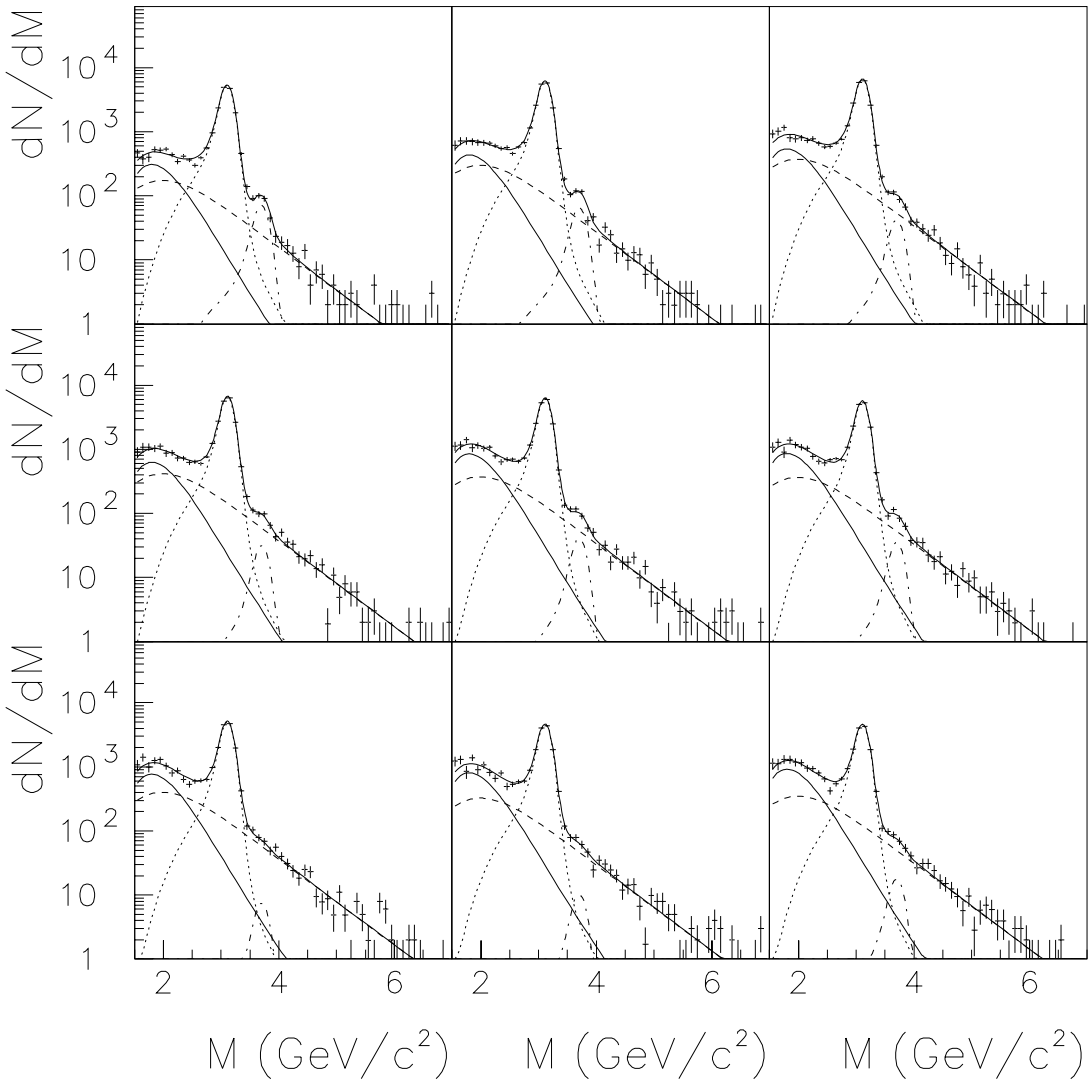

Figure 6.2: *PbPb signal mass distributions compared with the opposite-sign distribution fitting curves, after background subtraction.*

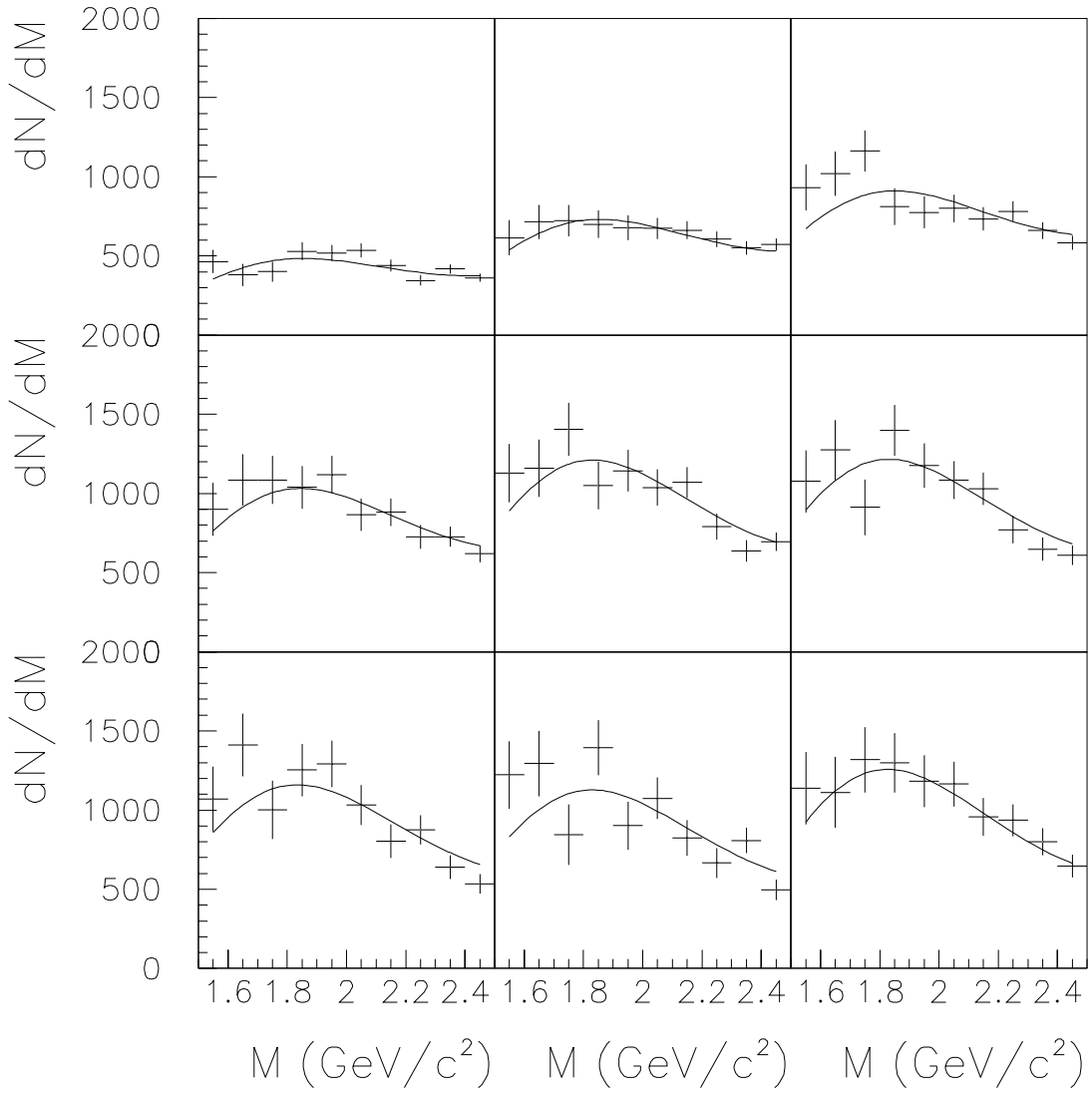

Figure 6.3: *PbPb signal mass distributions compared with the opposite-sign distribution fitting curves, after background subtraction. The IMR is shown.*

E_T bin	$\frac{D\overline{D}}{DY}$	χ^2
1	2.46 ± 0.32	1.9
2	2.01 ± 0.23	1.7
3	2.01 ± 0.22	1.6
4	2.10 ± 0.22	1.7
5	3.15 ± 0.29	1.5
6	3.27 ± 0.31	0.9
7	2.66 ± 0.27	1.7
8	3.46 ± 0.36	1.8
9	3.68 ± 0.37	0.8

Table 6.1: *$D\overline{D}/DY$ obtained when fitting the 9 PbPb mass spectra with $R_{BCK} = R_{BCK}^{MC}$.*

6.4.1 The charm mass

In chapter 4 the open charm differential distributions have been obtained with the PYTHIA event generator and for a charm mass value m_c=1.5 GeV/c^2. Since the adopted value of the charm mass influences the shapes of the generated distributions, the open charm differential distributions for the PbPb set-ups have been also generated with two alternative mass values in order to estimate the size of the induced effect.

From the comparison of the experimentally measured $c\overline{c}$ cross sections with leading order QCD calculations the charm mass value m_c=1.5 GeV/c^2 seems to be favoured (see chapter 1 and reference therein). When the value m_c=1.2 GeV/c^2 is used, a reasonable agreement between the measured cross sections and the QCD calculations still exists but the theoretical predictions clearly tend to overestimate the experimentally measured cross sections. On the other hand, when using m_c=1.8 GeV/c^2 the QCD calculations clearly underestimate the measured cross sections. Thereafter, I here assume that the actual charm mass value can range from 1.2 up to 1.5 GeV/c^2 and investigate the effect of the related incertitude on the $D\overline{D}/DY$ ratios. Tab.6.2 lists the $D\overline{D}/DY$ ratios obtained when the PbPb mass spectra are fitted with the Monte-Carlo $D\overline{D}$ fitting functions corresponding to the three different charm mass values. The discrepancy between the ratios obtained when using the two extreme charm mass values is $\simeq$15% , whilst it is $\leq$4% when the values m_c=1.5 and 1.35 GeV/c^2 are used. In the present analysis the value m_c=1.5 GeV/c^2 has been adopted. The above systematic incertitude on the $D\overline{D}/DY$ ratios affects all the ratios in the same direction and is therefore never explicitly included.

E_T bin	$\frac{D\overline{D}}{DY}$	$\frac{D\overline{D}}{DY}$	$\frac{D\overline{D}}{DY}$
	$m_c = 1.5 GeV/c^2$	$m_c = 1.35 GeV/c^2$	$m_c = 1.2 GeV/c^2$
1	2.46 ± 0.32	2.55 ± 0.32	2.83 ± 0.36
2	2.01 ± 0.23	2.09 ± 0.24	2.33 ± 0.27
3	2.01 ± 0.22	2.07 ± 0.23	2.36 ± 0.26
4	2.10 ± 0.22	2.15 ± 0.23	2.45 ± 0.26
5	3.15 ± 0.29	3.24 ± 0.30	3.66 ± 0.34
6	3.27 ± 0.31	3.35 ± 0.32	3.80 ± 0.36
7	2.66 ± 0.27	2.72 ± 0.27	3.10 ± 0.31
8	3.46 ± 0.36	3.54 ± 0.36	4.04 ± 0.42
9	3.68 ± 0.37	3.75 ± 0.37	4.27 ± 0.43

Table 6.2: *$D\overline{D}/DY$ obtained when the 9 PbPb opposite-sign mass distributions are fitted with the three different $D\overline{D}$ Monte-Carlo functionals corresponding to the 3 quoted values of m_c.*

6.5 Fit of the SU mass spectra

The analysis of the SU data has been performed in the same way as for the PbPb system. In fig.6.4 the fits of the 5 SU opposite-sign mass spectra are shown. In fig.6.5 the background subtracted fitting curves have been superimposed on the signal mass spectra. The same is shown in fig.6.6 for the IMR only. In tab.6.3 the extracted $D\overline{D}/DY$ ratios are listed together with the corresponding χ^2 of the fit. The associated $\simeq 10\%$ error is purely statistical.

E_T bin	$\frac{D\overline{D}}{DY}$	χ^2
1	1.62 ± 0.15	2.2
2	1.66 ± 0.14	1.6
3	1.95 ± 0.15	2.0
4	2.42 ± 0.13	1.4
5	2.07 ± 0.17	1.1

Table 6.3: *$D\overline{D}/DY$ obtained when fitting the SU opposite-sign mass spectra with the Monte-Carlo R_{BCK} values.*

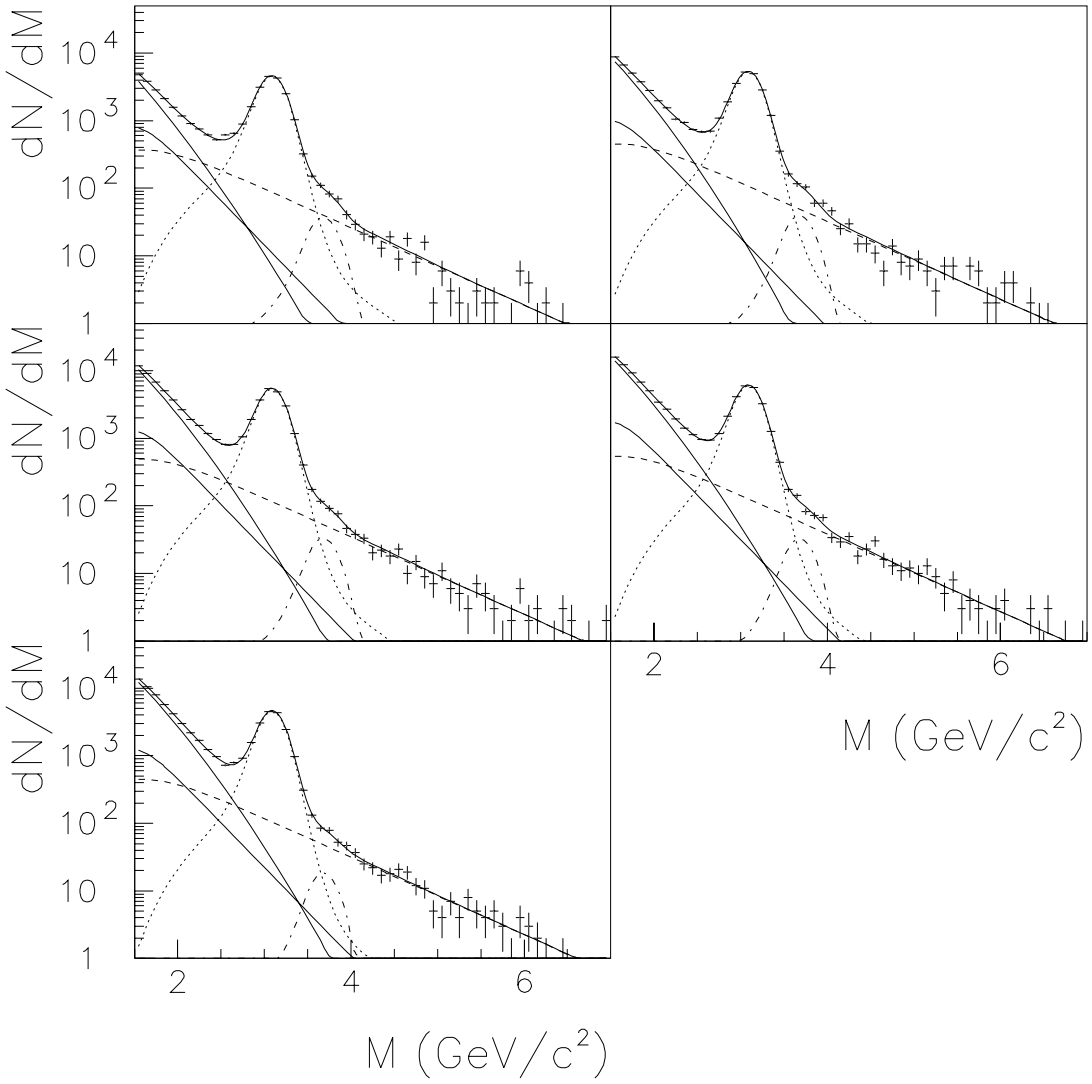

Figure 6.4: *Fit of the 5 SU opposite-sign mass distributions in the mass range 1.5< M <7 GeV/c^2.*

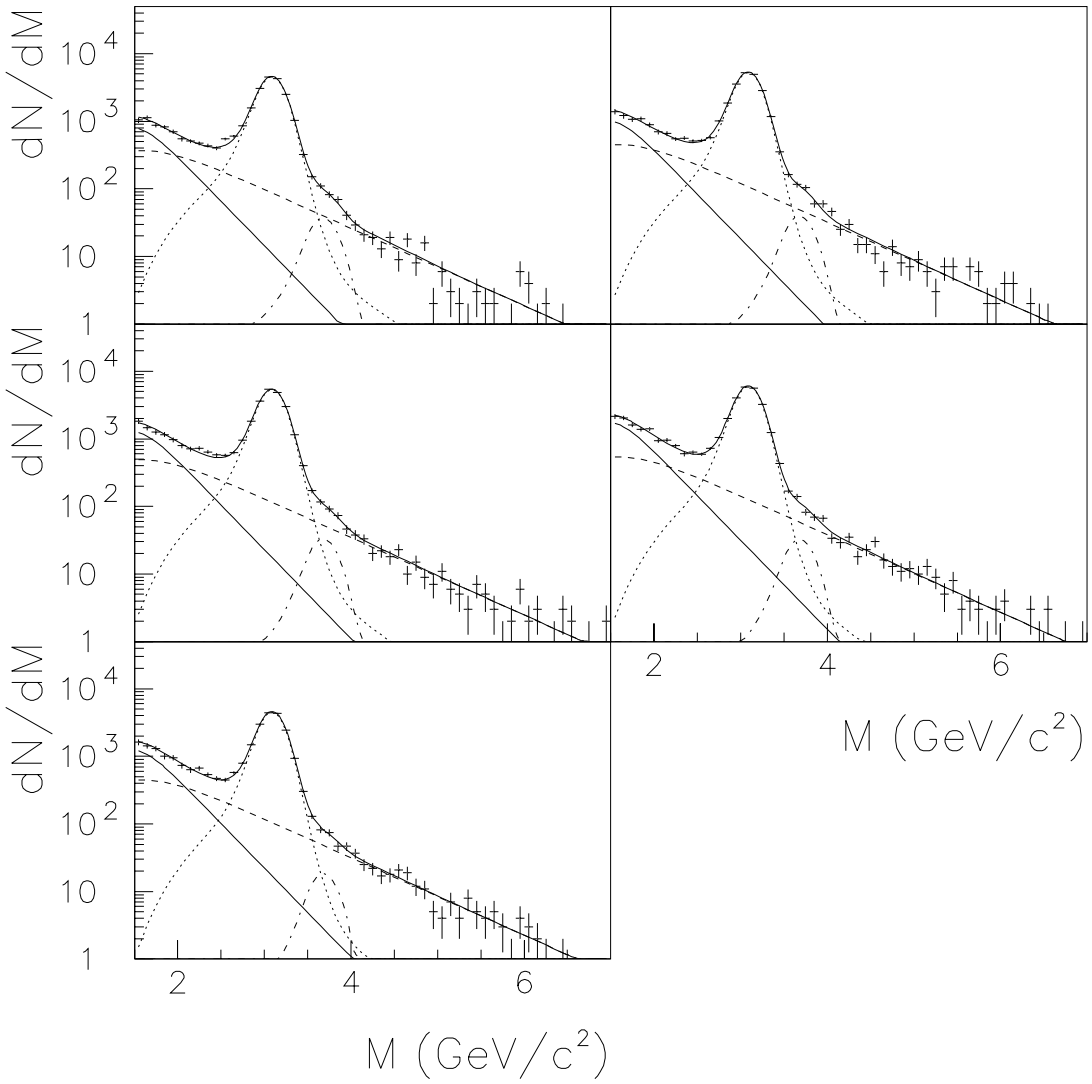

Figure 6.5: *SU signal mass distributions compared with the opposite-sign mass spectra fitting curves, after background subtraction.*

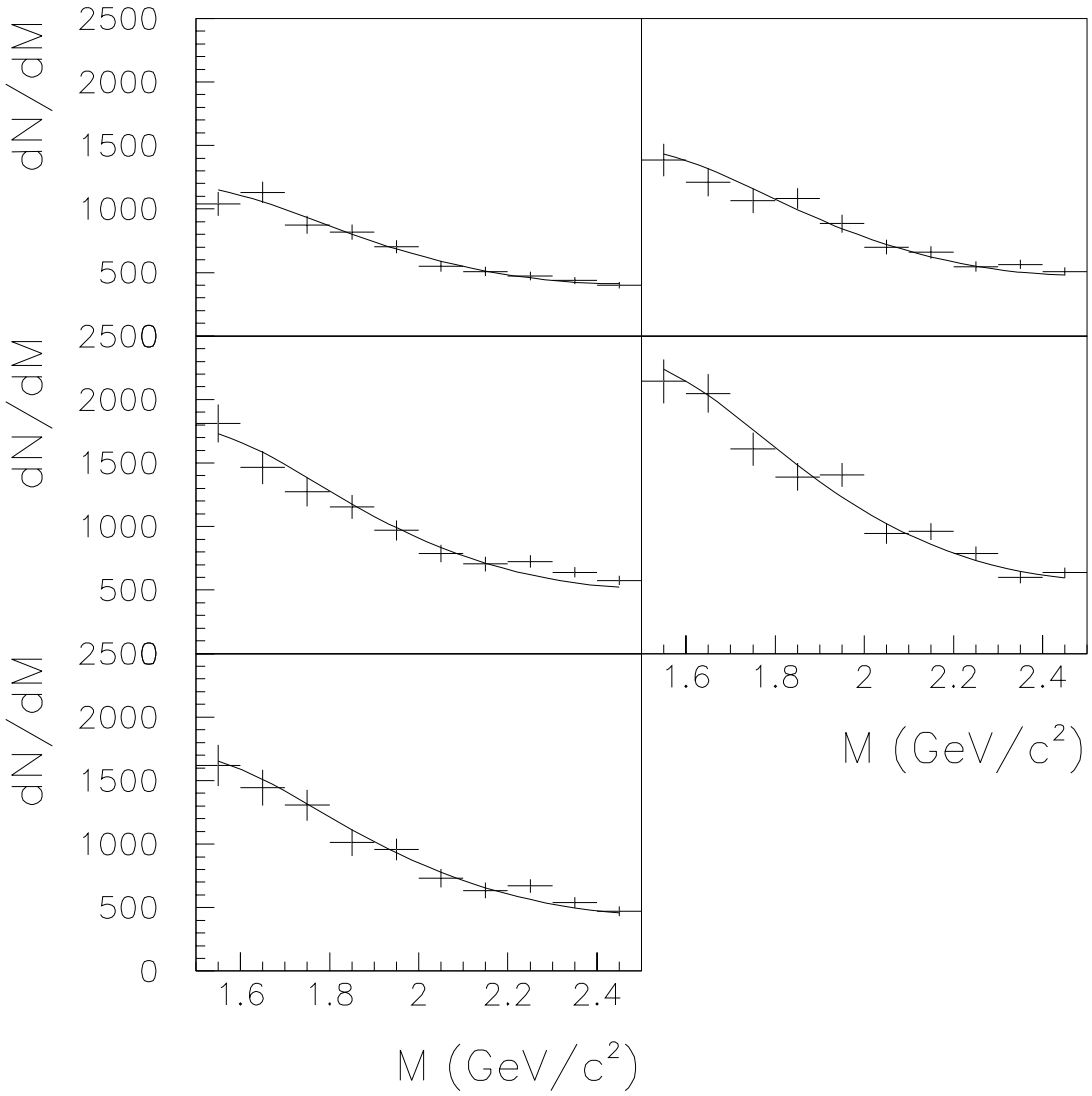

Figure 6.6: *SU signal mass distributions compared with the opposite-sign mass spectra fitting curves, after background subtraction. The IMR is shown.*

6.6 PbPb and SU results

When the $D\overline{D}$ contribution is left as a free parameter in the fit of the opposite-sign mass spectra and the background normalisation is fixed by the Monte-Carlo R_{BCK} values, a satisfactory description of all the mass spectra is achieved. The $D\overline{D}/DY$ is enhanced by a factor $\simeq 1.3$ in central S-U and $\simeq 1.8$ in central Pb-Pb interactions with respect to peripheral collisions. In fig.6.7 the $D\overline{D}/DY$ obtained from the fit of the SU and PbPb mass spectra are plotted as a function of the transverse energy E_T.

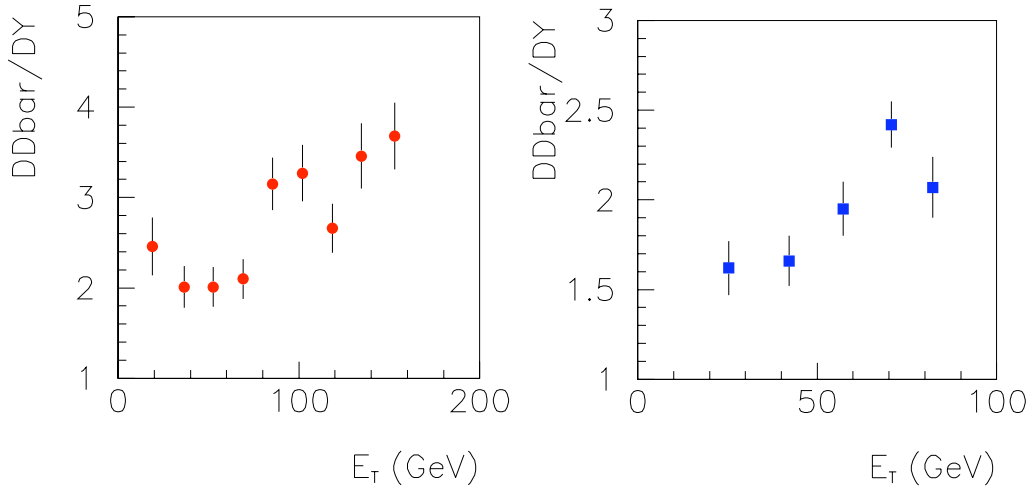

Figure 6.7: *The $D\overline{D}/DY$ ratios obtained when fitting the PbPb (left) and SU (right) mass spectra is plotted vs. the transverse energy E_T. No isospin correction has been applied.*

6.7 The p_T, cosθ, y differential distributions

To support the hypothesis that the IMR excess found in A-B collisions originates from an enhanced $D\overline{D}$ production, the p_T, cosθ and y differential distributions in the IMR can be studied. The p_T, cosθ and y differential distributions for the DY, $D\overline{D}$ and J/ψ are generated as described in chapter 4. The Monte-Carlo shapes are then (separately) normalised using the results of the fits of the mass spectra,

$$\int_0^{V_{max}} \frac{dN^{MC}}{dV} dV \;=\; \int_{1.5}^{2.5} \frac{dN}{dM} dM \text{ (with V=}p_T\text{, cos}\theta\text{, } y\text{)} \tag{6.6}$$

where V_{max} is the maximum value of the considered variable in the corresponding Monte-Carlo distribution for 1.5< M <2.5 GeV/c^2.
The enhanced $D\overline{D}$ contribution is therefore already included in the adopted normalisation. The resulting curves are then *superimposed* on the experimental distributions for 1.5< M <2.5 GeV/c^2.
The DY and $D\overline{D}$ Monte-Carlo p_T distributions clearly have different shapes, as visible in fig.6.8 where the experimental p_T distributions are shown for four of the PbPb bins, together with the superimposed Monte-Carlo curves after normalisation. On the other hand, in the cosθ and y distributions the shapes of the two contributions can not be easily distinguished, as shown in fig.6.11. The p_T distribution can be therefore used in order to support the results of the analysis of the mass spectra.

In fig.6.8 the most peripheral bins are better described by the Monte-Carlo shapes than the more central ones. The Monte-Carlo shapes used in fig.6.8 have been generated as detailed in chapter 4, where the value σ_{k_T}=0.8 GeV/c has been imposed. In chapter 4, the open charm differential distributions have been generated with PYTHIA, where the transverse momentum of the muon pair originates from the intrinsic transverse momentum k_T associated to the colliding partons. On the other hand, the DY and high mass resonances p_T differential distributions have been generated with the following parametrisation,

$$\frac{d\sigma}{dp_T} \propto p_T m_T K_1(\frac{m_T}{T}) \tag{6.7}$$

where K_1 is the first order modified Bessel function, i.e

$$K_1(\frac{m_T}{T}) = \frac{e^{-(m_T/T)}}{\sqrt{(m_T/T)}} \cdot P_6(T/m_T) \tag{6.8}$$

In order to check whether a better description of the p_T differential distributions can be obtained when also the DY and high mass resonances are generated with PYTHIA, the Monte-Carlo generation has been repeated using the PYTHIA 5.7 event generator with the MRS 43 parton distribution function[3] for *all* the contributing processes.

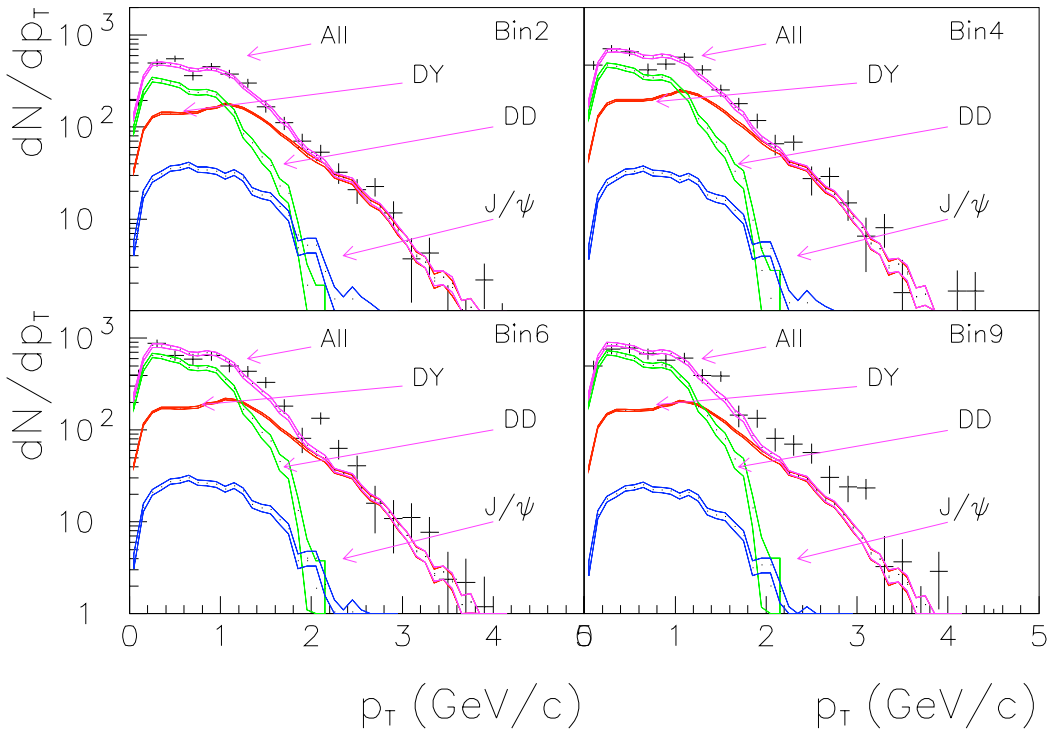

Figure 6.8: *PbPb p_T differential distribution for $1.5 < M < 2.5$ GeV/c^2 compared with the normalised Monte-Carlo predictions. The Monte-Carlo generation has been done as described in chapter 4, with σ_{k_T}=0.8 GeV/c. From top-left to bottom-right, 4 E_T bins with increasing centrality are shown.*

6.7.1 PYTHIA p_T distributions.

In chapter 4, the open charm has been generated with PYTHIA using the Gaussian intrinsic transverse momentum distribution with σ_{k_T}=0.8 GeV/c. The latter had in fact already been used in the SU analysis performed in ref.[1] whose Monte-Carlo shapes we directly use; we therefore adopted the same parametrisations for the pA and PbPb systems.

In the following, the 4 different (and reasonable) values σ_{k_T}=0.6, 0.8, 0.9, 1.0 GeV/c, are used to generate the DY, $D\overline{D}$ and J/ψ Monte-Carlo differential distributions. As shown in fig.6.9 for the PbPb system, the $D\overline{D}$ mass shape distribution is not particularly affected by changing the σ_{k_T} value, whilst the IMR DY shape is particularly sensitive to it. In fig.6.10 the DY Monte-Carlo shape as obtained in chapter 4 is compared with the PYTHIA generated ones and it turns out to be quite similar to the one generated with σ_{k_T}=0.8 GeV/c; the integrals of the two functions in the mass region 1.5< M <2.5 GeV/c^2 differ by $\simeq$ 7%.
The best value of σ_{K_T} is the one which leads to a better reproduction of all the mass, p_T, cosθ and y differential distributions. The mass differential distribution can not discriminate because in the high mass region, where for M > 4.5 GeV/c^2 only DY dimuons can be found, the DY Monte-Carlo shape does not sensibly change with changing k_T. The $cos\theta$ and rapidity distributions are also ruled out, since the dimuon contributions from DY, $D\overline{D}$ and J/ψ change with the chosen σ_{k_T} but the superposition of the 3 processes always gives a good description of the data, as shown in fig.6.11 for the most central PbPb E_T bin.
In fig.6.12, the Monte-Carlo generated p_T distributions are shown to be strongly affected by a change in the σ_{k_T} value. It is therefore on the basis of the results of the analysis of the p_T spectra that the best σ_{K_T} has to be chosen.

In fig.6.13 the PbPb DY and $D\overline{D}$ shapes corresponding to different σ_{k_T} values are compared.
From fig.6.12 it is clear that the best data reproduction is obtained when imposing $\sigma_{k_T} = 0.9$ GeV/c. This has been checked for all the 9 PbPb E_t bins. In fig.6.14, 6.15, 6.16 the experimental p_T, $cos\theta$ and y differential distributions for 4 representative PbPb E_t bins are compared with the normalised Monte-Carlo shapes for $\sigma_{k_T} = 0.9$ GeV/c.

6.7.2 Results

A good description of the p_T, y and $cos\theta$ distributions for the SU and PbPb systems has been obtained in the hypothesis that the excess measured in the previous section originates from an enhanced open charm production. Therefore, since no additional hypothesis have been introduced, the study of the p_T (y and $cos\theta$) spectra supports the given interpretation of the measured IMR excess.

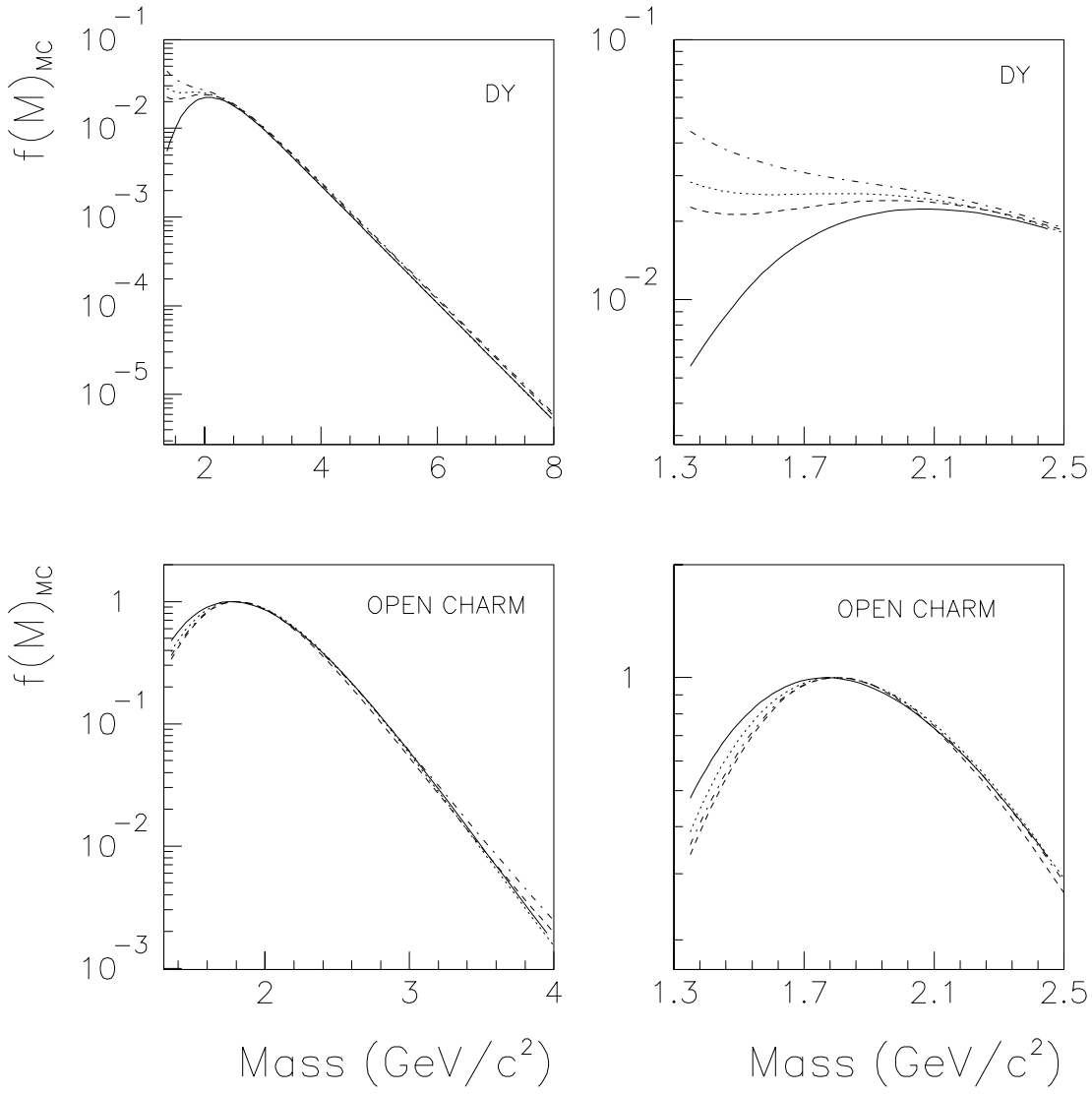

Figure 6.9: *Comparison of fitting function shapes for DY (top) and open-charm (bottom) obtained when fitting the Monte-Carlo shapes generated with PYTHIA and* σ_{k_T}*=0.6 GeV/c (full line), 0.8 GeV/c (dashed line), 0.9 GeV/c (dotted line), 1.0 GeV/c (dash-dotted line). The whole mass region (left) and the IMR (right) are shown.*

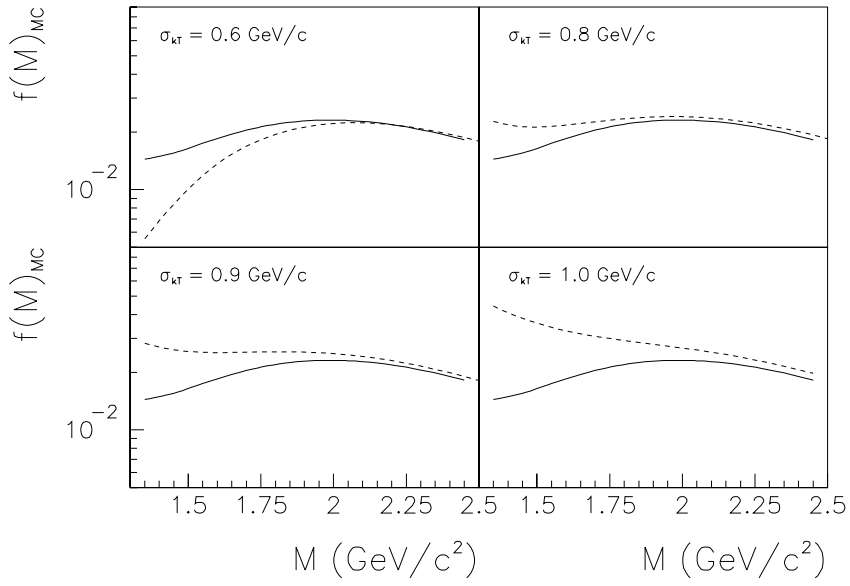

Figure 6.10: *Comparison of the PbPb Monte-Carlo DY fitting function shape obtained in chapter 4 (full line) with the ones obtained with PYTHIA and σ_{k_T}=0.6,0.8,0.9,1.0 GeV/c (dashed line).*

6.7.3 Fit of the mass spectra (revisited)

In the previous subsection we have seen that a nice agreement can be reached between the experimental and Monte-Carlo p_T, y and $cos\theta$ distributions if the PYTHIA event generator is used to generate all the processes contributing to the IMR, with σ_{K_T}=0.9 GeV/c. In order to establish the normalisation factors for the Monte-Carlo p_T, cosθ and y distributions, the mass distributions have been fitted with the Monte-Carlo mass shapes generated with the same σ_{K_T}. The corresponding $D\overline{D}/DY$ ratios have been therefore obtained. In tab.6.4, the $D\overline{D}/DY$ values obtained for the 9 PbPb E_T bins when using the PYHTIA generator with σ_{k_T} = 0.9 GeV/c, are compared with the previous ones. The difference between the two sets of values is smaller than the error on the $D\overline{D}/DY$ values ($\leq$ 13%). Since the SU $D\overline{D}/DY$ are affected by a similar error ($\leq$ 10%) and since the Monte-Carlo generation of all the needed processes with PYTHIA is extremely CPU time consuming, the $D\overline{D}/DY$ ratios extracted when using the set of Monte-Carlo shapes obtained in chapter 4 will be used in the following, both for the PbPb and the SU data sets. On the other hand, the pA sets of data discussed in the next section are characterised by a larger statistics in the IMR and are therefore more sensitive to small changes in the Monte-Carlo fitting function shapes. This has been verified analysing the pA data with both the Monte-Carlo fitting functions obtained with σ_{k_T}=0.9 GeV/c and with the ones obtained when using σ_{k_T}=0.8 GeV/c. When the latter is used the quality of the fit is poor and the $D\overline{D}/DY$ value strongly depends on the fitting procedure.

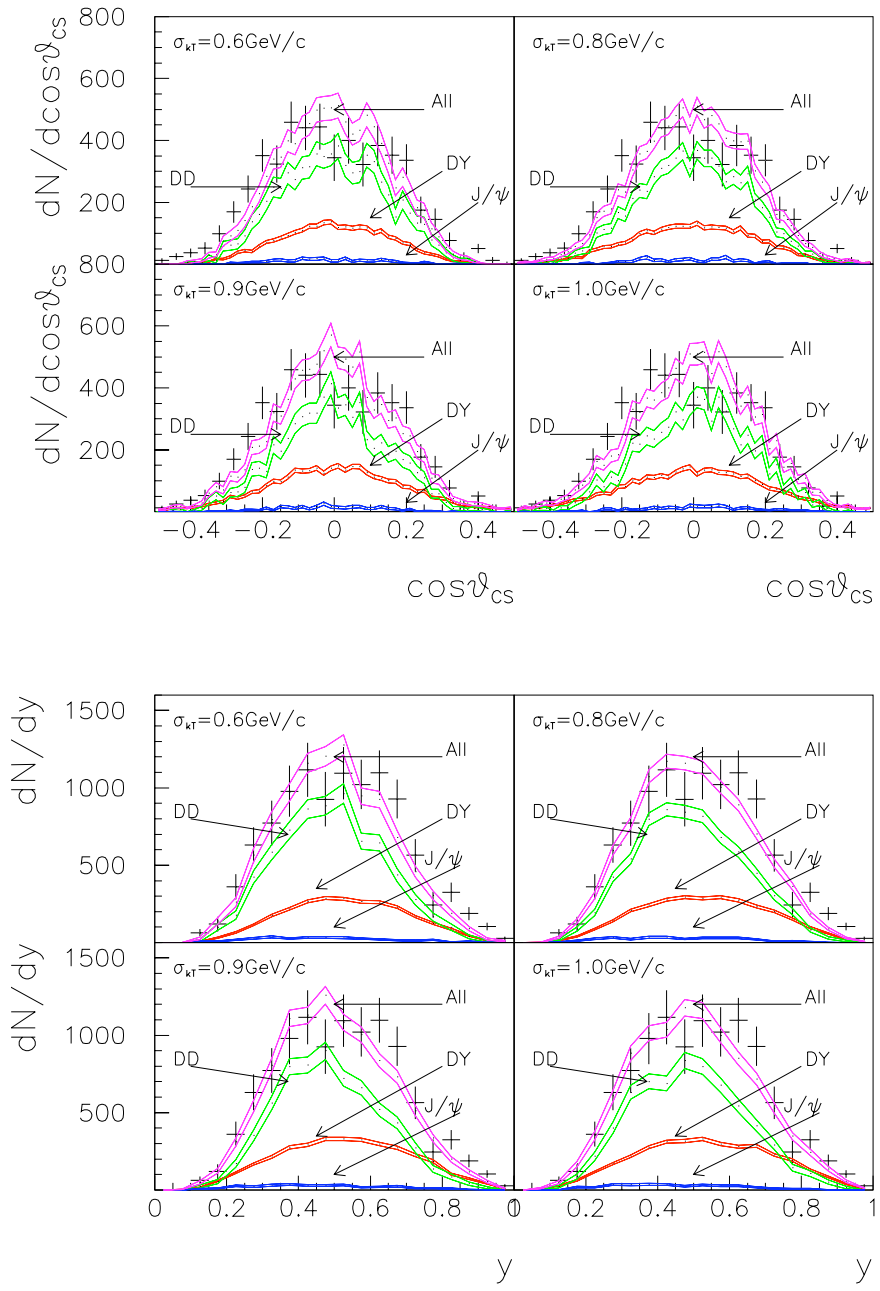

Figure 6.11: *PYTHIA generated cosθ and y differential distributions in the IMR (1.5 < M < 2.5 GeV/c^2) for the indicated 4 σ_{k_T} values, compared with the experimental PbPb cosθ and y distributions in the same mass region and for the most central E_T bin.*

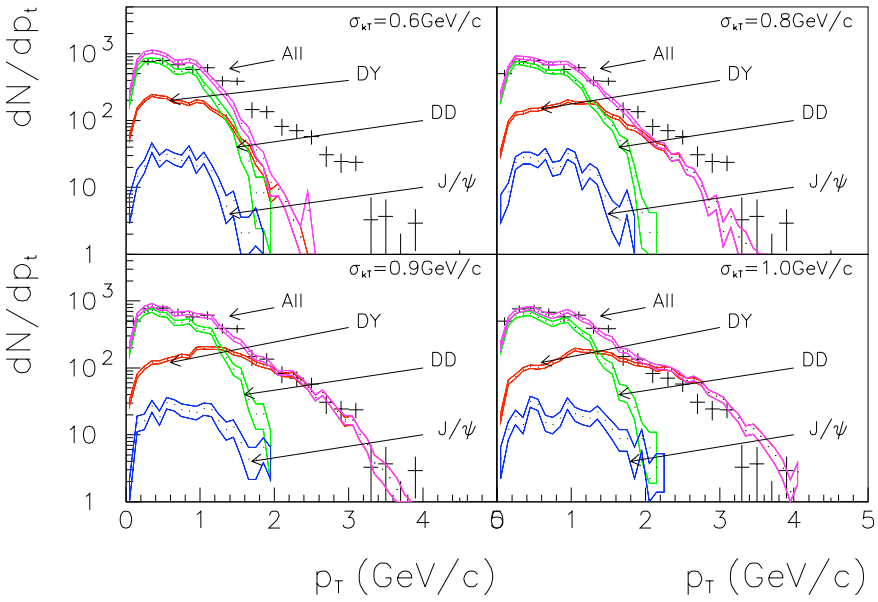

Figure 6.12: *IMR ($1.5 < M < 2.5\ GeV/c^2$) p_T differential distribution for the PbPb most central bin, compared with the PYTHIA generated p_T distributions for the 4 indicated σ_{k_T} values.*

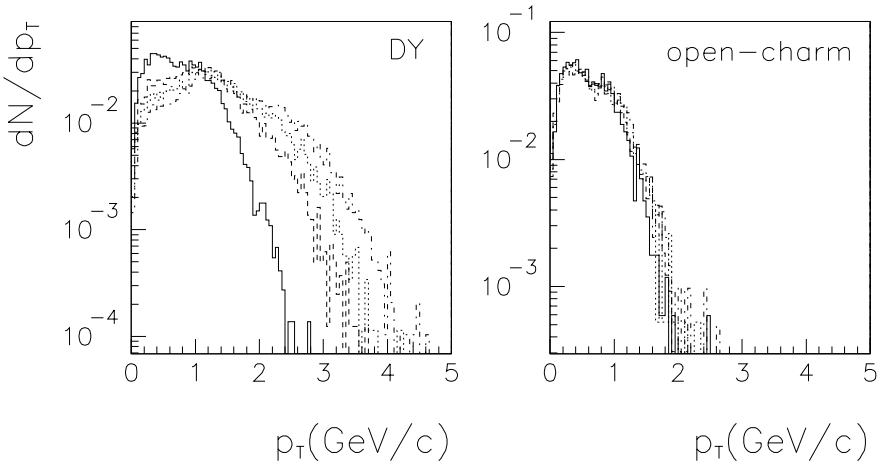

Figure 6.13: *PYTHIA generated DY (left) and $D\overline{D}$ (right) p_T differential distributions for σ_{k_T}=0.6,0.8,0.9,1.0 GeV/c. The larger the σ_{k_T} value, the more the DY distribution spreads towards higher p_T. The $D\overline{D}$ distribution does not show any strong k_T dependence.*

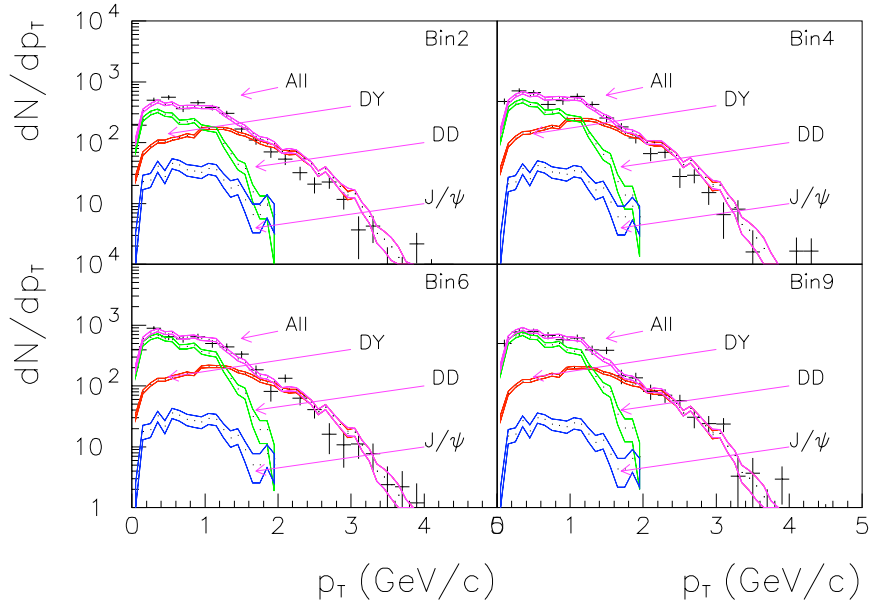

Figure 6.14: *PbPb p_T differential distributions for $1.5 < M < 2.5$ GeV/c^2 compared with the PYTHIA predictions for $\sigma_{k_T} = 0.9$ GeV/c. From top-left to bottom-right, 4 E_T bins corresponding to increasing centrality are shown.*

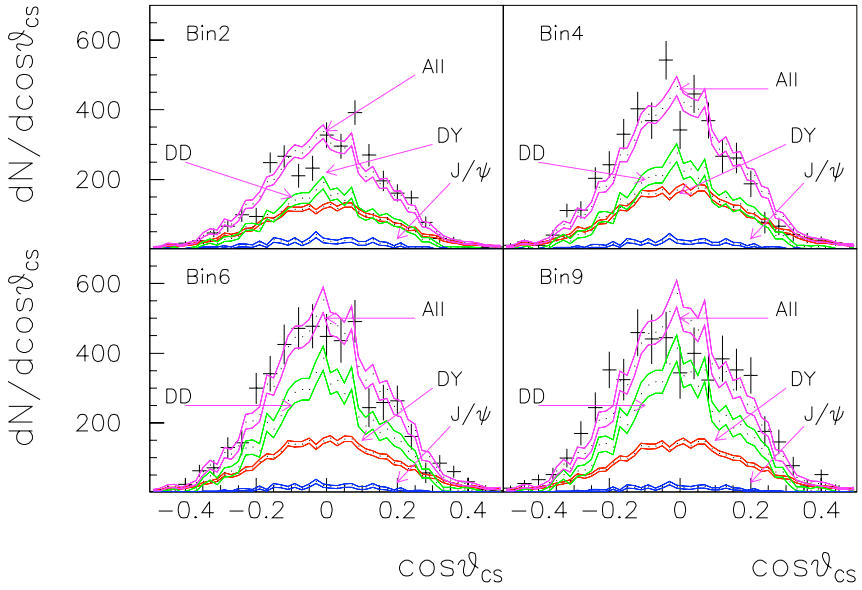

Figure 6.15: *PbPb cosθ differential distributions for $1.5 < M < 2.5$ GeV/c^2 compared with the PYTHIA predictions for $\sigma_{k_T} = 0.9$ GeV/c. From top-left to bottom-right, 4 E_T bins corresponding to increasing centrality are shown.*

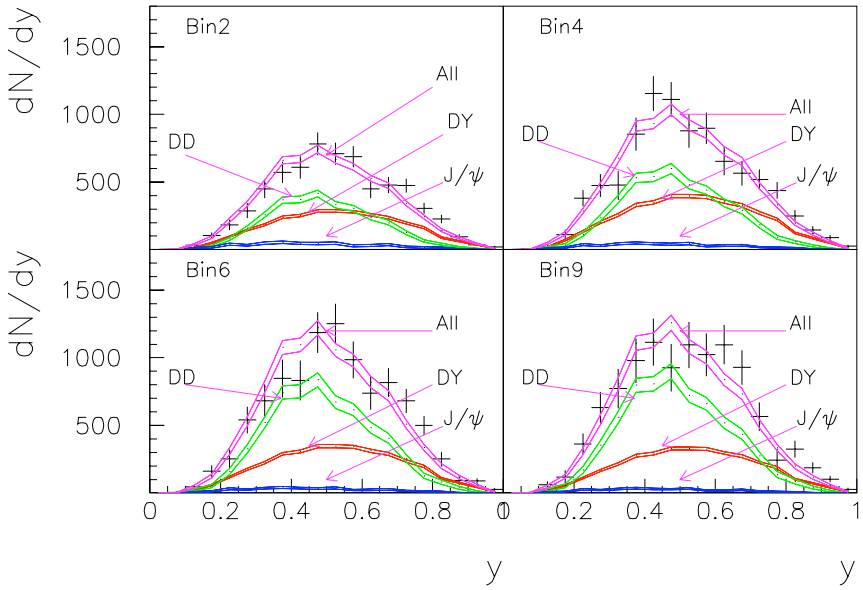

Figure 6.16: *PbPb rapidity differential distributions for* $1.5 < M < 2.5$ GeV/c^2 *compared with the PYTHIA predictions for* $\sigma_{k_T} = 0.9$ *GeV/c. From top-left to bottom-right, 4* E_T *bins corresponding to increasing centrality are shown.*

Thereafter, the pA analysis presented in the following has been performed using the Monte-Carlo fitting functions obtained with σ_{k_T}=0.9 GeV/c.

	PREVIOUS ANALYSIS		PYTHIA $\sigma_{k_T} = 0.9$ GeV/c	
E_T bin	$\frac{D\overline{D}}{DY}$	χ^2	$\frac{D\overline{D}}{DY}$	χ^2
1	2.46 ± 0.32	1.9	2.67 ± 0.30	2.9
2	2.01 ± 0.23	1.7	2.15 ± 0.25	2.9
3	2.01 ± 0.22	1.6	2.05 ± 0.25	1.8
4	2.10 ± 0.22	1.7	2.12 ± 0.24	1.8
5	3.15 ± 0.29	1.5	3.22 ± 0.31	1.5
6	3.27 ± 0.31	0.9	3.36 ± 0.30	1.0
7	2.66 ± 0.27	1.7	2.64 ± 0.28	1.8
8	3.46 ± 0.36	1.8	3.45 ± 0.38	1.8
9	3.68 ± 0.37	0.8	3.71 ± 0.39	1.0

Table 6.4: *$D\overline{D}/DY$ values and χ^2's obtained from the fit of the 9 PbPb mass spectra corresponding to the 9 PbPb E_T bins. The previous values are compared with the ones obtained using PYTHIA to generate all the Monte-Carlo shapes, with a Gaussian k_T distribution and σ_{k_T} = 0.9 GeV/c.*

6.8 Fit of the pA mass spectra

Since no IMR dimuon excess has been measured in pA collisions, the dimuon yield measured in pA interactions can be taken as a reference when studying nucleus-nucleus systems. The analysis of the pA data is therefore particularly important when the absolute value of the IMR excess observed in nucleus-nucleus collisions has to be determined.

Both the DY and the $D\overline{D}$ cross sections have been verified to linearly scale with A in pA interactions (see chapter 1). This implies that, when isospin corrections have been applied, a constant $D\overline{D}/DY$ ratio is expected in p-A collisions for any value of the target atomic number. Therefore, since the four pA sets of data have been collected with identical set-ups, except for the target material and length, a common isospin corrected $D\overline{D}/DY$ can be imposed and a simultaneous fit can be performed on the four mass spectra. Tab.6.5 lists the isospin correction factors I_{DY} (see chapter 1) calculated for the MRS A set of parton distribution functions and for M>1.5 GeV/c^2, -0.5< $cos\theta$ <0.5 and -0.52< y <0.48.
The simultaneous fit can be performed either on the whole mass spectra, including the high mass resonances contributions, or excluding the high mass resonances from the fit in order to reduce the number of free parameters. In the following both approaches are discussed and the results are subsequently compared.

System	Energy (GeV)	A	Z	I_{DY}
pAl	450	27	13	0.982
pCu	450	63	29	0.981
pAg	450	108	47	0.980
pW	450	184	74	0.978

Table 6.5: *Isospin correction factors for the DY, calculated for 450 GeV/c pA(A=Al, Cu, Ag, W) interactions with the MRS A set of PDF and for M>1.5 GeV/c^2, -0.5< cosθ <0.5 and -0.52< y <0.48.*

6.8.1 Fit of the whole mass spectra

When fitting the mass spectra in the mass range 1.5 (1.3) $< M <$ 8.0 GeV/c^2, 21 parameters are left free, i.e, the 4 DY, 4 J/ψ and 4 ψ' normalisation factors, the 4 J/ψ masses and the 4 J/ψ widths, and the common $D\overline{D}/DY$.

In fig.6.17 the result of the simultaneous fit of the 4 pA data is shown. In fig.6.18 the corresponding signal mass distributions are compared with the curves resulting from the fit of the opposite-sign mass spectra, after background subtraction. In fig.6.19 the signal distributions in the IMR can be better seen. We find

$$\frac{D\overline{D}}{DY} = 4.09 \pm 0.06 \ (\chi^2{=}3.4) \tag{6.9}$$

6.8.2 Fit of a restricted mass range

When fitting the restricted range of mass between $1.3 < M < 2.0$ and $4.5 < M <$ 8.0 GeV/c^2, only 5 parameters are left free, i.e., the 4 DY normalisation factors and the common $D\overline{D}/DY$.

In fig.6.20 the result of the simultaneous fit of the 4 pA data sets in the restricted mass region is shown. In fig.6.21 the signal mass distributions are compared with the fitting curves, background subtracted. In fig.6.22 the corresponding IMR signal mass distributions are shown. We find

$$\frac{D\overline{D}}{DY} = 4.36 \pm 0.09 \ (\chi^2{=}1.6) \tag{6.10}$$

The quality of the fit has improved with respect with the previous approach, and the $D\overline{D}/DY$ values differ by $\simeq$6% only.

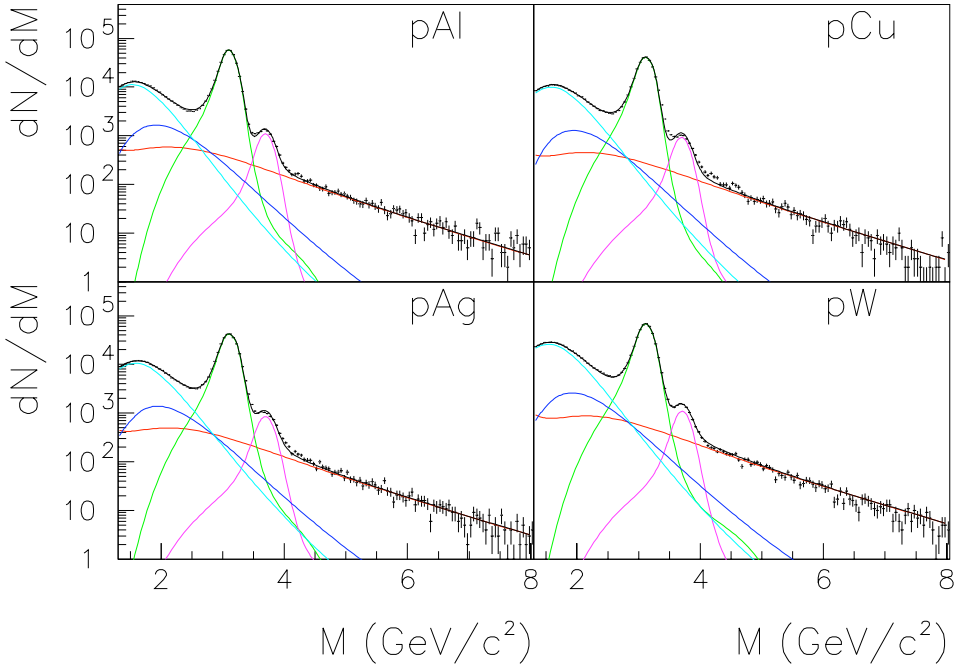

Figure 6.17: *Simultaneous fit of the 4 pA data sets in the whole mass range, 1.3< M <8.0 GeV/c^2. The nominal Monte-Carlo R_{BCK} values have been imposed.*

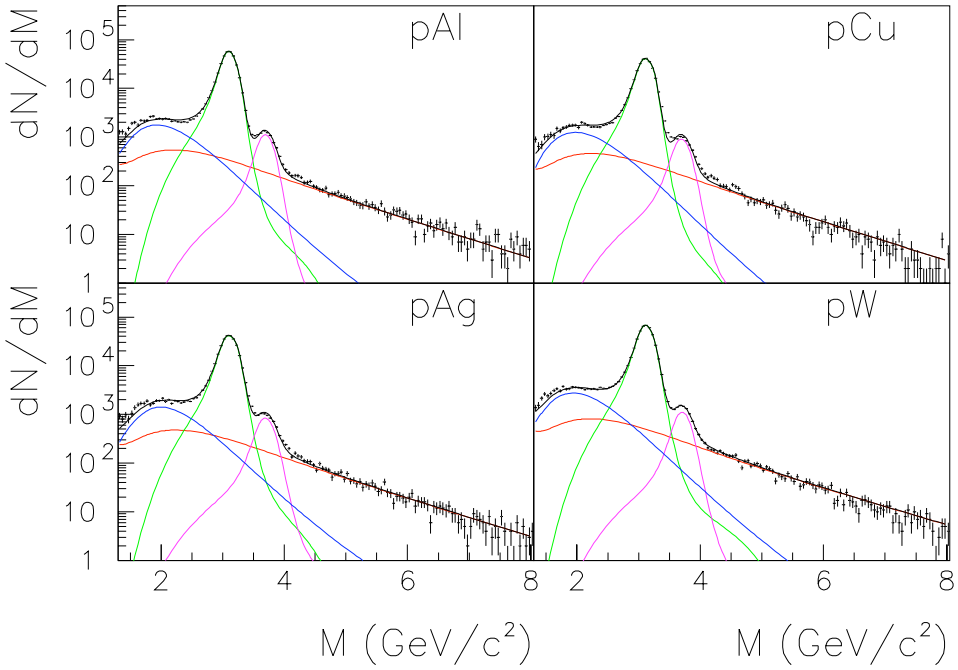

Figure 6.18: *Signal mass distributions compared with the curves resulting from the fit of the opposite-sign distributions shown in the previous figure, after background subtraction.*

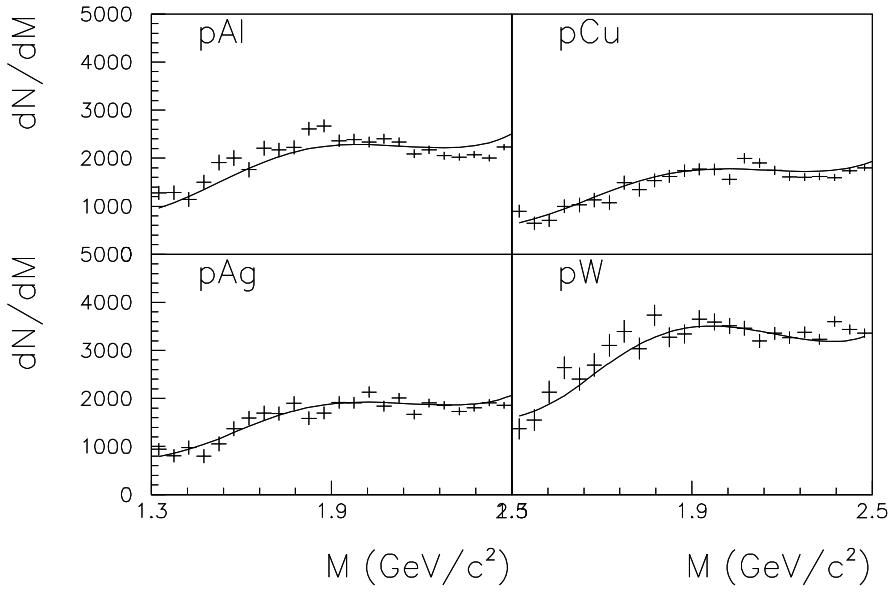

Figure 6.19: *Signal mass distributions compared with the curves resulting from the fit of the opposite-sign distributions shown in the previous figure, after background subtraction. The IMR is shown.*

6.8.3 pA : results and discussion

We have seen that the $D\overline{D}/DY$ ratios obtained for the 4 pA data with the two above different approaches differ by only $\simeq$6%. The larger χ^2 found in the first approach is probably due to the inclusion of the high mass resonances region, where, in order to have a small number of free parameters, the fit has not been optimised. For instance, if the widths of the 4 ψ' were freed, the quality of the fits at the ψ' level would improve (and so the overall χ^2), but the quality of the fit in the IMR would be the same. We then calculate the pA $D\overline{D}/DY$ reference value as the weighted average of the values given in eq.6.9 and eq.6.10. The incertitude associated with the average value is given by the maximum distance between the average value itself and the ones in eq.6.9 and eq.6.10, when the statistical error on the latter is taken into account. We therefore have

$$\frac{D\overline{D}}{DY}\,|_{pA}^{450GeV/c} \;=\; 4.20 \pm 0.25 \tag{6.11}$$

6.8.4 The pA p_T, cosθ and y distributions

In sec.6.7 the p_T, $cos\theta$ and y differential distributions of the SU and PbPb systems in the IMR region have been studied and it has been found that they can be well reproduced if PYTHIA is used to generate the Monte-Carlo shapes for all the contributing processes with σ_{k_T}=0.9 GeV/c. In the previous part of the present section,

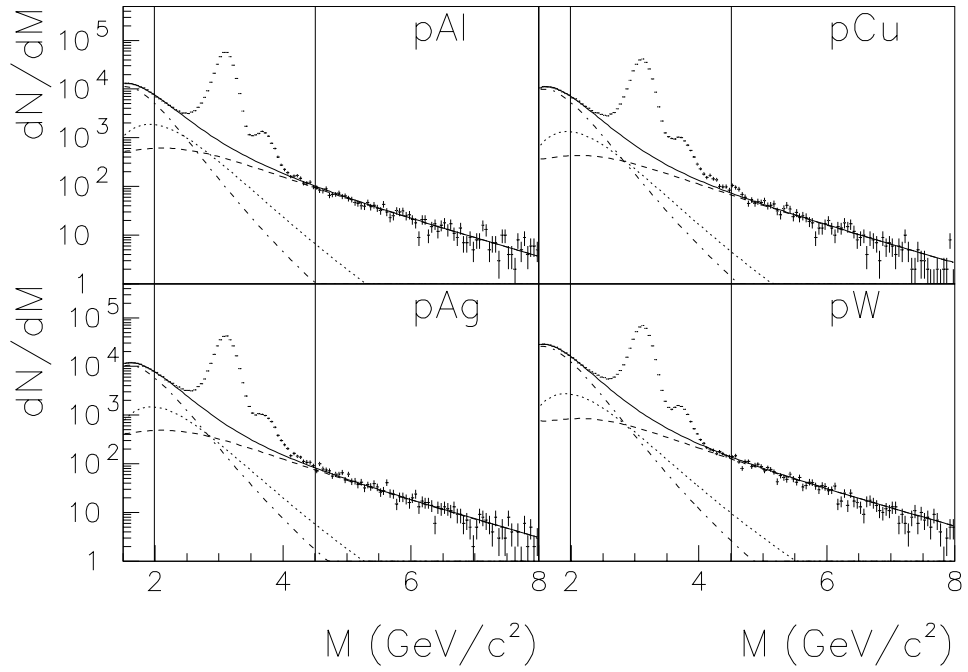

Figure 6.20: *Simultaneous fit of the 4 pA opposite-sign mass distributions in the mass range 1.3< M <2.0 GeV/c^2 and 4.5<M<8.0 GeV/c^2.*

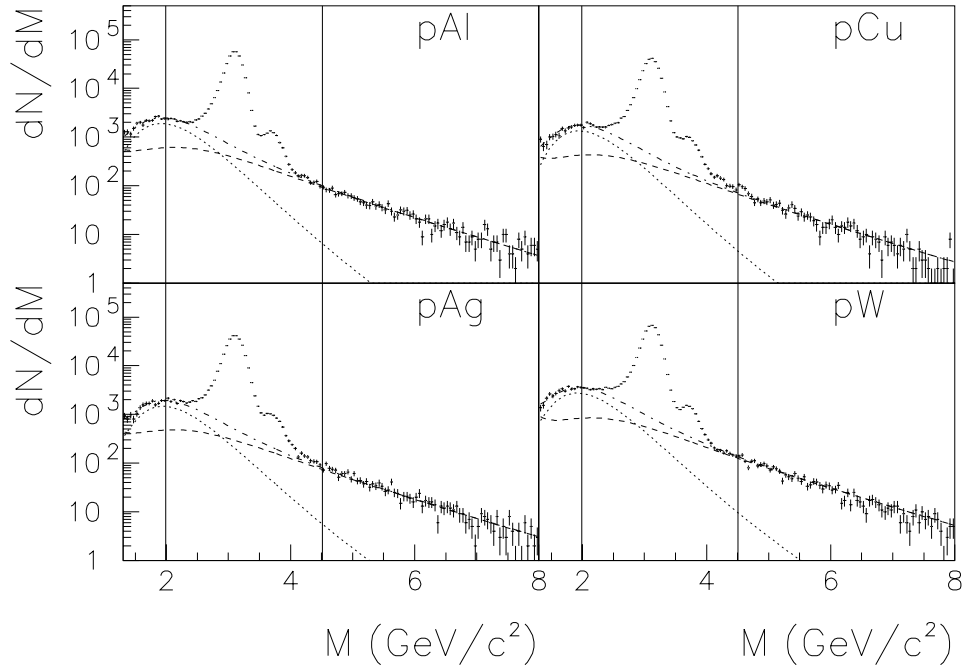

Figure 6.21: *Signal mass distributions compared with the curves resulting from the fit of the opposite-sign distributions shown in the previous figure, after background subtraction.*

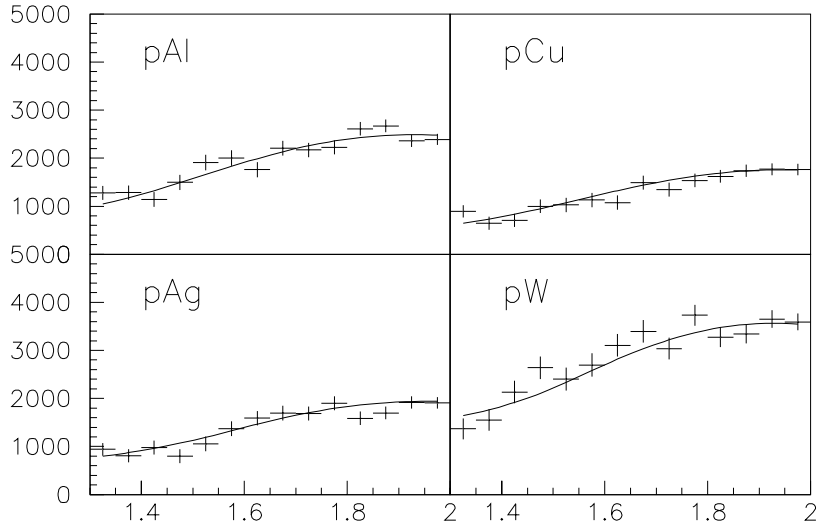

Figure 6.22: *Signal mass distributions compared with the curves resulting from the fit of the opposite-sign distributions shown in the previous figure, after background subtraction. The IMR is shown.*

a very good description of the pA mass distributions has also been achieved using the PYTHIA generated shapes with σ_{k_T}=0.9 GeV/c. In the following it is shown that the same nice agreement is found when the p_T, $cos\theta$ and y differential distributions for the pA systems are compared in the IMR region to the PYTHIA generated shapes normalised as in eq.6.6.

In fig.6.23 the pAl Monte-Carlo p_T, $cos\theta$ and y differential distributions are compared with the corresponding experimental distributions in the IMR; the Monte-Carlo distributions have been normalised as from eq.6.6 and have been generated with σ_{k_T}=0.9 GeV/c. The simulated curves well reproduce the experimental distributions with the exception of the large p_T region in the p_T spectrum. However, the PYTHIA event generator is based on leading order QCD calculations; if higher order corrections were taken into account a better data reproduction could be probably achieved. This different behaviour at large p_T was not visible on the PbPb and SU p_T differential distributions because of the lack of statistics for p_T >4 GeV/c.

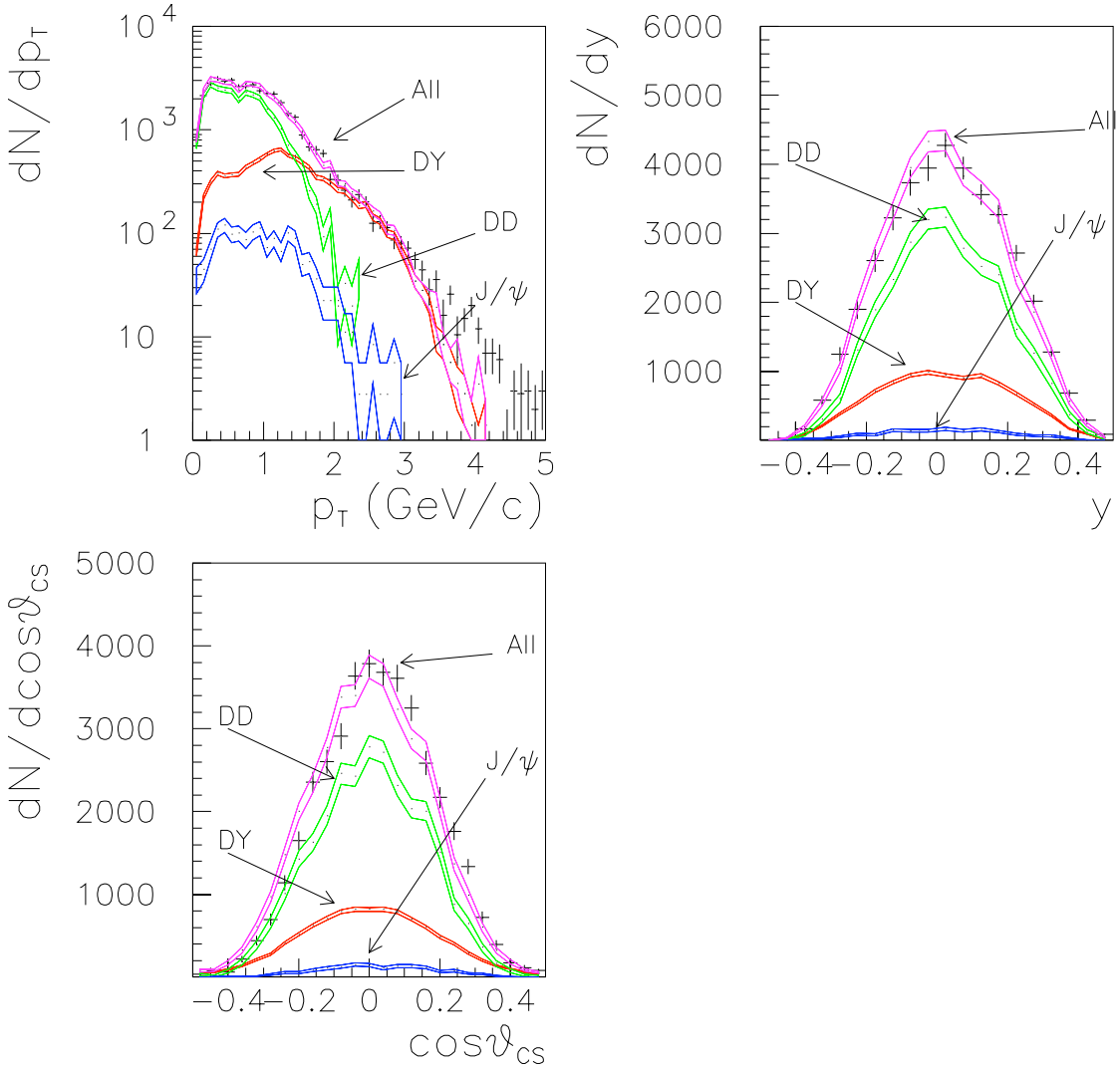

Figure 6.23: *pAl p_T, cosθ and rapidity differential distributions compared with the normalised PYTHIA generated distributions for σ_{k_T} = 0.9 GeV/c and* $1.5 < M < 2.5$ *GeV/c^2.*

6.9 Comparison with other methods

In the analysis of the SU and PbPb IMR presented at QM'96[2], the combinatorial background contribution to the IMR was fixed assuming that the multiplicity of secondaries in the peripheral S-U and Pb-Pb collisions is so large that charge correlation effects can be neglected. In this hypothesis the R_{BCK} factors were all set to 1.0. Even if we know that this approach is not correct, it can be instructive to perform the fit of the SU and PbPb mass spectra in the same hypothesis. In tab.6.6 the $D\overline{D}/DY$ ratios obtained when R_{BCK} =1.0 for all the PbPb E_T bins (1), is compared with the previously obtained values (0). The $D\overline{D}/DY$ values obtained in the two different approaches differ by $\simeq$ 20% in the more peripheral bins where the difference in the used R_{BCK} is $\leq$ 3%. The $D\overline{D}$ contribution in the more central collisions is enhanced by a factor of $\simeq$ 1.4 with respect with the one corresponding to the second E_T bin, a factor $\simeq$ 20% lower than the previously found enhancement. As expected, the use of our Monte-Carlo R_{BCK} factors leads to a more dramatic increase of the $D\overline{D}/DY$ values as a function of centrality, as shown in fig.6.24.

In tab.6.7 the same is listed for the SU system. The discrepancy between the two sets of values is $\simeq$10% in the more peripheral bins; the $D\overline{D}/DY$ enhancement amounts to 1.2, a factor $\simeq$ 8% lower than the previously measured enhancement. The larger sensitivity of the PbPb $D\overline{D}/DY$ values with respect to the two different sets of R_{BCK} is due to the larger contribution of the combinatorial background to the PbPb IMR mass spectra.

It is therefore mandatory to use the appropriate R_{BCK} values when dealing with systems where the combinatorial background strongly contributes to the IMR.

E_T bin	$\frac{D\overline{D}}{DY}\|_0$	$\frac{D\overline{D}}{DY}\|_1$
1	2.46 ± 0.32	3.20 ± 0.37
2	2.01 ± 0.23	2.52 ± 0.26
3	2.01 ± 0.22	2.41 ± 0.24
4	2.10 ± 0.22	2.40 ± 0.23
5	3.15 ± 0.29	3.35 ± 0.31
6	3.27 ± 0.31	3.35 ± 0.32
7	2.66 ± 0.27	2.74 ± 0.27
8	3.46 ± 0.36	3.46 ± 0.36
9	3.68 ± 0.37	3.68 ± 0.37

Table 6.6: *$D\overline{D}/DY$ obtained in the fit of the 9 PbPb mass spectra in the mass range 1.5< M <7.0 GeV/c^2, when the Monte-Carlo R_{BCK} values are used (0) and when R_{BCK}=1.0 for all the E_T bins (1).*

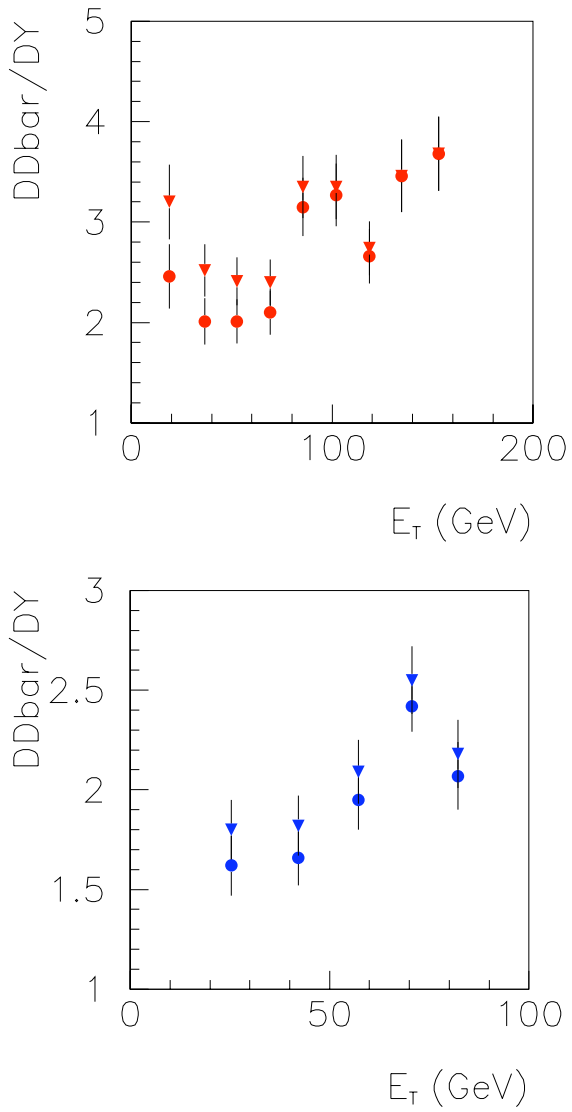

Figure 6.24: *The $D\overline{D}/DY$ ratios extracted from the analysis of the PbPb (top) and SU (bottom) systems is plotted vs. the transverse energy E_T. The values obtained when the Monte-Carlo R_{BCK} factors have been used (circles) are compared to the ones extracted when imposing R_{BCK}=1.0 for all E_T bins (triangles). No isospin correction has been applied.*

E_T bin	$\frac{D\overline{D}}{DY}\|_0$	$\frac{D\overline{D}}{DY}\|_1$
1	1.62 ± 0.15	1.80 ± 0.15
2	1.66 ± 0.14	1.82 ± 0.15
3	1.95 ± 0.15	2.09 ± 0.16
4	2.42 ± 0.13	2.55 ± 0.17
5	2.07 ± 0.17	2.18 ± 0.17

Table 6.7: *$D\overline{D}/DY$ obtained in the fits of the SU opposite-sign mass spectra when the Monte-Carlo R_{BCK} are used (0) and when R_{BCK}=1.000 for all the E_T bins (1).*

R_{BCK} free : PbPb and SU

It can be interesting to investigate if the shape of the mass differential distribution alone is able to determine the relative contributions of the different participating processes. We therefore fit the PbPb and SU mass spectra leaving the R_{BCK} as a free parameter in the fit. In fig.6.25 the different behaviour of the Monte-Carlo and free R_{BCK}'s is shown vs. the transverse energy E_T. The SU R_{BCK} free values are lower than the Monte-Carlo calculated ones, and vice-versa for the PbPb system. This is exactly the contrary of what we would expect, since charge correlation effects should decrease with increasing multiplicity, and the multiplicity of produced secondaries is linearly proportional to the transverse energy E_T. Furthermore, the SU free R_{BCK} factors are smaller than unity, and therefore lower than the value we expect when no charge correlation effect exists. The behaviour of the free PbPb R_{BCK} values well agree with the behaviour of our Monte-Carlo values, and the discrepancy between the two sets of values is not as large as for the SU system. On the other hand, the resulting $D\overline{D}/DY$ values differ by $\simeq 30 \div 50\%$ from the ones previously listed. As usual, even a small difference in the R_{BCK} value leads to large discrepancy on the extracted $D\overline{D}/DY$'s. This is again due to the larger contribution of the combinatorial background to the PbPb IMR.

We therefore conclude that the shape of the mass differential distribution alone can not give a reliable description of the IMR, and the Monte-Carlo R_{BCK} should be used to fix the combinatorial background contribution.

R_{BCK} free : pA

The $D\overline{D}/DY$ value quoted in eq.6.11 is affected by a very small statistical incertitude, much smaller than the incertitude associated with the SU and PbPb $D\overline{D}/DY$ ratios. The corresponding shape of the mass spectra in the IMR is better defined and here again we can investigate if the mass distribution alone can determine the relative importance of the $D\overline{D}$ and combinatorial background contributions. Since in the fit of the restricted mass range the number of free parameters is small, the

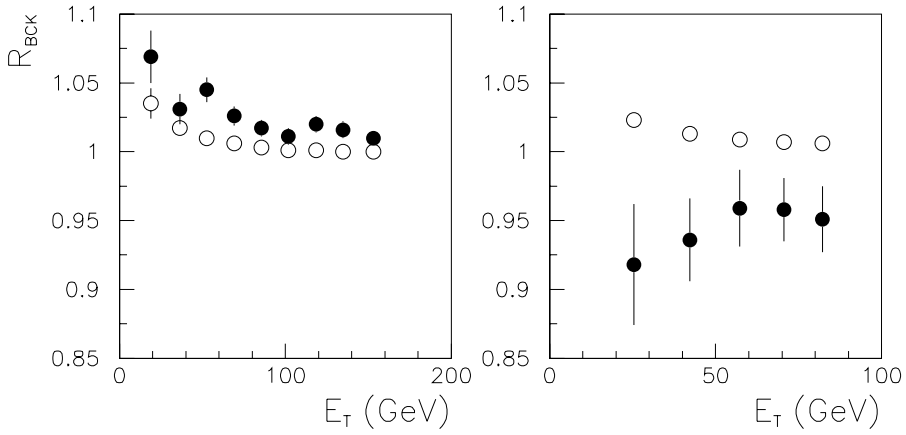

Figure 6.25: *R_{BCK} behaviour vs. E_T for the PbPb (left) and SU (right) systems: R_{BCK} free (filled circles) and Monte-Carlo R_{BCK} values (empty circles).*

total number of free parameters is still reasonable if the 4 R_{bck} factors are also left free. In fig.6.26 the result of the fit is shown on the signal mass spectra and in the IMR only. We find

$$\frac{D\overline{D}}{DY} = 4.22 \pm 0.13 \ (\chi^2{=}1.5) \tag{6.12}$$

which is in very good agreement with all the previous values. In tab.6.8 the found R_{bck} values are compared with the Monte-Carlo ones and the two sets of values very nicely agree. This impressive agreement is due to the limited number of degree of freedom allowed in the simultaneous fit of the pA mass spectra, where a common $D\overline{D}/DY$ has been imposed. If the pA data had been analysed one by one, leaving the R_{BCK} value as a free parameter in the fit, the R_{BCK} values would have been larger by a factor ≤ 10 %.

We have seen that the analysis of the pA data is stable against changes in the method used to perform the fit of the mass spectra, and that the shape of the mass spectra alone is able to determine the normalisations of the different processes contributing in the IMR. Thereafter, the discrepancy between the value in eq.6.12 and the value quoted in eq.6.10, which have both been obtained when fitting the restricted mass range, can be considered as an evaluation of the systematic error due to the method used for the combinatorial background subtraction. This discrepancy being very small, $\simeq 3\%$, it will be neglected in what follows.

6.10 Conclusion

In the present chapter we have shown that the SU and PbPb mass differential distributions can be well described as a superposition of dimuons from the DY process

$R_{BCK}\mid_0$	$R_{BCK}\mid_f$
1.06 ± 0.02	1.069 ± 0.005
1.06 ± 0.02	1.051 ± 0.005
1.06 ± 0.01	1.053 ± 0.005
1.05 ± 0.01	1.058 ± 0.003

Table 6.8: *The Monte-Carlo nominal R_{BCK} values (0) are compared with the ones obtained when simultaneously fitting the 4 pA systems in the mass range 1.3< M <2.0 and 4.5< M <8.0 GeV/c^2 whilst leaving the R_{BCK} factors as free parameters in the fit (f).*

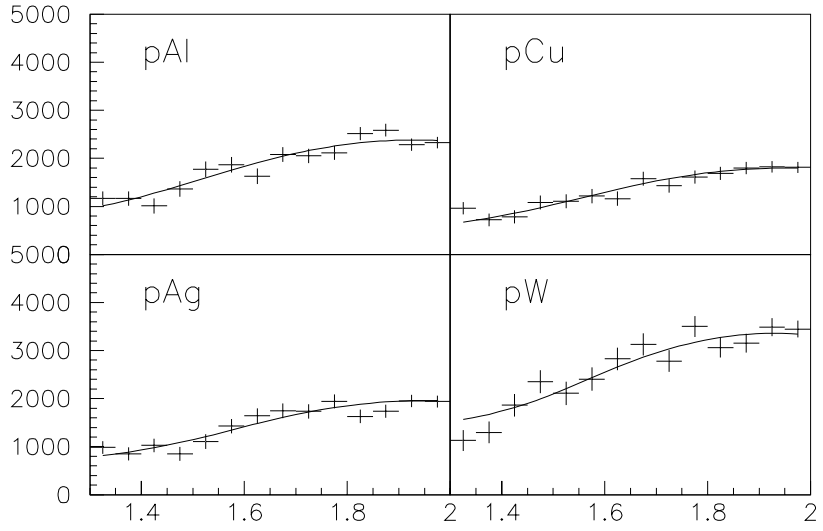

Figure 6.26: *Fit of the pA data in the restricted mass range 1.3 < M < 2.0 and 4.5< M <8.0 GeV/c^2. The PYTHIA generated Monte-Carlo shapes, with σ_{k_T} = 0.9 GeV/c, have been used. The Monte-Carlo R_{BCK} have been left as free parameters in the fit. Only the IMR is shown.*

and from the decay of charmed hadron pairs, after background subtraction. The latter has been performed using the R_{BCK} factors calculated in chapter 5. The systematic error associated with the method adopted for the combinatorial background subtraction has been found to be very small, $\simeq$3%, and it is therefore always neglected in what follows.

We find that the $D\overline{D}/DY$ ratios extracted from the fit of the PbPb and SU mass spectra increase with the system size and the collision centrality. In order to support the hypothesis that the found excess is due to an enhanced open charm production,

the p_T, cosθ and y differential distributions have been compared with the PYTHIA generated shapes, normalised as from the fit of the mass spectra with the inclusion of the enhanced charm component. With no additional hypothesis, a nice description of all the studied distributions has been obtained.

The pA systems have then been studied in order to determine the $D\overline{D}/DY$ pA reference value corresponding to no excess in the IMR. Again, the p_T, cosθ and y differential distributions have been compared with the PYTHIA shapes as above explained, obtaining a very good description of all the studied experimental distributions.

In the last section, the results of the present work have been compared with the results we would have got if the previous NA38/NA50 approach had been used as far as the R_{BCK} factor is concerned. If we imposed R_{BCK}=1.0 for all E_T bins, the steep increase with centrality of the $D\overline{D}/DY$ obtained for the PbPb system would have been smeared out, as shown in fig.6.24.

Finally, the option of leaving the R_{BCK} as a free parameter in the fit is shown to generally lead to a wrong estimation of the excess; only when the number of free parameters in the fit is small and the imposed constraints are extremely strong, as when studying the four pA systems in a simultaneous way, the shape of the mass differential distribution alone can be able to correctly determine the normalisation parameters of the contributing processes.

Bibliography

[1] Amir Bohrani, PhD thesis, April 1996, Uni. Paris 6.

[2] E.Scomparin, for the NA50 Collaboration, at the Quark Matter '96 Conference, Heidelberg, Germany (1996)

[3] PDFLIB 7.09, Users's Manual, CERN/PPE (1997)

Chapter 7

Results and discussion

In the previous chapter, the pA, SU and PbPb dimuon mass spectra in the IMR have been described as a superposition of DY dimuons and dimuons from the semi-leptonic decay of charmed hadrons (also indicated as $D\overline{D}$), after background subtraction. The DY and $D\overline{D}$ contributions have been extracted by means of a fit of the mass spectra, obtaining the 'measured' $D\overline{D}/DY$ ratio. As a result, an enhancement in the open charm yield has been found in nucleus-nucleus collisions. The found enhancement increases with the collision centrality and the system size.

In this chapter, the absolute value of the found enhancement with respect to QCD expectations is calculated and the excess measured in SU and PbPb collisions is compared, after normalisation to the pA result. This is accomplished computing the open charm yield expected in p-A, S-U and Pb-Pb collisions at the relevant energies, on the basis of the FNAL and CERN direct measurement of charm production in pion and proton induced collisions. For each system, the expected $D\overline{D}/DY$ is then calculated.

The ratio of the measured and expected $D\overline{D}/DY$'s, which measures the size of the open charm enhancement found in the fit of the mass spectra, is then derived and plotted against the number of participants in the collision.

The final results are then discussed in the light of the existing theoretical interpretations and qualitatively compared with the results of the HELIOS/3 experiment and with the previous NA38/NA50 results.

7.1 The expected open charm cross section

In fig.7.1, from ref.[1], the cross sections for forward ($x_F > 0$) D^0,$\overline{D^0}$ and D^+,D^- production, as measured in proton and pion induced reactions at CERN and FNAL, are plotted as a function of the centre of mass energy. The results obtained on nuclear targets have been divided by the target atomic mass number A. The error bars in fig.7.1 have been obtained in ref.[1] adding the statistical and systematic errors in quadrature, including the incertitude on the branching ratio.

It is well known that leading order (LO) QCD calculations, on which the event generator PYTHIA is based, do not reproduce the absolute value of the charm cross section; the same is true when the measured DY cross section is compared with leading order pQCD calculations. On the other hand, as shown in chapter 1 and in the same ref.[1], the differential distributions of charmed mesons are well reproduced by PYTHIA. Besides, this is the reason why the PYTHIA event generator has been used to generate the open charm differential distributions as explained in chapter 4. In fig.7.1, the dotted line represents PYTHIA predictions scaled up by an ad-hoc factor K_{PYTHIA}, which corrects for the above mentioned discrepancy between LO pQCD predictions and absolute cross section measurements. Since PYTHIA does not correctly reproduce the ratio D^+/D^0, two different K_{PYTHIA} factor have been used in fig.7.1 for neutral (K_{PYTHIA}=3.5) and charged (K_{PYTHIA}=7.) charmed mesons. As shown in fig.7.1, PYTHIA well reproduces the overall centre of mass energy dependence of the open charm cross section. Since the same K_{PYTHIA} has been used for all the considered cms energies, we can conclude that the K_{PYTHIA} factor does not depend on the cms energy of the collision.

Thereafter, PYTHIA has been used to compute the expected cross sections for open charm dimuon production in 450 GeV/c, 158 A GeV/c and 200 A GeV/c p-p collisions. In the analysis presented in the previous chapter, two different values of the width of the intrinsic transverse momentum of the colliding partons have been used, i.e., σ_{k_T}=0.8 GeV/c for SU and PbPb and σ_{k_T}=0.9 GeV/c for pA (see chapter 4 and 6). In the following, the same values have been adopted. For the sake of comparison, the open charm cross section for 450 GeV/c p-p collisions has also been computed with σ_{k_T}=0.8 GeV/c.

The cross section for open charm production can be directly extrapolated from the experimental results plotted in fig.7.1, without referring to an event generator like PYTHIA. On the other hand, in order to calculate the dimuon production from charmed mesons (and baryons) in the phase space covered by NA50, the kinematics of the charmed hadron semi-leptonic decay into muons has to be taken into account. Moreover, branching ratio weighting has to be introduced and kinematic cuts applied. We then proceed as follows :

- Compute the *dimuon mass differential spectra for charmed pair production* :

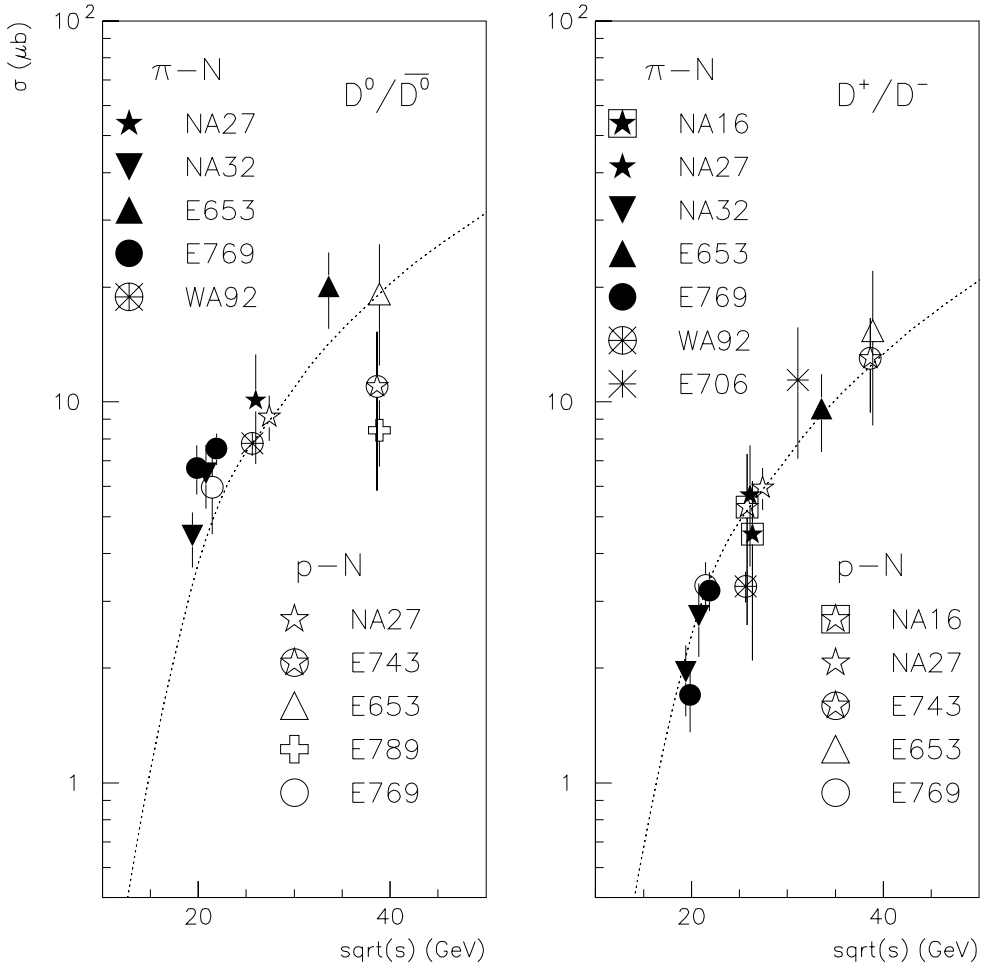

Figure 7.1: *Cross section for forward ($x_F > 0$) D^0, $\overline{D^0}$ (left) and D^+, D^- (right) production in p-p collisions measured in proton and pion induced reactions, as a function of the c.m.s. energy. The solid lines represent the pp PYTHIA calculation scaled up by a factor 3.5 (left panel) and 7.0 (right panel)[1].*

1. Use PYTHIA, with m_c=1.35 GeV/c^2, to compute the differential cross section $d\sigma^{pp}_{c\overline{c}}/dM$ for the process

$$pp \rightarrow c\overline{c} \rightarrow D\overline{D} \rightarrow \mu\overline{\mu} \tag{7.1}$$

at 450 GeV/c, 158 GeV/c and 200 GeV/c. As in chapter 4, in order to improve the statistics of generated events and reduce the needed CPU time, a 100% branching ratios has been assigned to the semi-leptonic channel $H_c \rightarrow \mu\nu_\mu X$ (where H_c is a generic charmed hadron), and 0% to all the other decay channels. The appropriate B.R. weighting can be applied in a second time, as later explained.

2. Weight the differential spectra with the K_{PYTHIA} factors suggested in ref.[1], i.e., 3.5 for neutral D mesons and 7 for charged ones. The K_{PYTHIA} value adopted for baryons and strange mesons has a negligible influence on the final value of the cross section for open charm dimuon production, after branching ratio weighting. For baryons (mainly Λ_c) the value K_{PYTHIA}=7 has been used since the Λ_c and D^+ cross sections have been measured to be compatible[3, 4] and since D^+'s and Λ_c's are equally generated by PYTHIA when m_c=1.5 GeV/c^2. The same enhancement factor, K_{PYTHIA}=7, has also been used for strange D mesons and anti-baryons, which contribution is anyway negligible.

3. Within the above choice of the generation parameters, the *total cross section for charmed pair production* in p-p collisions at the related energy can be obtained integrating the mass differential cross section. These same cross section values are then imposed when repeating the calculations with m_c=1.5 GeV/c^2 and m_c=1.2 GeV/c^2.

- Calculate the *cross section for open charm dimuon production in the NA50 phase space* :

1. Weight the computed mass differential spectra for charmed pair production with the branching ratios for the charmed meson and baryon decays into muons. The adopted B.R. values have already been listed in chapter 4.

2. Impose the NA50 kinematic cuts on the y and $cos\theta_{CS}$ variables as listed in chapter 3 and consider only dimuon events with M>1.5 GeV/c^2. No explicit cut has been applied on x_F. Since the open charm pairs have been generated for -1< x_F <1, our absolute cross section has to be divided by a factor 2 when comparing with the CERN and FNAL results presented for x_F >0.

3. Integrate the weighted differential distribution in order to obtain the total cross section for open charm dimuon production in pp collisions in our experimental kinematic domain and for M> $1.5 GeV/c^2$.

4. Assume that the open charm cross section in nucleus-nucleus collisions can be linearly extrapolated from the cross section measured in p-p interactions at the same energy. Then, multiply the calculated p-p cross section by A×B, where A and B are the projectile and target atomic numbers, in order to obtain the cross section for open charm dimuon production in A-B collisions.

Fig.7.2 illustrates the above described different stages in the cross section calculation for 158 GeV/c Pb-Pb collisions and for m_c=1.35 GeV/c^2. In tab.7.1 the calculated cross sections are listed for the three studied systems at the related energies and for m_c=1.2, 1.35 and 1.5 GeV/c^2. The values obtained with the three different m_c differ after kinematic cuts are applied; this is due to the different shapes of the charm distributions generated with different m_c. The cross section for 450 GeV/c p-p interactions have been calculated for both σ_{k_T}=0.8 GeV/c and σ_{k_T}=0.9 GeV/c finding a discrepancy of $\simeq$ 0.3% *before* B.R. weighting and kinematic cuts and of $\simeq$ 8% between the final values. The latter is due to the modification of the p_T distribution of the generated and reconstructed open charm dimuons within our acceptance window, as shown in the previous chapter. The calculated cross section is affected by a statistical error due to the number of generated events ($\approx$ 0.2%) and by a systematic incertitude due to the square of the $\simeq$12% uncertainty on the B.R.'s.

7.1.1 The expected $D\overline{D}/DY$ ratio

From the calculated open charm dimuon cross section, the expected number N of open charm dimuons in the dimuon mass spectrum measured by NA38/NA50 can be calculated using the equation

$$N = \sigma^{AB}_{c\overline{c}\rightarrow\mu^+\mu^-} A_{D\overline{D}} \cdot L \tag{7.2}$$

where $\sigma^{AB}_{c\overline{c}\rightarrow\mu^+\mu^-}$ (μb) is the cross section for open charm dimuon production in AB collisions (A$\geq$1 and B>1) for M>1.5 GeV/c^2, and after kinematic cuts have been applied. L is the luminosity in μb^{-1} and $A_{D\overline{D}}$ is the acceptance for open charm dimuons in the mass range M> 1.5 GeV/c^2. The luminosity L has been evaluated using eq.7.2 for the J/ψ. The J/ψ cross section has been taken from ref.[5] for the PbPb system and from ref.[6] for the SU one, whilst for the 450 GeV/c pW system the results of a recent analysis[7] have been used, which are in very good agreement with the results of ref.[8]. The acceptances listed in chapter 4 have been used and the number of J/ψ have been deduced from the fits of the all E_T mass spectra. The errors on the computed luminosity mainly reflect the incertitude on the J/ψ cross

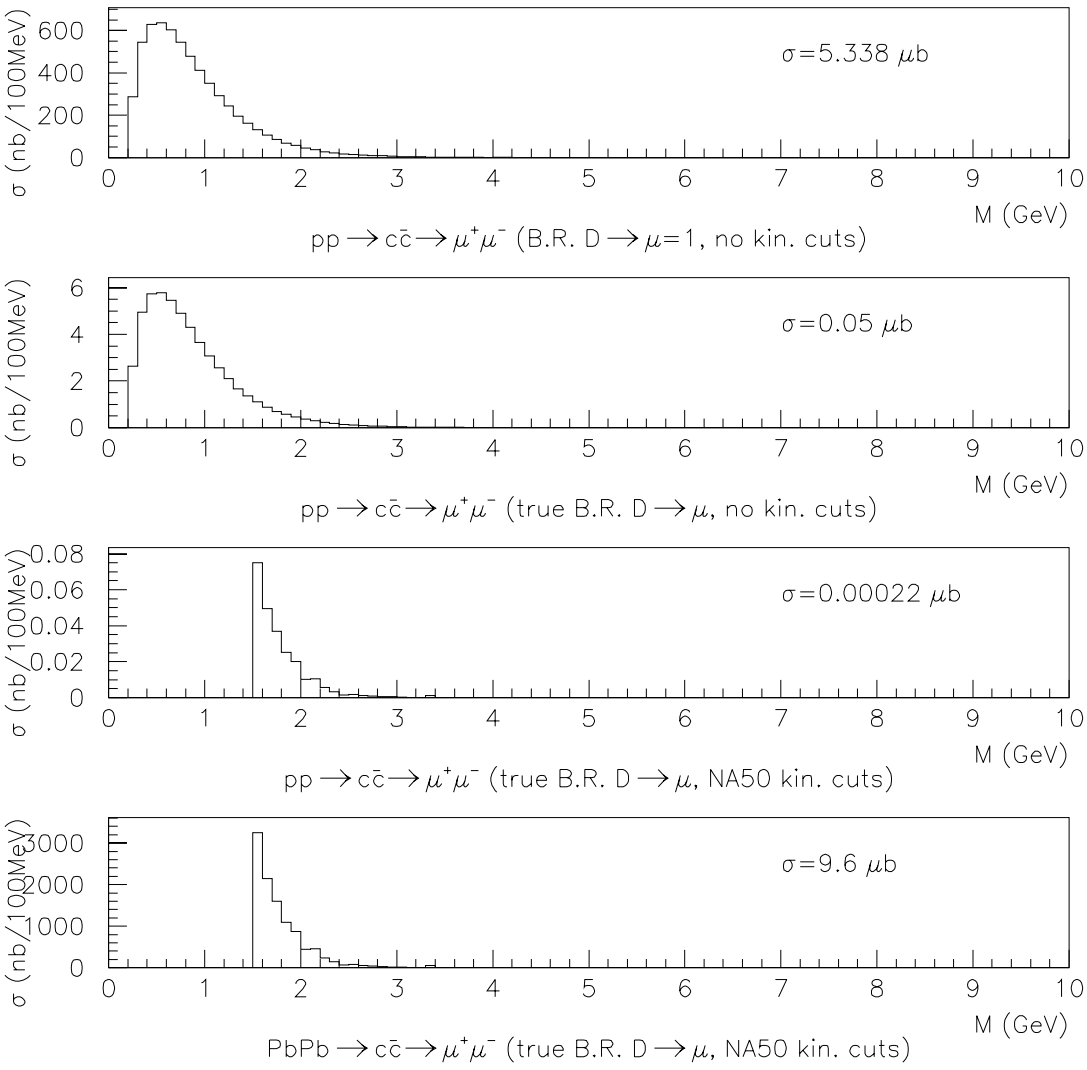

Figure 7.2: *Different stages in the calculation of the cross section for open charm dimuon production in Pb-Pb collisions at 158 A GeV/c and for* m_c*=1.35 GeV/*c^2.

Process	σ_{k_T} (GeV/c)	σ (μbarn) (m_c=1.2 GeV/c^2)	σ (μbarn) (m_c=1.35 GeV/c^2)	σ (μbarn) (m_c=1.5 GeV/c^2)
p-p 450 GeV/c	0.8	22.62 ± 0.04	22.62 ± 0.04	22.62 ± 0.04
p-p B.R.	0.8	0.19 ± 0.05	0.22 ± 0.05	0.20 ± 0.05
p-p B.R., k.c.	0.8	0.0009 ± 0.0002	0.0014 ± 0.0003	0.0015 ± 0.0004
p-W B.R., k.c.	0.8	0.17 ± 0.04	0.25 ± 0.06	0.28 ± 0.08
p-p 450 GeV/c	0.9	22.68 ± 0.03	22.68 ± 0.03	22.68 ± 0.03
p-p B.R.	0.9	0.23 ± 0.05	0.25 ± 0.06	0.23 ± 0.06
p-p B.R., k.c.	0.9	0.0012 ± 0.0003	0.0015 ± 0.0003	0.0019 ± 0.0004
p-W B.R., k.c.	0.9	0.21 ± 0.05	0.27 ± 0.06	0.35 ± 0.08
p-p 158 GeV/c	0.8	5.338 ± 0.008	5.338 ± 0.008	5.338 ± 0.008
p-p B.R.	0.8	0.04 ± 0.01	0.05 ± 0.01	0.05 ± 0.01
p-p B.R., k.c.	0.8	0.00017 ± 0.00004	0.00022 ± 0.00005	0.00026 ± 0.00006
Pb-Pb B.R., k.c.	0.8	7.4 ± 1.8	9.6 ± 2.3	11.3 ± 2.7
p-p 200 GeV/c	0.8	7.62 ± 0.01	7.62 ± 0.01	7.62 ± 0.01
p-p B.R.	0.8	0.06 ± 0.01	0.07 ± 0.01	0.07 ± 0.01
p-p B.R., k.c.	0.8	0.00025 ± 0.00006	0.00030 ± 0.00008	0.00039 ± 0.00009
S-U B.R., k.c.	0.8	1.9 ± 0.5	2.7 ± 0.6	3.0 ± 0.7

Table 7.1: *Cross sections calculated for the three studied systems at the related energies. The four different cross section values listed for each of the three systems correspond to : B.R.($D \rightarrow \mu$) = 1 and no.kin.cuts (p-p), true B.R.($D \rightarrow \mu$) and no.kin.cuts (p-p B.R.) true B.R.($D \rightarrow \mu$) and NA50 k.c (p-p B.R., k.c.) true B.R.($D \rightarrow \mu$) and NA50 k.c and nuclear effects (A-B B.R., k.c.).*

	PbPb	SU	pW
$\sigma^{meas.}_{J/\psi}$ (μb)	21.9 ± 1.6	7.77 ± 0.84	0.68 ± 0.048
$N^{meas.}_{J/\psi}$	151593 ± 704	113115 ± 578	438000 ± 1314
$A_{J/\psi}$	0.0744	0.164	0.144
L (μb^{-1})	93550 ± 6800	88770 ± 9600	$(4400 \pm 315.7) \cdot 10^3$

Table 7.2: *Quantities needed to calculate the luminosity for the PbPb, SU and pW systems : measured J/ψ cross section $\sigma^{meas.}_{J/\psi}$, number of J/ψ measured in the fit to the indicated systems and J/ψ acceptance. The calculated luminosities are also listed.*

section measurement. Tab.7.2 lists all the quantities needed for the calculation of the luminosities and the calculated luminosity values.

The cross section for hard processes is expected to scale with A in p-A and with $A \times B$ in A-B collisions. More generally, at fixed impact parameter b the cross section for the considered hard process in a nucleus-nucleus collision is expected to be proportional to the number of effective nucleon-nucleon collisions[13]. This has been verified for the DY in both p-A and A-B collisions[9, 5]. The DY process can therefore be used as a reference in order to evaluate any deviation of the open charm cross section from the expected behaviour, as already done in chapter 6 on the measured quantities. The expected $D\overline{D}/DY$ ratios can therefore be calculated and compared with the ones listed in chapter 6 for all the studied systems. For the PbPb and SU systems the number of DY dimuon pairs is taken from the result of the fit of the all E_T mass spectrum. For the pA systems, where the same number of DY pairs is used when calculating the measured and the expected $D\overline{D}/DY$, the number of DY dimuon pairs measured for any of the four pA systems can be taken as a reference; the number of expected open charm dimuons has to be calculated for the same pA system. In the following the pW system is used, as already done in the previous section.
Tab.7.3 lists the acceptances, the number of open-charm dimuons and DY dimuons and the resulting expected $D\overline{D}/DY$ ratios for the PbPb, SU and pW systems; the values in tab.7.3 have been obtained when the charm mass value m_c=1.5 GeV/c^2 is used to generate the open charm mass differential distribution and the fit is started at M=1.5 GeV/c^2. The error on the expected number of open charm dimuon comes from the error on the luminosity L.

	PbPb	SU	pW
$A_{D\overline{D}}$ $(M > 1.5GeV/c^2)$	0.0111	0.0482	0.0218
A_{DY} $(M > 1.5GeV/c^2)$	0.0281	0.0901	0.0578
$N_{D\overline{D}} \mid_{expect.}$	11771 ± 856	12720 ± 1375	33093 ± 2256
$N_{DY} \mid_{meas.}$ (all E_T)	45924 ± 1033	29437 ± 843	33070 ± 593
$\frac{\frac{N_{D\overline{D}}}{A_{D\overline{D}}}}{\frac{N_{DY}}{A_{DY}}} \mid_{expect.}$	0.648 ± 0.049	0.808 ± 0.090	2.63 ± 0.19

Table 7.3: *Quantities needed to compute the expected number of dimuons from open charm decay for the PbPb, SU and pW systems and for m_c=1.5 GeV/c^2. The listed number of dimuons from DY is necessary in order to calculate the ratio $D\overline{D}/DY$ which is also given.*

7.2 The pA reference

If the $D\overline{D}/DY$ ratio obtained in chapter 6 for the pA systems is compared with the one calculated in the previous sections, we find

$$E \mid_{pA} = \frac{D\overline{D}/DY \mid_{meas.}}{D\overline{D}/DY \mid_{expec.}} = \frac{4.20 \pm 0.25}{2.63 \pm 0.19} = 1.60 \pm 0.15 \tag{7.3}$$

It is necessary to check whether the above value of E corresponds to a cross section for charmed pair production compatible, at the related energy, with the cross sections extrapolated from the FNAL and CERN results plotted in fig.7.1. Therefore, from the cross sections for inclusive D production measured at CERN and FNAL, the $c\overline{c}$ cross section can be deduced as outlined in ref.[2], i.e.

- Divide the FNAL and CERN inclusive $\sigma(D/\overline{D}, x_f > 0)$ by a factor 2 to get the exclusive $D\overline{D}$ pair cross section.
- In order to account for the partial x_F coverage, multiply by a factor 2 in p induced collisions and 1.6 in π induced ones or, vice-versa, divide our experimental value by a factor 2.
- Account for the Λ_c and D_s contributions to the total cross section. From the experimentally measured Λ_c and D_s cross sections, the following seems to hold

$$\frac{\sigma(D_s)}{\sigma(D^+ + D^0)} \simeq 0.2 \tag{7.4}$$

$$\frac{\sigma(\Lambda_c)}{\sigma(D^+ + D^0)} \simeq 0.3 \tag{7.5}$$

Thereafter, the $c\overline{c}$ cross section can be obtained multiplying the exclusive $D\overline{D}$ cross section by a factor 1.5.

The open charm cross section measured in 450 GeV/c pp collisions, can be calculated using the value listed in tab.7.1 multiplied by the $E\mid_{pA}$ factor 1.60 ± 0.15 and divided by 2 in order to correct for the x_F coverage,

$$\sigma_{c\bar{c}}^{pp,450GeV/c} = (22.68 \pm 0.03) \cdot \frac{(1.60 \pm 0.15)}{2} = 18.14 \pm 1.70\ \mu b \tag{7.6}$$

If we also take into account the 24% uncertainty on the calculated cross section for open charm dimuon production due to the squared 12% uncertainty on the B.R., we find an overall 25% error on the value quoted in eq.7.6. In fig.7.3 the $c\overline{c}$ cross section extrapolated from our cross section for open charm dimuon production in pA collisions at 450 GeV/c, as quoted in eq.7.6, with the additional systematic error due to B.R., is compared with the previous FNAL and CERN experimental results. We find that our point does not significantly deviate from the $\sqrt{s}$ systematics, as shown by the dotted curve in fig.7.3. From the dotted curve in fig.7.1 we can see that the chosen PYTHIA enhancement factors, as suggested in ref.[1], give a curve which does not perfectly interpolate all experimental points. A larger enhancement factor for neutral mesons could perhaps give a better agreement, and a lower $E\mid_{pA}$.

Since the open charm cross section measured in 450 GeV/c pA collisions is in agreement with previous experimental results, the corresponding cross section for open charm dimuon production can be used as a reference when studying the PbPb and SU systems.

7.3 Results

In tab.7.4 the ratios of the measured and expected $D\overline{D}/DY$'s are listed after normalization to the 450 GeV/c pA result. The normalised ratio E is defined as

$$E = \frac{E\mid_{AB}}{E\mid_{pA}} = \frac{\frac{D\overline{D}}{DY}\mid^{AB}_{meas.}}{\frac{D\overline{D}}{DY}\mid^{AB}_{expec.}} \cdot \frac{\frac{D\overline{D}}{DY}\mid^{pA}_{expec.}}{\frac{D\overline{D}}{DY}\mid^{pA}_{meas.}} \tag{7.7}$$

The errors on E in tab.7.4 come from two sources :

- The statistical error on the $D\overline{D}/DY$ extracted from the fit of the mass differential distributions as performed in the previous chapter.
- The error on the calculation of the luminosity L ($7\div10\%$), which originates from the incertitude on the measured J/ψ cross section.

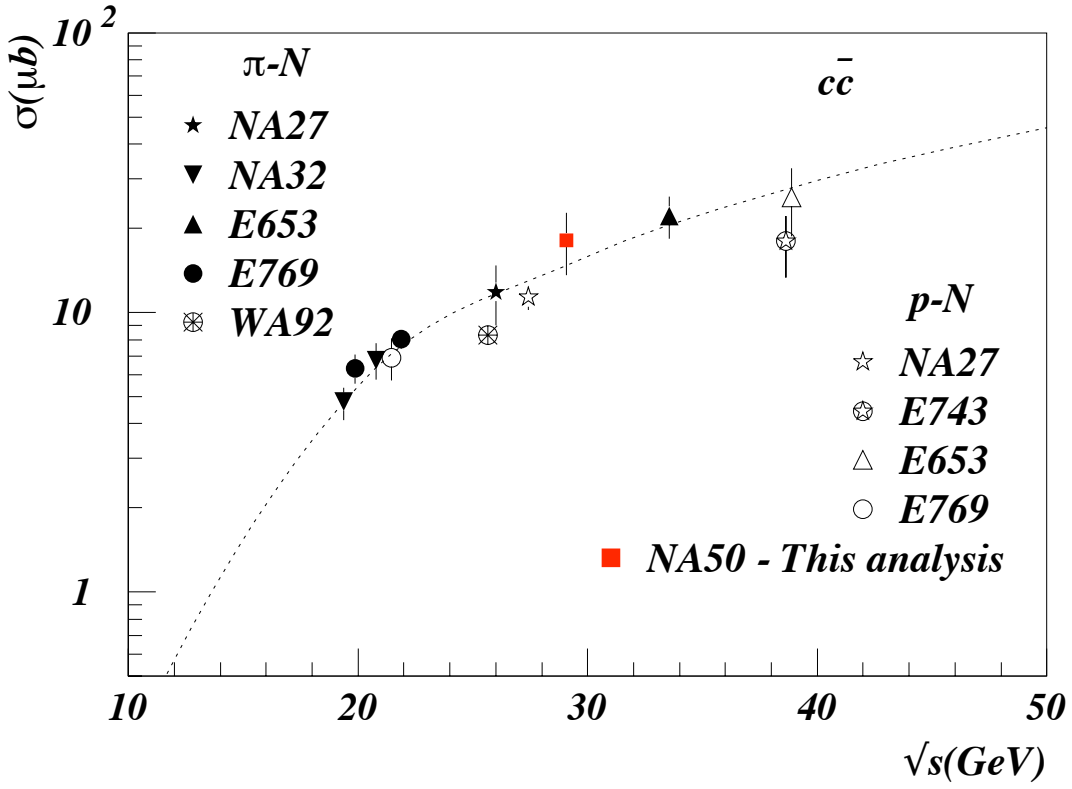

Figure 7.3: *Cross sections for forward (x_F>0) $c\bar{c}$ production compared with the value extrapolated from this analysis.*

	Energy (GeV/c)	E_T bin (GeV)	$\langle N_{part} \rangle$	$E_{open-charm}$
pW	450	all	$5. \pm 2.$	1.00
SU	200	1	$43. \pm 7.$	1.26 ± 0.18
SU	200	2	$65. \pm 6.$	1.29 ± 0.18
SU	200	3	$84. \pm 5.$	1.51 ± 0.20
SU	200	4	$101. \pm 5.$	1.88 ± 0.23
SU	200	5	$116. \pm 3.$	1.61 ± 0.22
PbPb	158	1	$63. \pm 18.$	2.38 ± 0.36
PbPb	158	2	$110. \pm 11.$	1.94 ± 0.27
PbPb	158	3	$149. \pm 11.$	1.94 ± 0.26
PbPb	158	4	$189. \pm 12.$	2.03 ± 0.26
PbPb	158	5	$231. \pm 13.$	3.05 ± 0.36
PbPb	158	6	$273. \pm 11.$	3.16 ± 0.38
PbPb	158	7	$310. \pm 10.$	2.57 ± 0.33
PbPb	158	8	$347. \pm 11.$	3.35 ± 0.43
PbPb	158	9	$381. \pm 7.$	3.56 ± 0.45

Table 7.4: *Enhancement of the open-charm dimuon yield with respect to pA results for the pW, PbPb and SU systems. The enhancement E has been calculated for each of the considered E_T bin; the number of participant nucleons in the collision is also listed. The errors on E come from the error on the measured $D\overline{D}/DY$ ($\simeq$10%) and from the error on the calculation of the luminosity (7$\div$10%). The systematic errors due to the normalisation to the $E\,|_{pA}$ value, 8%, and to the 12% incertitude in the B.R. measurement, have not been included because they would affect all the listed values in the same way (and direction).*

Two more systematic errors have not been included in the final error calculation because they affect all the listed E values in the same way (and direction) :

- The error carried by $E\,|_{pA}$ (9%), since all the measured E, $E\,|_{pA}$ included, have been normalised to $E\,|_{pA}$.
- The $\approx$ 24% error on the calculated cross sections for open charm dimuon production, which originates from the squared 12% incertitude on the used B.R.'s.

In fig.7.4 the same values have been plotted as a function of the number of participant nucleons N_{part} in the collision. The number of participants in the collision can be easily deduced using the known b vs. E_T correlation (see chapter 5); for each average value of the impact parameter b, the number of participants from the projectile and target nuclei can be computed using VENUS. The line superimposed on fig.7.4

corresponds to a fit to the plotted points with the function

$$E = m \cdot (N_{part} - 5.0) + 1.0 \tag{7.8}$$

with

$$m = 0.0068 \pm 0.0004 \tag{7.9}$$

and χ^2=1.2. Eq.7.8 implies that

$$\frac{\frac{(D\overline{D})}{DY}\,|^{AB}_{meas.}}{\frac{(D\overline{D})}{DY}\,|^{AB}_{expec.}} \propto N_{part} \tag{7.10}$$

which in turn means that the found open charm enhancement increases *quadratically* with the collision centrality, as explained in the following :

- The total number of participants, or number of wounded nucleons in a collision, at a impact parameter b, is proportional to the transverse energy E_T. If each wounded nucleon produces a fraction q of the total measured transverse energy, we can write[10] :

$$E_T = qN_{part} \tag{7.11}$$

- The number of DY pair produced in a collision at impact parameter b, is proportional to the number of effective nucleon-nucleon collisions $N_{coll}(b)$,

$$N_{DY}(b) \propto N_{coll}(b) \tag{7.12}$$

  which, when integrated over all impact parameter b, leads to

$$N_{DY}\,|_{all-E_T} \propto AB \tag{7.13}$$

- The number of effective nucleon-nucleon collisions N_{coll} also linearly increases with the number of wounded nucleons N_{part}[11]. We can therefore define[10] :

$$k(b) = \frac{N_{coll}(b) + 1}{N_{part}(b)} \propto q\frac{N_{DY(E_T)}}{E_T} \tag{7.14}$$

  The coefficient k is by definition equal to 1 in p-p and p-A collisions, but larger than 1 in nucleus-nucleus interactions where each wounded nucleon can participate to more than one elementary collision. The value of k therefore increases with the atomic number of the colliding nucleus and with the cms energy, since the number of N-N collisions depends on the inelastic nucleon-nucleon cross section[10], and increases with centrality within the same nuclear system.

Since the number of participants N_{part} in the collision and the number of produced DY pairs both linearly increase with the transverse energy E_T, the measured excess in the open charm dimuon yield increases *quadratically* with the collision centrality. This can be made evident if eq.7.10 is written as

$$\frac{D\overline{D}(b)\mid_{meas.}}{D\overline{D}\mid_{expec.}} \propto N_{part}(b) \cdot \frac{DY(b)\mid_{meas.}}{DY\mid_{all-E_T}} \propto k\frac{N_{part}^2}{AB} \tag{7.15}$$

Since the open charm hadro production is a hard process, its contribution to the dimuon yield is expected to linearly increase with the collision centrality (see chapter 1). We could therefore imagine that the open charm enhancement originates from a new softer source, and define

$$D\overline{D}(b)\mid_{meas.}^{total} = D\overline{D}(b)\mid_{meas.}^{new-source} + D\overline{D}(b)\mid_{meas.}^{hadro-prod.} \tag{7.16}$$

With the above, eq.7.15 could also be written as

$$D\overline{D}(b)\mid_{meas.}^{new-source} \propto N_{part}^2 \tag{7.17}$$

Thereafter, the quadratical dependence of the total open charm dimuon yield on the collision centrality reveals the existence of a new source for open charm production in nucleus-nucleus collisions already at SPS energy.

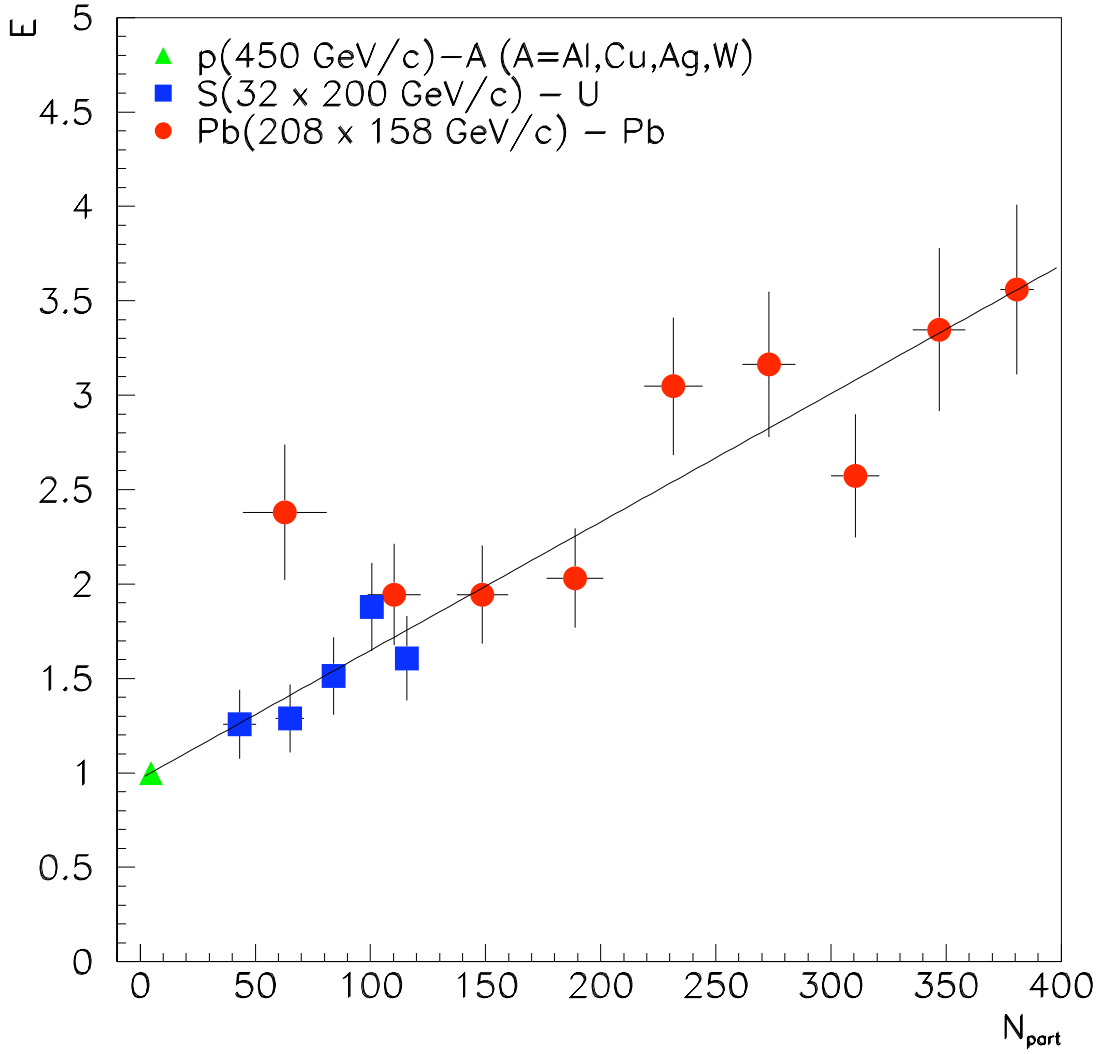

Figure 7.4: *Enhancement E of the open-charm dimuon yield, as defined in eq.7.7, versus the number of participant nucleons, as measured in 450 GeV/c p-A, 200 A GeV/c S-U and 158 A GeV/c Pb-Pb collisions. The corresponding values are listed in tab.7.4.*

7.4 Discussion

Since the results of the present work have been only very recently communicated to the scientific community[24, 25, 26], only few models exist which give a quantitative description of the measured IMR excess. In fact, different interpretations of the measured IMR excess also exist as, for instance, an enhanced dimuon yield from secondary Drell-Yan production. Furthermore, since the combinatorial background contribution to the IMR in very central PbPb collisions amounts to 95% of the opposite-sign dimuon events, it is necessary to prove that the measured excess is not unsubtracted background.

7.4.1 The measured excess *is not* unsubtracted BCK

In order to check whether the dimuon excess in the intermediate mass region can be accounted for with the background contribution only, the following test has been performed :

- The open charm contribution has been fixed at its expected value, as calculated in the present chapter.
- As in the previous analysis, the DY contribution is free but determined by the very high mass region, M>4.5 GeV/c^2.
- The background contribution is left free, i.e., the R_{BCK} factor is a free parameter in the fit of the opposite sign mass spectra.

In fig.7.5 the result of the fit to the most central PbPb bin is shown. It is evident that the shape of the measured excess can not be reproduced by the combinatorial background shape. Besides, the obtained R_{bck} values are unreasonably large; for instance, when fitting the most central PbPb bin we obtain R_{bck}=1.025, leading to a negative signal for M$\simeq$1.3 GeV/c^2.

7.4.2 D meson final state re-scattering

In a very recent paper[14], the open-charm enhancement measured in the present work is interpreted as due to a modification of the p_T differential distribution of charmed mesons. This modification, provoked by final state re-scattering of the D mesons inside the interaction volume created in the collision, would increase the percentage of D mesons decaying in the NA50 phase space. On the other hand, the actual open charm yield integrated over the whole phase space would remain unchanged. The model presented in ref.[14] is based on the following reasoning :

- The p_T differential distributions of the secondary hadrons produced in a nucleus-nucleus collision can be parametrised with an exponential

$$\frac{dN}{m_T dm_T} \propto e^{-(m_T - m)/T_{eff}} \tag{7.18}$$

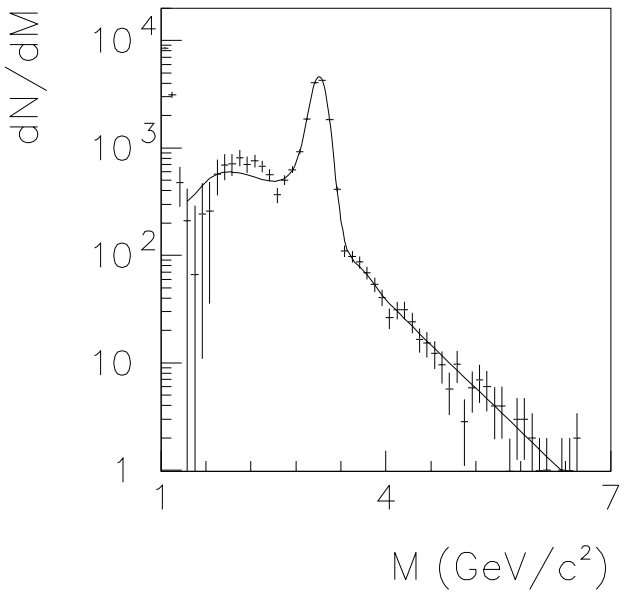

Figure 7.5: *Signal dimuon mass spectra for the 9^{th} PbPb bin. The curve has been obtained fitting the opposite-sign mass spectra; in the fit the open charm contribution has been fixed at the expected value whilst the R_{BCK} factor has been left free.*

The *slope* parameter T_{eff} has been measured[19, 20] to depend linearly on the particle mass and to increase with the size of the system created in the nucleus-nucleus collision. This is attributed to a collective transverse flow, which in turn is due to final state re-scattering among the secondary particles.

- D mesons are assumed to be affected by final state re-scattering in the same way as other hadrons do, thus T_{eff} for D mesons in central Pb-Pb collisions has the same value as the one measured for protons and ϕ mesons, T_{eff}=290 MeV.

- D mesons are assumed to thermalise within their *local* environment at the local temperature T. In the model, if T_{eff}=290 MeV, T $\approx$ 150 MeV.

- Open charm production is then computed using PYTHIA to simulate pp interactions at 158 GeV/c, with m_c=1.3 GeV/c^2 and σ_{k_T}=1 GeV/c. The charm pair differential distributions are thus obtained. The $\sigma_{c\bar{c}}^{PbPb}$ is derived using the $\sigma_{c\bar{c}}^{pp}$ for 200 A GeV/c pp collisions from ref.[21] and then correcting for the energy difference. The expected number of produced charm pairs is then calculated. The charm quarks then fragmentate (hadronize) in charmed hadrons.

- In the D mesons rest frame a local thermal momentum is randomly chosen from a thermal distribution and then boosted back to the laboratory frame.

In this way, both the transverse flow due to final state re-scattering and the longitudinal flow are taken into account. Thus, a strong correlation still exist between the scattered D mesons, due to the assumed longitudinal flow. If the D mesons where no more correlated, the generated cosθ distribution before kinematic cuts would be flat, which is not the case.

- An average branching ratio of 12% is assumed for the semileptonic decays of D mesons to muons.

- The NA50 acceptance cuts, as given in chapter 5 of the present work, are applied on the D meson differential distributions.

In fig.7.6 the predicted effect of final state re-scattering on the mass, rapidity and cosθ differential distribution *within* the NA50 acceptance is shown. The effect on the shape of the spectra is well visible on the mass distribution, whilst the shape of the cosθ and rapidity distributions are little affected. The strength of the effect depends on the chosen value for the local temperature T, as shown in fig.7.7 for the m_T distribution. To quantify the open charm enhancement in the NA50 phase space, the ratio R of accepted dimuon yield after and before final state re-scattering is defined. It is found that, when T=150 MeV, R=3.

If the measured open charm enhancement was actually due to the above mentioned mechanism, we would have probably not been able to reproduce the experimental p_T distributions as it was done in chapter 6. In chapter 6, the experimental p_T distributions were reproduced using the p_T differential shapes predicted by PYTHIA and normalised to the results of the fit of the mass spectra. Since we obtained a good data reproduction without invoking any additional mechanism, such as final state re-scattering, the hypothesis that such a mechanism plays an important role in the observed enhancement can be probably ruled out. Unfortunately, in ref.[14] the calculated dimuon p_T distribution has not been given, making it impossible to draw a direct comparison between the prediction of the final state re-scattering model and our p_T distributions.

It could be argued that, because of acceptance effects, the expected modification of the p_T distribution of the generated D mesons could be hardly resolved when the dimuon reconstructed spectra are studied. In fig.7.8 the generated and reconstructed p_T spectra of open charm dimuons are shown for two different values of σ_{k_T} and after kinematic cuts. For a dimuon invariant mass of 1.5 GeV/c^2, the difference in the generated spectra is $\approx$ a factor 2. The same factor is found when comparing the reconstructed spectra. We therefore conclude that even a small change in the generated spectra, within the phase space covered by NA50, would be easily resolved at the reconstruction level.

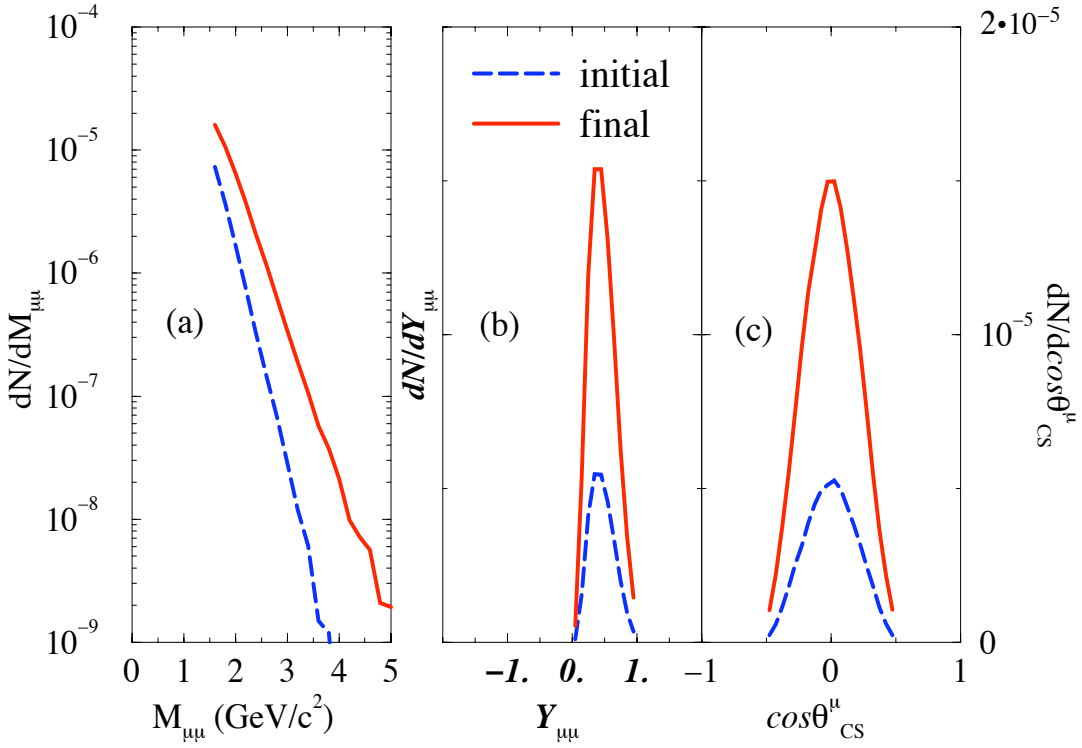

Figure 7.6: *(a) Invariant mass, (b) pair rapidity (c) $cos\theta_{CS}$ distributions of dimuons from D meson decays within NA50 acceptance as calculated in the model[14].*

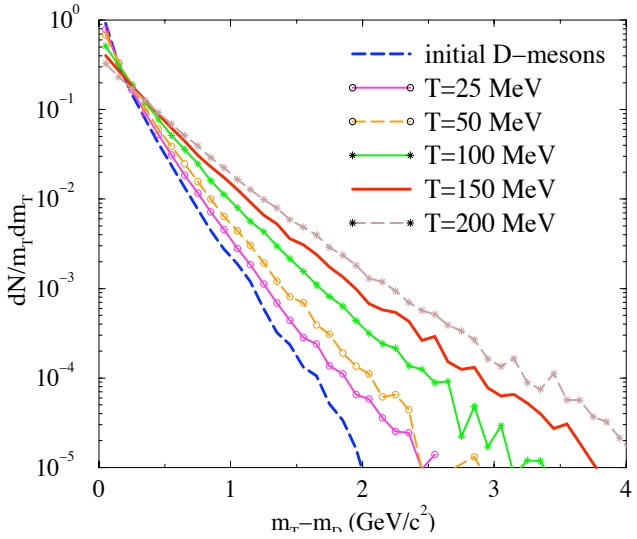

Figure 7.7: *m_T spectra of D mesons at mid-rapidity after final state re-scattering for different local temperature T[14].*

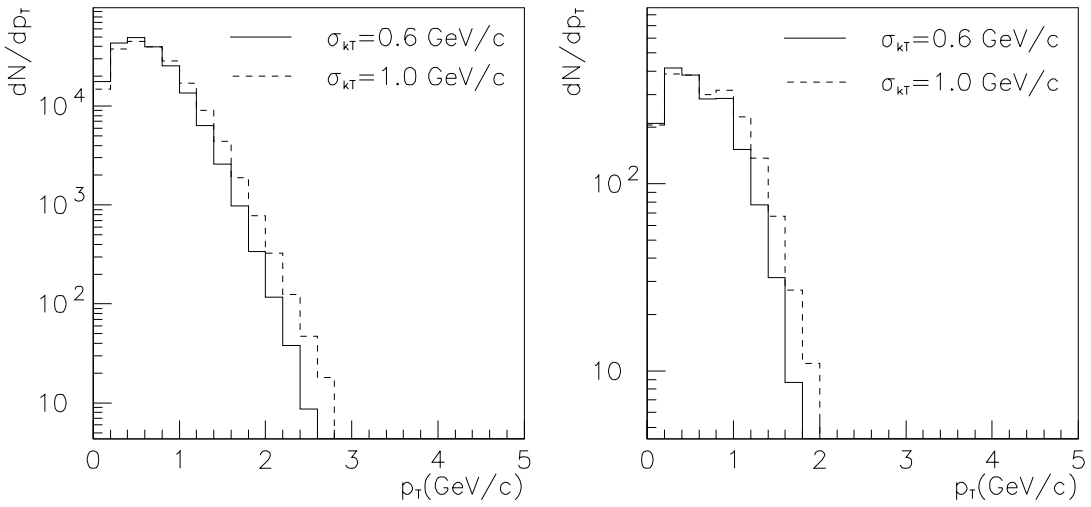

Figure 7.8: *Generated and reconstructed p_T differential distribution of dimuons from charmed hadron decays. Kinematic cuts have been applied on both distributions. Two different values of σ_{k_T} are compared. The two different σ_{k_T} values induce an equal difference on the generated and the reconstructed spectra.*

Initial state re-scattering

The authors in the same ref.[14] indicate that multiple scattering of partons in the initial state accounts for less than 10% of the observed excess.

Gluon anti-shadowing

Gluon anti-shadowing is the effect seen in the region of values of the parton longitudinal momentum fraction x where the ratio R, defined as the ratio of the PDF's for gluons in a heavy nucleus and in a proton, is larger than 1 (see chapter 1). For the values of x where R is larger than 1, the density of gluons in the nucleus is larger than the density of gluons in a free nucleon; the increased number of gluons could therefore lead to an enhanced heavy quark production. At SPS charm production takes places for $x \approx 0.2$, where gluon anti-shadowing is close to its maximum. In ref.[14] the contribution of gluon anti-shadowing to the open charm enhanced production has been evaluated to account for no more than $\approx 20\%$ of the observed excess.

7.4.3 Open charm production in soft baryon-baryon collisions

In ref.[15], a model for charm production in soft baryon-baryon collisions is developed. In the octet model for J/ψ and ψ' production and suppression in a hadron

gas (see chapter 1), the fully formed ψ' can be easily broken by the interactions with co-moving hadrons. In ref.[15] it is argued that the aforementioned comovers could either be fully formed hadrons (interacting via the exchange of gluons) or bare gluons. If a high density of bare energetic gluons existed in the interaction volume created in nucleus-nucleus collisions, the heavy quark production could be enhanced with respect to the yield measured in p-A interactions. Two energetic gluons could in fact easily interact to create a heavy quark pair via the gluon fusion process; two hadrons with the same energy would instead interact through the exchange of gluons carrying only a small fraction x of the hadron momenta, thus having a much smaller probability of exceeding the heavy quark mass threshold. Gluons would be produced in soft baryon-baryon collisions because of the strong field created when, after the collision, one q and one $\overline{q}$ (or a diquark) pull apart. Since the produced gluons would finally hadronize, the characteristics of their momentum spectrum could be deduced from the measured hadron spectra. Therefore, they would mainly be found in the mid-rapidity region.

To quantify the expected heavy quark pair production, the authors assume that in pA collisions the created gluons hadronize before they had time to fuse in a heavy quark pair. In nucleus-nucleus collisions the opposite is assumed, i.e., all the created gluons interact and produce heavy quark pairs. In this hypothesis, the excess measured in the previous NA38 analysis of the 200 A GeV/c SU system can be fairly well described, as shown in fig.7.9; the calculated enhancement shows a marked E_T dependence which qualitatively agrees with the results of the present work.

The same calculation is being performed for the 158 A GeV/c PbPb system[12], but since the results are still not known, no conclusive comparison can be drawn with the results of the present thesis.

7.4.4 Secondary DY production at SPS

In ref.[16] the role of secondary DY production in nucleus-nucleus collisions at SPS energy is studied. Secondary DY production is due to the electro-magnetic annihilation of the valence quarks of the secondary hadrons created in the collision. The dimuon yield from the secondary DY process is calculated as the sum of the contributions from all the possible hadron-hadron collisions, weighted by the inverse of the total hadron-hadron cross-section. Clearly, valence quark annihilation is most important in pion-nucleon, nucleon-antinucleon and pion-pion collisions. If only interactions between fully formed final state hadrons are allowed, the expected dimuon yield from secondary DY is found to be negligible in p-A interactions ($\approx$ 2%). In the same hypothesis, the predicted enhancement in 200 A GeV/c S-U and 160 GeV/c Pb-Pb amounts to 25% and 45% respectively for M$\simeq$1.5 GeV/c^2.

Next the authors include the contribution of DY dimuon from the annihilation of

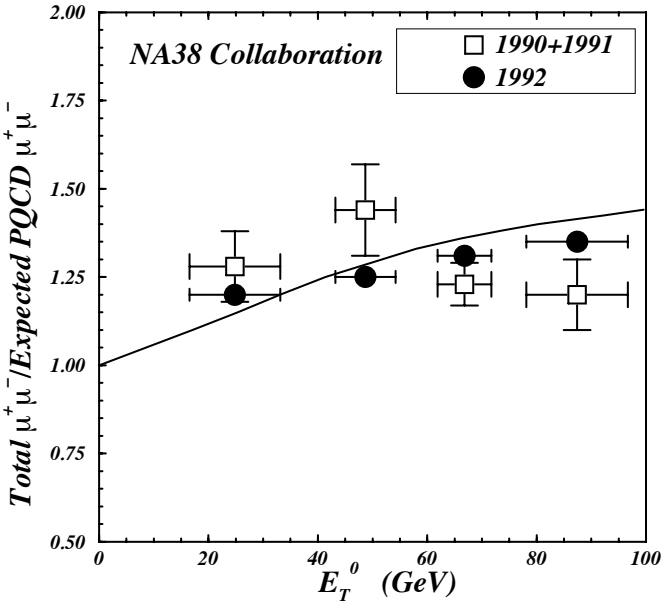

Figure 7.9: *Ratio of the total opposite-dimuon yield in 200 A GeV/c S-U collisions as measured by NA38 and expected from pQCD. The full line represents the same ratio as calculated in the frame of the model developed in ref.[15]. The ratio is plotted against the transverse energy E_T of the collision.*

partons which still have to hadronise, the so called primordial or pre-resonance $q\overline{q}$ annihilation. This is done considering that the secondary DY production can take place before the hadron formation time $\tau_F \approx$ 1 fm has elapsed. If secondary interactions are allowed for τ >0.5 fm, the predicted enhancement in the mass range 1.5< M <2 GeV/c^2 is in quite good agreement with the excess measured in the IMR region.

The authors point out that perturbative calculations cease to be totally reliable for M<2 GeV/c^2 and should not be trusted when M<1 GeV/c^2.

In the above described model the meson-baryon interactions are responsible for a fraction ≥90% of the produced secondary DY. Therefore, as the authors themselves conclude, the relative importance of this secondary dilepton source should *linearly increase* with the multiplicity of pions produced in the collision, in clear disagreement with the finding of the present work.

7.4.5 Comparison with the HELIOS/3 results

The HELIOS/3 experiment[17] at the CERN SPS has measured the dimuon production in the low and intermediate mass regions in 200 A GeV/c p-W and S-W

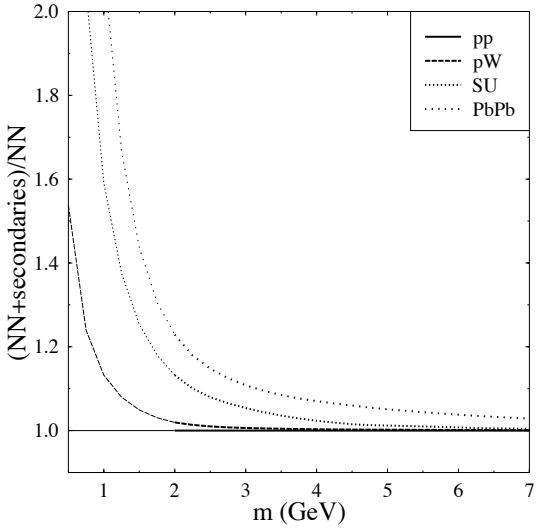

Figure 7.10: *Mass spectra of the dilepton produced in primary and secondary hadronic collisions normalized to the dileptons produced in primary nucleon-nucleon scattering only. The ratio is shown for different colliding systems, pp, 200 GeV/c p-W, 200 A GeV/c S-U and 160 A GeV/c Pb-Pb and for y_{cms}=0.5. The thinner parts of the lines indicate the mass region where perturbative calculations cease to be completely reliable[16].*

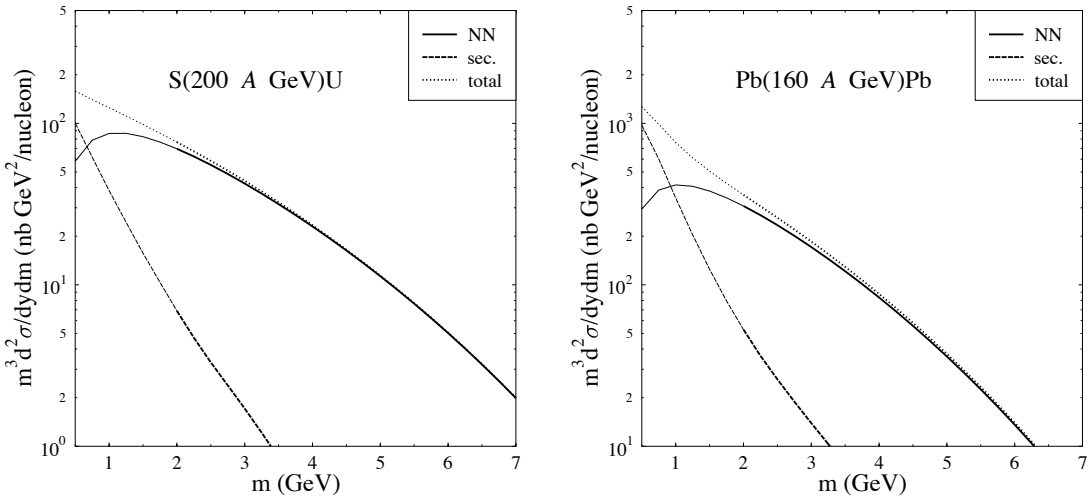

Figure 7.11: *Differential DY cross section per unit rapidity at y_{cms}=0.5. The calculation has been performed for the 200 A GeV/c S-U (left) and 160 A GeV/c Pb-Pb (right) 10% most central collisions. The shape of the different contributions to the total DY cross section are shown. The contribution of the pre-resonance DY production is not shown. The thinner part of the lines indicated the mass region where perturbative calculation cease to be completely reliable[16].*

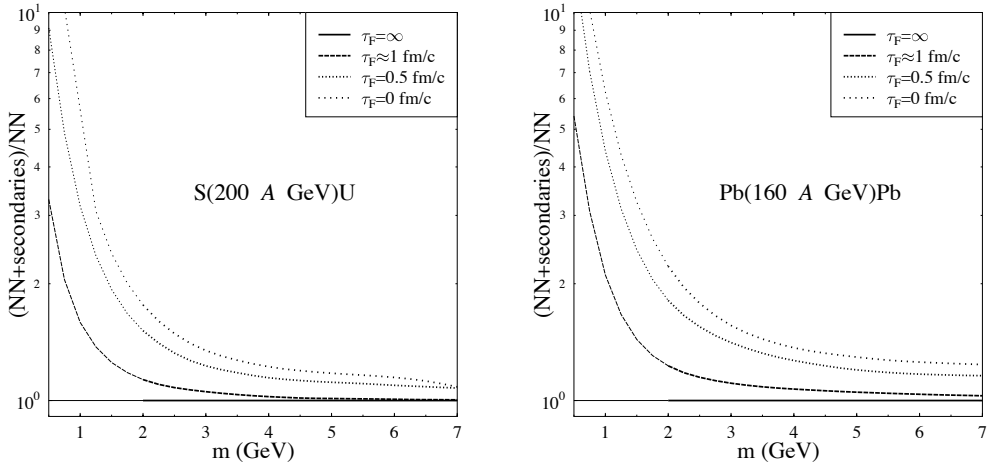

Figure 7.12: *Mass spectra of the dilepton produced in primary and secondary hadronic collisions normalized to the dileptons produced in primary nucleon-nucleon scattering only. Preresonance DY production is also taken into account varying the hadron formation time. The ratio is shown for 200 A GeV/c S-U (left) and 160 A GeV/c Pb-Pb (right) collisions and for y_{cms}=0.5. When τ_F=0.5, the dilepton enhancement amounts to a factor 3 in Pb-Pb collisions and to a factor 2 in S-U collisions. The thinner parts of the lines indicate the mass region where perturbative calculations cease to be totally reliable[16].*

collisions. The experiment was not originally designed to measure the dimuon production in the IMR region, but the amount of data collected in that region of mass were large enough to motivate the search for a dimuon enhancement both in the low and in the intermediate mass regions. The experiment covers the rapidity interval $3.0< y <7.0$. The SW data have been grouped in 6 different classes corresponding to different values of the charged particle multiplicity. The charged particle multiplicity was measured in the pseudorapidity range $3.7< \eta <5.5$. Three more classes have also been defined, the minimum bias class, constructed from all multiplicy classes, the peripheral event class, corresponding to the sum of classes 1 and 2, and the central event one, corresponding to the multiplicity classes 3÷6. The combinatorial background contribution has been determined similarly to what has been done in the present work. For 200 A GeV/c S-W and p-W collisions the calculated R_{BCK} factors are R_{BCK}=1.14±0.02 and R_{bck}=1.57±0.10 respectively. Both values are large if compared to the result of the present thesis; this difference is due to the different acceptance of the spectrometer; furthermore, the apparatus of HELIOS/3 presented different acceptances for positive and negative muons and no image cut was implemented[23].
The intermediate mass region has been analysed in two different ways. First, a direct comparison has been drawn between the p-W and the S-W data normalized to their respective charged particle multiplicities. In the second type of analysis, only

the IMR has been studied and reproduced with the superposition of the known contributing processes. No fit was performed. This second approach is somewhat more similar to the approach we used in the present work. The expected contributions are the tails of the low mass vector mesons, ρ, ϕ, ω, the DY muon pairs and dimuons from the semi-leptonic decay of charmed mesons. The open charm dimuon mass spectrum has been determined using PYTHIA 5.6, whilst the expected open charm dimuon contribution in S-W interactions has been computed from the cross section measured by NA38 in p-W collisions at 200 GeV/c, $\sigma^{c\overline{c}}$=(8.2±0.2) $\mu b/nucleon$. The DY mass shape was determined with PYTHIA 5.6, tuning the intrinsic k_T value in order to get the best reproduction of the experimental p_T distribution. The DY cross section expected in p-W and S-W collisions at 200 GeV/c has been calculated in the frame of the naif parton model, i.e., no dependence on the scale Q^2 has been included (see chapter 1), and then multiplied by a common K_{DY}=2.5±0.5. The cross section for DY production has been calculated in the kinematic range defined by -1< x_F <1 and 1≤ M ≤4 GeV/c^2; this implies that no additional cuts on $cos\theta$ has been applied. Notice that a direct extrapolation of the DY contribution from the high mass region was not feasible because of lack of data. The expected dimuon contribution from the above listed sources have then been normalized to the charged multiplicity, as done for the experimental data.

The excess is then given as the ratio D/S of measured and expected sources in the two mass regions 1.35< M <2.5 and 1.6< M <2.5 GeV/c^2. Only the multiplicity classes 3,4,5,6 are used, because of the little statistics collected in the more peripheral ones. Of the total error on the D/S ratio, 70-80% comes from the data whilst 20% comes from the calculated expected sources. The D/S ratio is affected by a ≈ 20%-30% incertitude for the mass region 1.6< M <2.5 GeV/c^2 and 10%-20% incertitude for the wider mass region range. In fig.7.13 the measured D/S ratio is plotted against the charged multiplicity for the two indicated IMR ranges.

The ratio D/S is not immediatly comparable with the open charm enhancement given in the present work. In fact it is in general very difficult to compare the D/S ratios measured by experiments covering different kinematic domains. The comparison between our results and HELIOS/3 can thus be only qualitative. The HELIOS/3 Collaboration concludes that the measured excess linearly depends on the charged particle multiplicity. It is actually difficult to agree with such conclusion, since only the most central bins have been analyzed and the bin number 3, although included in the final analysis, still presents a large statistical incertitude. On the overall, it is reassuring that the HELIOS/3 Collaboration indipendently measures an excess in the IMR region, qualitatively confirming the results of the NA38/NA50 Collaboration.

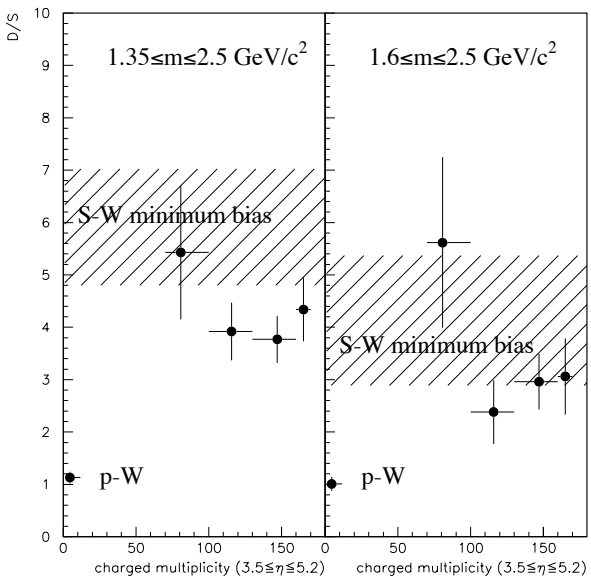

Figure 7.13: *The HELIOS/3 D/S ratio as a function of the charged multiplicity. The charged multiplicty has been measured in the pseudorapidity interval 3.5≤ η ≤5.2. The shaded area corresponds to D/S=5.91±1.11 and 4.13±1.24 as measured on the minimum bias class of events.*

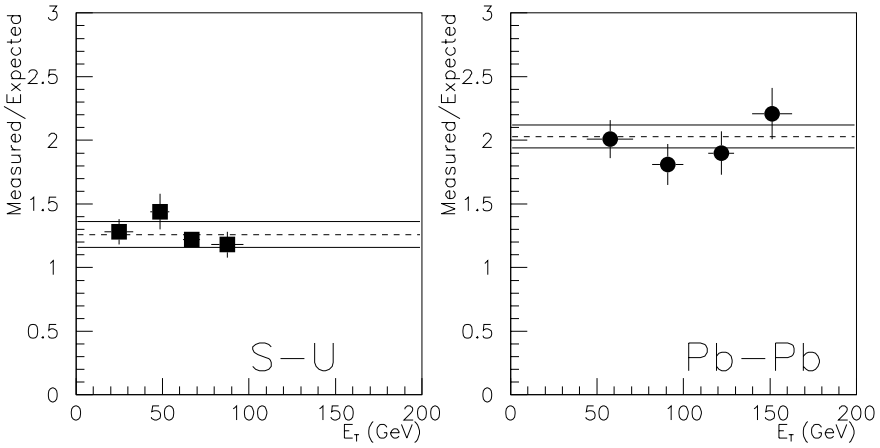

Figure 7.14: *Centrality dependence of the excess in 200 A GeV/c S-U (1992, NA38) and 158 A GeV/c Pb-Pb collisions (1995, NA50) as presented at QM'96 by the NA38/NA50 Collaboration[18].*

7.4.6 Comparison with the NA38/NA50 previous results

The NA38/NA50 Collaboration at QM'93[22] presented the results of the analysis of the 200 A GeV/c SU data whereas the results of the analysis of the low statistics 158 A GeV/c PbPb (1995) data were presented at QM'96[18]. The excess was measured in the form of the D/S ratio and plotted as a function of the transverse energy E_T, as shown in fig.7.14 Qualitatively, the QM'96 data do not disagree with the present finding when the main differences in the two performed analysis are taken into account. When the SU and PbPb sets of data were analysed, a common R_{BCK} factor equal to 1 for all centrality bins and both systems was assumed. We now know that this is not correct. If, for instance, a larger R_{BCK} factor had been assumed for the more peripheral PbPb bin, the quadratical dependence of the excess on the collision centrality would have been more evident. Notice however that the D/S presented at QM'96 for the PbPb set of data already suggested a stronger than linear increase of the excess with centrality.

7.5 Conclusion

The NA38/NA50 data collected in 450 GeV/c p-A, 200 A GeV/c S-U and 158 A GeV/c Pb-Pb collisions have been analysed. The dimuon mass spectra in the IMR are well described by a superposition of dimuons from charmed meson (and baryon) semi-leptonic decays and DY, after combinatorial background subtraction. The combinatorial background subtraction has been performed calculating the contribution of the charge correlated background with the help of a specifically developed Monte-Carlo chain. The dimuon production from open charm in S-U and Pb-Pb interactions, normalized to the pA results, is enhanced with respect to leading order pQCD calculations, where the open charm production is assumed to scale with $A \times B$. A factor $\simeq 1.6$ enhancement is found in central S-U collisions and a factor $\simeq 3$ in central Pb-Pb. The analysis of the intermediate mass region p_T spectra provides further support to the hypothesis that the excess dimuons originate from open charm decays. The measured excess shows a marked quadratical dependence on the collision centrality. A clear theoretical understanding of the underlying physical process is still lacking but the measured centrality dependence of the excess could rule out some of the proposed interpretations.

This work, which was only very recently presented[25, 24, 26], triggered a considerable interest from the heavy-ion community, both from the theoretical and the experimental side. An example is the report prepared after the Meeting on Heavy Ion Physics at the SPS, held in September 1998, which was meant to assess the present status of the field, to list the remaining open questions and to evaluate the physics issues for which the SPS fixed target programme remains competitive in the near future. In the resulting final report, the following lines can be read : "[...] we would like to mention open charm as an area presently not covered by any of the

existing experiments. Open charm production is closely related to charmonium production. There are indirect indications (by NA50) for an enhancement (compared to A^2 scaling of pp results) in open charm production. A direct measurement is needed for confirmation, and the feasibility should be seriously studied"[27].

Bibliography

[1] P.Braun-Munzinger et al., Eur. Phys. J., C : 1, 1-2 (1998) 123-30

[2] S.Frixione et al., Heavy Flavours II A J Buras and M Lindner Advanced Series on Directions in High-Energy Physics World Sci., Singapore.

[3] G.A.Alves et al., E769 Collaboration, Phys.Rev.Lett., 77(12) (1996)2388

[4] S.Barlag et al., ACCMOR Collaboration, Phys.Lett. B 247(1) (1990)113

[5] M.C.Abreu et al, NA50 Collaboration, Physics Letters B410(1997)327

[6] M.C.Abreu et al, NA50 Collaboration, Physics Letters B410(1997)337

[7] C.Soave, Analysis of the pAl 1997 and pW 1996 data sets, NA50 Coll. meeting, July 1997.

[8] L.Fredj, Ph.D de l'Universit Blaise Pascal, Clermont II, LPC-Clermont, 1991.

[9] Ito et al., E288 Collaboration, Phys.Rev.D 23 (1981) 604.

[10] D.Kharzeev, Nucl.Phys.A610,(1996)418c-433c.

[11] J.Ftacnik et al., Phys.Lett.B 196,no.3,(1987)387.

[12] C-Y Wong, private communication.

[13] Frederic Fleuret, PhD thesis, April 1997, E.P.,Paris.

[14] Z.Lin et al., Preprint nucl-th/9808033, 1998.

[15] C-Y Wong et al., Preprint hep-ph/9510233, 1995 and Phys. Lett., B : 367 (1996) 50-54.

[16] C.Spieles at al., Preprint hep-ph/9706525, 1997.

[17] A.L.S. Angelis et al., HELIOS/3 Collaboration, Preprint CERN-EP-98-082, submitted to Z.Phys.

[18] E.Scomparin for the NA50 Collaboration at QM'96, Nucl. Phys., A : 610(1996) (331c-341c)

[19] N.XU for the NA44 Collab., Nucl. Phys. A610, 175c (1996); I.G. Bearden et al., NA44 Collab., Phys. Rev.Lett.78,2080 (1997).

[20] G.Roland for the NA49 Collab., Proceedings at the QM'97 Conference.

[21] C.Lourenço, Ph.D. Thesis, Universidad Tecnica de Lisboa, 1995.

[22] C.Lourenco, for the NA38 Collaboration at the Quark Matter '93 Conference, Borlange, Sweden (1993).

[23] I.Kralik, Ph.D. thesis, Inst. of Experimental Physics, Slovak Academy of Science, Kosice, 1995.

[24] E.Scomparin for the NA50 Collaboration, Workshop on Quarkonium Production in Relativistic Nuclear Collisions, Seattle, May 11-15, 1998

[25] C.Soave for the NA50 Collaboration, XXIX International Conference on High Energy Physics, ICHEP'98, Vancouver, July 23-29, 1998

[26] E.Scomparin for the NA50 Collaboration, Strangeness in Quark Matter 98 Conference, Padova, July 20-24, 1998

[27] Status Report of the Relativistic Heavy Ion Programme at the CERN SPS, September 1998.

ACKNOWLEDGEMENTS

It is my own and deep pleasure to here thank all the people who helped me during the preparation of this thesis. The work here presented has been developed in strict and continuous collaboration with Dr.Enrico Scomparin. I am enormously grateful to Dr.Enrico Scomparin who guided my work and introduced me in the difficult world of the analysis of the NA50 data. I believe that these last years have been, up until now, the most fruitful and interesting years of my working experience.

I also thank Mrs.Sanda Dita and Mr.Serban Constantinescu for their precious help in the background calculation using the Fake Opposite Sign method which we used for the Pb-Pb set of data.

Thank you to my Supervisor Prof.E.Chiavassa, who carefully read this work and supported me when necessary, and Mrs.Claudie Gerschel who accepted to report on my work on the committee for the final examination of my PhD thesis.

Finally, I want to thank all the people in the NA50 Collaboration, and in particular the ZDC group within the same Collaboration, for their sympathy and their constant practical help.

And deep from my heart...

Grazie Enrico per tutto il tuo aiuto, per la tua compagnia, per la tua simpatia, per il tuo appoggio morale e tecnico e per avermi sempre seguita con attenzione. Grazie per tutto quello che mi hai insegnato e per la fiducia che mi hai trasmesso.

Grazie Roberta per la tua allegria, per il tuo aiuto pratico sempre efficiente e sorridente, per l'affetto di cui mi hai circondato e per la splendida settimana passata assieme ad Otranto. Grazie Roberta e Francesco per la vostra compagnia a Brookhaven e NYC che ricorderò sempre con una punta di nostalgia. Grazie Stefania per la tua simpatia e per essere sempre stata pronta ad aiutarmi quando necessario. Grazie all'affetto delle persone che mi hanno circondato in questi anni, tra cui voi tutti già citati ed Alfredo, Anna, Beppe, Emilio, Ermanno, Mauro e Nora. Merci aussi à Anna Piaget pour toutes les attentions qu'elle m'a dédiées. Grazie inoltre al simpaticissimo Prof.Mauro Anselmino per il seminario interessante che ho con lui preparato per il passaggio al secondo anno di dottorato.

Grazie poi a tutte le persone che, meno direttamente coinvolte nel mio lavoro, mi hanno dato il loro tempo, la loro amicizia ed il loro amore, rendendomi facile il compito di vivere bene essendo soddisfatta dell'esistenza. Thank you Paul, for all your patience, your constant moral support, for having always known that I could make it and for our life together. Grazie a Monica e Douglas per essermi sempre stati vicini. Grazie a Cinzia per le lunghe camminate nei boschi e le interminabili chiacchierate. Grazie a Federico per avermi sempre ed ancora circondata di affetto. Thank you Christoph for your sympathy, your close friendship and for the wonderful little holiday in Vienna. Grazie a Luca e Barbara, per tutti i momenti belli condivisi. Grazie a Mauro, Corinne, Florian e Isabelle e Celine per i tanti momenti difficili ed i tanti momenti divertenti passati assieme nella preparazione di Huis Clos. Grazie a tutte le persone che hanno saputo apprezzare anche questo lato della mia esistenza. Thank you also to all the people who gave me their company, even when occasional, come il dolce Eugenio and the calm and reliable Michael.

Last but not least, grazie a Chi ha fatto si che io abbia la madre, il padre e la sorella che ho. Grazie a loro per essermi sempre stati vicini.